

UNIVERSITY of CALIFORNIA
Santa Barbara

**Development of The Fundamental Components of A Superconducting Qubit
Quantum Computer**

A dissertation submitted in partial satisfaction of the
requirements for the degree of

Doctor of Philosophy

in

Physics

by

Radoslaw (Radek) Cezary Bialczak

Committee in charge:

Professor John M. Martinis, Chair
Professor Andrew N. Cleland
Professor Wim van Dam

June 2011

The dissertation of Radoslaw (Radek) Cezary Bialczak is approved:

Professor Andrew N. Cleland

Professor Wim van Dam

Professor John M. Martinis

April 2011

Development of The Fundamental Components of A Superconducting Qubit

Quantum Computer

Copyright © 2011

by Radoslaw (Radek) Cezary Bialczak

To my parents,
Halina Rypina Youssef and Magdi Youssef
and my grandparents,
Zdzisława and Franciszek Rypina

Acknowledgements

Like many of life's journeys, this one was not undertaken alone. I have many people to thank for their help during my physics Ph.D. First, I'd like to thank my advisor, John Martinis, for providing the infrastructure and funding to do our research and for educating us as scientists. He taught us how to implement complex technical projects in a way that combined scientific creativity with engineering precision and sustainability. Unlike a lot of Ph.D. advisors, he also ensured that we learned the communication, salesmanship, and writing skills that are such an important part of being a successful scientist and a successful professional in any field. John, also thank you for taking us climbing all those times. It was lots of fun! I would also like to thank Andrew Cleland with whom we collaborated closely. Andrew, thank you for making yourself available when I needed advice about my science career and thank you for making time to attend our group meetings in addition to your own, and providing crucial input on our research. I also wanted to thank Sasha Korotkov and his group. Your theoretical work was extremely useful for understanding our experiments. In addition, I would like to thank the staff of the UCSB Nanofabrication Facility. Without such a smoothly running cleanroom, the work in this thesis would not have been possible. Finally, I also wanted to thank Wim van Dam for agreeing to be on my committee on short notice and for reviewing my thesis.

It has been an honor and pleasure to work with so many great people in our research

group. I have learned a lot from all of you and it's been a lot of fun. I will miss our lab! Robert and Matthias, thank you for mentoring me when I first joined the group. Erik and Max, you guys have been great friends and climbing buddies. We need to get together for another epic outdoor trip like Yosemite! Dan Sank, thank you for being chill and genuine and for having a true passion for physics which was very inspirational. Haohua and Nadav, I appreciate all the times you have helped me when I had questions on research and needed a second opinion. Jim, thank you for going out of your way to help everyone, especially with the tedious administrative tasks. We appreciate it a lot more than we show it. Aaron, Markus, Martin, Matthew, and Rami, it was a pleasure to have you as lab and office mates. All the discussions, pranks, and lunches made day to day lab life a lot of fun. Amit, Anthony, Jian, Julian, Mike, Peter, Ted, Yi, Yu, the group grew pretty quickly so we didn't get to know each other too well, but it was a pleasure to work with all of you.

I also owe much thanks to everyone from the UCSB chapter of Engineers Without Borders, especially Mary Dinh, David Bothman, Vered Doctori, Kimberley Kline, Luke Bawazer, Nikki Virgilio, and everyone on the Kenya and Peru Projects. You guys all made a really big impact on my life and I learned a lot from everyone at EWB. EWB played a very important role in my life. It helped me gain real leadership skills, taught me how to start and manage a logistically and financially complex project from scratch, and allowed me to make a direct positive impact on the lives of others. Although I'm

very focused on science when in lab, I love to work with people and EWB was an outlet to do so outside of lab. EWB also opened my mind and broadened my horizons by giving me the opportunity to travel to different parts of the world and to experience how others live by living among them. EWB gave me a new perspective on life and made me appreciate the simple things in life more.

Finally, I would like to thank my family without whom none of this would be possible. To my parents, Halina and Magdi, and my grandparents, Zdzisława and Franciszek, I want to thank you for always encouraging me and loving me unconditionally. Thank you for always being there for me and working so hard against great hardship so that I could have a shot at a better life. A Ph.D. feels like a small and easy task compared to my parents' journey. They legally immigrated to the U.S. and started here with no English, few possessions, and little money. They went on to raise a great family, run multiple successful businesses, and live the American dream. Many people don't appreciate the hard work and intellect needed to successfully start from scratch in a new place against great odds like my parents did. I have always looked up to my parents for this accomplishment and they, along with my grandparents, have served as an inspiration and as my role models throughout my life. To my sister Natalia Youssef, despite my sometimes blunt nature, you have always been there for me. I value your input and am lucky to have such a great sister! Music and art are the soul of humanity and you are very talented in both. Never give up on these, especially as you become occupied

with career and family later in life. Last, but definitely not least I would like to thank my girlfriend, Loan Nguyen. Loan, thank you for your love and for being there for me. It's been said that to be truly happy one needs something to do, someone to love, and something to hope for. For me, that someone is you! You are my love and my best friend.

Curriculum Vitæ

Radoslaw (Radek) Cezary Bialczak

Education

- 2011 (exp.) Doctor of Philosophy, Physics, University of California, Santa Barbara
- 2007 Master of Arts, Physics, University of California, Santa Barbara
- 2004 Bachelor of Arts, Physics, Cornell University

Publications

R. C. Bialczak, M. Ansmann, M. Hofheinz, M. Lenander, E. Lucero, M. Neeley, A. D. O’Connell, D. Sank, H. Wang, M. Weides, J. Wenner, T. Yamamoto, A. N. Cleland, J. M. Martinis Fast tunable coupler for superconducting qubits *Physical Review Letters* **106**, 060501 (2011).

H. Wang, Matteo Mariantoni, Radoslaw C. Bialczak, M. Lenander, Erik Lucero, M. Neeley, A. D. O’Connell, D. Sank, M. Weides, J. Wenner, T. Yamamoto, Y. Yin, J. Zhao, John M. Martinis, A. N. Cleland Deterministic entanglement of photons in two superconducting microwave resonators *Physical Review Letters* **106**, 060401 (2011).

T. Yamamoto, M. Neeley, E. Lucero, R. C. Bialczak, J. Kelly, M. Lenander, Matteo Mariantoni, A. D. O’Connell, D. Sank, H. Wang, M. Weides, J. Wenner, Y. Yin, A. N. Cleland, John M. Martinis Quantum process tomography of two-qubit controlled-Z and controlled-NOT gates using superconducting phase qubits *Physical Review B* **82**, 184515 (2010).

Erik Lucero, Julian Kelly, Radoslaw C. Bilaczak, Mike Lenander, Matteo Mariantoni, Matthew Neeley, A. D. O’Connell, Daniel Sank, H. Wang, Martin Weides, James Wenner, Tsuyoshi Yamamoto, A. N. Cleland, John M. Martinis Reduced phase error through optimized control of a superconducting qubit *Physical Review A* **82**, 042339 (2010).

M. Neeley, R. C. Bialczak, M. Lenander, E. Lucero, M. Mariantoni, A. D. O’Connell, D. Sank, H. Wang, M. Weides, J. Wenner, Y. Yin, T. Yamamoto, A. N. Cleland, J. M. Martinis. Generation of Three-Qubit Entangled States using Superconducting Phase Qubits. *Nature* **467**, 570-573 (2010).

R. C. Bialczak, M. Ansmann, M. Hofheinz, E. Lucero, M. Neeley, A. D. O’Connell, D. Sank, H. Wang, J. Wenner, M. Steffen, A. N. Cleland, J. M. Martinis. Quantum Process Tomography of a Universal Entangling Gate Implemented with Josephson Phase Qubits. *Nature Physics* **6**, 409–413 (2010).

A. D. O’Connell, M. Hofheinz, M. Ansmann, R. C. Bialczak, M. Lenander, E. Lucero, M. Neeley, D. Sank, H. Wang, M. Weides, J. Wenner, J. M. Martinis, A. N. Cleland. Quantum ground state and single-phonon control of a mechanical resonator. *Nature* **464**, 697–703 (2010).

H. Wang, M. Hofheinz, M. Ansmann, R. C. Bialczak, E. Lucero, M. Neeley, A. D. O’Connell, D. Sank, M. Weides, J. Wenner, A. N. Cleland, J. M. Martinis. Decoherence Dynamics of Complex Photon States in a Superconducting Circuit. *Physical Review Letters* **103**, 3200404 (2009).

H. Wang, M. Hofheinz, J. Wenner, M. Ansmann, R. C. Bialczak, M. Lenander, E. Lucero, M. Neeley, A. D. O’Connell, D. Sank, M. Weides, A. N. Cleland, J. M. Martinis. Improving the Coherence Time of Superconducting Coplanar Resonators. *Applied Physics Letters* **95**, 233508 (2009).

M. Ansmann, H. Wang, R. C. Bialczak, M. Hofheinz, E. Lucero, M. Neeley, A. D. O’Connell, D. Sank, M. Weides, J. Wenner, A. N. Cleland, J. M. Martinis. Violation of Bell’s inequality in Josephson phase qubits. *Nature* **461**, 504–506 (2009).

M. Neeley, M. Ansmann, R. C. Bialczak, M. Hofheinz, E. Lucero, A. D. O’Connell, D. Sank, H. Wang, J. Wenner, A. N. Cleland, M. R. Geller, J. M. Martinis. Emulation of a Quantum Spin with a Superconducting Phase Qudit. *Science* **325**, 722 (2009).

M. Hofheinz, H. Wang, M. Ansmann, R. C. Bialczak, E. Lucero, M. Neeley, A. D. O’Connell, D. Sank, J. Wenner, J. M. Martinis, A. N. Cleland. Synthesizing arbitrary quantum states in a superconducting resonator. *Nature* **459**, 546–549 (2009).

C. Song, T. W. Heitmann, M. P. DeFeo, K. Yu, R. McDermott, M. Neeley, J. M. Martinis, B. L. T. Plourde. Microwave response of vortices in superconducting thin films of Re and Al. *Physical Review B* **79**, 174512 (2009).

H. Wang, M. Hofheinz, M. Ansmann, R. C. Bialczak, E. Lucero, M. Neeley, A. D. O’Connell, D. Sank, J. Wenner, A. N. Cleland, J. M. Martinis. Measurement of the decay of Fock states in a superconducting quantum circuit. *Physical Review Letters*

101, 240401 (2008).

M. Hofheinz, E. M. Weig, M. Ansmann, R. C. Bialczak, E. Lucero, M. Neeley, A. D. O’Connell, H. Wang, J. M. Martinis, A. N. Cleland. Generation of Fock states in a superconducting quantum circuit. *Nature* **454**, 310–314 (2008).

N. Katz, M. Neeley, M. Ansmann, R. C. Bialczak, M. Hofheinz, E. Lucero, A. D. O’Connell, H. Wang, A. N. Cleland, J. M. Martinis, A. N. Korotkov. Reversal of the Weak Measurement of a Quantum State in a Superconducting Phase Qubit. *Physical Review Letters* **101**, 200401 (2008).

M. Neeley, M. Ansmann, R. C. Bialczak, M. Hofheinz, N. Katz, E. Lucero, A. D. O’Connell, H. Wang, A. N. Cleland, J. M. Martinis. Process tomography of quantum memory in a Josephson-phase qubit coupled to a two-level state. *Nature Physics* **4**, 523–526 (2008).

A. D. O’Connell, M. Ansmann, R. C. Bialczak, M. Hofheinz, N. Katz, E. Lucero, C. McKenney, M. Neeley, H. Wang, E. M. Weig, A. N. Cleland, J. M. Martinis. Microwave Dielectric Loss at Single Photon Energies and milliKelvin Temperatures. *Applied Physics Letters* **92**, 112903 (2008).

E. Lucero, M. Hofheinz, M. Ansmann, R. C. Bialczak, N. Katz, M. Neeley, A. D. O’Connell, H. Wang, A. N. Cleland, J. M. Martinis. High-fidelity gates in a Josephson qubit. *Physical Review Letters* **100**, 247001 (2008).

M. Neeley, M. Ansmann, R. C. Bialczak, M. Hofheinz, N. Katz, E. Lucero, A. D. O’Connell, H. Wang, A. N. Cleland, J. M. Martinis. Transformed Dissipation in Superconducting Quantum Circuits. *Physical Review B* **77**, 180508(R) (2008).

R. C. Bialczak, R. McDermott, M. Ansmann, M. Hofheinz, N. Katz, E. Lucero, M. Neeley, A. D. O’Connell, H. Wang, A. N. Cleland, J. M. Martinis. $1/f$ Flux Noise in Josephson Phase Qubits. *Physical Review Letters* **99**, 187006 (2007).

M. Steffen, M. Ansmann, R. C. Bialczak, N. Katz, E. Lucero, R. McDermott, M. Neeley, E. M. Weig, A. N. Cleland, J. M. Martinis. Measurement of the Entanglement of Two Superconducting Qubits via State Tomography. *Science* **313**, 1423–1425 (2006).

N. Katz, M. Ansmann, R. C. Bialczak, E. Lucero, R. McDermott, M. Neeley, M. Steffen, E. M. Weig, A. N. Cleland, J. M. Martinis, A. N. Korotkov. Coherent state evo-

lution in a superconducting qubit from partial-collapse measurement. *Science* **312**, 1498–1500 (2006).

M. Steffen, M. Ansmann, R. McDermott, N. Katz, R. C. Bialczak, E. Lucero, M. Neeley, E. M. Weig, A. N. Cleland, J. M. Martinis. State tomography of capacitively shunted phase qubits with high fidelity. *Physical Review Letters* **97**, 050502 (2006).

A. N. Pasupathy, J. Park, C. Chang, A. V. Soldatov, S. Lebedkin, R. C. Bialczak, J. E. Grose, L. A. K. Donev, J. P. Sethna, D. C. Ralph, P. L. McEuen Vibration-assisted electron tunneling in C140 single-molecule transistors. *Nano Lett.* **5**, 203 (2005).

A.N. Pasupathy, R.C. Bialczak, J. Martinek, L.A.K. Donev, J.E.Grose, P.L. McEuen, D.C.Ralph The Kondo effect in the presence of itinerant-electron ferromagnetism. *Science* **306**, 86 (2004).

Abstract

Development of The Fundamental Components of A Superconducting Qubit Quantum
Computer

by

Radoslaw (Radek) Cezary Bialczak

Superconducting qubits have emerged as a promising architecture for building a scalable quantum computer. In this thesis we use a particular type of superconducting qubit architecture, the flux-biased phase qubit, to build and characterize the fundamental components of a quantum computer: universal quantum gates and a scalable qubit coupling architecture.

A universal quantum gate allows for the construction of any arbitrary quantum computing operations, and is the analog of classical universal logic gates like the NAND gate. We build this gate using a pair of coupled flux-biased phase qubits where the coupling magnitude is fixed. We characterize this coupled qubit system and show how to construct the gate from the Hamiltonian of this two-qubit system. The universal quantum gate must also be characterized to verify that it has been constructed properly. However, to completely characterize a quantum gate, its output must be mapped out for any arbitrary input. Due to the infinite Hilbert space of qubits, such a characterization

is more involved than simply obtaining a truth table, as would be done for classical computational logic. To achieve a complete characterization of a quantum gate we use a technique called quantum process tomography (QPT). We perform QPT on our universal gate, the “square-root of i -swap” gate, and for the first time in any solid state qubit architecture we completely characterize a universal quantum gate. As a result of this gate characterization, we discover that our gate performance is limited by qubit dephasing times. We are also able to measure noise correlations in the coupled qubit system using QPT. We find that by increasing the coupling strength between the qubits, we can build faster gates. This lets us get around the limits imposed by dephasing times by increasing the speed at which we can execute our universal gate. However, increasing the coupling strength of our fixed coupling scheme leads to increased errors during single qubit operations and measurement. In addition, we also discuss the difficulties in scaling up fixed coupling schemes to many qubits.

To address these issues, we design a tunable coupling architecture that allows us to operate at higher coupling strengths during the gate operation and near zero coupling during single-qubit operations and measurement. This minimizes single-qubit errors and measurement crosstalk while allowing for a much faster universal gate. We experimentally show that using this coupler the measurement crosstalk can be minimized and the inter-qubit coupling strength can be tuned arbitrarily, over nanosecond time scales, within a sequence of operations that mimics actual use in an algorithm. Unlike pre-

viously demonstrated tunable couplers, this novel tunable coupling circuit is designed to be modular and physically separate from the qubits. It also allows superconducting qubits to be coupled over long distances. This allows the coupler to be used as a module to connect a variety of elements such as qubits, resonators, amplifiers, and readout circuitry over distances much larger than nearest-neighbor. Such design flexibility is likely to be useful for scaling up a quantum computer and allows for the construction of new superconducting microwave circuits with tunable interactions between elements.

Contents

1	Foreword	1
1.1	A guide for the reader	1
2	Introduction to Quantum Computing	3
2.1	Why is quantum computing important? A historical perspective.	3
2.2	Qubit physics in a nutshell	5
2.2.1	Qubit basics and the Bloch sphere	6
2.2.2	The density operator formalism and multiple qubits	8
2.2.3	Quantum operations	12
2.2.4	Qubit-environment interactions: decoherence and visibility	13
2.3	Classical v.s. quantum computation	15
3	Superconducting Qubits	19
3.1	Superconducting qubits compared to other architectures	20
3.2	The Josephson junction: the key element of superconducting qubits	21

3.3	Types of superconducting qubits	29
4	Single Phase Qubit Design and Operation	33
4.1	The flux-biased phase qubit	33
4.2	Single Qubit Biasing, Measurement, Readout and Logic Operations . . .	37
4.2.1	Flux Bias and Measurement	37
4.2.2	Readout	41
4.2.3	Logic Operations	44
4.3	Experimental Characterization of A Single Qubit	46
4.3.1	Calibrating the readout, qubit reset, and bias points	47
4.3.2	Step Edge: fine calibration of the bias point	53
4.3.3	S-curve: measurement pulse amplitude calibration	56
4.3.4	Spectroscopy	59
4.3.5	Rabi Oscillations	64
4.3.6	Measuring energy relaxation	69
4.3.7	Measuring dephasing	72
5	Connecting Phase Qubits Using Fixed Coupling	77
5.1	Fixed Capacitive Coupling	77
5.1.1	Two-qubit circuit Hamiltonian and the swap operation	78

5.1.2	Measuring coupled qubits: single-shot measurement and measurement crosstalk	82
5.1.3	Detuning and errors due to fixed coupling	83
5.2	Experimental bring-up and characterization of capacitively coupled phase qubits	85
5.2.1	Calibrating qubit operating biases for turning on and for minimizing the coupling interaction	85
5.2.2	The swap experiment	88
5.2.3	Measuring on/off ratio of capacitively coupled qubits	92
5.2.4	Phase calibration for two-qubit microwave pulses	94
5.2.5	State tomography of the 16 two-qubit basis states	98
6	Demonstration and Characterization of A Universal Quantum Gate	105
6.1	What is a universal quantum gate?	105
6.2	Experimental characterization of a universal quantum gate using quantum process tomography (QPT)	109
6.2.1	Motivation	109
6.2.2	Quantum process tomography of the SQiSW gate	111
6.2.3	Improving gate performance	116
7	Connecting Phase Qubits Using Tunable Coupling	119

7.1	Motivation and prior work	119
7.2	This tunable coupler design	120
7.3	Coupler characterization and dynamic performance	123
7.3.1	Static performance: tuning the avoided-level crossing	124
7.3.2	Static performance: Measurement crosstalk minimization	125
7.3.3	Dynamic performance: the tunable swap operation	126
7.4	Scalability: the on/off ratio and stray capacitances, long-distance coupling and modularity	130
7.5	Technical points: multistability of the coupler circuit and influence of coupler bias on qubit bias	133
7.5.1	Coupler reset protocol	134
7.5.2	Compensation for qubit bias shift due to coupler bias	137
7.5.3	Future work on tunable coupling	138
A	Device Fabrication	141
A.0.4	Substrate	142
A.0.5	Base wiring deposition and patterning	143
A.0.6	Dielectric deposition and patterning	143
A.0.7	Junction base electrode Al deposition and definition	144
A.0.8	Josephson junction oxidation and definition	145
A.0.9	Top wiring and shorting strap definition	146

A.0.10 Dielectric etch	146
A.0.11 Shorting strap etch	147
B Electronics And Low Temperature Experimental Set-up	149
B.1 Low temperature setup	149
B.1.1 The SQUID lines	151
B.1.2 The flux bias and measurement/z-pulse lines	152
B.1.3 The microwave line	152
B.2 Room temperature electronics	154
C Calculation of capacitive coupling Hamiltonian	157
D Quantum Tomography calibrations and physicality	161
D.1 Calibrating out measurement errors	161
D.2 State tomography data and measurement calibration	165
D.3 Physicality of the χ Matrix	165
D.4 MATLAB and Mathematica code used for state tomography analysis . .	170
D.4.1 State tomography pre-processing using Mathematica	170
D.4.2 State tomography data analysis using MATLAB	178
D.5 MATLAB code used for process tomography analysis	184
D.5.1 MATLAB code used for process tomography	184

Chapter 1

Foreword

1.1 A guide for the reader

The subsequent chapters will proceed as follows. Chapter 2 contains a brief overview of qubit physics, how quantum computers differ from classical computers, and why quantum computation is important. Chapter 3 contains a brief overview of superconducting qubits and introduces the different superconducting qubit types. Chapter 4 introduces the flux-biased phase qubit that will be used throughout this thesis and provides a detailed discussion of experiments needed to calibrate and characterize a single flux-biased phase qubit. Chapter 5 introduces the fixed coupling architecture used to implement our universal gate, the “square-root of i -swap” gate. It also discusses in detail how the coupling architecture can be characterized. We also show that we can

precisely control two qubits by preparing the full set of two-qubit basis states with high fidelity. In Chapter 6, we move on to implementing the universal gate and characterizing it using quantum process tomography. We analyze the quantum process tomography and use it to determine that our gate performance is limited by decoherence. We propose a tunable coupling scheme which allows us to perform gate operations on much faster timescales, thereby lowering the errors from decoherence. In Chapter 7, we introduce the tunable coupling scheme and characterize it in detail.

In the appendices, we include more technical, but nevertheless important and useful details. Appendix A contains a discussion of the microfabrication steps used to fabricate the qubit devices used in this thesis. Appendix B contains an overview of the low temperature and room temperature electronics and filtering used in the experiment. Appendix C contains the calculation of the Hamiltonian for two capacitively coupled qubits. Appendix D contains technical points of the quantum process tomography analysis, including computer code used to analyze the quantum process tomography data.

Through out the thesis, important terms and non-standard definitions are in bold and important concepts are italicized.

Chapter 2

Introduction to Quantum Computing

2.1 Why is quantum computing important? A historical perspective.

Classical programmable computing has been the driving force behind the information age that has so extensively transformed our lives. What we think of as a classical programmable computer, such as a PC or a supercomputer like the IBM Deep Blue, is based on a theoretical model of computation called the Turing machine, developed by Alan Turing in 1937 [81]. Shortly after, Turing's work was combined with the prior work of Alonzo Church to show that [20] a Turing machine is capable of simulating any algorithmic process **efficiently**, *i.e.* in a time that scales no slower than a polynomial of the size of the problem. However, in the 1970's, work on probabilistic computing

showed that other computational schemes could produce efficient solutions to problems which did not have efficient solutions on a Turing Machine and its variants [71]. This work motivated the work of David Deutsch in the 1980's which showed [23] that a computer based on quantum mechanics could efficiently solve certain problems that had no efficient solution on a classical computer. Deutsch's work was followed in the 1990's by that of Shor and Grover [69, 30]. Shor showed that the problem of factoring prime numbers, which had no efficient solutions on classical computers, could be solved more efficiently using a quantum computer. Grover showed that the quantum version of the algorithm used to search an unsorted list of n entries had a \sqrt{n} speed up compared to the classical version. Both of these problems have important practical applications. The search problem is important in searching databases like those used by many Internet websites and search engines, and the factoring problem is important in encryption. However, there is another very important area of application for quantum computers.

In 1982, Richard Feynman showed that a Turing machine could not simulate quantum effects in physical systems efficiently and proposed that a quantum computer could be used to do so [28]. These simulations are at the heart of theoretical chemistry and, as such, are the basis for modeling a variety of physical systems, from single molecules to large biological macromolecules like proteins. Classical computer simulations of these molecular systems, although computationally inefficient, have advanced greatly since

the 1980's due to the miniaturization of transistor logic, which has increased classical computing power exponentially. However, Moore's law, which describes the exponential advances in the miniaturization of computer logic, predicts that this miniaturization will reach its limits by 2015-2020. Therefore, new models of computation such as quantum computing must be explored.

Hence, although quantum computing is presently applicable only to the small subset of problems consisting of search, factoring, and quantum simulation, it is important because these problems are at the heart of many fields of science and engineering today. Furthermore, research into quantum information has inspired the development of other new technologies such as quantum encryption, which have found very important potential applications in areas like secure communication.

The above answers "why quantum computing?" Now let us answer the question "what is a quantum computer?" In the simplest sense, a quantum computer is a collection of quantum bits, or **qubits**, that can interact to perform logic operations. Therefore, to understand what a quantum computer is and how it differs from classical computers, we must first understand the physics of single qubits.

2.2 Qubit physics in a nutshell

The basics of qubit physics will only be covered briefly in this thesis, only to highlight concepts that will be used in the chapters that follow. If the reader is interested in

more detail, then there are many excellent texts where more information can be found. For general quantum mechanics, texts by Sakurai [66], Gottfried [29], and Cohen-Tannoudji [21] are good starting points. As explained below, a qubit is a quantum two-level system, therefore the quantum theory of two-level systems forms the theoretical foundation of quantum computing. Much of the initial work on the physics of quantum two-level systems was done on systems of photons interacting with atoms. Therefore texts on atom-photon interactions are very useful in gaining a better understanding of the theory behind single-qubit experiments like the Rabi, Ramsey, T_1 , and spin echo experiments that will be discussed in this thesis. Notable texts on atom-photon interactions are those by Allen/Eberly [1] and Weissbluth [84]. For texts specifically focused on quantum computing, the most popular would probably be by Nielsen and Chuang [58]. It reviews both the physics theory and the computer science behind quantum information. However, it is a bit dated so newer texts on quantum information are also helpful [38, 14].

2.2.1 Qubit basics and the Bloch sphere

A single qubit is a two-level quantum system. The simplest example is the spin of an electron where the up and down spin states represent the two quantum states $|1\rangle$ and $|0\rangle$. Excitations at a frequency $\omega_{01}/2\pi = (E_{|1\rangle} - E_{|0\rangle})/\hbar$ are used to drive transitions between the energy levels of the qubit states, $|1\rangle$ and $|0\rangle$. Hence, like the 0 and 1 states

of classical bits, qubits can be in their two states, $|0\rangle$ and $|1\rangle$. However, unlike classical bits, they can also be in both the $|0\rangle$ and $|1\rangle$ states simultaneously. Such states are called **superposition states** and are written as $\alpha|0\rangle + \beta|1\rangle$, where α and β can be complex numbers. In an actual experiment we measure the qubit to be either in the $|0\rangle$ or the $|1\rangle$ state with probability given by the square of the amplitude of α or β , respectively. This must satisfy $|\alpha|^2 + |\beta|^2 = 1$ to conserve probability.

A visually intuitive picture of a qubit can be constructed by rewriting a single-qubit superposition state in its most general mathematical representation

$$|\psi\rangle = e^{i\gamma} \left(\cos \frac{\theta}{2} |1\rangle + e^{i\phi} \sin \frac{\theta}{2} |0\rangle \right) \quad (2.1)$$

where $|\psi\rangle$ is the label given to a general single qubit state. Since only probabilities $|\langle 0|\psi\rangle|^2$ and $|\langle 1|\psi\rangle|^2$ are measured, the phase factor γ has no observable effect and can be set to zero. The variables θ and ϕ are real numbers that together define a point on the surface of a unit sphere, as shown in Figure 2.1. This sphere is known as the **Bloch sphere** and it allows for a convenient visual representation of single qubit states and operations on those states. As given by (2.1), the point on the the Bloch sphere surface defined by θ and ϕ represents a pure quantum state. The vector \vec{r} , also called the **Bloch vector** or **state vector**, is defined below and can represent a pure or mixed state.

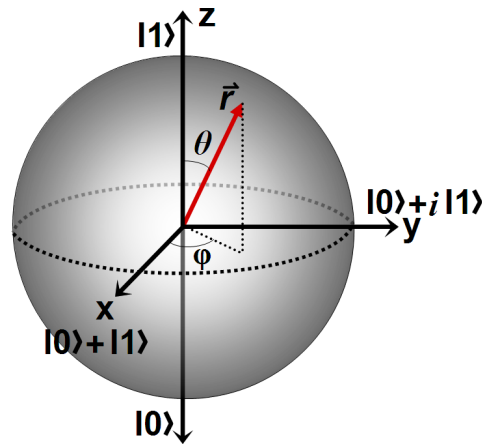


Figure 2.1: **The Bloch sphere.** This solid unit sphere is a convenient way to visually represent a general single-qubit quantum state and operations on it. The angles θ and ϕ correspond to those given in the equation for a general quantum state in (2.1). The vector, \vec{r} , is given by the mapping in (2.6) and can represent a pure quantum state if it falls on the surface of the Bloch sphere or a mixed quantum state if it falls inside the sphere. The qubit states $\{|0\rangle, |1\rangle, (|0\rangle + i|1\rangle)/\sqrt{2}, (|0\rangle + |1\rangle)/\sqrt{2}\}$ can be found at the intersections of the unit sphere with the x, y, and z axes, where the factor of $\sqrt{2}$ has been left off for visual clarity. Qubit operations can be represented as linear combinations of rotations about the x, y, and z Bloch sphere axes.

2.2.2 The density operator formalism and multiple qubits

Qubit physics can also be formulated using the mathematics of **density matrices**, also known as **density operators**. This formalism can be used to model pure states like those that can be represented using the state-based formalism shown in (2.1), but unlike the state-based formalism, it can also model statistical mixtures of quantum states. It also can be easily generalized to quantum systems composed of multiple parts, such as multiple qubits. It also facilitates the modeling of operations on such multipartite systems and the effects of decoherence. This formalism will be used extensively in this thesis, especially in the chapters dealing with the characterization of universal quantum

gates. The basics of density matrices can be found in [84, 21, 66].

The density operator can be defined as follows. If a quantum system is in one of a number of states $|\psi_i\rangle$ with probability p_i , then the density operator, ρ , for that system is defined as [58]

$$\rho \equiv \sum_i p_i |\psi_i\rangle \langle \psi_i| \quad (2.2)$$

Any arbitrary density matrix must satisfy a few important properties. First, any density matrix must have unit trace, $tr(\rho) = 1$, because

$$\begin{aligned} tr(\rho) &= \sum_i p_i tr(|\psi_i\rangle \langle \psi_i|) \\ &= \sum_i p_i = 1 \end{aligned} \quad (2.3)$$

Also, any density matrix is positive semidefinite because

$$\begin{aligned} \langle \gamma | \rho | \gamma \rangle &= \sum_i p_i \langle \gamma | \psi_i \rangle \langle \psi_i | \gamma \rangle \\ &= \sum_i p_i |\langle \gamma | \psi_i \rangle|^2 \\ &\geq 0 \end{aligned} \quad (2.4)$$

where $|\gamma\rangle$ is any arbitrary state. Finally, $tr(\rho^2) \leq 1$, because

$$\begin{aligned}
tr(\rho^2) &= tr \sum_i (p_i |\Psi_i\rangle \langle \Psi_i|) (p_i |\Psi_i\rangle \langle \Psi_i|) \\
&= \sum_i p_i^2 tr(|\Psi_i\rangle \langle \Psi_i| |\Psi_i\rangle \langle \Psi_i|) \\
&= \sum_i p_i^2 tr(|\Psi_i\rangle \langle \Psi_i|) \\
&= \sum_i p_i^2 \leq 1
\end{aligned} \tag{2.5}$$

If the state described by ρ is a pure state then $tr(\rho^2) = 1$, otherwise $tr(\rho^2) < 1$. The density matrix formalism can also be mapped to the Bloch sphere picture by writing a density operator as

$$\rho = \frac{I + \vec{r} \cdot \vec{\sigma}}{2} \tag{2.6}$$

where $\vec{\sigma} = \sigma_x \hat{x} + \sigma_y \hat{y} + \sigma_z \hat{z}$ and $\{\sigma_x, \sigma_y, \sigma_z\}$ are Pauli matrices [66] and \vec{r} is a real, three-dimensional vector with $\|\vec{r}\| \leq 1$. Pure states have $\|\vec{r}\| = 1$ and mixed states have $\|\vec{r}\| < 1$.

Another important class of quantum states are **entangled states**. Entangled states are a special class of multi-qubit states which cannot be written as a Kronecker product of individual single qubit states [38]. For example, a given entangled state, $|\Psi_e\rangle$, for qubits A and B is entangled if there are no $\alpha_{0,1}$ or $\beta_{0,1}$ such that $|\Psi_e\rangle = (\alpha_0 |0\rangle_A + \alpha_1 |1\rangle_A)(\beta_0 |0\rangle_B + \beta_1 |1\rangle_B)$. This non-separable nature of entangled states has important consequences. It implies that for an entangled set of qubits, the measurement

of one qubit in the set affects the measurement of the other qubits. This can be understood using a simple example of the two-qubit entangled state $|\Phi_e\rangle = (|0\rangle_A |0\rangle_B + |1\rangle_A |1\rangle_B)/\sqrt{2}$. If we measure qubit A and get 0 (1) then qubit B must necessarily be 0 (1) as well. Thus the measurement results are correlated or entangled. This correlation will exist even when the qubits are separated in space or time or if the axis of measurement is changed. Our example state above is known as a Bell state and, along with other multi-qubit entangled states, it exhibits measurement correlations that do not exist in classical systems [7]. Entanglement can give rise to quantum interference effects which can be exploited for quantum computing [58]. Entangled states can also be used to demonstrate more exotic physical phenomena such as the teleportation of quantum states [8].

As mentioned at the beginning of this section, an important strength of the density matrix formalism is that it can easily describe systems of multiple qubits. A multi-qubit state that is not an entangled state can be described by the Kronecker product of the density matrices of the states of the individual qubits. That is, for a system of n qubits, the density matrix of the multi-qubit system, ρ_{system} , is given by $\rho_{system} = \rho_1 \otimes \rho_2 \otimes \dots \otimes \rho_n$. The ρ_i are the density matrices of the individual qubit states, with $i = 1, 2, \dots, n$. Additionally, density matrices can be used to address individual components of composite quantum systems by tracing out the subsystems that are not of interest. For example, if we are interested only in the density operator for qubit A, but have

available only the density matrix for a composite system of two qubits, A and B , we can trace out qubit B by using the partial trace over B : $\rho^A \equiv tr_B(\rho^{AB})$. As discussed in [58], the partial trace tr_B is defined by $tr_B(|a_1\rangle\langle a_2| \otimes |b_1\rangle\langle b_2|) \equiv |a_1\rangle\langle a_2| tr(|b_1\rangle\langle b_2|)$ where $|a_1\rangle$ and $|a_2\rangle$ are any two vectors in the state space of A and $|b_1\rangle$ and $|b_2\rangle$ are any vectors in the state space of B and $tr(|b_1\rangle\langle b_2|) = \langle b_1|b_2\rangle$.

2.2.3 Quantum operations

Operations on quantum states and interactions of a qubit with its environment can be represented as linear combinations of the identity operator, I , and rotations about the X , Y , and Z axes of the Bloch sphere. Operations are usually symbolized using the symbol U because *all quantum operations are unitary and linear* [58, 66]. So a rotation about the X axis by an angle θ would be written as $U = X_\theta$. With the density matrix formalism, it is easy to mathematically describe a system of qubits interacting with an external environment.

One merely abstracts away everything but the system of qubits into a separate environmental density matrix, ρ_{env} . Then a partial trace over this environment density matrix is performed in order to isolate just the system of qubits

$$\varepsilon(\rho) = tr_{env}[U(\rho \otimes \rho_{env})U^\dagger] \quad (2.7)$$

where $\epsilon(\rho)$ represents the result of the operation, U , on the system of qubits ρ .

Quantum operations, like density operators, can be represented as matrices. Analogously operations on multiple qubits can be tensored together just like density matrices of multi-qubit systems. For example, given a system of 4 qubits we can represent a X_π rotation on qubit 1, a $Y_{\pi/2}$ rotation on qubit 2, a Z_π rotation on qubit 3 and an X_π rotation on qubit 4 as: $X_\pi \otimes Y_{\pi/2} \otimes Z_\pi \otimes X_\pi$. Certain combinations of single qubit and two-qubit operations can be used to carry out any logical quantum operation. This special combination of operations is known as a **universal quantum gate** and will be discussed in Chapter 6 of this thesis.

2.2.4 Qubit-environment interactions: decoherence and visibility

Energy relaxation and **dephasing** are two main deleterious pathways through which qubits interact with their environment in a way that causes them to lose quantum coherence over time. Together, these two interactions are typically called **decoherence** effects [58]. As with much of qubit physics, the terminology and physical mechanisms behind decoherence have their origins in the field of NMR and atom-photon interactions [84, 1]. Visual representations of energy relaxation and dephasing in the energy level and Bloch sphere frameworks are shown in Figure 2.2. Energy relaxation is the process by which a qubit in the excited state ($|1\rangle$) decays to the ground state ($|0\rangle$) by dissipating energy into its environment, much like in spontaneous emission in atomic

physics. Dephasing causes the qubit energy level spacing, and hence the ω_{01} transition frequency, to randomly fluctuate due to interactions with the environment. This causes the loss of phase coherence, ϕ , of the quantum state as given in (2.1).

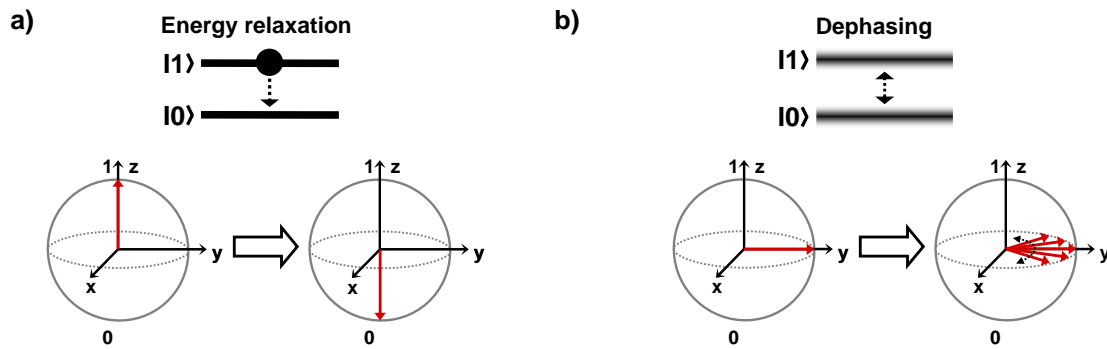


Figure 2.2: **Decoherence.** Energy relaxation and dephasing are the two types of qubit decoherence mechanisms by which a qubit can lose quantum coherence by interacting with its environment. Here, these two processes are illustrated using the energy level and Bloch sphere representations. **a)** In energy relaxation, a qubit in the excited state will decay to the ground state via energy relaxation. **b)** Dephasing causes the energy level spacing between the qubit states to jitter leading to a loss of phase coherence in the qubit state as discussed in the text.

The strength of each decoherence mechanism can be experimentally quantified by measuring the time it takes for a qubit to lose coherence by a certain factor. As will be discussed later in Chapter 4, decoherence caused by energy relaxation can be mathematically described using an exponential function that decays in time. Therefore, to quantify the amount of energy relaxation, we can measure the time it takes qubit coherence to decay by a factor of $1/e$. However, the $1/e$ time is also used to quantify the coherence due to dephasing where the mathematical time dependence has a Gaussian component. These $1/e$ times are commonly assigned the labels T_1 , for energy

relaxation, and T_ϕ , for dephasing. Since energy relaxation also causes loss of phase coherence, the two times are often expressed as one characteristic decoherence timescale, T_2 , where $1/T_2 = 1/(2T_1) + 1/T_\phi$. Using the quantum master equation approach it can also be shown that $T_2 \leq 2T_1$ as derived in [84].

Another class of qubit errors that is important are those that lead to a decrease in **visibility** [83], a quantity related to measurement. Visibility can be understood as discussed below and as shown in Figures 2.3a and b. Ideally, we should be able to prepare the $|0\rangle$ and $|1\rangle$ states with unit probability. However, due to interactions of the qubit with its environment, or because of imperfections in qubit control, readout, or measurement this probability is often less than unity. For example, if we expect the probability of the qubit being in the $|0\rangle$ state, P_0 to be 1.0, but we instead measure .95 and if we expect the probability of the qubit being in the $|1\rangle$ state, P_1 to be 1.0, but we measure .90, then the visibility is $.90 - (1.0 - .95) = .85$.

2.3 Classical v.s. quantum computation

Now that we have a better understanding of what a qubit is, we can compare quantum computers to classical computers. A quantum computer is fundamentally different from a classical computer, both in the way it is physically implemented and in how it encodes and manipulates information. The most significant difference between classical and quantum computers is that quantum computers are not limited to the binary subspace

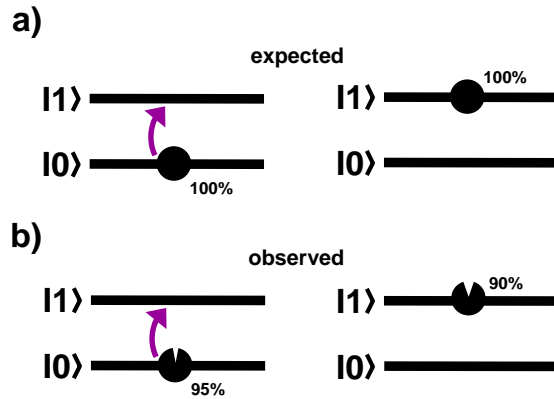


Figure 2.3: **Visibility**. We expect to be able to prepare the $|0\rangle$ and $|1\rangle$ states with unit probability. **(b)** Due to visibility errors however, this is not always possible. Here we illustrate the preparation of the $|0\rangle$ state with 95% probability and the $|1\rangle$ state with 90% probability. Hence the visibility is 85%.

of just a 0 or a 1 as is the case for a classical boolean bit. Instead, quantum computers operate on the much larger qubit space which is a 2 dimensional complex vector space where the phase and amplitude of a qubit state can take on an infinite number of values. Quantum computers are also capable of being prepared in superposition. This ability endows a quantum computer with an inherent parallelism not available to classical computers. This parallelism can be demonstrated with a simple example. Let us compare the information that can be encoded and processed using a given number of classical and quantum bits. Using a given sequence of 6 classical bits we can encode *one number at a time*, say 101010 or 42. However, because quantum states can be in superpositions, 6 quantum bits can be used to encode and process 2^6 values *simultaneously* using the superposition state $\alpha_0 |000000\rangle + \alpha_1 |000001\rangle + \dots + \alpha_{44} |101100\rangle + \dots + \alpha_{63} |111111\rangle$. Where it is the set of 64 complex values, $\{\alpha_0, \alpha_1, \dots, \alpha_{63}\}$, that contains this informa-

tion. However, there is a hidden cost to this “free” parallelism because the quantum coherence of the states must be preserved during operation and for many qubits. This is difficult to implement experimentally. Not all is lost however, because a class of techniques called **quantum error correction** has been developed to correct for certain errors due to decoherence effects [58].

One might also wonder if there is a precise set of criteria that define a quantum computer. Such a set was developed during the 30 or so years since the idea for a quantum computer was first put forward. These criteria are known as The DiVincenzo Criteria [27] and state that, at the least, a quantum computer must:

1. Be a scalable physical system with well-defined qubits.
2. Be initializable to a simple fiducial state such as $|000\dots\rangle$.
3. Have long decoherence times.
4. Have a universal set of quantum gates.
5. Permit high quantum efficiency, qubit-specific measurements.

Many experimentally realizable quantum systems have, in theory, been shown to satisfy the DiVincenzo criteria.



Figure 2.4: A sample of various qubit architectures. The tradeoffs among different qubit architectures are more apparent when they are grouped by physical size. Architectures with qubits of small physical size, such as ion traps, have less channels via which they can interact with their environment. As a result they have longer coherence times, but are harder to couple to each other. On the other hand, large qubits, like superconducting qubits, have more modes through which they interact with their environment. As a result, they are easier to couple, but have shorter coherence times. However, superconducting qubits have fast operation times, so compared to their smaller counterparts they are able to perform a similar number of quantum operations before they lose coherence.

A select few of these have been implemented experimentally and have been used to successfully carry out some very basic quantum computing experiments. Some of these are mentioned in Figure 2.4 and include photons, trapped ions, spins in semiconductors, NV centers in diamond, superconducting qubits, and even more exotic systems like electrons on liquid helium. The particular quantum computing architecture discussed in this thesis is based on **superconducting qubits**.

Chapter 3

Superconducting Qubits

The idea of using superconducting circuits for quantum information processing was inspired by experimental investigations of macroscopic quantum tunneling in superconducting tunnel junctions in the 1980's [48] and work on Cooper pair box transistors in the 1990's [13]. It was discovered that superconductors act as macroscopic quantum systems and that the energy level spectrum of superconducting tunnel junctions could be used to construct a quantum bit. The first superconducting qubits were demonstrated in the late 1990's using Cooper pair box devices [13, 56]. Over the past two decades, many proof-of-concept experiments have been carried out using superconducting qubits that show them to be a promising quantum computing architecture [85, 49, 42, 44]. This section provides a very brief overview of superconducting qubits. Many good reviews of the field of superconducting qubits already exist and we refer the reader to them for

more details [44, 26, 85, 25].

3.1 Superconducting qubits compared to other architectures

Superconducting qubits have distinct advantages and challenges compared to the other quantum computing architectures mentioned at the end of the previous chapter. These are more apparent when the various quantum computing architectures are compared by physical size, as shown in Figure 2.4. Superconducting qubits are the largest of the different architectures. Hence they have the advantage of being easily constructed using standard microfabrication techniques. Also, the impedances and operating frequencies of superconducting qubits can be designed to be close to those of standard RF and microwave electronic components, which have impedances of $\sim 50\Omega$ and operate in MHz and GHz frequencies [26]. Therefore, well understood linear electronic components such as capacitors, inductors, and transmission lines can be used to easily couple superconducting qubits to readout and control circuitry and to each other. However, in order to provide electrical conductivity while preserving quantum coherence, these components must be made out of superconducting metals, which unlike normal metals are non-dissipative.

Although superconducting qubits and their associated superconducting circuitry are

non-dissipative, they are larger in size and as a result there are more channels through which superconducting qubits can lose coherence by interacting with their environment. Thus, coherence times are shorter for superconducting qubits as compared with other qubit implementations. *However, coherence times alone do not determine performance because the important metric is the number of operations that can be carried out before a qubit loses coherence.* For superconducting qubits, the coherence times are on the order of a half to a few microseconds while operation times are 5 – 20 nanoseconds, allowing superconducting qubits to perform a number of operations that is comparable to the number performed by other qubit implementations. However, in order to scale superconducting quantum computers to many qubits and to be able to perform quantum error correction, longer coherence times are needed. Hence, there is much work underway to uncover and eliminate all major pathways of decoherence in superconducting qubits.

3.2 The Josephson junction: the key element of superconducting qubits

The superconducting tunnel junction, called the Josephson junction [6], is the key element from which superconducting qubits are constructed. Therefore, it is important to thoroughly understand its operation. As shown in Figure 3.1a, it is composed of

an insulator sandwiched between two superconducting metal electrodes. In the experiments presented in this thesis, the electrode metal used is aluminum and the insulator is aluminum oxide.

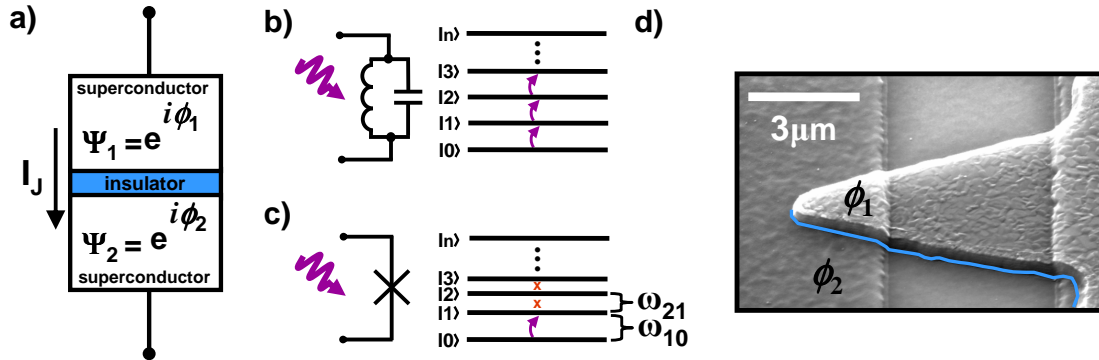


Figure 3.1: The Josephson Junction and the importance of non-linearity. **a)** A Josephson junction is composed of two superconducting electrodes sandwiching an insulator. In this thesis the electrodes are made of aluminum and the insulator is aluminum oxide. **b)** When a linear circuit such as an LC resonator is cooled to mK temperatures, it behaves like a simple harmonic oscillator with equally spaced energy levels. This prevents any individual transition from being selectively addressed. As a result a two-level system needed for a qubit cannot be formed from a linear circuit. **c)** A non-linear circuit, such as a Josephson junction (represented by the X symbol), has unequally spaced energy levels and as a result the lowest two levels can be excited with only minimal excitation of the other levels. This non-linearity allows the Josephson junction to be used as a qubit. **d)** A scanning electron micrograph of an actual Josephson junction used in this thesis. The insulator is highlighted in blue and the top and bottom electrodes are labeled with the phases ϕ_1 and ϕ_2 of the superconducting wavefunction in each of the electrodes.

Josephson junctions are unique because they are the only known circuit elements that exhibit a strong non-linearity and that can operate at low temperatures without dissipation.

To understand the need for non-linearity, a comparison with linear circuit elements is helpful. As shown in Figure 3.1b, when linear circuits, such as LC oscillators, are

cooled to mK temperatures, they behave like quantum harmonic oscillators, *i.e.* their energy levels are equally spaced [24]. A qubit cannot be formed from a system with equally spaced levels because an excitation that is resonant with one pair of adjacent levels will be resonant with all other pairs of adjacent levels. Therefore it is impossible to excite just one pair of levels and use that pair as the two-level system for the qubit. If the level spacing is non-linear, as is the case with Josephson junctions (Figure 3.1c), each pair of levels has a different transition frequency. As a result, a transition between the two lowest levels can be excited with minimal excitation of other levels. Thus the ground and excited states of the non-linear system create the two-level subspace that constitutes a qubit. However, because there are energy levels present above the excited state, the maximum number of single qubit operations that can be performed coherently scales, to first order, as the quality factor of the qubit transition times the nonlinearity [25]

$$\#_{qubitops} = Q_{01} \frac{|\omega_{01} - \omega_{12}|}{\omega_{01}} \quad (3.1)$$

where the ω_{mn} are the transition frequencies between states $|m\rangle$ and $|n\rangle$ and Q_{01} is the quality factor of the qubit transition given by $Q_{01} = \omega_{01}/\Delta\omega_{01}$, where $\Delta\omega_{01}$ is the full width at half maximum of the qubit resonance at frequency $\omega_{01}/2\pi$ [76]. The

quality factor is also related to the energy relaxation time, T_1 via

$$T_1 = \frac{Q_{01}}{\omega_{01}} \quad (3.2)$$

Low temperature operation is required because the superconducting transition temperature, T_c , of superconducting metals that can be used to build complex microelectronic devices falls in the range of a fraction to a few Kelvin. We use aluminum with a superconducting transition temperature of $T_c = 1.2$ K. However, T_c is not what defines the upper limit on the operating temperature of superconducting qubits. The reason why milli-Kelvin temperatures are necessary is because we want to control superconducting qubits using inexpensive electronics. By constructing qubits with level spacing $\omega_{01}/2\pi \approx 5 - 20$ GHz, we can use standard off-the-shelf microwave electronics, which are widely and cheaply available thanks to the cell phone industry. Therefore, what sets the upper limit on operating temperature is that thermal excitations can create unwanted excitations from the qubit ground to the excited state, preventing proper qubit initialization if $\hbar\omega_{01} \ll kT$ is not maintained. This limits operating temperatures to tens of milli-Kelvin.

In electrical circuits, Josephson junctions can be represented by the cross circuit symbol as shown in Figure 3.2a. In the classical description of a Josephson junction,

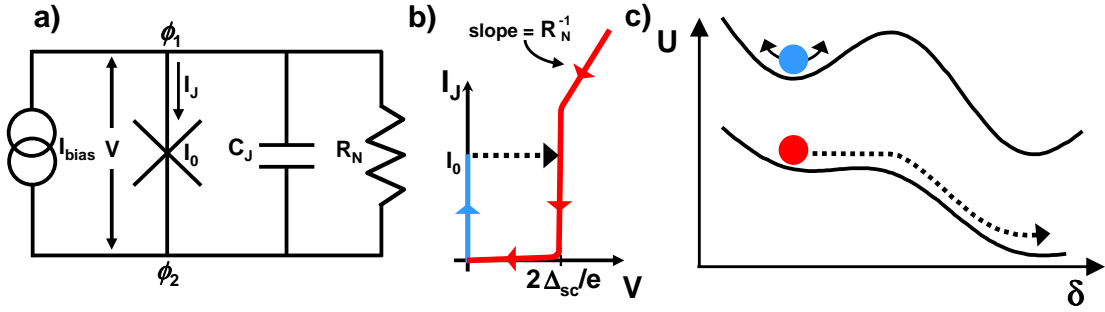


Figure 3.2: **Josephson junction physics.** **a)** A circuit of a current-biased Josephson junction. As discussed in the text, a capacitance, C_J , is included to take into account the capacitance between the electrodes of the physical junction and a resistance, R_N is added to model the dissipation in the system. When the current through the junction, I_J , exceeds the critical current, I_0 , the junction makes a hysteretic jump (dashed arrow) from the superconducting to the normal state. **b)** The current through the junction, I_J , as a function of the voltage, V , across it. The superconducting state is on the blue vertical line at $V = 0$ and the normal state is along the rest of the curve, as indicated in red. **c)** A Josephson junction in the superconducting state can also be represented as a particle with mass $C_J(\hbar/2e)$ oscillating in a washboard potential given by U . In the normal state, the wells become shallow and the particle “rolls” down the potential.

the current and voltage through and across the junction are given by

$$I_J = I_0 \sin \delta \quad (3.3)$$

$$V = \frac{\Phi_0}{2\pi} \frac{d\delta}{dt} \quad (3.4)$$

where $\Phi_0 = h/2e$ is the superconducting flux quantum, $\delta = \phi_1 - \phi_2$ is the difference in the superconducting phase across the junction. The capacitance C_J is due to the parallel plate geometry of the junction electrodes. If the current, I_J , flowing through the junction exceeds the junction critical current, I_0 , the junction will switch from the

superconducting to the normal state at which point it will have a normal state resistance R_N . The dependence of I_0 on R_N and temperature is given by the Ambegaokar-Baratoff relation [6]

$$I_0 = \frac{\pi \Delta_{sc}(T)}{2 e R_N} \tanh(\Delta_{sc}/2kT) \quad (3.5)$$

where Δ_{sc} is the superconducting gap energy, T is the temperature of the junction, k is the Boltzmann constant, and e the magnitude of the charge of an electron. For aluminum $\Delta_{sc} \approx 190\mu eV$. We operate the qubits at ~ 25 mK so therefore I_0 is given by the value at $T = 0$.

It is important to note that the superconducting phase difference across the junction, δ , corresponds to the electromagnetic flux in units of Φ_0 , so that $\delta = 2\pi\Phi/\Phi_0$. Also it should be noted that using equations (3.3) and (3.4) in the conventional definition, $V = L_J(dI_J/dt)$, the Josephson junction can be thought of classically as a tunable inductor

$$L_J = \frac{\Phi_0}{2\pi I_0 \cos \delta} \quad (3.6)$$

When a Josephson junction is biased with a current, and the voltage across it is measured, a trace like the one shown in Figure 3.2b can be obtained, where I_0 , Δ_{sc} , and R_N as indicated in the figure. The junction displays hysteretic behavior between the superconducting and normal states of operation. In the superconducting state, the

junction operates on the vertical current branch at $V = 0$. When I_0 is exceeded, it makes a hysteretic jump to the normal state branch at $2\Delta_{sc}/e$, returning to the superconducting state via the normal state branch.

The quantum behavior of a Josephson junction can be understood by first writing down the classical Hamiltonian for a single junction using Kirchoff's equations. From Figure 3.2a this gives $C_J(dV/dt) + V/R_N + I_J = I_{bias}$. For qubits, the junction will not be operated in the normal state therefore the dissipative term containing R_N can be ignored. We can then proceed to substitute in (3.3) for I_J , and (3.4) for V yielding $(\hbar/2e)C_J\ddot{\delta} + I_0 \sin \delta = I_{bias}$. This can be rewritten in a form more easily recognizable as the Euler-Lagrange equation [79], $d/dt(\partial L/\partial \dot{\delta}) - \partial L/\partial \delta = 0$

$$\frac{d}{dt} \left(\frac{\hbar}{2e} \right)^2 \frac{\partial C_J \dot{\delta}^2}{\partial \dot{\delta}} - \frac{\partial \hbar}{\partial \delta} \frac{1}{2e} [I_0(1 - \cos \delta) - I_{bias} \delta] = 0 \quad (3.7)$$

Therefore, the Lagrangian is

$$L = \left[\left(\frac{\hbar}{2e} \right)^2 \frac{C_J \dot{\delta}^2}{2} \right] - \left[\frac{\hbar}{2e} I_0 (1 - \cos \delta) - \frac{\hbar}{2e} I_{bias} \delta \right] \quad (3.8)$$

Since $L = K(\dot{\delta}) - U(\delta)$, the kinetic energy can be directly read off (3.8)

$$K(\dot{\delta}) = \left(\frac{\hbar}{2e} \right)^2 \frac{C_J \dot{\delta}^2}{2} = \left[\frac{Q^2}{2C_J} \right] \quad (3.9)$$

Where the charge on the capacitor, $Q = C_J V = C_J(\hbar/2e)\dot{\delta}$, has been substituted to show that the kinetic energy is just the charging energy of this capacitor. Similarly, the potential energy can be read off (3.8)

$$U(\delta) = \frac{\hbar}{2e} I_0 (1 - \cos \delta) - \frac{\hbar}{2e} I_{bias} \delta \quad (3.10)$$

and consists of the energy of the bias current and the magnetic energy of the Josephson current. The Hamiltonian, H , can then be constructed from the Lagrangian using $H(p, \delta) = p\dot{\delta} - L$ where p is the canonical momentum

$$p = \frac{\partial}{\partial \dot{\delta}} = \left(\frac{\hbar}{2e}\right)^2 C_J \dot{\delta} = \left(\frac{\hbar}{2e}\right) Q = \hbar n \quad (3.11)$$

where $n = Q/2e$ is the number of Cooper pairs on the junction capacitor. Hence, the Hamiltonian is

$$H = E_C n^2 - E_J \cos \delta - \frac{\hbar}{2e} I_{bias} \delta \quad (3.12)$$

where $E_C = (2e)^2/2C_J$ is the junction charging energy and $E_J = (\hbar/2e)I_0$ is termed the Josephson energy. As illustrated in Figure 3.2c, this is just the Hamiltonian of a particle with momentum $Q(\hbar/2e)$, mass $C_J(\hbar/2e)$, and position δ oscillating in a “washboard” potential given by (3.10) and depicted in Figure 3.2c. When the junction switches into the normal state (also called the voltage state), the particle escapes from the well and runs down the washboard potential.

To construct the quantum mechanical version of (3.12), it must be noted that Q and δ do not commute and hence must be quantum mechanical operators described by a wave function so that

$$\begin{aligned} Q &\rightarrow \hat{Q} \\ \delta &\rightarrow \hat{\delta} \\ [\hat{Q}, \hat{\delta}] &= 2ei \end{aligned} \tag{3.13}$$

and the quantum mechanical version of (3.12) is obtained by replacing n and δ by their quantum mechanical operator analogs

$$H = E_C \hat{n}^2 - E_J \cos \hat{\delta} - \frac{\hbar}{2e} I_{bias} \hat{\delta} \tag{3.14}$$

This Hamiltonian of a single junction is the basis for the Hamiltonians that describe the different implementations of superconducting qubits [85].

3.3 Types of superconducting qubits

There are 3 main types of superconducting qubits upon which all other superconducting qubits are based: the charge, the flux, and the phase qubit [26, 25, 85]. The Hamiltonian of each type is a variant of (3.14). The circuit, potential, and quantum mechanical variable for each type is shown in Figure 3.3. How they differ can be best understood by comparing the relative strengths of the energy scales E_J and E_C .

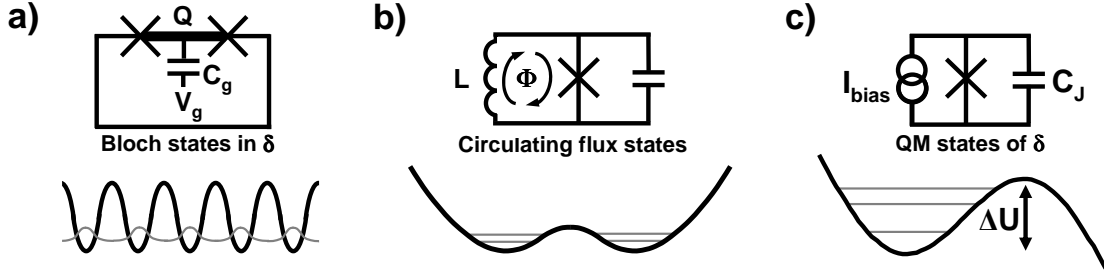


Figure 3.3: **Types of superconducting qubits.** The three main types of superconducting qubits, as described in the text: **a)** charge **b)** flux **c)** phase. The work in this thesis was performed using a variant of the phase qubit. The variable used for the qubit states is listed below the circuit.

The "Cooper pair box", or **charge qubit** [13, 56, 85], shown in Figure 3.3a is constructed from two Josephson junctions in close proximity. The island between the junctions is so small that its charging energy is large enough for the island to exhibit Coulomb blockade behavior, *i.e.* $E_C \gg E_J$. This allows Cooper pairs to tunnel on and off the island, one at a time. The eigenstates of the charge qubit are given by $E_C(\hat{n} - n_g)^2 |n\rangle = E_n |n\rangle$, where $n_g = -C_g V_g / 2e$ is the charge on the gate capacitor in units of Cooper pairs and is tuned using the gate electrode V_g . The number of Cooper pairs on the island is represented by the number operator, \hat{n} . For values of n_g such as $n_g = 1/2$, a degeneracy exists for $|0\rangle$ and $|1\rangle$. However, if a small Josephson coupling, E_J , is turned on, it acts like the Zeeman field in a NMR experiment and lifts the degeneracy, forming the two levels of the qubit. The charging energy, E_C , acts like the transverse magnetic field in a NMR experiment. Also, it is very sensitive to noise in the offset charge due to V_g when the qubit is biased away from the degeneracy point.

The **flux qubit** [55, 85, 25] is shown in Figure 3.3b and consists of a junction shunted with an inductor $L \lesssim L_J(0)$. The flux qubit parameters are such that $E_C \ll E_J$, minimizing the charge noise that is present in charge qubits. It is operated with the external flux, $\Phi_{ext}/(2\pi\Phi_0) = \delta = \pi$. The external flux plays a role similar to the gate electrode in the charge qubit. Therefore, analogous to the charge qubit degeneracy point $n_g = 1/2$, this creates a potential with symmetric wells with pairs of degenerate levels separated by a barrier of height $3(L_J/L - 1)^2 E_J$. The symmetric wells correspond to the counterclockwise and clockwise persistent currents circulating in the loop formed by L . Macroscopic quantum tunneling between the wells lifts the degeneracy, with the lowest resulting pair of levels forming the qubit states. The advantage of the flux qubit is its large nonlinearity which can be more than 100%, compared to the 10% nonlinearity of the charge qubit. This comes at a cost because the high nonlinearity exposes the flux qubit to critical current and flux noise. These have minimal effect at the symmetric bias point, but away from this “sweet spot” these noise sources severely limit performance [85].

The final superconducting qubit type, and the one on which the work in this thesis is based, is called the **phase qubit** [25, 52], as shown in Figure 3.3c. It is just a current-biased Josephson junction, as described by (3.14). Like the flux qubit, the phase qubit is operated with parameters such that $E_C \ll E_J$. However, it is biased so that $I_{bias} \approx I_0$, giving $\delta \leq \pi/2$. With the bias near the critical current, the potential can be approximated

by the cubic potential $U(\delta) = \Phi_0/2\pi(I_0 - I_{bias})(\delta - \pi/2) - (I_0\Phi_0/12\pi)(\delta - \pi/2)^3$, as shown in Figure 3.3c. The barrier that traps the qubit states in the potential well has a height

$$\Delta U = \frac{2\sqrt{2}I_0\Phi_0}{6\pi} \left(1 - \frac{I}{I_0}\right)^{3/2} \quad (3.15)$$

The lowest two levels in the well form the qubit states. The classical oscillation frequency at the bottom of the well, ω_p , is called the **plasma frequency** and corresponds roughly to the qubit transition frequency, $\omega_{01} \simeq 0.95\omega_p$,

$$\omega_p = \frac{1}{\sqrt{L_J(I)C_J}} = \frac{1}{\sqrt{L_J(0)C_J}} [1 - (I/I_0)^2]^{1/4} \quad (3.16)$$

Typically the phase qubit is operated with about $\Delta U/\hbar\omega_p \approx 4 - 10$ levels in the well and a nonlinearity of $\approx 5\%$. It must be biased using a high impedance current bias and it has a built-in measurement scheme which exploits the large difference in tunneling rates of the two qubit states, which will be discussed in the next chapter. The phase qubit is different from the other two qubit types because it does not need to be biased at a “sweet spot” in order to be insensitive to charge noise.

Chapter 4

Single Phase Qubit Design and Operation

4.1 The flux-biased phase qubit

The qubit used for the experiments in this thesis has come to be called the **flux-biased phase qubit** [75, 37, 49]. From the electrical circuit for this qubit (Figure 4.1a), it can be seen that it is just a phase qubit where the high impedance current bias has been constructed from a loop of inductance L through which an external flux, Φ , is applied. The Thevenin equivalent of the flux bias can be written as a current source with magnitude $I_{bias} = \Phi/L$ as shown in Figure 4.1b. From now on this will be called the **flux bias** of the qubit. This circuit is very similar to that of a flux qubit, but unlike

the flux qubit, here $L \gtrsim 2L_J(0)$, and the operating bias is like that of a phase qubit with $I_J \lesssim I_0$.

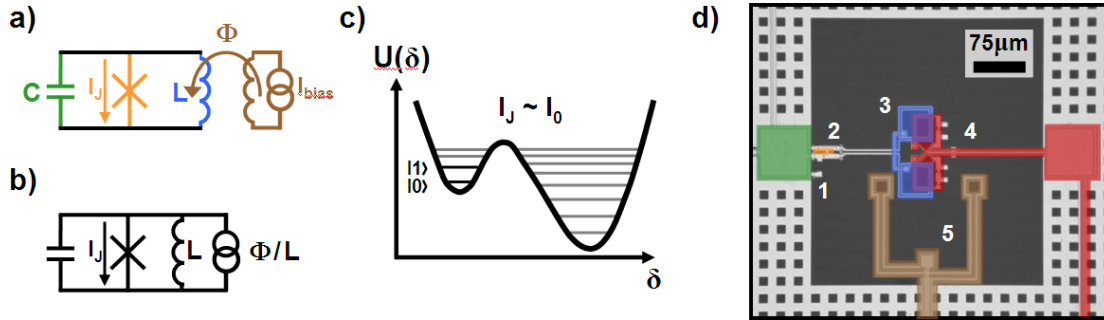


Figure 4.1: **The flux-biased phase qubit.** **a)** The circuit for flux-biased phase qubit. The small physical size of the qubit junction gives it a small capacitance and as a result it needs to be shunted by a large capacitance, C , in order to maintain the qubit frequency near 6 GHz. The qubit is biased using an external flux, Φ , which leads to the Thevenin equivalent circuit shown in **b)**. This flux bias modifies the washboard potential of the junction, adding a parabolic term as shown in (4.1). **c)** The potential energy as a function of the phase, δ , across the qubit junction, as given by (4.1). **d)** An optical micrograph of a finished microfabricated flux-biased phase qubit. The different elements are: 1. qubit shunt capacitor C , 2. qubit Josephson junction, 3. qubit inductor L , 4. readout SQUID, 5. flux bias coil

In the particular designs used in this thesis, the qubit junction area is small ($\approx 1 - 2 \mu\text{m}^2$). This is because the qubit can couple to so called **two-level states (TLS's)** in the junction oxide and exchange energy with them [50, 70]. Two-level states can also be found in the dielectric materials used in the qubit shunt capacitor and in the dielectric separating overlapping on-chip leads. Recent work [50, 70] suggests that a TLS is formed from the two conformational states of a dangling bond of a defect in a dielectric material. For certain qubit biases, an unoccupied energy level of a TLS can align on-resonance with an occupied qubit level. When this happens, the two will

exchange energy. Reducing the junction size decreases the number of TLS's in the junction tunnel barrier, but it also reduces the qubit capacitance, C_J . Therefore, in order to maintain the qubit frequency in the 6 GHz range, the junction must be shunted by a large external capacitor, C , as shown in Figure 4.1 [75]. As with the standard phase qubit, the potential of the flux-biased phase qubit can be written down using Kirchoff's laws and consists of the phase qubit washboard potential terms that are cosine and linear in δ , but also with an additional parabolic bias term due to the energy of the current flowing in L

$$U(\delta) = -\frac{I_0\Phi_0}{2\pi} \cos\delta + \frac{1}{2L} [\Phi - \delta\Phi_0/2\pi]^2 \quad (4.1)$$

Unless stated otherwise, the qubit devices used to take the data in this thesis were designed with

$$\begin{aligned} L &\simeq 750pH \\ I_0 &\simeq 1.6\mu A \\ C &\simeq 1pF \\ C_J &\simeq 50fF \end{aligned} \quad (4.2)$$

The parameter values listed in (4.1) allow the qubit potential to have only two minima when biased near the critical current, as shown in Figure 4.1c. The left and right wells have $\approx 4 - 10$ and $\gtrsim 300$ levels, respectively and the lowest two levels in the left well form the qubit states. Having two wells simplifies qubit initialization and opera-

tion, as will be discussed later. However, parameters can deviate from the ideal values above due to fabrication errors or other problems so the qubits must be carefully calibrated and tested in order to verify the actual parameter values. An actual fabricated device is shown in Figure 4.1d, with some of the components identified in the caption. It must be noted that the qubit inductor loop, L , is gradiometrically constructed and positioned so that it will be insensitive to all external flux aside from that of the flux bias coil. Unless stated otherwise, the top and bottom wiring is made from aluminum. The dielectric material used for the capacitor, C , and to separate overlapping wires for crossovers is amorphous silicon (a-Si:H). The insulator used for the Josephson junctions is amorphous aluminum oxide (AlO_x). A ground plane surrounds the qubit to isolate it from unwanted microwave modes. Square, $\sim 10\mu\text{m} \times 10\mu\text{m}$, holes are etched into the ground plane to prevent the trapping of magnetic flux as the qubit chip is cooled below the superconducting transition temperature of aluminum. It is necessary to avoid trapped flux because mobile flux vortices can cause dissipation [6]. Further details of the microfabrication of the qubits used for this thesis are discussed in Appendix A.

4.2 Single Qubit Biasing, Measurement, Readout and Logic Operations

A single qubit is manipulated and measured using four different subsystems, which are shown schematically in Figure 4.2. These subsystems bias the qubit, operate on qubit states using microwave pulses, measure the result of these operations, and read out the measurement results. A brief overview of each subsystem follows, and examples of how each subsystem is characterized experimentally will be presented in section 4.3. However, these subsystems have been described in depth elsewhere [3, 57] and the reader interested in more details can refer to those sources. The circuit of the cryogenic wiring of these subsystems and a brief overview of the room temperature electronics that control these subsystems can be found in Appendix B.

4.2.1 Flux Bias and Measurement

As discussed above, biasing of the qubit is accomplished by applying a flux, Φ , through the qubit inductor L , as shown in Figure 4.2. However, why not just directly inject the bias current into the qubit circuit instead of coupling the bias into the qubit circuit using the mutual inductance M between the qubit and flux bias loops? This is because energy from the qubit can dissipate out into the environment through the flux bias line. The mutual inductance coupling serves to transform [57] the flux bias line characteristic

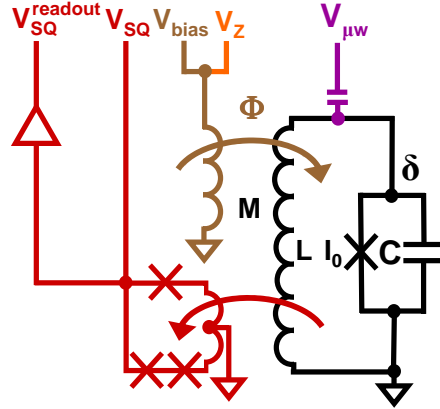


Figure 4.2: **Qubit bias, measurement, readout, and control subsystems.** Circuit of flux-biased phase qubit with different subsystems color-coded. **(Red)** The superconducting quantum interference device (SQUID) used for reading out the qubit state is to the left of the qubit circuit (Black) and is composed of 3 Josephson junctions. The V_{SQ} ($V_{SQ}^{readout}$) line is used to bias (measure) the SQUID. **(Brown)** The V_{bias} line provides the flux-bias used to bias the qubit. It controls the Φ term in (4.1). **(Orange)** The V_Z line applies the measurement pulses used to measure the qubit and the z-pulses used to generate z-axis rotations on the Bloch sphere. The z-pulses are also used for fine adjustments to the qubit bias that need to be executed on nanosecond timescales because the V_{bias} line operates on much slower, microsecond timescales. **(Violet)** The $V_{\mu w}$ line is capacitively coupled to the qubit circuit and is pulsed with microwave pulses that control rotations about the x and y axes of the Bloch sphere. The reason for coupling the flux bias signal into the qubit through an inductive transformer and for coupling the the microwave signal through a coupling capacitor is discussed in the text and is done to limit qubit dissipation through the V_{bias} and $V_{\mu w}$ lines.

impedance of 50Ω up by a factor of $(L/M)^2 = (750\text{pH}/8\text{pH})^2 \simeq 10^4$ so that the the qubit sees a large impedance out into the environment via the flux bias line. This large effective impedance limits the dissipation through the flux bias line.

The flux bias controls the Φ term in (4.1) and therefore it tilts the potential well. A few representative snapshots of the qubit potential are illustrated in Figure 4.3 for different flux bias values, V_{bias} . The flux bias serves as a coarse and slow adjustment knob for the qubit potential. Flux bias signals are typically a few microseconds long

and have amplitudes of hundreds of millivolts to a couple volts, and as shown in Appendix B, are applied across a $1\text{k}\Omega$ series resistor to generate a current bias. However, qubit logic operations need to be generated on nanosecond timescales in order to maximize the number of operations before coherence is lost. This requires a fine and fast control knob for the qubit potential. As shown in Figure 4.2, this is accomplished by pulsing the same flux bias line, via V_Z , with pulses a few nanoseconds in length. As diagrammed in Appendix B, the $1\text{k}\Omega$ V_{bias} line must be impedance matched to the 50Ω V_Z line using a custom made tee circuit to prevent the V_Z signals from being reflected at the point where the two lines merge into one. Coincidentally, the V_Z pulses can also be used to measure the qubit state, as will be discussed shortly. When these pulses are used to control the qubit bias, they will be called **z-pulses**, but when they are used to measure the qubit, they will be called **measurement pulses**. They differ in their pulse shape, with the z-pulse being a flat-top Gaussian usually 10's to 100's of nanoseconds in length, and the measurement pulse having a linear roll-off with a fixed width of tens of nanoseconds, as will be described shortly.

The measurement scheme currently used for flux-biased phase qubits is based on the tunneling rate of the qubit $|1\rangle$ state, Γ_1 , being much larger than the tunneling rate of the qubit ground state, Γ_0 , which for a well defined well that has a barrier ΔU , is given by [52]

$$\Gamma_0 \simeq 52(\omega_p/2\pi)\sqrt{\Delta U/\hbar\omega_p}e^{-7.2\Delta U/\hbar\omega_p} \quad (4.3)$$

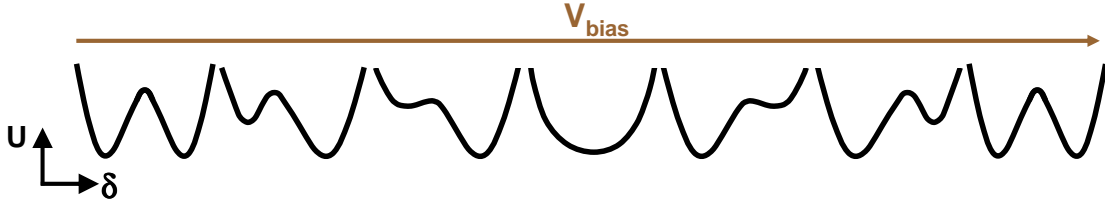


Figure 4.3: **Effect of flux bias on qubit potential** The potential as given by (4.1), for 7 values of applied flux, Φ . Each snapshot shows the potential of the potential energy, U , as given by (4.1) as a function of the superconducting phase difference across the qubit junction, δ . The second snapshot from the left corresponds to the case of biasing the qubit near the critical current as shown in Figure 4.1c. Increasing the flux bias (V_{bias}) changes the well depths in a periodic fashion, with a period of approximately one flux quantum, Φ_0 .

where ω_p is the plasma frequency given by (3.16) and ΔU is the qubit well potential barrier height given by (3.15). The ratio of the tunneling rates between adjacent levels n and $n + 1$ in the qubit well is approximately

$$\frac{\Gamma_{n+1}}{\Gamma_n} \simeq 300 \quad (4.4)$$

As depicted in Figures 4.4a and b, we can use the above difference in rates to measure the qubit. A measurement pulse can be applied that has been calibrated to lower the tunneling barrier, ΔU , by just enough so that only the $|1\rangle$ or higher states will tunnel or escape into the deep right well. The state will then relax to the bottom of the right well at a rate approximately given by n_r/T_1 , where n_r is the number of levels in the right well [88]. Usually $n_r \sim 300$ and $T_1 \sim 500\text{ns}$. On the other hand, if the qubit is

in the $|0\rangle$ state (Figure 4.4b), no tunneling occurs because $\Gamma_0 \lll \Gamma_1$. Therefore, the presence (absence) of tunneling into the deep right well allows us to measure if the qubit is in the $|1\rangle$ ($|0\rangle$) state. This measurement scheme is powerful because for multiple qubits it allows us to measure all the qubits at the same time. Hence it is called a **single-shot measurement** scheme. However, the qubit state is destroyed as it tunnels into the right well. Therefore, this measurement is called a quantum demolition measurement. Qubits can also be measured without destroying the qubit state by using a **quantum non-demolition (QND) measurement**. QND measurement schemes are useful in implementing particular types of quantum error correction protocols.

Now that the qubit state has either tunneled into the large well on the right (qubit = $|1\rangle$) or has remained in the qubit well (qubit = $|0\rangle$), the difference between these two events must be read out by the external circuit.

4.2.2 Readout

The result of the measurement is read out by first adjusting the flux bias, V_{bias} , so that the qubit potential is nearly symmetric, as shown in Figure 4.5b and c. This leaves the result of the measurement in a deep potential well. If the result was left in a shallow well, it could be easily excited out of that well by other signals, causing errors in measurement. Therefore, by remaining in a deep well, the measurement result is protected against errors. Also, at this symmetric point the two wells are maximally separated

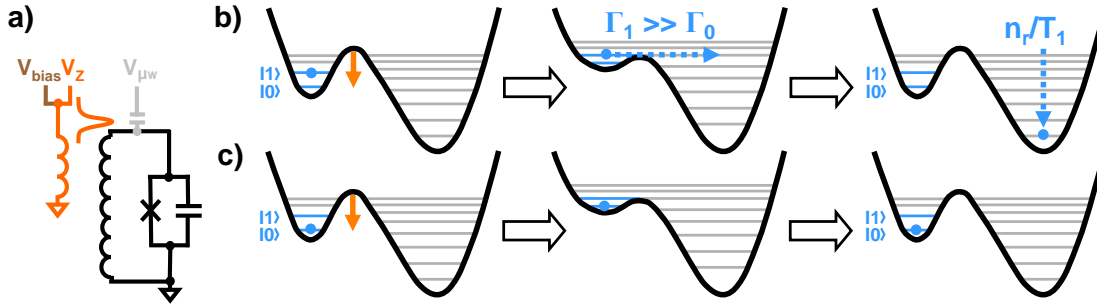


Figure 4.4: **Qubit measurement scheme.** The tunneling rate of the $|1\rangle$ state, Γ_1 , is much greater than that of the $|0\rangle$ state, Γ_0 , allowing us to use the presence (absence) of a $|1\rangle$ state tunneling event to measure if the qubit is in the $|1\rangle$ ($|0\rangle$) state. **a)** A pulse on the V_Z line decreases the height of the potential barrier by a calibrated amount that only allows the $|1\rangle$ or higher states to tunnel out. What follows after this depends on whether the qubit is in the $|0\rangle$ or $|1\rangle$ state **b)** If the qubit is in the $|1\rangle$ state, it will tunnel out to the right well and decay to the lowest right well state at a rate $\sim n_r/T_1$, where $T_1 \simeq 500\text{ns}$ is the energy relaxation time and $n_r \simeq 300$ is the number of levels in the large well to the right of the qubit well. **b)** If the qubit is in the $|0\rangle$ state then no tunneling occurs and the state remains in the qubit well when the measurement pulse is applied. These two cases can be distinguished later using the readout mechanism that will be discussed shortly. If a higher state outside the $\{|0\rangle, |1\rangle\}$ qubit manifold is occupied, then the qubit will be measured as being in the $|1\rangle$ state.

in flux by about one flux quantum, Φ_0 . This flux difference is easily read out using a superconducting quantum interference device (SQUID), as shown in Figures 4.5d and e and discussed below [6, 57].

Only the relevant points about the SQUID used here and shown in Figure 4.2 will be discussed. More details about the design and operation of the readout SQUID can be found elsewhere [57, 3]. The key point is that *the SQUID as a whole has a critical current, I_0^{SQUID} , that depends on the flux threading the SQUID loop. The flux generated by the qubit loop L couples into the SQUID loop thereby allowing us to read out the flux state of the qubit by measuring I_0^{SQUID}* (see Figure 4.5a) [6]. As mentioned above,

the flux in the qubit loop depends on whether the qubit state was in the $|0\rangle$ or $|1\rangle$ state, with the two flux states differing by approximately one flux quantum, Φ_0 . As shown in Figure 4.1d, the SQUID loop is gradiometrically constructed and is symmetrically placed with respect to the flux bias coil in order to be sensitive only to the flux in the qubit loop and not the flux applied by the flux bias coil or any other external flux sources. The mutual inductance coupling the SQUID loop to the qubit loop is $\sim 70pH$.

The sequence of signals on the V_{SQ} and $V_{SQ}^{readout}$ lines during the readout is described in Figure 4.5d and e. To perform the readout, the SQUID bias voltage, V_{SQ} , is ramped up until the SQUID switches to the voltage state. This switching voltage is read out by a gain of 1000 pre-amplifier. A clock is started at the beginning of the V_{SQ} ramp and the time at which the switch occurs, t_{switch} is recorded. This switching time is approximately Gaussian distributed about one of two values, $t_{|0\rangle}$ or $t_{|1\rangle}$, depending on the qubit flux state.

Care must be taking when operating the SQUID in order to prevent qubit dissipation from quasiparticles [43]. If the voltage across the SQUID exceeds twice the superconducting gap, $2\Delta_{sc}/e \simeq 400\mu V$, quasiparticles will be rapidly generated. To prevent the generation of quasiparticles when the SQUID switches, the SQUID with critical current of $I_0^{SQUID} \simeq 2\mu A$, is shunted to ground using a resistance $R_{shunt} \simeq 30\Omega$. This forces the switching voltage across it to be $I_0^{SQUID} R_{shunt} = 60\mu V \sim (1/3)2\Delta_{sc}/e$. More of the experimental details behind calibrating the readout will be discussed in Section 4.3.

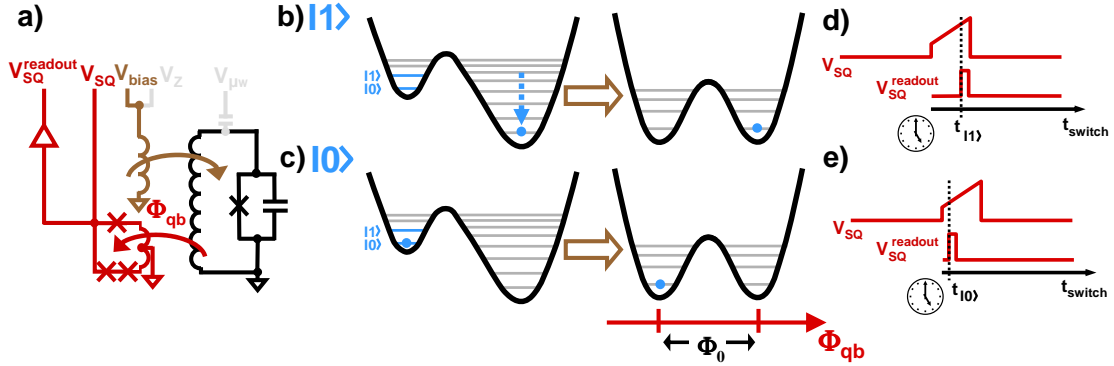


Figure 4.5: **Readout scheme.** **a)** The qubit is read out using a superconducting quantum interference device (SQUID), shown in red. The critical current of the 3-junction SQUID depends on the flux, Φ_{qb} , in the qubit loop. The SQUID bias is ramped using V_{SQ} while the voltage across the SQUID is measured using $V_{SQ}^{readout}$. **b) and c)** Depending on the state the qubit is in, Φ_{qb} will differ by approximately one flux quantum, Φ_0 , between the two states, $|0\rangle$ and $|1\rangle$. **d) and e)** This flux difference is detected by ramping V_{SQ} and monitoring $V_{SQ}^{readout}$. The SQUID will switch to the voltage sometime during the ramp. The ramp voltage at which it switches depends on the SQUID critical current, which itself depends on the state of the qubit. A timer is started at the beginning of the SQUID ramp and stopped when a voltage across the SQUID is detected using $V_{SQ}^{readout}$. The time elapsed since the beginning of the ramp, t_{switch} is recorded as the switching time. Hence t_{switch} is approximately Gaussian distributed about the values $t_{|0\rangle}$ or $t_{|1\rangle}$ and tells us if the qubit was in the $|0\rangle$ or $|1\rangle$ state.

4.2.3 Logic Operations

As mentioned in Chapter 2, qubit logic operations consist of rotations around Bloch sphere axes [58]. Rotations about the x , y , and z axes by an angle θ will be labeled X_θ , Y_θ , and Z_θ , respectively. Arbitrary rotations can be constructed from linear combinations of the rotations about the x , y , and z axes. The amplitude of the microwave pulse determines the Bloch sphere angle θ and the phase of the pulse determines the Bloch sphere angle ϕ . However, the definition of $\phi = 0$, *i.e.* the x -axis, is a subtle, but important point. The microwave source used to output the microwave pulses con-

tains a phase locked loop (PLL) circuit that is set to an arbitrary phase [64]. We define $\phi = 0$ to be this arbitrary phase and this defines the phase of the X_θ pulse. The pulse with a $+\pi/2$ phase shift relative to this arbitrary phase is defined to be the Y_θ pulse. Therefore, *when we talk about the **rotating frame of reference**, we mean that this is the reference frame where $\phi = 0$ is defined to be the arbitrary phase that the PLL circuit of the microwave source is set to.* The full-width at half max of the microwave pulses is typically $\sim 8 - 10$ nanoseconds. As shown in Figure 4.2, the microwave line is capacitively coupled into the qubit circuit. This prevents any DC signals from reaching the qubit and also ensures that the 50Ω characteristic impedance of the microwave line is transformed up to a much larger effective impedance, limiting the dissipation through the microwave line in a similar way to what was discussed earlier for the flux bias line, V_{bias} . Rotations about the Z axis are achieved by pulsing the measurement line (V_Z) with Gaussian flat-top pulses whose area determines the amount of rotation, ϕ . These “z-pulses” effectively detune the qubit from the rotating frame defined by the microwave source and as a result create an effective rotation about the Z axis of the Bloch sphere. More details behind the electronics that generate and control these pulses can be found in Appendix B.

4.3 Experimental Characterization of A Single Qubit

In order to use a qubit, the various subsystems mentioned above must be tested, characterized and calibrated. Testing is necessary to discover errors and variations introduced during fabrication, faulty connections in the electronics, and other issues that might prevent proper operation. We also need to calibrate the parameters needed to reset the qubit into the ground state and to bias, measure, read out and perform operations of the qubit. Many of these experiments can be understood in terms of pulse sequences on the bias, microwave, and readout lines. An example of such a **pulse sequence** is shown in Figure 4.6. The horizontal axis is the time axis and the vertical axis is the amplitude of each signal. The various lines correspond to the various subsystems such as the flux bias, SQUID readout/bias, measurement/z-pulse, and microwave lines.

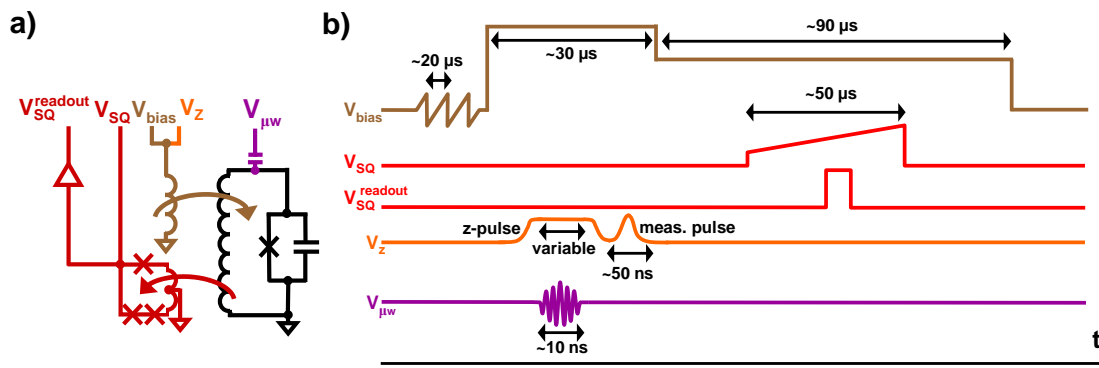


Figure 4.6: **Example pulse sequence.** **a)** Flux-biased phase qubit circuit with lines that will be pulsed to control the flux bias (V_{bias}), measurement (V_Z), readout (V_{SQ} and $V_{SQ}^{readout}$) and microwave control ($V_{\mu w}$). **b)** A typical qubit pulse sequence with voltages on each of the qubit lines depicted in time. Pulse amplitudes and widths are not drawn to scale, but approximate timescales are labeled where appropriate.

This representation is schematic, and the amplitude and duration of the various signals will not be drawn to scale, unless stated otherwise. However, the bias and readout pulses take place on timescales of a tens to hundreds of microseconds. The microwave, measurement, and z pulses are each usually a few to a hundred nanoseconds long with nanosecond rise/fall times for the latter two and GHz frequency oscillations for the microwave pulses. Hence the bias and readout lines will be sometimes referred to as DC lines since they change slowly compared to the nanosecond timescales of the measurement/z-pulse and microwave lines.

4.3.1 Calibrating the readout, qubit reset, and bias points

Without a working readout, further debugging is impossible; therefore the first subsystem that needs to be tested and calibrated is the readout SQUID. Pinholes in the Josephson junctions that make up the SQUID or other fabrication or wiring errors can make the SQUID inoperable. A test that verifies basic operation of the SQUID is a measurement of the voltage across the SQUID as a function of the current injected into the SQUID, a current-voltage or **IV measurement**. It is a very simple measurement that can be quickly done with an analog oscilloscope and voltage source, and is a good way to refresh those old-school oscilloscope skills that every grad student should be familiar with! The two lines used to bias and measure the voltage across the SQUID are used to take the IV. As shown in Appendix B, a current bias for the SQUID is created

by applying a voltage, V_{SQ} across a $10k\Omega$ series resistor. The voltage across the SQUID is measured using the $V_{SQ}^{readout}$ line via a gain of 1000 pre-amplifier, symbolized by the triangle in Figures 4.2 and 4.6. An oscilloscope is used in x-y mode to plot the current versus voltage trace, and a typical IV trace is shown in Figure 4.7a.

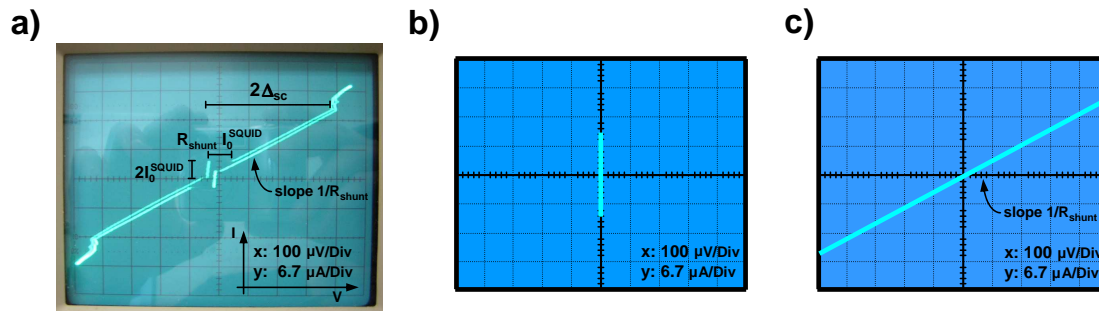


Figure 4.7: **SQUID IV measurement.** **a)** This is the most basic measurement used to ensure the readout SQUID is working. It involves measuring the voltage across the squid (x-axis) as a function of the current biasing the SQUID (y-axis). Using this measurement, the critical current of the SQUID, I_0^{SQUID} , and the superconducting gap for aluminum, Δ_{sc} , should be measured and checked against the design values, here $\sim 2\mu A$ and $190\mu eV$, respectively. The switching voltage should correspond to the product of the critical current times the shunt resistance (here $R_{shunt} \simeq 30\Omega$) and should be much less than the superconducting gap voltage Δ_{sc}/e in order to minimize generation of quasiparticles which will cause dissipation. **b)** A schematic example of one possible failure mode for the readout SQUID where there is a superconducting short to ground bypassing the SQUID. **c)** Another possible failure mode of the readout SQUID. When the SQUID is open, the connection to ground will be completed via a finite resistance and will be indicated by a sloped line on the SQUID IV measurement. In the case pictured here, the connection to ground is via the shunt resistance, as indicated by the slope of the line.

A few common errors worth mentioning can be encounter in this measurement. The most common ones result from shorts between on-chip electrodes, which are superconducting, or from shorts somewhere in the normal-metal wiring leading down to the device (see Appendix B for wiring diagram). A superconducting short is usually due

to a fabrication error that causes shorts between aluminum electrodes that make up the on-chip SQUID circuit, and will appear as a vertical line trace on an IV measurement as demonstrated schematically in Figure 4.7b. A short to ground via a finite resistance will look like a sloped line as in Figure 4.7c. This normal metal short can be due to a on-chip trace being open or a connection to ground in the dilution refrigerator via a normal metal resistor. The SQUID critical current and the superconducting gap, Δ_{sc} , for aluminum should also be recorded from the IV of the SQUID, as shown in Figure 4.7a. These should be compared to the expected design values of $\sim 2\mu\text{A}$ and $\sim 190\mu\text{eV}$, respectively.

Now that the readout SQUID has been shown to function at a basic level, a measurement is performed to check if the SQUID and qubit respond properly to the flux bias. This measurement also yields the values necessary for setting various qubit bias points needed to initialize, operate on, and read out the qubit. In our lab we have named this experiment the **SQUID steps** measurement because of the step-like appearance of the data (Figures 4.8b and c). The sequence of pulses used to carry out this experiment is shown in Figure 4.8a. The flux bias, Φ , in (4.1) is slowly varied, and for each flux bias point the SQUID is ramped, forcing it to switch into the voltage state. As mentioned in the previous section, the SQUID critical current, and hence the voltage that it switches to is dependent on the flux through the SQUID loop which itself depends on the qubit state.

As mentioned in the previous section, by measuring the time from the start of the SQUID ramp, we can distinguish between the switching events that correspond to the qubit being in the $|0\rangle$ or $|1\rangle$ state. This allows us to map out how the depths of the wells of the flux-biased phase qubit potential change as a function of flux bias. If the actual qubit parameters correspond to the design values given in (4.2), the SQUID step data will look like Figure 4.8b. Each of the two overlapping sloped lines, which we have termed **branches**, corresponds to a qubit potential minimum. If there would be no flux bias dependence to the data, it would indicate a problem with either the on-chip flux bias trace or the lines in the dilution refrigerator leading down to the on-chip flux bias line. Therefore, the V_{bias} line should be checked for continuity or shorts by verifying that its series resistance is $1k\Omega$ (see Appendix B). Once this SQUID step dataset is obtained, the bias values needed to initialize, operate and read out the qubit can be read off directly from the SQUID step data.

First, we need to calibrate the flux bias values needed to initialize the qubit into one particular minimum of the qubit potential. This is the initialization procedure called for in the second DiVincenzo criterion and the need for it can be understood as follows. Cooling the device to $\sim 25mK$ relaxes the qubit state at random into one of the wells in the qubit potential. After we operate on the qubit and measure the state, the state might end up in a different well. Therefore, if we want to perform further experiments on the qubit, we will need a way to “reset” the qubit back to the well that we originally

defined to represent the qubit well. As shown in Figure 4.8b, for the case of two overlapping branches, *i.e.* two minima, the initialization is accomplished by first biasing the qubit to a point where only one branch is present. This “reset bias” is labeled as r in Figures 4.8b and c. However, if the qubit critical current, I_0 , was larger or the qubit inductance, L , was smaller than the ideal values listed (4.2), there would be more than two overlapping branches at any given flux bias. An example of 3 overlaps (3 simultaneous qubit potential wells) is shown in Figure 4.8c. As a result, the initialization protocol is more complex and involves cycling the qubit bias multiple times between two bias points, r_1 and r_2 . These two points are chosen as the reset biases because at these points there is a minimal number of overlapping branches. As discussed in more detail in [3], a minimum of 3 resets is needed to ensure that the probability of the qubit being initialized into one of the other wells is $< 10^{-4}$. The pulse sequence for this reset will be shown below.

Once the qubit is initialized to a given branch, appropriate bias points on that branch need to be calibrated. The first will be the bias at which the qubit will be operated on and measured. This will be called the **operating bias**. At this stage, the selection of an operating bias is coarse and all that is needed is the value of a flux bias point near the edge of the branch into which the qubit has been initialized. This flux bias point is labeled as o in Figures 4.8b and c. At this edge, one of the wells will be shallow enough to be used as the well for the qubit states. In the next calibration experiment, the **step**

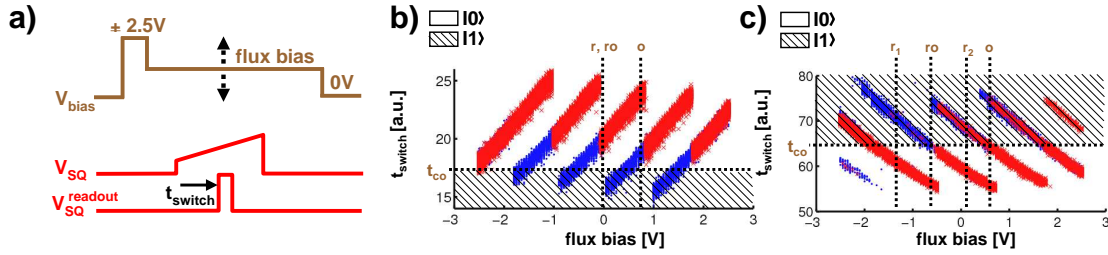


Figure 4.8: **SQUID steps measurement.** The SQUID steps measurement is an important experiment that allows us to obtain calibration values needed to initialize, measure and bias the qubit. **a)** The pulse sequence of the SQUID steps experiment. The flux bias is first set to its maximum positive amplitude of $+2.5V$. Then it is immediately set to the flux bias value that is being scanned in the SQUID steps measurement. At this point, the SQUID is ramped and the switching time is recorded. This same pulse sequence is repeated with the same flux bias value, but with the initial flux bias set to its maximum negative amplitude of $-2.5V$. Due to the hysteresis in the SQUID step branches, initially setting the flux bias to its maximum positive and negative values is necessary in order to fully map out the regions where there are overlapping branches. This can be understood by noting that the red (blue) points in **b)** and **c)** are where the flux bias was initially set to $+2.5V$ ($-2.5V$). **b)** A dataset of a typical SQUID step experiment. The significance of each of the calibration values marked as t_{co} (cutoff time), r (reset bias), o (operating bias), ro (readout bias) is explained in the text. The qubit state is read out at the readout bias. If the switching time t_{switch} at the readout bias falls at or above the cutoff, t_{co} , then the qubit is read out as being in the $|0\rangle$ state, otherwise the qubit is read out as being in the $|1\rangle$ state. **c)** A SQUID step experiment where the qubit critical current and inductance are such that there are more wells in the qubit potential or equivalently more overlaps in the SQUID steps. This requires an additional reset bias point as indicated by r_1 and r_2 .

edge experiment, the operating bias will be chosen more precisely.

Finally, after the qubit is measured it will need to be biased to a **readout bias** where the two wells of the potential will be approximately symmetric and separated by about one flux quantum. At this readout bias, we also need to find the value of the SQUID switching time, t_{switch} , that maximally separates the switching times corresponding to the $|0\rangle$ state from those corresponding to the $|1\rangle$ state. We have called this value the **cutoff time** and have labeled it as t_{co} in Figures 4.8b and c.

4.3.2 Step Edge: fine calibration of the bias point

The step edge experiment allows us to verify that the reset biases found in the SQUID steps measurement properly initialize the qubit into the $|0\rangle$ state. It also allows us to calibrate the operating bias on a finer scale so that the current through the qubit is as close to the critical current as possible, but without making the qubit well so shallow that the $|0\rangle$ state tunnels out. Biasing near the critical current gives the qubit a larger non-linearity. To see this we can let $\omega_{01} \simeq \omega_p$ in the expression for the number of single-qubit operations possible given a particular non-linearity, (3.1). From (3.16), we can see that the plasma frequency decreases as the operating bias approaches a value where the current through the qubit junction is close to the junction critical current. Therefore, as given by (3.1), the non-linearity and the number of single qubit operations that can be performed will increase. To measure the depth of the qubit well for each operating bias, we can use equation (3.15) for the barrier height ΔU and equation (3.16) for the plasma frequency. We can then calculate an approximate value for the qubit level spacing $\hbar\omega_p$ and this will allow us to obtain the approximate number of levels in the qubit well, $\Delta U/\hbar\omega_p$, which gives us an indication of how deep the qubit well is. We can typically get so close to the critical current that only $\Delta U/\hbar\omega_p \sim 4 - 10$ levels are in the qubit well.

In the step edge experiment, we monitor the barrier height as a function of qubit operating bias by measuring the probability of tunneling of the $|0\rangle$ state. The data is

step-like in appearance because of the exponential dependence of the $|0\rangle$ state tunneling rate, Γ_0 , on the height of the tunneling barrier of qubit well, ΔU , as given earlier in (4.3). As the operating bias is increased and the edge of a branch is approached, ΔU decreases to zero and the zero state escapes. The pulse sequence for this experiment is shown in Figure 4.9a, and is illustrated for a device that has 3 overlapping branches in order to demonstrate the more complex reset sequence. As shown in Figure 4.9a, the flux bias pulse sequence is divided into 3 regions: reset, operating bias, and readout bias. The reset and readout biases have already been calibrated in the SQUID steps experiment. Here, we will verify these calibrations and we will also calibrate the operating bias.

The step edge data for a typical qubit is shown in Figure 4.9b. The probability of the $|0\rangle$ state tunneling out of the qubit well is plotted as a function of the qubit operating bias. Although a purely exponential dependence of the $|0\rangle$ state tunneling probability on the operating bias is expected, as given by (4.3), periodic sharp features are often superimposed on the rising step edge. These features are due to an enhancement in the tunneling probability for tunneling between the states in the qubit well and the deep right well, an effect known as **resonant tunneling**. Resonant tunneling takes place when the operating bias is scanned tilting the potential as previously shown in Figure 4.3. During the tilting, the levels in the qubit well and the deep right well align and a resonant tunneling event occurs. Aside from the resonant tunneling features, the $|0\rangle$ tunneling probability has an exponential dependence on operating bias as expected,

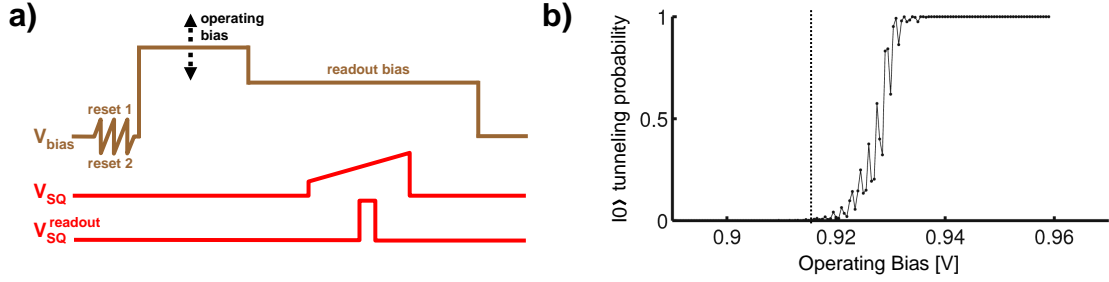


Figure 4.9: The step edge experiment. The purpose of the step edge experiment is two-fold. First, we want to verify that the reset and readout biases as well as the cutoff times calibrated in the SQUID steps experiment allow us to properly initialize and read out the qubit. We also want to find the value of the qubit operating bias that is as close as possible to the qubit critical current, but not so close that the qubit $|0\rangle$ state starts tunneling out of the qubit well. As discussed in the text, biasing near the critical current gives a larger non-linearity and as a result allows us to perform more single qubit operations as given by (3.1). **a)** Pulse sequence for a step edge experiment for a qubit with SQUID steps like those in Figure 4.8c. To ensure that the qubit is reset only to one branch, the reset is repeated 3 times using the “ r_1 ” and “ r_2 ” values calibrated in the SQUID steps experiment. Three reset cycles ensure that the probability of the qubit being initialized into one of the other branches is $< 10^{-4}$. Then the flux bias is set to the operating bias value (“o”) for $\sim 30\mu\text{s}$. Finally, the flux bias is set to the readout bias value (“ro”) for $\sim 90\mu\text{s}$ and its state is read out using the SQUID. This sequence is repeated for a range of values of the operating bias. For each operating bias value, the pulse sequence is repeated 1200 times and the probability of tunneling of the $|0\rangle$ state is given by (number of repetitions where $t_{\text{switch}} > t_{\text{co}}$)/1200. **b)** A typical step edge data set. As the operating bias is increased, the qubit well gets shallower and the tunneling of the $|0\rangle$ state increases exponentially, as discussed in the text. The resonant features on top of the exponential curve correspond to resonant tunneling events and are explained in the text. The value of the operating bias that gives the largest non-linearity while giving the smallest $|0\rangle$ state tunneling probability is indicated on the step edge data by the dotted line and usually corresponds to the qubit well having approximately $U/\hbar\omega_p \sim 4 - 10$ levels.

indicating that the qubit has been properly initialized and that the calibrations in the SQUID steps experiment have been performed correctly.

Now that we have verified proper initialization and readout and know that the SQUID steps calibrations are correct, we can calibrate the operating bias using the step edge data. We do this by choosing a value that gives a number of levels, $\Delta U/\hbar\omega_p$,

as close to 4 as possible, giving the highest possible non-linearity. The operating bias value at which this takes place is indicated by the dotted vertical line in Figure 4.9b and this will value is the calibrated qubit operating bias. Typically a formal calculation of the number of levels in the qubit well is not necessary in order to calibrate the qubit operating bias. It can be calibrated visually from the step edge data by choosing the operating bias closest to the rising step where the probability of $|0\rangle$ state tunneling is still zero.

4.3.3 S-curve: measurement pulse amplitude calibration

The next step is to calibrate the amplitude of the measurement pulse needed to reduce the qubit well tunneling barrier height, ΔU , by an amount that will ensure that the $|1\rangle$ state fully tunnels out into the deep right well while the $|0\rangle$ state population remains in the qubit well. This is done using a measurement we have named the **s-curve** due to the “s” shape of the data trace. However, because we have no way to prepare the qubit in the $|1\rangle$ state yet, we have to find the appropriate measurement pulse amplitude by measuring the tunneling probability of the $|0\rangle$ state as a function of the amplitude of the qubit measurement pulse. As stated earlier in (4.4), we know that approximately $\Gamma_1/\Gamma_0 \simeq 300$ [52]. Therefore, if we set the amplitude of the measurement pulse to give a 5% $|0\rangle$ state tunneling probability, we will guarantee that the $|1\rangle$ state will fully tunnel out of the qubit well. This “5% method” for obtaining the measurement pulse

amplitude can be shown to be correct by using a more complex experiment where the qubit is excited into the $|1\rangle$ state and an s-curve measurement for the $|1\rangle$ state is obtained and compared to the $|0\rangle$ state s-curve. This measurement will not be discussed here and is described in reference [3].

The pulse sequence for the s-curve experiment is shown in Figure 4.10a, where now a new row has been added to the pulse sequence to represent the voltage, V_Z , on the measurement pulse line. As shown earlier in Figure 4.2 and as discussed in Appendix B, the measurement pulse signal is applied through a separate RF line (labeled V_Z) with 50Ω characteristic impedance which is tee'd into the DC flux bias line (labeled V_{bias}) using a bias tee. More details on the electronics that generate the measurement pulse can also be found in Appendix B.

It is important to understand the dynamics of how the shape of the measurement pulse alters the qubit potential as a function of time. The exact measurement pulse shape is shown in the inset to Figure 4.10a. The rising edge of the pulse tilts the potential, lowering the tunneling barrier, ΔU . The pulse is held at the measurement pulse amplitude value for ~ 10 ns. Then, as the pulse gradually falls to zero over a time of ~ 40 ns, the potential is tilted back to the same point as before the measurement pulse was applied. The hold time allows the occupied state to tunnel out and decay in the deep well to the right of the qubit well at the n_r/T_1 rate mentioned previously. Bypassing this hold time and tilting the potential back right away would have resulted in some

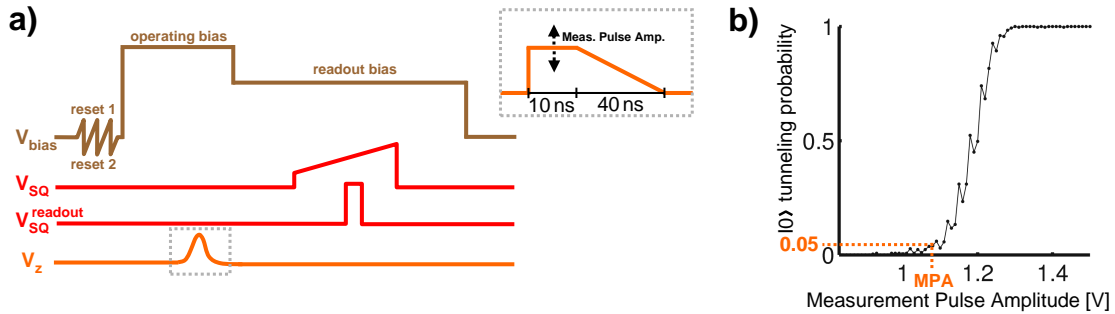


Figure 4.10: **S-curve experiment.** This experiment is used to find the measurement pulse amplitude needed to selectively tunnel out only the $|1\rangle$ state in order to measure the qubit as previously described in Figure 4.4. **a)** The pulse sequence for the s-curve experiment. The bias and readout are operated in the same way as in the step-edge experiment. On the pulse sequence diagram, a new line for the measurement/z-pulse (V_z) is added and shows that we measure the qubit during the time that it is biased at the operating bias. Although the measurement pulse will be represented on pulse sequences as having a Gaussian envelope, the measurement pulse shape used in the experiments is shown in the inset. Increasing the measurement pulse amplitude tilts the potential in a slower, more controlled fashion compared to increasing the operating bias in the step edge experiment. The measurement amplitude will be calibrated in the s-curve experiment and is indicated by the double-tipped dashed arrows. We choose this pulse shape to reduce visibility errors, as explained in the text. **b)** Typical data for an s-curve experiment. The tunneling probability of the $|0\rangle$ state is plotted as a function of measurement pulse amplitude. As the measurement pulse amplitude is increased, the potential is tilted reducing the barrier, ΔU , between the two wells until eventually the $|0\rangle$ state fully tunnels out of the qubit well. As discussed in the text, the calibrated measurement pulse amplitude is set to the value that corresponds to a 5% $|0\rangle$ state tunneling probability because this guarantees that the $|1\rangle$ state will fully tunnel out of the qubit well.

of the state tunneling back from the deep right well, reducing the qubit visibility. A theoretical analysis of this error mechanism can be found in [88].

The data for a typical s-curve experiment is shown in Figure 4.10b. The probability of the $|0\rangle$ state tunneling out of the qubit well is plotted as a function of measurement pulse amplitude. Again, the sharp peaks that are superimposed on the s-curve data indicate that resonant tunneling is taking place. The measurement pulse amplitude that

corresponds to a 5% tunneling probability of the $|0\rangle$ state is indicated by the dotted line.

It is instructive to review some common errors in the set-up of the s-curve measurement. One common error is that the tunneling probability remains at zero, or does not fully reach 1 even for large values of the measurement pulse amplitude. This is most likely caused by the operating bias being calibrated to a qubit well depth that was too deep in the step-edge experiment. To fix this, the operating bias can be re-calibrated to a value closer to the step edge. Another error is due to setting the hold time discussed above to a value that is shorter than the time it takes for the state to relax in the deep right well. If this is the case, then when the qubit is in the $|1\rangle$ state, the state will tunnel to the right deep well, but will not have enough time to relax in that well. As a result, it will tunnel back into the qubit well and the $|0\rangle$ state tunneling probability will not rise fully to 1 in the s-curve data. If on-chip heating is present or if the operating bias is set to a qubit well that is too shallow, the s-curve data will begin from a non-zero $|0\rangle$ state tunneling probability. The qubit then needs to be re-biased to a deeper well. If heating is the problem, then the cryogenic wiring described in Appendix B must be checked for proper thermal sinking and attenuation.

4.3.4 Spectroscopy

Calibrating the operating bias to a specific value fixes the energy level structure of the qubit. If the energy levels of the qubit are fixed, the frequencies of the transitions

between these levels can now be measured. This is done by initializing the qubit into the $|0\rangle$ state and subsequently driving the qubit into the $|1\rangle$ state with a microwave pulse whose frequency is scanned, but whose duration is fixed at a value much longer than the qubit energy relaxation time, T_1 . For each frequency point, the probability of the qubit being read out in the $|1\rangle$ state is measured. It is important to note that, if the qubit is in a higher state than the $|1\rangle$ state, it will also be read out as tunneled. The pulse sequence for a typical spectroscopy experiment is shown in Figure 4.11a. To reduce visual clutter, the readout lines (V_{SQ} and $V_{SQ}^{readout}$) have been left off the pulse sequence diagram in Figure 4.11a. These lines will not be shown in pulse sequences in subsequent experiments with the understanding that the readout sequence is still executed in the same manner as in the step edge experiment in Figure 4.9a.

Let us briefly go over the important transitions that we can measure using a spectroscopy experiment. The most important transition is the $0 \rightarrow 1$ transition between the qubit $|0\rangle$ and $|1\rangle$ states. Its frequency should correspond to the expected design value given by $\omega_{01}/2\pi = 1/(2\pi\sqrt{LC}) \simeq 1/(2\pi\sqrt{(750 \times 10^{-12})(1 \times 10^{-12})}) \simeq 6$ GHz. The $0 \rightarrow 2$ transition has a frequency slightly below 12GHz. However, it can be excited at half this frequency through a two-photon process that virtually occupies the $|1\rangle$ state [84]. Thus the two-photon $0 \rightarrow 2$ transition frequency will be slightly below the qubit frequency, at approximately the $1 \rightarrow 2$ transition frequency. At this point in the qubit calibration, we cannot generate a π pulse therefore we cannot excite the $1 \rightarrow 2$

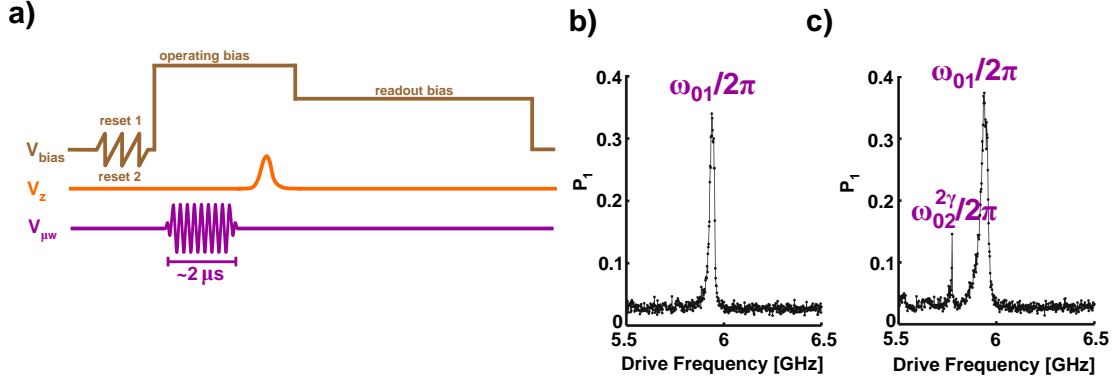


Figure 4.11: Spectroscopy experiment. This experiment allows us to measure the frequency response of: any of the transitions between the energy levels in the qubit well, any resonant microwave modes in on-chip wiring or within the qubit sample box, or any resonant excitations of two-level defect states (TLS's). The most important transition frequencies are the qubit transition $\omega_{01}/2\pi$ frequency and the frequency of the two-photon $0 \rightarrow 2$ transition, $\omega_{02}^{2\gamma}/2\pi$. The origin of the two-photon $0 \rightarrow 2$ transition and how it can be used to measure the non-linearity of the qubit are discussed in the text. The two-photon $0 \rightarrow 2$ transition and some microwave and TLS modes can only be excited at high microwave power. **a)** Pulse sequence for the spectroscopy experiment. The flux bias and readout pulse sequences are the same as in the step edge and s-curve experiments. The readout lines have been left off the spectroscopy experiment pulse sequence diagram in order to reduce visual clutter. However, the qubit readout is still performed in the same manner as shown earlier in the step-edge and s-curve pulse sequences. To perform spectroscopy, the qubit is first initialized into the $|0\rangle$ state and a long microwave pulse of a given frequency is applied to the qubit. The qubit is then measured using the calibrated measurement pulse amplitude value found in the s-curve experiment. The experiment is repeated for a range of microwave pulse frequencies and for each frequency we record the probability that the qubit was measured to be in the $|1\rangle$ state, P_1 . To avoid decay from decoherence during the microwave excitation, the microwave pulse length must be much longer than the energy relaxation time, T_1 , of the qubit which will later be measured to be $\sim 500\text{ns}$. Here, we use $2\mu\text{s}$ for the length of the microwave pulse. Spectroscopy experiments can be done at various microwave drive powers. **b)** At low microwave power, the spectroscopy data only shows the qubit transition being excited. **c)** The scan over the same frequency as in b), but at higher microwave drive power shows both the qubit $0 \rightarrow 1$ as well as the two-photon $0 \rightarrow 2$ transitions being excited.

transition directly. Therefore, measuring the the two-photon $0 \rightarrow 2$ transition frequency and the qubit $0 \rightarrow 1$ frequency allows us to approximately measure the non-linearity of the qubit, as given by (3.1). Since it requires two photons, the two-photon $0 \rightarrow 2$ transi-

tion is only excited at high microwave power. In addition to mapping out the spectrum due to the Josephson junction, the spectroscopy experiment is also useful because it reveals any unwanted microwave resonant modes and TLS transitions. The microwave modes can be box modes from the aluminum box enclosing the qubit chip or microwave resonances from on-chip wires or wirebonds. If these microwave and TLS modes are sufficiently close in frequency to the qubit $\omega_{01}/2\pi$ frequency and if the qubit is driven at high enough power to excite them, they will act as pathways for energy leakage from the qubit.

The data for the spectroscopy experiment is shown in Figures 4.11b and c. Using low microwave power in the pulse sequence shown in Figure 4.11a, we obtain the data shown in Figure 4.11b. The probability of the qubit being read out as being in the $|1\rangle$ state, P_1 , is plotted as a function of the frequency of the microwave source. The same data, at high microwave power, is shown in Figure 4.11c, where now the two-photon $0 \rightarrow 2$ transition is being excited due to the higher power of the microwave drive. The qubit transition frequency and the two-photon $0 \rightarrow 2$ frequency are labeled as $\omega_{01}/2\pi$ and $\omega_{02}^{2\gamma}/2\pi$, respectively. Using equation (3.2), we can estimate the qubit energy relaxation time from the quality factor, Q_{01} , of the $0 \rightarrow 1$ resonant response. However, at high microwave power the resonant responses are broadened preventing us from obtaining an accurate value of the quality factor, Q_{01} . Again, Q_{01} is given by $\omega_{01}/\Delta\omega_{01}$ where $\Delta\omega_{01}$ is the full-width at half-max of the $0 \rightarrow 1$ response. The low

microwave power data gives a qubit response that is not artificially power-broadened allowing us to get a rough measurement of the coherence time. Shortly, we will describe an experiment specifically tailored for the measurement of the energy relaxation and dephasing times T_1 and T_2 , respectively.

Spectroscopy data can also be taken in another way which makes the locations of TLS and resonance modes in the frequency spectrum visually clear. We call this version of the spectroscopy experiment **fine spectroscopy** [70]. An example of fine spectroscopy data is shown in Figure 4.12. Fine spectroscopy uses the same pulse sequence as shown in Figure 4.11a for regular spectroscopy, but each scan of drive frequency is repeated for a range of values of the qubit operating bias. Figure 4.12 shows fine spectroscopy data. For each operating bias (horizontal axis), the drive frequency (vertical axis) is scanned over a small frequency range around the qubit transition frequency $\omega_{01}/2\pi$. At each frequency and operating bias data point, the probability, P_1 for being in the $|1\rangle$ state is measured and plotted in grayscale. For each operating bias point, the measurement pulse amplitude needs to be re-calibrated because the qubit well depth changes, as indicated by the insets of the qubit potential in Figures 4.12a and b.

The data for the low microwave power fine spectroscopy scan is plotted in Figure 4.12a and shows just the qubit transition frequency, $\omega_{01}/2\pi$, as a function of operating bias. A high microwave power scan for a different device is shown in Figure 4.12b. In addition to the qubit transition frequency, the high power scan also shows the two-

photon $0 \rightarrow 2$ transition frequency, just below the qubit transition frequency. The insets depicting the qubit potential at two different operating biases are meant to emphasize that as the qubit well becomes shallower, the non-linearity increases, as shown by the increasing separation between the $\omega_{01}/2\pi$ and the $\omega_{02}^{2\gamma}/2\pi$ frequencies in Figure 4.12b. Based on previous work [70, 50], we know that the splittings in Figure 4.12, labeled with the vertical arrows, correspond to the qubit levels coupling either to a two-level state defect or to a microwave resonance mode. In order to distinguish coupling to a TLS from coupling to a microwave mode, the temperature of the qubit sample can be cycled up to a couple Kelvin, and if the splittings do not move in frequency in response to the temperature cycling, then they are most likely microwave resonance modes.

Aside from locating TLS and microwave modes near the qubit frequency, the fine spectroscopy scan is also very useful because it can be used to extract the actual values of qubit parameters C , I_0 , and L . These can deviate from the design values given in 4.2 due to variations and errors in fabrication. We can extract the actual fabricated parameter values by realizing that $\omega_{01} \simeq .95\omega_p$ and fitting equation (3.16) to the low power fine spectroscopy data. This completes the spectroscopy calibrations.

4.3.5 Rabi Oscillations

Now that we have identified the qubit $0 \rightarrow 1$ transition frequency, we can drive transitions between the $|0\rangle$ and $|1\rangle$ states by pulsing the qubit with microwave pulses of fixed

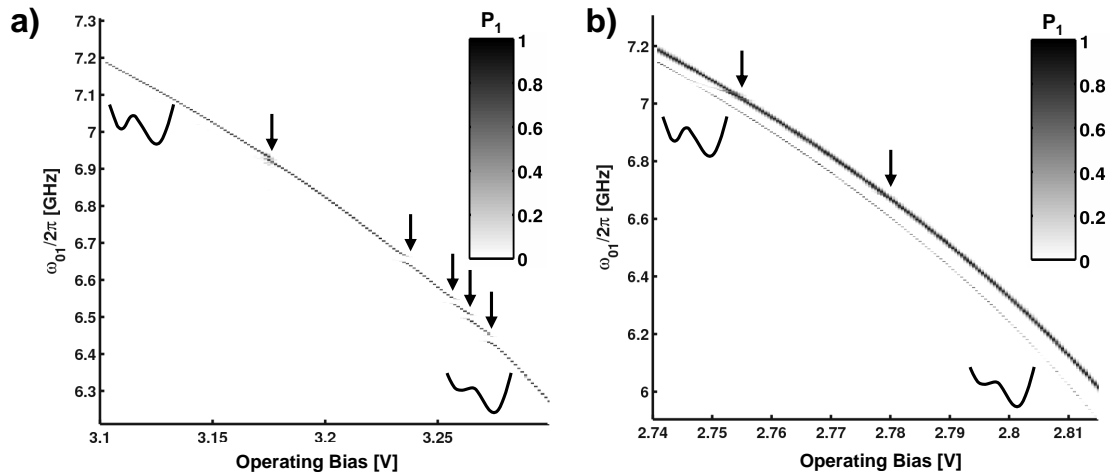


Figure 4.12: **Fine Spectroscopy** This experiment is much like the previous spectroscopy experiment, except that here the qubit operating bias is also varied. Therefore these scans plot the probability of the qubit being read out as in the one state, P_1 (grayscale), as a function of the frequency of the microwave pulse (vertical axis) and the qubit operating bias (horizontal axis). In order to complete these scans in a reasonable time, data is taken only in a small frequency range around the qubit transition frequency, $\omega_{01}/2\pi$. These scans are particularly useful for revealing TLS and microwave modes in the spectrum, which are labeled with the vertical arrows in the data. **a)** A fine spectroscopy scan taken at low microwave power only shows the qubit frequency, $\omega_{01}/2\pi$. **b)** Fine spectroscopy data taken at high microwave power shows how both $\omega_{01}/2\pi$ (top, darker curved line) and $\omega_{02}^{2\gamma}/2\pi$ (bottom, lighter curved line) depend on the qubit operating bias.

frequency, $\omega_{01}/2\pi$. This is demonstrated on the Bloch sphere in Figure 4.13a. The total area under the microwave pulse envelope determines the amount of rotation, θ , on the Bloch sphere, as shown in Figure 2.1. The microwave power of the pulse determines the frequency of this rotation. Therefore, by varying the length or amplitude of these fixed-frequency microwave pulses, we can calibrate what pulse lengths or amplitudes are required to generate pulses with $\theta = \pi$ and $\theta = \pi/2$ which will be used to construct single-qubit X and Y pulses. This experiment is commonly called a Rabi oscillation

experiment [21, 1, 84], but we will call it a **Rabi** for convenience. The Rabi will also be very useful in studying measurement crosstalk between two qubits, as will be discussed later in Chapter 7.

As mentioned above, in a Rabi experiment both the microwave pulse length or amplitude can be varied. We will discuss only the method where the pulse length is varied. The pulse sequence for this type of Rabi is shown in Figure 4.13b. To simplify pulse sequence diagrams further, we have now left off the flux bias line (V_{bias}) and combined the measurement/z-pulse line (V_Z) and the microwave line (V_{mw}). This is done only to reduce visual clutter and in the experiment the flux bias, readout, microwave, and measurement/z-pulse signals are all still executed on separate physical wires, as shown originally in Figure 4.6.

Typical Rabi data is shown in Figure 4.13c, where the probability of the qubit being measured in the $|1\rangle$ state is plotted as a function of the Rabi pulse length, t_{rabi} . The microwave pulse length needed for a rotation by $\theta = \pi$ is given by the value of t_{rabi} at the first maximum of the Rabi oscillation, as indicated by the dotted line in Figure 4.13c. The Rabi pulse length or amplitude needed for a $\pi/2$ pulse is half the value needed for a π pulse. The decay in the oscillations is due to energy relaxation and dephasing. The main purpose of the Rabi experiment is to obtain the microwave pulse lengths needed for π and $\pi/2$ pulses. Therefore, the exact mathematical formula for the decay of the Rabi envelope is not important, but it can be found in reference [1]. The oscillation fre-

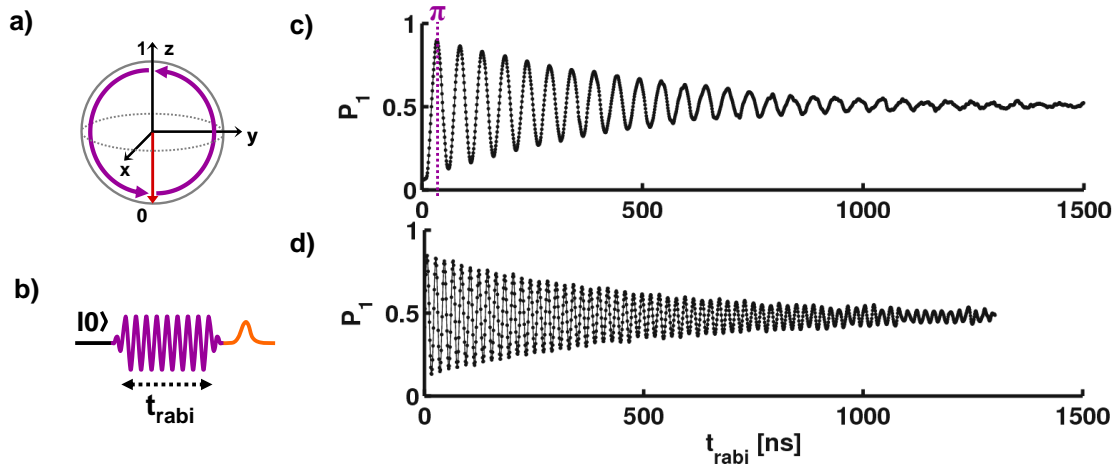


Figure 4.13: **Rabi experiment.** In the Rabi experiment, we drive the qubit with microwave pulses at the $\omega_{01}/2\pi$ qubit transition frequency. **a)** The Bloch vector will oscillate between the $|0\rangle$ and $|1\rangle$ states on the Bloch sphere. The frequency of this oscillation is determined by the power of the microwave drive and the amount of rotation on the Bloch sphere, θ , is determined by the area under the microwave pulse. **b)** The pulse sequence for the Rabi experiment. The flux bias and readout lines have been left off the diagram to reduce visual clutter. However, the readout and bias are still executed in the same manner as in the spectroscopy and s-curve experiments. The measurement/z-pulse (V_Z) and microwave (V_{mw}) lines have also been combined into a single line to save space, but in the actual experiment these signals are applied on separate physical wires as previously described in Figure 4.2. Pulses on the microwave line (V_{mw}) are color-coded in violet and those on the measurement/z-pulse line (V_Z) are color-coded in orange. The Rabi experiment begins by initializing the qubit into the $|0\rangle$ state and then applying a microwave pulse with frequency $\omega_{01}/2\pi$. The probability of the qubit being read out as being in the $|1\rangle$ state, P_1 , is measured. This is repeated for a range of Rabi pulse lengths, t_{rabi} . **c)** This is the Rabi experiment data and shows oscillations in P_1 as a function of Rabi pulse length. The decaying envelope is due to decoherence. The pulse length corresponding to a $\theta = \pi$ rotation is labeled with the vertical dashed line. The value needed for a $\pi/2$ rotation is just half of the π value. This calibrates the microwave pulse lengths needed for the π and $\pi/2$ pulses that form the basic single-qubit logic operations. **d)** A Rabi done at higher microwave drive power as compared to c). As a result, the frequency of Rabi oscillations increased from 19 MHz to 50 MHz. As discussed in the text, faster pulses allow us to perform more single-qubit operations before the qubit loses coherence.

quency of the Rabi data in Figure 4.13c is $\sim 19\text{MHz}$. A Rabi scan at higher microwave drive power is shown in Figure 4.13d, where the oscillation frequency has increased

to $\sim 50\text{MHz}$. A higher Rabi oscillation frequency allows for faster single-qubit pulses and the faster the single-qubit pulses, and thus more single-qubit logic operations can be performed before the qubit state loses coherence via energy relaxation (T_1) and/or dephasing (T_2).

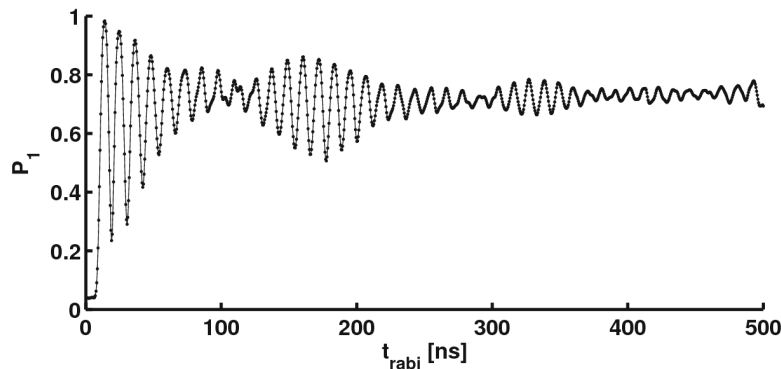


Figure 4.14: Rabi data where the beating behavior is due to either the qubit being biased too close to a microwave mode or TLS or the Rabi oscillation frequency being near or larger than $(\omega_{01} - \omega_{02}^{2\gamma})/2\pi$ and hence driving the two-photon $0 \rightarrow 2$ transition.

Before moving on to the next section, it is instructive to highlight two error modes that can be encountered in a Rabi experiment. One type of error produces Rabi oscillations that surprisingly do not seem to decay, as if the decoherence times T_1 and T_2 are nearly infinite. This is caused by incorrectly setting the delay of the measurement pulse so that the qubit is measured while the Rabi microwave pulse is still interacting with the qubit. This can be fixed by delaying the measurement pulse so that the measurement takes place well after the Rabi pulse. However, it cannot be so far after the Rabi pulse that the probability of being in the $|1\rangle$ state decays significantly due to decoherence.

Another common error is when the Rabi oscillation envelope exhibits a beating pattern as shown in Figure 4.14. This is usually due to the Rabi oscillation frequency being near or greater than $(\omega_{01} - \omega_{02}^{2\gamma})/2\pi$ and hence the nearby two-photon $0 \rightarrow 2$ transition also ends up being driven by the Rabi microwave pulse. The beating behavior can also be due to the excitation frequency of a TLS or microwave mode being near the qubit $\omega_{01}/2\pi$ frequency. For both cases, decreasing the microwave drive power will help. In the case of excitation of the two-photon $0 \rightarrow 2$ transition, the operating bias can also be set to a shallower well so that the non-linearity increases. In the case of a nearby microwave mode or TLS, the qubit operating bias will need to be re-calibrated to a value where the qubit $\omega_{01}/2\pi$ frequency is far from the frequencies of these modes or TLS's.

4.3.6 Measuring energy relaxation

Now that we have calibrated the ability to control the Bloch sphere angle θ (see Figure 2.1), we can apply a π microwave pulse ($\theta = \pi$) to excite the qubit into the $|1\rangle$ state and then let it relax over time back to the $|0\rangle$ state. This allows for a measurement of the energy relaxation time, T_1 . A detailed theoretical treatment of the measurement of the energy relaxation time, T_1 , can be found in references [1, 84]. The pulse sequence for this experiment, which we call the **T_1 experiment**, is shown in Figure 4.15a. The qubit is pulsed with a π pulse and after a delay, t_{meas} , the probability, P_1 , of the qubit being in the $|1\rangle$ state is measured. This sequence is repeated for increasing values of

t_{meas} . Typical T_1 data is shown in Figure 4.15b. The decay envelope is exponential

$$P(t_{meas}) = P_{0T} + Ve^{-t_{meas}/T_1} \quad (4.5)$$

and the T_1 time is defined as the time at which the probability of the qubit being in the $|1\rangle$ state has decayed by $1/e$ from its maximum value. A fit of the data in Figure 4.15b to (4.5) yields an energy relaxation time, $T_1 \simeq 503\text{ns}$, where $P_{0T} \sim 0.05$ is the stray $|0\rangle$ state tunneling probability calibrated in the s-curve measurement and $V \sim 0.85$ to 0.93 is the qubit visibility, discussed previously in Chapter 2.

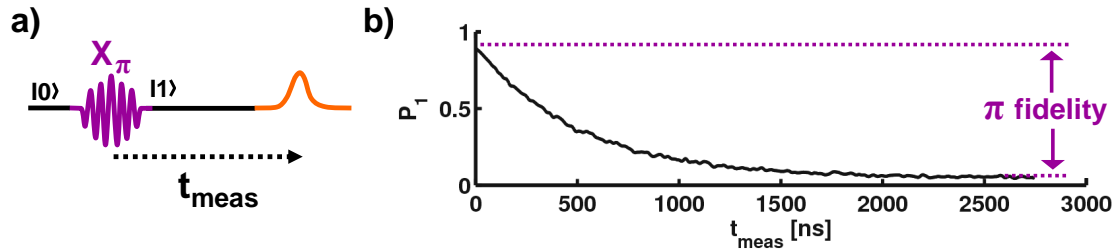


Figure 4.15: **Measuring the energy relaxation time, T_1** **a)** The pulse sequence for the T_1 experiment. A π pulse is applied to a qubit initialized to the $|0\rangle$ state, exciting it into the $|1\rangle$ state. A measurement pulse is applied at a time t_{meas} after the π pulse and measures the probability of the qubit being in the $|1\rangle$ state. **b)** The data for the T_1 experiment. The probability of the qubit being measured in the $|1\rangle$ state, P_1 , is plotted as a function of the measurement time, t_{meas} and decays from maximum in an exponential fashion. The T_1 time is defined as the time at which P_1 has decreased by a factor of $1/e$ from its maximum value and can be obtained by fitting the data to exponential function given in (4.5). For the data shown here, we obtain $T_1 \simeq 503\text{ns}$ from the fit. Using the T_1 data we can measure the fidelity of our π pulses, as indicated by on the figure and discussed in the text. A pulse with unit fidelity would excite the qubit fully into the $|1\rangle$ state so that at $t_{meas} = 0$, $P_1 = 1.0$. In practice, due to visibility errors and energy relaxation during the actual π pulse the π pulse fidelity is typically around ~ 0.92 .

However, what happens if the π pulse length was not calibrated properly in the Rabi

experiment? For example, if the qubit operating bias has drifted since the spectroscopy calibrations this would cause the Rabi pulse to drift off-resonance. One easy way to check for this error is by using the T_1 experiment. We can fix the t_{meas} time at the value corresponding to maximum P_1 in the T_1 experiment data. At this value of t_{meas} , we can measure P_1 at different operating bias values around which the Rabi was originally done. The P_1 will peak at some value of the operating bias when the microwaves are on-resonance with the qubit. Then we can re-bias the qubit to this value and repeat the T_1 scan, which will now be guaranteed to be on-resonance. From this on-resonance T_1 data, we measure the π pulse fidelity. We do this by taking the difference between the maximum and minimum P_1 values of the properly calibrated T_1 scan. It must be noted that this off-resonance error does not affect the measurement of actual value of T_1 because detuning would only lower the maximum value of P_1 in the T_1 data, *i.e.* it would only affect the visibility term, V , in (4.5), but would not alter the T_1 term. The data in Figure 4.15b has been already re-calibrated in this fashion to ensure a properly calibrated on-resonance π pulse. In Figure 4.15b, the π pulse fidelity is labeled using the dashed lines and is ~ 0.92 .

Another error is similar to the Rabi beating error that was discussed in the previous section. The T_1 data will not have a smooth decay envelope, but will have noticeable, periodic oscillations superimposed on the exponential decay. As with the Rabi, this error is due to either the qubit being biased near a microwave mode or a TLS, or the

microwave power being so high and the non-linearity so low that the two-photon $0 \rightarrow 2$ transition is excited. As with the Rabi, it can be fixed by re-biasing the qubit to a shallower well or away from microwave modes and TLS's.

4.3.7 Measuring dephasing

To complete the characterization and calibration of a single qubit, we only need to measure the dephasing time. The simplest way to measure dephasing is using a **Ramsey experiment** [82, 51, 1, 84] which can be visualized on the Bloch sphere as shown in Figure 4.16a, with the corresponding pulse sequence shown in Figure 4.16b. A $\pi/2$ pulse is first applied to a qubit initialized to the ground state. The $\pi/2$ pulse rotates the Bloch vector onto the equator. We then wait for a time t_{ramsey} , for dephasing to act on the state. During the t_{ramsey} wait time, a z-pulse is applied to the qubit to detune it from the rotating frame defined by the microwave source. The reason for this detuning will be explained shortly. Finally, another $\pi/2$ pulse is applied to the qubit to rotate the state back onto the z axis and then the probability of the qubit being in the $|1\rangle$ state is measured. The data for a Ramsey with 80 MHz detuning is shown in Figure 4.16c. The oscillation frequency of the Ramsey corresponds to the amount of detuning. The mathematical form of the decay envelope is not important because we still take the value of t_{ramsey} at which the oscillation amplitude has decayed by a factor of $1/e$ from maximum as the measure of dephasing. However, it should be noted that the mathematical form

of the Ramsey decay envelope does have both exponential components due to energy relaxation and Gaussian components due to dephasing. Details on this can be found in references [82, 51, 1, 84].

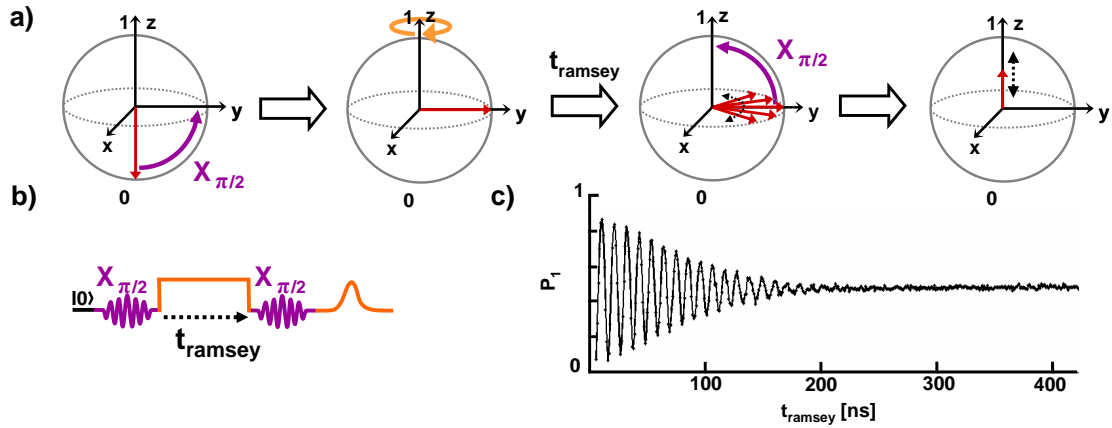


Figure 4.16: **Ramsey measurement.** The Ramsey experiment allows us to quantify the dephasing acting on a single qubit. **a) and b)** The pulse sequence for the Ramsey experiment can be understood using the Bloch sphere formalism. The qubit is initialized into the $|0\rangle$ state and a $\pi/2$ pulse is applied about the x-axis. This puts the state vector in the x-y plane and allows dephasing to act on the state. During the time that the state vector is in the x-y plane, the qubit is also pulsed with a z-pulse that detunes the qubit from the rotating frame of the microwave source. This allows for a more accurate measurement of dephasing, as explained in the text. The state vector is left in the x-y plane for a time t_{ramsey} and then another $\pi/2$ pulse is applied to rotate the state vector onto the z-axis. The probability of the qubit being in the $|1\rangle$ state is then measured and the whole sequence is repeated for increasingly longer t_{ramsey} times. As a result of the detuning produced by the z-pulse, the Bloch vector is spinning around its z-axis with respect to the rotating frame of the microwaves. Therefore, the final $\pi/2$ pulse can catch the dephased state vector at various angles ϕ in the x-y plane. This leads to oscillations in the final length of the state vector along the z-axis, as indicated by the double tipped dashed arrow in a). **c)** The Ramsey data showing P_1 measured as a function of t_{ramsey} . The oscillation frequency is determined by the amount of detuning which in this case is $\sim 80\text{MHz}$. The decay is due to dephasing and the time, T_2^{ramsey} , at which the oscillations have decayed by $1/e$ from maximum is $T_2^{ramsey} \simeq 120\text{ns}$.

It is important to understand the need for the detuning z-pulse during the t_{ramsey} time. Looking at the Bloch sphere sequence in Figure 4.16a, the two $\pi/2$ pulses in

a Ramsey can together be thought of as one π rotation. Therefore, when the z-pulse is off, the experiment can be thought of as a π pulse interrupted by a time, t_{ramsey} , during which dephasing can act on the state. The problem with doing this experiment without the z-pulse is that if the qubit bias happened to drift off-resonance from the microwave drive, it would cause the data to artificially appear to decay in time because this small detuning would produce a slow oscillation. For example, if the qubit bias drifted so that the qubit was 2MHz off-resonance from the microwave drive it would lead to oscillations with a period of 500ns. Therefore, by detuning the qubit from the microwave source by a known large amount, we set the timescale at which the oscillations take place and hence ensure that the decay from the oscillations will not be confused with the decay due to dephasing. As mentioned above, the T_2^{ramsey} time that quantifies the dephasing as measured by the Ramsey experiment is given by the t_{ramsey} value at which the oscillation amplitude decays by $1/e$ from its maximum. For the data in Figure 4.16c, we find $T_2^{ramsey} \simeq 120\text{ns}$.

The noise source that causes dephasing in superconducting qubits is known to be flux noise, which has a $1/f$ spectrum [12, 51]. This means that the qubit phase (ϕ in Figure 2.1) exhibits a low frequency drift that is correlated in time. As a result of this correlation, the drift can be canceled out by letting the phase drift for a given time and then reversing the drift direction and waiting for the same amount of time for the phase to drift back in the reverse direction. In order to implement this reversal, we merely add

a π pulse at a time exactly midway between the two Ramsey $\pi/2$ pulses. This “modified Ramsey” is more commonly known as a **spin echo** experiment [1, 84, 82].

The pulse sequence and corresponding Bloch sphere operations for a spin echo experiment are shown in Figures 4.17a and b. The time between $\pi/2$ pulses is still the variable that is scanned, but now it is split into two equal length segments $t_{se}/2$. As the Bloch sphere sequence shows, the π pulse reverses the dephasing direction by exchanging the $|0\rangle$ and $|1\rangle$ states. Just like in the Ramsey experiment, we detune the qubit from the microwave drive during the $t_{se}/2$ times and thereby induce oscillations in the spin echo data. Typical spin echo data is shown in Figure 4.17c. The probability, P_1 , of the qubit being measured in the $|1\rangle$ state is plotted as a function of the total wait time t_{se} . As with the Ramsey experiment, the echoed dephasing time, T_2^{echo} , is given by the value of t_{se} at which the oscillation amplitude has decayed by $1/e$ from its maximum. Here $T_2^{echo} \simeq 300\text{ns}$.

Now we have fully calibrated and characterized a single qubit. We can use these calibrations in the characterization and calibration of a sample with two coupled qubits, as will be discussed in the chapters that follow.

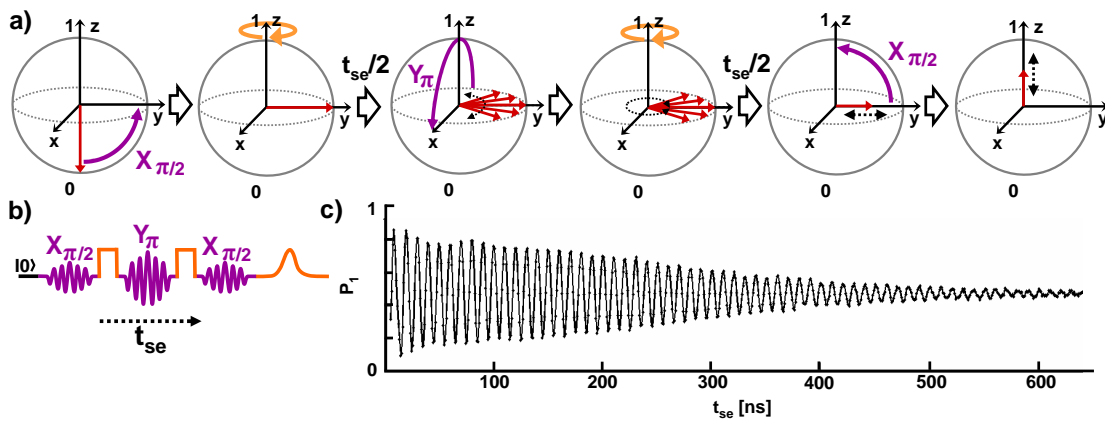


Figure 4.17: **Spin echo experiment.** The spin echo is similar to the Ramsey experiment, but now a π pulse is inserted midway in time between the two $\pi/2$ pulses in order to reverse the direction of the dephasing. **a) and b)** As with the Ramsey, the qubit starts in the $|0\rangle$ state and a $\pi/2$ pulse is applied that rotates the state vector around the x-axis into the x-y plane. At this point the qubit is detuned using a z-pulse, for reasons discussed in the text. It is then left to dephase for a time $t_{se}/2$. A π pulse is then applied about the y-axis that reverses the dephasing direction. Then the qubit is again left detuned for a time $t_{se}/2$ during which the dephasing produced during the first waiting period is “echoed” away. A final $\pi/2$ pulse returns the state vector to the z-axis and the probability of the qubit being in the $|1\rangle$ state, P_1 , is measured. The dashed vertical arrow in the final Bloch sphere snapshot emphasizes that P_1 oscillates in time due to the detuning. **c)** Spin echo data. The data is much like the Ramsey data with the oscillations due to the detuning from the z-pulse. The $1/e$ time here is roughly 300ns.

Chapter 5

Connecting Phase Qubits Using Fixed Coupling

5.1 Fixed Capacitive Coupling

The large size of superconducting phase qubits and the ability to connect them using standard electrical components, like capacitors and inductors, makes them much easier to couple together compared to other quantum computing architectures [85, 49, 36].

The simplest way to couple two superconducting phase qubits is by using an interdigitated capacitor, as shown in the circuit in Figure 5.1. Each qubit still has its own set of wiring as depicted earlier in Figure 4.2. Therefore, the parameters of each qubit can be adjusted separately and each or both can be measured, read out and operated on to-

gether or separately [54, 74]. Using **capacitive coupling** allows us to couple the qubits at microwave frequencies while effectively isolating them at lower frequencies so that flux bias signals on one qubit do not affect the other qubit.

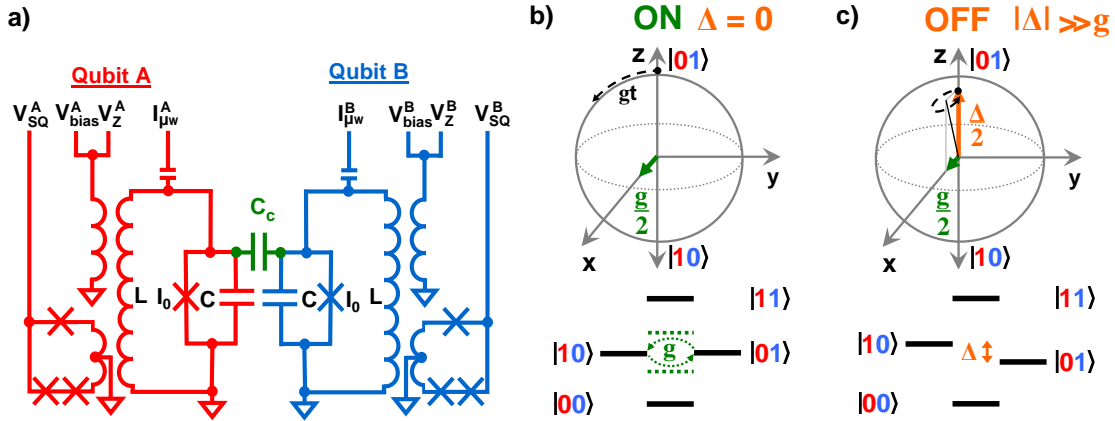


Figure 5.1: **Capacitively-coupled qubits.** **a)** An interdigitated capacitor $C_c \simeq 2$ fF couples the qubits, yielding an interaction strength $g/2\pi = 11$ MHz. To turn off the interaction we can pulse the V_Z lines to detune the qubits. **b)** Energy-level diagram with coupling interaction turned on. When qubits are on-resonance ($\Delta = 0$), their interaction swaps the populations of the $|01\rangle$ and $|10\rangle$ states at a frequency given by the coupling strength $g/2\pi$. The Bloch sphere representation of the $|10\rangle$ and $|01\rangle$ subspace shows state rotation (dashed line) about the x-axis due to the interaction g . **c)** When off-resonance $|\Delta| \gg g$, qubit swapping (dashed line) is effectively turned off.

5.1.1 Two-qubit circuit Hamiltonian and the swap operation

The Hamiltonian for the circuit in Figure 5.1a can be easily derived using the same technique of combining Kirchoff's equations with the Lagrangian formalism and converting classical variables to quantum operators, as was used to derive the Hamiltonian for a single qubit in (3.14). An example derivation is included in Appendix C. The only rele-

vant term in the full two-qubit Hamiltonian is the interaction term [36, 85, 49], H_{int} , that contains cross terms involving the superconducting phases of both qubits. As shown in the calculations in Appendix C, for the case of capacitively coupled qubits that are biased on resonance ($\omega_{01}^A \simeq \omega_{01}^B$) this interaction term, in the rotating frame, reduces to

$$H_{int} = \frac{g}{2} (\sigma_{X_A} \sigma_{X_B} + \sigma_{Y_A} \sigma_{Y_B}) \quad (5.1)$$

The $\{\sigma_{X_{A,B}}, \sigma_{Y_{A,B}}\}$ are the Pauli operators for qubits A and B. The constant, g , is the coupling strength and is given by

$$g = \frac{C_c}{(C + C_c)} \omega_{01}^{A,B} \quad (5.2)$$

where C and C_c are the fixed values of the qubit and coupling capacitors, respectively. For the capacitive coupling experiments in this thesis the parameters in (5.2) are $C \simeq 1pF$, $C_c \simeq 2fF$ and $\omega_{01}^{A,B}/2\pi \simeq 5 - 6GHz$, so that $g/2\pi \simeq 11MHz$. Although this coupling strength cannot change because the value of the capacitor, C_c , is fixed, the interaction between the qubits can be minimized by biasing the qubits off resonance by an amount that is much greater than the coupling strength, *i.e.* $|\omega_{01}^A - \omega_{01}^B| \gg g$.

Pauli operators provide a compact way of writing the interaction Hamiltonian, as in (5.1). However, they provide little immediate visual intuition. Therefore, it is instructive to write the interaction Hamiltonian in a way that visually shows the effect of H_{int}

on the two-qubit states

$$H_{int} = (g/2) (|01\rangle\langle 10| + |10\rangle\langle 01|) \quad (5.3)$$

By writing H_{int} in this way, we see that the coupling interaction swaps the populations of the $|01\rangle$ and $|10\rangle$ states. Since only the $|01\rangle$ and $|10\rangle$ states interact, the coupled qubit system can be represented using a reduced state space defined by $|01\rangle$ and $|10\rangle$. As shown in Figure 5.1, this reduced state space can be mapped to the Bloch sphere picture by choosing the $|01\rangle$ and $|10\rangle$ states as the poles of the Bloch sphere. When the qubits are placed on-resonance so that $\Delta \equiv \omega_{01}^A - \omega_{01}^B = 0$ (see Figure 5.1b), then H_{int} can be visualized as causing the populations of the $|01\rangle$ and $|10\rangle$ states to swap with a frequency $g/2\pi$. When the qubits are biased far off-resonance so that $|\Delta| \gg g$, as shown in Figure 5.1c, the swapping is minimized, effectively “turning off” the interaction.

We would like to write the interaction Hamiltonian in matrix form so that we can use it as a quantum operation in the density matrix formalism that was discussed in Chapter 2. To do this, we can look at the $\{|01\rangle, |10\rangle\}$ Bloch sphere representation in Figure 5.1b and see that when the qubits are on-resonance ($\Delta = 0$), H_{int} can be represented as a rotation around the x-axis by an angle $\theta = gt_{swap}$, where t_{swap} is the time that the qubits remain on resonance. For a single qubit, a rotation about the x-axis

by an angle θ can be written as the quantum operation [58]

$$X_\theta = \begin{bmatrix} \cos(\theta/2) & -i \sin(\theta/2) \\ -i \sin(\theta/2) & \cos(\theta/2) \end{bmatrix} \quad (5.4)$$

Therefore, the operator representation of H_{int} is given by the unitary two-qubit matrix, U_{int} , that describes a $X_{\theta=gt_{swap}}$ rotation between the $|01\rangle$ and $|10\rangle$ states in the $\{|00\rangle, |01\rangle, |10\rangle, |11\rangle\}$ basis.

$$U_{int} = \begin{bmatrix} 1 & 0 & 0 & 0 \\ 0 & \cos(gt_{swap}/2) & -i \sin(gt_{swap}/2) & 0 \\ 0 & -i \sin(gt_{swap}/2) & \cos(gt_{swap}/2) & 0 \\ 0 & 0 & 0 & 1 \end{bmatrix} \quad (5.5)$$

We can now treat the coupling interaction as a quantum gate that can act on density matrices that represent two-qubit states. For an interaction time $gt_{swap} = \pi$, the state amplitudes are swapped so that $|01\rangle \rightarrow -i|10\rangle$ and $|10\rangle \rightarrow -i|01\rangle$. This operation can be used to create a universal quantum gate as will be discussed in the next chapter. However, before we move on to universal quantum gates, we must characterize the coupling scheme and discuss important limitations of fixed coupling, such as measurement crosstalk and limited scalability.

5.1.2 Measuring coupled qubits: single-shot measurement and measurement crosstalk

Since each qubit has its own measurement line, the state of both qubits can be measured simultaneously in a single measurement. This is commonly referred to as a **single shot measurement**. There is one major issue with measuring qubits coupled using a fixed coupling scheme: **measurement crosstalk** [54, 40]. Measurement crosstalk can be understood using the example shown in Figure 5.2. If we prepare the two-qubit system, $|AB\rangle$, in the $|10\rangle$ state and measure qubit A then qubit A's occupied $|1\rangle$ state will tunnel out into the deep right well. After it tunnels, the state will decay in the deep right well and as it does so it will radiate microwaves out into the coupled qubit circuit at a range of frequencies corresponding to the transitions between the various levels in the deep right well. These microwaves will excite qubit B into the $|1\rangle$ state and therefore a $|10\rangle$ state will end up being erroneously measured as a $|11\rangle$ state due to the measurement crosstalk. The measurement crosstalk can be minimized by calibrating the timing of each qubit's measurement pulse so that both pulses arrive at each qubit at the same time [54]. After the measurement is completed and the data is recorded, the set of two-qubit probabilities, $\{P_{01}, P_{10}, P_{11}, P_{00}\}$, can be mathematically corrected in order to calibrate out the measurement crosstalk. This is discussed in the next chapter and in Appendix D.

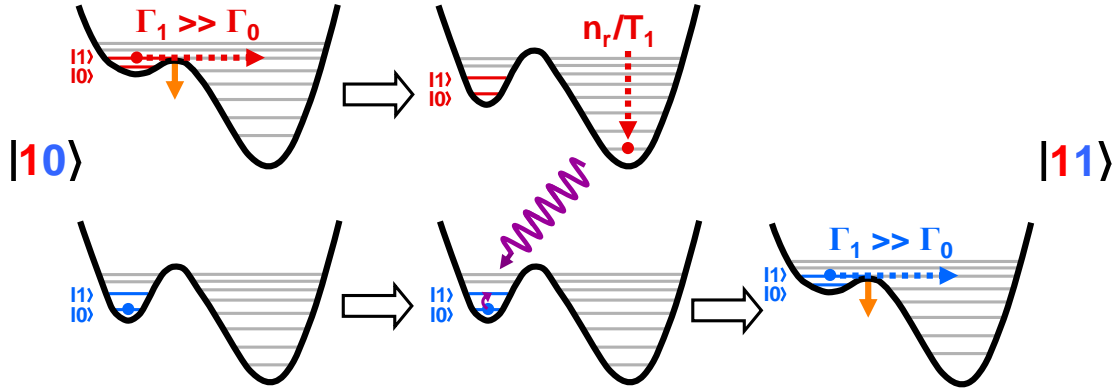


Figure 5.2: **Measurement crosstalk mechanism.** To demonstrate the mechanism of measurement crosstalk for capacitively coupled qubits, we show an example case of qubits prepared in the $|10\rangle$ state. When the first qubit is measured (top/red), it will tunnel out into the right well and decay at the rate n_r/T_1 discussed in the previous chapter. However, as it decays it will emit microwaves at broadband frequencies which will excite the second qubit (bottom/blue) into the $|1\rangle$ state causing the system to be erroneously measured as being in the $|11\rangle$ state. Measurement crosstalk can be minimized during measurement by ensuring that both measurement pulses reach both qubits simultaneously. Measurement crosstalk can also be mathematically calibrated out of the data post-measurement as discussed in the next chapter and in Appendix D.

5.1.3 Detuning and errors due to fixed coupling

As mentioned at the beginning of this chapter, although the coupling strength is fixed in this capacitive coupling architecture, the coupling interaction can be minimized by detuning the qubits as shown in Figure 5.1c. From (5.5), when the detuning, $\Delta \equiv \omega_{01}^A - \omega_{01}^B$, is set to a value, Δ_{off} , such that $\Delta_{off} \gg g$, the off-diagonal elements in U_{int} will be small and have average amplitude g/Δ_{off} , effectively turning off the coupling interaction. The error due to a finite Δ_{off} is given by [31]

$$\varepsilon_g = g^2 / (\Delta_{off}^2 + g^2) \quad (5.6)$$

Here, $\Delta_{off}/2\pi \simeq 200$ MHz was used to turn off a coupling interaction with $g/2\pi = 11$ MHz, yielding $\epsilon_g = g^2/(\Delta_{off}^2 + g^2) \simeq 0.055$. Hence the **on/off ratio** of a coupler becomes a very important figure of merit for coupling architectures [10, 11] because the coupling must be minimized to prevent errors during single-qubit operations and measurement. Ideally we would define the on/off ratio as g_{on}/g_{off} , but for a fixed coupling scheme g is fixed so we have to use a different definition and we have to measure the on/off ratio differently. After we show how to calibrate coupled qubits in the next section, we will present one way to measure the on/off ratio for this fixed coupling architecture.

This discussion also brings to attention a fundamental flaw of fixed coupling schemes. They are not scalable architectures because for many qubits one will run out of frequency bandwidth if every qubit needs to be detuned from all others. In addition, the qubits must also be detuned from transition frequencies between levels outside the qubit manifold (such as the two-photon $0 \rightarrow 2$ transition) and from resonance frequencies of microwave modes and two-level state defects. This issue has come to be known as the **frequency crowding problem** [10] and can be overcome by using tunable coupling, which will be discussed in Chapter 7.

5.2 Experimental bring-up and characterization of capacitively coupled phase qubits

In order to correctly operate both qubits simultaneously, calibrations must be performed that adjust the relative qubit frequencies, ensure that pulses reach qubits simultaneously, and calibrate other two-qubit parameters. The coupled-qubit calibration experiments build upon the single-qubit calibrations so all the single-qubit calibrations must be completed before starting two-qubit calibrations. The same formalism of pulse sequences will be used here, but for two-qubit pulse sequence diagrams the measurement/z-pulse line (V_Z) and the microwave line ($V_{\mu w}$) will be combined into one row even though the two signals are applied to separate physical wires, as discussed in Appendix B. The flux bias (V_{bias}) and readout SQUID signals (V_{SQ} and $V_{SQ}^{readout}$) will be left off pulse diagrams for visual clarity, although both are still being executed. The two-qubit calibrations differ from single-qubit ones because both qubits are measured simultaneously giving a set of two-qubit probabilities $\{P_{00}, P_{01}, P_{10}, P_{11}\}$.

5.2.1 Calibrating qubit operating biases for turning on and for minimizing the coupling interaction

First, we find the qubit operating biases needed to minimize the coupling interaction.

We do this by detuning the qubits off resonance by an amount Δ , where the magnitude

of Δ must be much larger than the coupling strength g in order to minimize the coupled-qubit interaction given by (5.5). As briefly mentioned at the beginning of this chapter, the capacitively coupled samples in this thesis have $g/2\pi \simeq 11$ MHz, therefore we typically calibrate the qubits to have an off-resonance detuning of at least $\Delta_{off}/2\pi \simeq 200$ MHz. We do this by setting the operating biases of the qubits so that they are at least 200 MHz off resonance, as measured by a two-qubit spectroscopy experiment whose pulse sequence is shown in Figure 5.3a. The operating bias is adjusted on one or both qubits until the spectroscopy data shows that the resonant responses of the two qubits are at least 200MHz apart. Any time the operating bias of a qubit is changed, the calibrations of the measurement pulse amplitude for that qubit must be repeated. Figure 5.3b shows this data, where the two-qubit probabilities $\{P_{10}, P_{01}, P_{11}\}$ of the qubits being in the $\{|10\rangle, |01\rangle, |11\rangle\}$ states, respectively, are plotted as a function of the microwave pulse frequency. The P_{00} probability can be calculated from the others using $P_{00} = 1 - P_{10} - P_{01} - P_{11}$.

Once we find the appropriate operating biases that give $\Delta_{off}/2\pi \simeq 200$ MHz, we proceed to the calibration for biasing the qubits on-resonance ($\Delta \simeq 0$) and thereby turning on the coupling interaction. The qubits are brought on resonance by pulsing qubit B with a z-pulse of an appropriate amplitude. The z-pulse can also be applied to qubit A, but with opposite polarity, to bring it on resonance with qubit B, but we'll discuss just the former case here. We need to calibrate the qubit B z-pulse amplitude that will bias

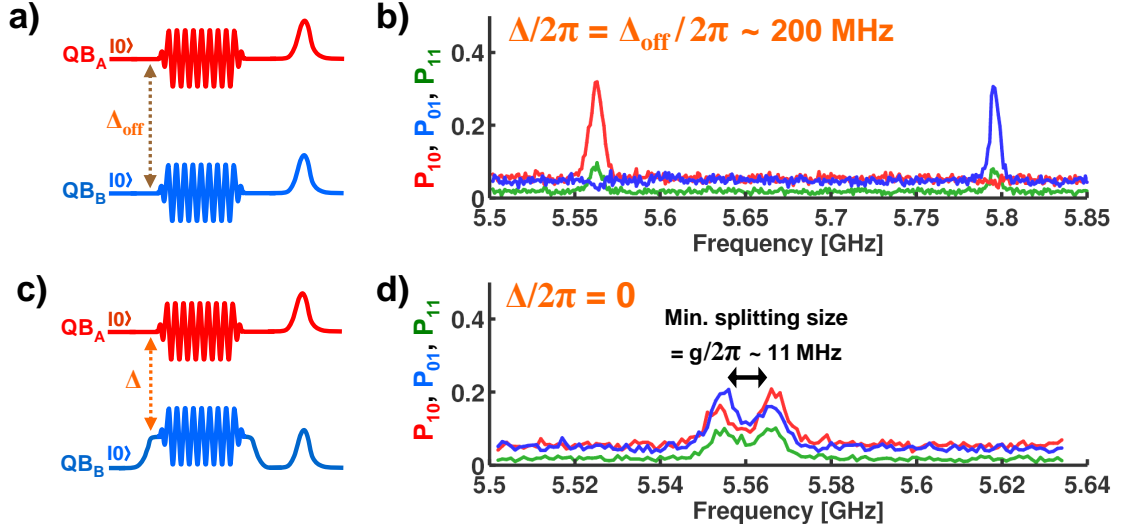


Figure 5.3: Calibrating on and off resonance biases using two-qubit spectroscopy. The coupling interaction, H_{int} , is turned off (on) by biasing the qubits off (on) resonance. On resonance, $\Delta \equiv \omega_{01}^A - \omega_{01}^B \simeq 0$, while off-resonance $\Delta = \Delta_{\text{off}}$. Here, the coupling strength is approximately $g/2\pi \simeq 11$ MHz. Therefore, we use $\Delta_{\text{off}}/2\pi \simeq 200$ MHz to minimize the coupling interaction during single-qubit operations and measurement, which minimizes the error given in (5.6) by setting $\Delta_{\text{off}} \gg g$. **(a)** Pulse sequence for the two-qubit spectroscopy experiment used to calibrate the qubit operating biases to obtain $\Delta_{\text{off}}/2\pi \simeq 200$ MHz. This experiment is just single qubit spectroscopy, but performed on both qubits simultaneously. The qubits are initialized into their ground states, are simultaneously pulsed with $\sim 2\mu\text{s}$ long microwave pulses of fixed frequency, and finally the two-qubit probabilities $\{P_{10}, P_{01}, P_{11}\}$ are measured. This sequence is repeated for a pulse frequency range large enough to capture the resonance peaks of both qubits. As shown by the brown dotted arrow, the qubit operating biases are adjusted until the spectroscopy data in that frequency range shows that the resonance frequencies of the qubits, $\omega_{01}^{A,B}$, are no less than 200 MHz apart. **(b)** Two-qubit spectroscopy data that shows the two-qubit probabilities $\{P_{10}, P_{01}, P_{11}\}$ as a function of the microwave pulse frequency for qubit operating biases where $\Delta_{\text{off}}/2\pi \simeq 200$ MHz. The peak in P_{10} (P_{01}) corresponds to an excitation of qubit A's (qubit B's) $0 \rightarrow 1$ transition **(c)** To calibrate the parameters needed to bring the qubits on resonance, the qubits are first biased to the $\Delta \simeq \Delta_{\text{off}}$ value found above. Then, to turn the coupling interaction on, a z-pulse is applied to qubit B and its amplitude is adjusted until the detuning, $\Delta \simeq 0$. **(d)** When the qubits are biased on resonance, the coupling interaction will make their overlapping $0 \rightarrow 1$ resonance peaks split, with the minimum splitting size equal to the coupling strength $g/2\pi \simeq 11$ MHz. The z-pulse that gives the minimum splitting defines the on-resonance point. Here we show the spectroscopy data for the z-pulse amplitude where $\Delta \simeq 0$ showing an ~ 11 MHz wide splitting.

qubit B on resonance with qubit A. To do this, two-qubit spectroscopy is performed for various values of the z-pulse amplitude on qubit B, as shown in the pulse sequence in Figure 5.3c. When the resonance peaks overlap and split due to the coupling interaction as shown in Figure 5.3d, we know that we are close to the on-resonance point. The z-pulse amplitude that corresponds to the minimum splitting size is the on-resonance point. Figure 5.3d shows the data where the z-pulse amplitude on qubit B gives the minimum splitting size. The minimum splitting size is approximately equal to the coupling strength, $g/2\pi \simeq 11$ MHz, as expected. If there is no splitting in the two-qubit spectroscopy data, then this indicates some error is present that is preventing the qubits from coupling. After this calibration, we can now minimize the coupling interaction by biasing the qubits off-resonance, thereby also minimizing the error (5.6) during single qubit operations and measurement and we can also put the qubits on-resonance in order to turn on the coupling interaction.

5.2.2 The swap experiment

Now we can use the results of the calibrations of the previous section to experimentally show how the two-qubit probabilities $\{P_{00}, P_{10}, P_{01}, P_{11}\}$ evolve in time under the capacitive coupling interaction given by (5.5). To accomplish this we use the pulse sequence shown in Figure 5.4a. We call this pulse sequence the **swap experiment**. We first bias the qubits, in their ground states, to the off-resonance value of $\Delta_{off}/2\pi \simeq 200$

MHz, as calibrated in the last section. This allows us to then apply a π pulse to qubit A with minimal error, as given by (5.6). Then we apply the z-pulse to qubit B, biasing the qubits an amount Δ within resonance, and letting them evolve under the coupling interaction (5.5) for a time t_{swap} . Then we measure both qubits and obtain the set of two-qubit probabilities $\{P_{10}, P_{01}, P_{11}\}$. We repeat the sequence for a range of z-pulse amplitudes and times t_{swap} . As mentioned previously, we obtain P_{00} from the remaining probabilities using $P_{00} = 1 - P_{10} - P_{01} - P_{11}$. The π pulse can be applied to qubit B instead, but again only one case will be discussed for simplicity.

The data obtained from a correctly calibrated swap experiment is shown in Figure 5.4b for the case of $\Delta \simeq 0$, *i.e.* with the qubits on-resonance. The two-qubit probabilities are plotted as a function of the interaction time t_{swap} during which the qubits were held on-resonance, allowing the interaction (5.5) to act on the two-qubit state. As expected, the populations of the $|10\rangle$ and $|01\rangle$ states swap at a frequency $g/2\pi \simeq 11$ MHz. The P_{11} signal (dark green) should be zero and a non-zero P_{11} value indicates the presence of errors due to measurement crosstalk which were discussed earlier. The maximum amplitude of P_{11} in the swap experiment gives us a quantitative measure of the amount of measurement crosstalk.

If Δ is varied by scanning the z-pulse amplitude on qubit B, we obtain the data shown in Figure 5.4c, where the color scale gives the values of the probabilities P_{01} and P_{10} . Varying Δ helps us precisely locate the z-pulse amplitude value needed to bias

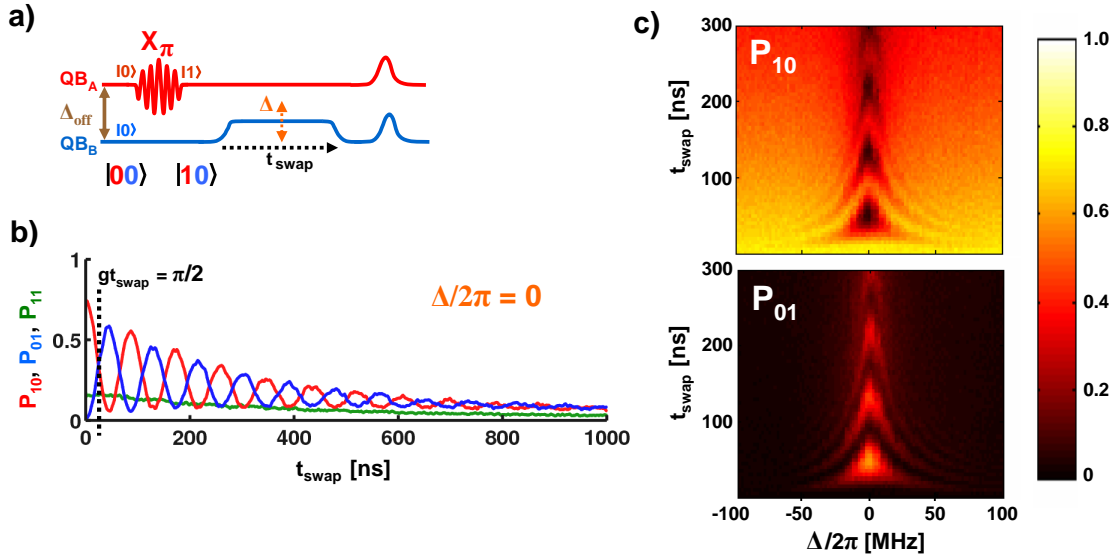


Figure 5.4: **The swap experiment.** **a)** Pulse sequence for the swap experiment. A π pulse is applied to qubit A, putting the system into the $|10\rangle$ state. A z-pulse is applied that biases qubit B an amount Δ within resonance of qubit A. The system is then left to evolve for a time t_{swap} after which the two-qubit probabilities $\{P_{01}, P_{10}, P_{11}\}$ are measured. **b)** The swap data for the on resonance case where $\Delta = 0$. The swapping frequency gives us a measure of the coupling strength, here $\simeq 11\text{MHz}$. The time marked by the dashed line corresponds to $gt_{\text{swap}} = \pi/2$, and is important because at this point in time a square root of i-swap operation is created. This operation can be used to make a universal quantum gate, as will be described in the next chapter. **c)** Swap data where both t_{swap} and Δ are varied. With the expected chevron pattern as the oscillation amplitude decreases off resonance.

qubit B exactly on-resonance with qubit A, and this point is labeled as $\Delta/2\pi = 0$ in Figure 5.4c.

At times, we will obtain swap data that looks like the data shown in Figure 5.5b. A correctly calibrated swap experiment should have the P_{11} signal decaying almost smoothly with minimal oscillation. Here however, the crosstalk, P_{11} , is quite high and exhibits oscillations that seem to be in-phase with either the P_{10} or P_{01} probabilities. These oscillations are due to the qubits not being measured simultaneously, as shown

in the pulse sequence in Figure 5.5a. Non-simultaneous measurement also leads to higher measurement crosstalk, as discussed in Section 5.1.2 and in [54]. Differences in measurement pulse propagation times down the two separate qubit measurement lines ($V_Z^{A,B}$) can be due to differences in cable lengths or errors in the settings in the qubit control software. This can be fixed by delaying the measurement pulse on the qubit that is being measured first so that the two qubits will end up being measured simultaneously [54].

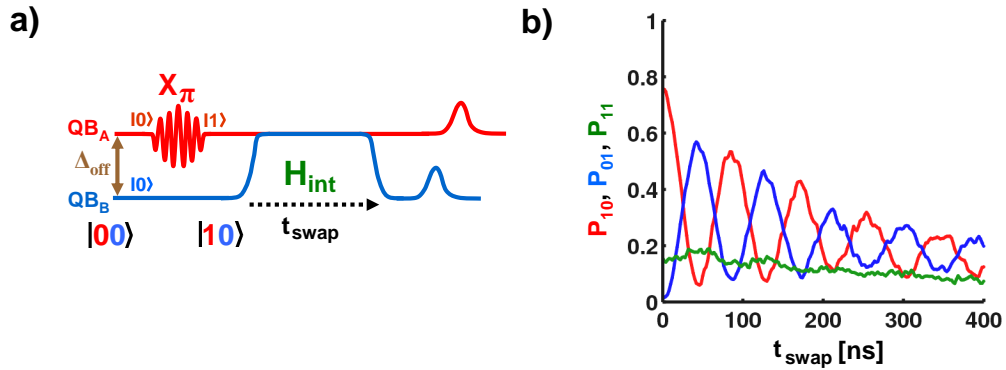


Figure 5.5: Synchronizing measurement pulses for two-qubit experiments. A common calibration error in the swap experiment is when the measurement pulses do not reach both qubits simultaneously. Ideally, we would like both qubits to be measured simultaneously, but due to differences in wiring length or software errors measurement pulses do not reach the qubits simultaneously. **a)** A pulse sequence for the swap experiment where qubit B is measured first. **b)** As discussed in the text, non-simultaneous measurement leads to higher measurement crosstalk error as manifested by an oscillating P_{11} signal in the swap data. The swap data shown here demonstrates this and corresponds to the pulse sequence in a) where qubit B was measured first. If the measurement is not simultaneous, the P_{11} trace will oscillate in phase with either P_{01} or P_{10} . The trace it is in phase with determines the qubit that is measured first. In the data above, P_{11} oscillates in phase with P_{01} , hence qubit B is measured first. To synchronize the measurement pulses a time delay can be added to the V_Z line of the qubit that is being measured first either by adding a delay in the qubit control software or by physically making the wire longer.

Figure 5.5b shows the data corresponding to the pulse sequence in Figure 5.5a. The P_{11} oscillations are in phase with the P_{01} oscillations. From the discussion on the mechanism of measurement crosstalk earlier in this chapter, this indicates that qubit B is being measured before qubit A. Figure 5.4b shows data after a delay was added to qubit B so that there is only minimal oscillation in the P_{11} amplitude. Now that the measurement pulses have been calibrated to reach both qubits simultaneously, the same time axis can be used when talking about measurement/z-pulse sequences on the two individual qubits. This is important because any unwanted time offsets between the V_Z lines can lead to phase accumulation between the qubits which will cause errors when trying to execute two-qubit pulses or specific quantum gates.

Once nice swap data like that shown in Figure 5.4 is obtained and the expected coupling strength is confirmed by measurements of the swap frequency at $\Delta = 0$, the relative phases of the microwave pulses on qubits A and B can be calibrated. However, before moving on to the phase calibration, we can use the swap experiment to measure the on/off ratio of this fixed capacitive coupling architecture.

5.2.3 Measuring on/off ratio of capacitively coupled qubits

We measure the on/off ratio using the swap experiment depicted in Figure 5.4. As Figure 5.4c shows, the amplitude of the swapping oscillations decreases with detuning as expected [10]. In Figure 5.6, we plot the change in the peak-to-peak swap amplitude

as a function of detuning Δ and compare it to the theoretical prediction given by (5.6). Apart from a small reduction in the amplitude arising from visibility, the data is in good agreement with theory. At detunings $|\Delta|/2\pi > 50$ MHz, the swap amplitude is small and cannot be distinguished from the noise floor. From the maximum detuning bias of $\Delta/2\pi = 200$ MHz and from the coupling strength $g/2\pi = 11$ MHz obtained from spectroscopy measurements and the data in Figure 5.4b, we compute the swap amplitude ratio $.6/(1.8 \times 10^{-3}) \simeq 300$ as the measure of the on/off ratio. The swap amplitude data in Figure 5.6 agrees with the theory in (5.6) so we can now safely assume that the on/off ratio can simply be taken to be $(\Delta/g)^2 = (200/11)^2 \simeq 300$.

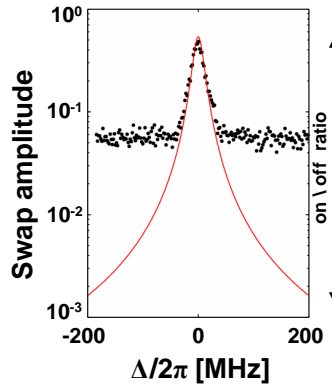


Figure 5.6: **Measuring on/off ratio using the swap experiment** Peak-to-peak swapping amplitude versus detuning Δ , plotted with the predicted dependence $g^2/(g^2 + \Delta^2)$ in red. The vertical scale of the latter is adjusted to match the on-resonance amplitude at $\Delta = 0$. Determination of the swapping probability is limited to $> 6 \times 10^{-2}$ by measurement noise. The calculated on/off ratio is indicated by the vertical arrow and is $\simeq 300$.

5.2.4 Phase calibration for two-qubit microwave pulses

So far, only one qubit has been pulsed at a time, so keeping track of the relative phases of pulses on different qubits has not been important. The phase, ϕ , of a single-qubit pulse was important, but only relative to one qubit's Bloch sphere axes. Also, phases are only important for $\pi/2$ pulses, as pulsing from $\theta = 0$ to π ideally rotates the Bloch vector to the same point irregardless of the phase, ϕ , of the π pulse. For generating simultaneous microwave pulses on two coupled qubits, the situation is more complicated. This is because the Bloch spheres of the individual qubits can have a relative phase offset as shown by ϕ_{offset} in Figure 5.7. Therefore, in order to properly pulse one qubit with say, an $X_{\pi/2}$ pulse, and the other with say, a $Y_{\pi/2}$ pulse, it is necessary to define a zero phase as a reference and to measure the phase offset, ϕ_{offset} , between the Bloch spheres of the individual qubits as shown in Figure 5.7. The X axis of qubit A will be defined to be the 0° phase reference and we'll label it $\phi_A = 0$. All phases discussed will be relative to this definition of zero phase.

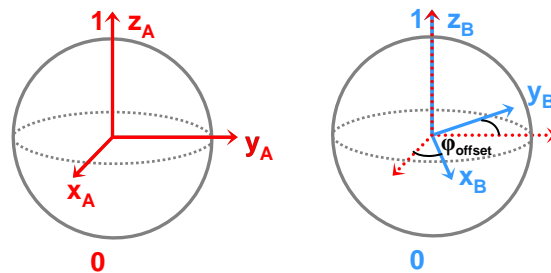


Figure 5.7: **Bloch sphere depiction of two-qubit phase offset.** The x and y axes of the Bloch spheres of qubits A (red) and B (blue) have a random offset, ϕ_{offset} , that needs to be taken into account in order to properly perform simultaneous rotations on both qubits.

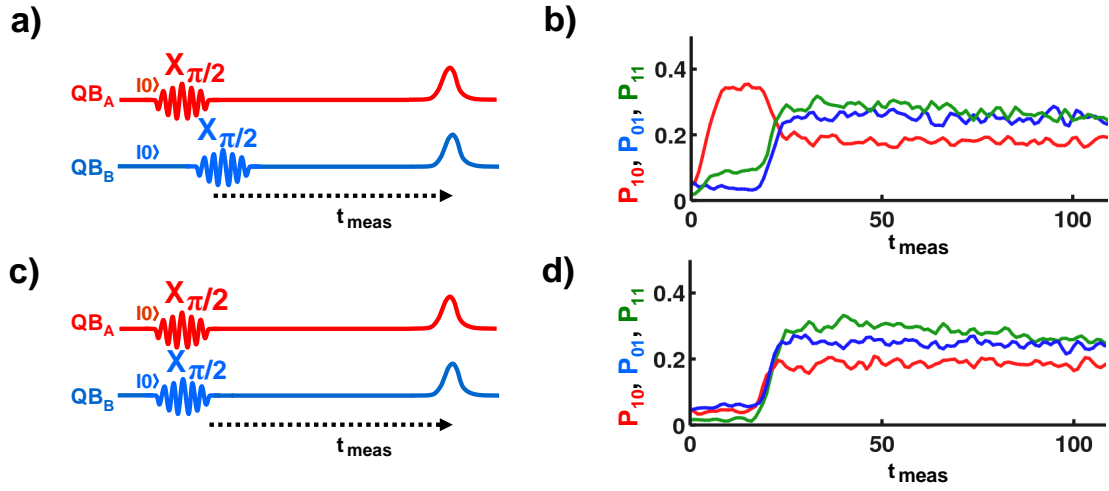


Figure 5.8: **Synchronizing microwave pulses for two-qubit experiments.** The path lengths taken by the microwave pulses on separate qubits might differ, therefore the microwave pulses on separate qubits must be synchronized in time so that they reach both qubits simultaneously. **a)** First, the time offset between the two microwave lines must be measured and compensated for. This is done by pulsing both qubits, initially in the $|00\rangle$ state and biased at least 200 MHz off-resonance, with identical pulses (here $X_{\pi/2}$). Then, after a wait time t_{meas} , the two-qubit probabilities $\{P_{01}, P_{10}, P_{11}\}$ are measured. The pulse sequence is repeated for increasing values of t_{meas} . **b)** The data for the pulse sequence in a) where P_{10} rises approximately 18 ns earlier than P_{01} indicating that a time delay of 18 ns needs to be added before qubit A's microwave pulses in order to make microwave pulses reach both qubits simultaneously. **c) and d)** Pulse sequence and data with the 18 ns delay on qubit A added. Now, both P_{01} and P_{10} rise simultaneously indicating that the microwave lines on the two qubits are synchronized in time.

However, as with the measurement/z-pulse lines, to guarantee proper calibration of relative phases, a calibration must first be made to ensure that identical microwave pulses generated at the same time on separate qubits will reach both qubits simultaneously. Differences in microwave pulse propagation times between the two qubits can arise from differences in cable lengths or errors in the settings in the qubit control software. These differences will cause phase offsets and must be eliminated. To check for simultaneity of microwave pulses, both qubits are pulsed concurrently with π or $\pi/2$

pulses, and the time between the microwave and measurement pulses, t_{meas} , is scanned while the set of two qubit probabilities is measured, as shown in Figure 5.8. The pulses will be simultaneous if it is observed that both the P_{10} and P_{01} probabilities rise simultaneously. If they do not, a delay can be added in software to the qubit whose probability of being in the $|1\rangle$ state rises first. An example of the pulse sequence and data where $\pi/2$ pulses were generated simultaneously, but reach qubit A first, is shown in Figures 5.8a and b. The pulse sequence and data where a delay has been added to qubit A to make the pulses reach A and B simultaneously is shown in Figures 5.8c and d. Now that the microwave pulses have been calibrated to reach both qubits simultaneously, we can proceed to calibrate the microwave pulse phase offset, ϕ_{offset} .

The phase calibration consists of two experiments. The pulse sequence for the first experiment is shown in Figure 5.9a. The qubits are initialized into the $|00\rangle$ state, biased off-resonance ($\Delta_{off}/2\pi \simeq 200$ MHz) and qubit A is pulsed with an $X_{\pi/2}$ pulse (so that $\phi_A = 0$) while qubit B is pulsed with a $Y_{\pi/2}$ pulse (so that $\phi_B = \pi/2$). The qubits are then biased on-resonance for an interaction time, t_{swap} , and the two-qubit probabilities are measured. The time t_{swap} is varied giving the data shown in Figure 5.9b where a time t''_{swap} is selected at which the P_{10} and P_{01} probabilities are most out of phase, as marked by the dashed line.

In the second part of the phase calibration experiment, t_{swap} is fixed so that $t_{swap} = t''_{swap}$. Qubit A is pulsed with an $X_{\pi/2}$ pulse (so that $\phi_A = 0$) and qubit B is simultane-

ously pulsed with an $\pi/2$ pulse, but now the phase of that pulse, ϕ_B , is scanned. The pulse sequence and data for this experiment are shown in Figure 5.9c and Figure 5.9d, respectively. The value of ϕ_{offset} can be read off this data and occurs at the value of ϕ_B where P_{01} is increasing and first crosses P_{10} , as labeled in Figure 5.9d by the dashed line. This is because at this value of ϕ_B , the two signals are in-phase.

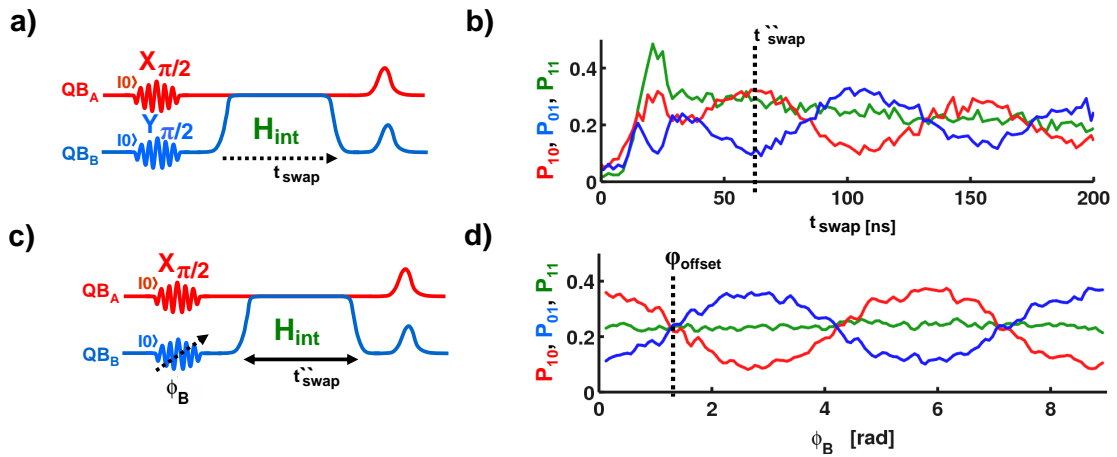


Figure 5.9: Calibration of relative phases for microwave pulses. This calibration consists of two experiments. **a)** The pulse sequence for the first experiment. The qubits are initialized into the $|00\rangle$ state, biased off-resonance ($\Delta_{off}/2\pi \simeq 200$ MHz), and then qubit A is pulsed with an $X_{\pi/2}$ pulse (so that $\phi_A = 0$) while qubit B is pulsed with a $Y_{\pi/2}$ pulse (so that $\phi_B = \pi/2$). After a time t_{meas} the two-qubit probabilities $\{P_{01}, P_{10}, P_{11}\}$ are measured and the whole pulse sequence is repeated for increasing values of t_{meas} . **b)** The data of the two-qubit probabilities measured as a function of t_{meas} for the sequence in a). The t_{swap} value at which P_{10} and P_{01} are most out of phase is recorded as t_{swap}'' . It is indicated using the dashed line and will be used for the second part of the phase calibration. **c) and d)** The second part of the phase calibration experiment. Again, both qubits are pulsed with $\pi/2$ pulses, but now the phase of qubit B, ϕ_B , is scanned while the phase of qubit A is fixed at $\phi_A = 0$. The interaction time is also fixed at t_{swap}'' . The data now shows out of phase oscillations between P_{10} and P_{01} as a function of the phase on qubit B, ϕ_B . The phase corresponding to the offset discussed in Figure 5.7, ϕ_{offset} , is indicated using the dashed line and occurs at the point where the P_{01} signal is increasing and first crosses the P_{10} signal.

This completes the calibration of single and coupled qubits. Now we can gener-

ate the appropriate π and $\pi/2$ pulses needed to prepare the single qubit basis states $\{|0\rangle, |1\rangle, (|0\rangle + |1\rangle)/\sqrt{2}, (|0\rangle + i|1\rangle)/\sqrt{2}\}$ that were previously shown in Figure 2.1. From these basis states, any arbitrary single-qubit state can be built up. However, to check both the single and two-qubit calibrations, we must be able to prepare the full basis set of two-qubit states correctly. The full two-qubit basis set is given by the Kronecker product of the single-qubit basis states: $\{|0\rangle, |1\rangle, (|0\rangle + |1\rangle)/\sqrt{2}, (|0\rangle + i|1\rangle)/\sqrt{2}\} \otimes \{|0\rangle, |1\rangle, (|0\rangle + |1\rangle)/\sqrt{2}, (|0\rangle + i|1\rangle)/\sqrt{2}\}$. As a check of the accuracy of the calibrations, we can use appropriate combinations of calibrated π and $\pi/2$ pulses to prepare the 16 two-qubit basis states and compare our prepared states to what would be theoretically expected.

5.2.5 State tomography of the 16 two-qubit basis states

Before proceeding, we define a shorthand notation for single qubit basis states that will make writing out complex two-qubit states clearer and more compact. As shown in the first column of the table in Figure 5.10a, we define the single-letter labels $\{H, V, D, R\}$ to represent the single-qubit states which are listed in the second column and displayed on the Bloch sphere in Figure 5.10b. In the third column, the table also lists the single-qubit pulses needed to prepare each state from a qubit initialized to the $|0\rangle$ state. This shorthand notation is based on the similar convention commonly used in optics [35].

It is important to verify that we are able to prepare the full set of 16 two-qubit basis

Label	State	Pulse
H	$ 0\rangle$	I
V	$ 1\rangle$	X_π
D	$(0\rangle + 1\rangle)/\sqrt{2}$	$Y_{\pi/2}$
R	$(0\rangle + i 1\rangle)/\sqrt{2}$	$X_{-\pi/2}$

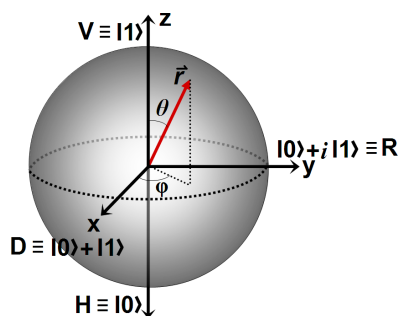


Figure 5.10: Shorthand labels for single qubit states and the single qubit operations needed to prepare these states. Using this shorthand, complex two-qubit states like $(|0\rangle + i|1\rangle)/\sqrt{2} \otimes (|0\rangle + |1\rangle)/\sqrt{2}$ can be written compactly as RD .

states accurately because they are needed to fully characterize the universal quantum gate that we demonstrate in the experiments in the next chapter. To verify the accuracy of the preparation of these states we use **state tomography** to measure the density matrix of each prepared state and compare the results against theoretically expected density matrices.

State tomography is a technique for measuring the density matrix of a quantum state. Just as one could map out the physical “state” of a classical object by scanning across x,y, and z axes in space, we can map out quantum states by projecting each qubit’s state onto the x, y, and z axes of its Bloch sphere. From such projective measurements, we can mathematically reconstruct the two-qubit density matrix for that state. There are many good references on state tomography [77, 45, 35, 22, 61, 58] so the theory of tomography will not be explained further here. The important point is that using state tomography we can reconstruct the density matrix of any experimentally prepared single or multi-qubit state. The MATLAB and Mathematica source code used to obtain

the density matrix from the state tomography data can be found in Appendix D, along with comments that explain each step.

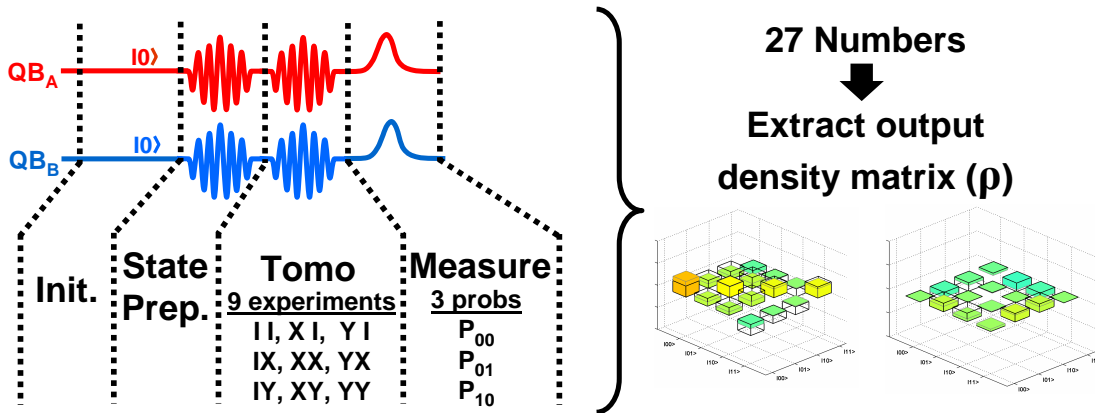


Figure 5.11: **Pulse sequence for state tomography.** The qubits are initialized into their ground states and appropriate pulses are applied to generate one of the 16 two-qubit basis states from the set $\{|0\rangle, |1\rangle, (|0\rangle + |1\rangle)/\sqrt{2}, (|0\rangle + i|1\rangle)/\sqrt{2}\} \otimes \{|0\rangle, |1\rangle, (|0\rangle + |1\rangle)/\sqrt{2}, (|0\rangle + i|1\rangle)/\sqrt{2}\}$. Immediately after the state preparation pulses, tomography pulses are applied to project the state onto the x, y and z axes of each qubit’s Bloch sphere. A projection of the state along the x-axis of the Bloch sphere is given by a $Y_{\pi/2}$ tomography pulse. A projection of the state along the y-axis of the Bloch sphere is given by a $X_{-\pi/2}$ tomography pulse. A projection of the state along the z-axis of the Bloch sphere does not require a pulse and is equivalent to the identity operation because the qubit measurement already provides a projection along the z-axis of the qubit Bloch sphere. We define the shorthand labels, $X \equiv Y_{\pi/2}$ and $Y \equiv X_{-\pi/2}$, for these pulses so the set of 3 tomography pulses is written as $\{I, X, Y\}$. The set of two-qubit probabilities is then measured. For each state, this is repeated 9 times for the 9 different possible two-qubit axes projections. From this data, a density matrix that fully describes the state can be reconstructed for each of the 16 states, as described in Appendix D and in references [77, 45, 35, 22, 61, 58].

The pulse sequence for the state tomography of a two-qubit state is diagrammed in Figure 5.11. The qubits are kept off-resonance throughout the sequence because here we are performing state tomography only on the basis states and not on more complex states that require the coupling interaction for their preparation. First, the qubits are

initialized into the $|00\rangle$ state and a basis state is prepared by pulsing both qubits with the appropriate pair of microwave pulses needed to prepare that state, as given in the table in Figure 5.10a. The state tomography pulses follow immediately after the state preparation pulses. A set of 3 different tomography pulses is applied to each qubit. Each set of 3 pulses corresponds to a projection of the state along the 3 axes of the Bloch sphere. A projection of the state along the x-axis of the Bloch sphere is given by a $Y_{\pi/2}$ tomography pulse. A projection of the state along the y-axis of the Bloch sphere is given by a $X_{-\pi/2}$ tomography pulse. A projection of the state along the z-axis of the Bloch sphere does not require a pulse and is equivalent to the identity operation because the qubit measurement already provides a projection along the z-axis of the qubit Bloch sphere. We define the shorthand labels, $X \equiv Y_{\pi/2}$ and $Y \equiv X_{-\pi/2}$, for these pulses so that set of 3 tomography pulses is written as $\{I, X, Y\}$. Since there are 3 axes per qubit, for two qubits the set of 9 possible tomography pulses is given by $\{I, X, Y\} \otimes \{I, X, Y\}$. Immediately after the tomography pulses, the two-qubit probabilities, $\{P_{00}, P_{10}, P_{01}, P_{11}\}$, are measured. Only 3 of the 4 probabilities are independent because $P_{00} + P_{10} + P_{01} + P_{11} = 1$ must hold. As a result, state tomography measures 3 independent numbers in 9 experiments, for a total of 27 numbers per tomography experiment of which 15 are independent. These 27 numbers are used to mathematically reconstruct the density matrix of the experimentally prepared state as described in Appendix D and in references [77, 45, 35, 22, 61, 58]. This procedure is repeated for

each of the 16 two-qubit basis states. How well the states have been prepared can be quantified by calculating the **state fidelity** [74] which is given by

$$F_{state} = Tr\sqrt{\rho^{1/2}\rho_{exp}\rho^{1/2}} \quad (5.7)$$

where ρ_{exp} and ρ are, respectively, the experimentally obtained and theoretically expected density matrices. Using this formula directly on the density matrices obtained from the tomography experiment yields lower fidelities. This is because errors from measurement crosstalk and single qubit pulse fidelities drastically affect the data. However, the effects of these two error sources are predictable, and were measured in the single and two-qubit calibrations described earlier. Therefore, these errors can be calibrated out from this data, as described in Appendix D. The density matrices for the full set of 16 two-qubit basis states with the measurement crosstalk and visibility errors calibrated out are shown in Figure 5.12, and those without the calibrations are listed in Appendix D. The state fidelities of the calibrated input states were calculated to be, on average, $\sim 98\%$. Without calibration they were $\sim 75\%$. The 2% loss is understood and is due to the T_1 decay that takes place during the time of a microwave pulse [47]. The 98% state fidelity shows that the qubits and the π and $\pi/2$ microwave pulses on each qubit are properly calibrated. Now that we have confirmed that everything is well calibrated, we can proceed to a more complex experiment where we demonstrate and

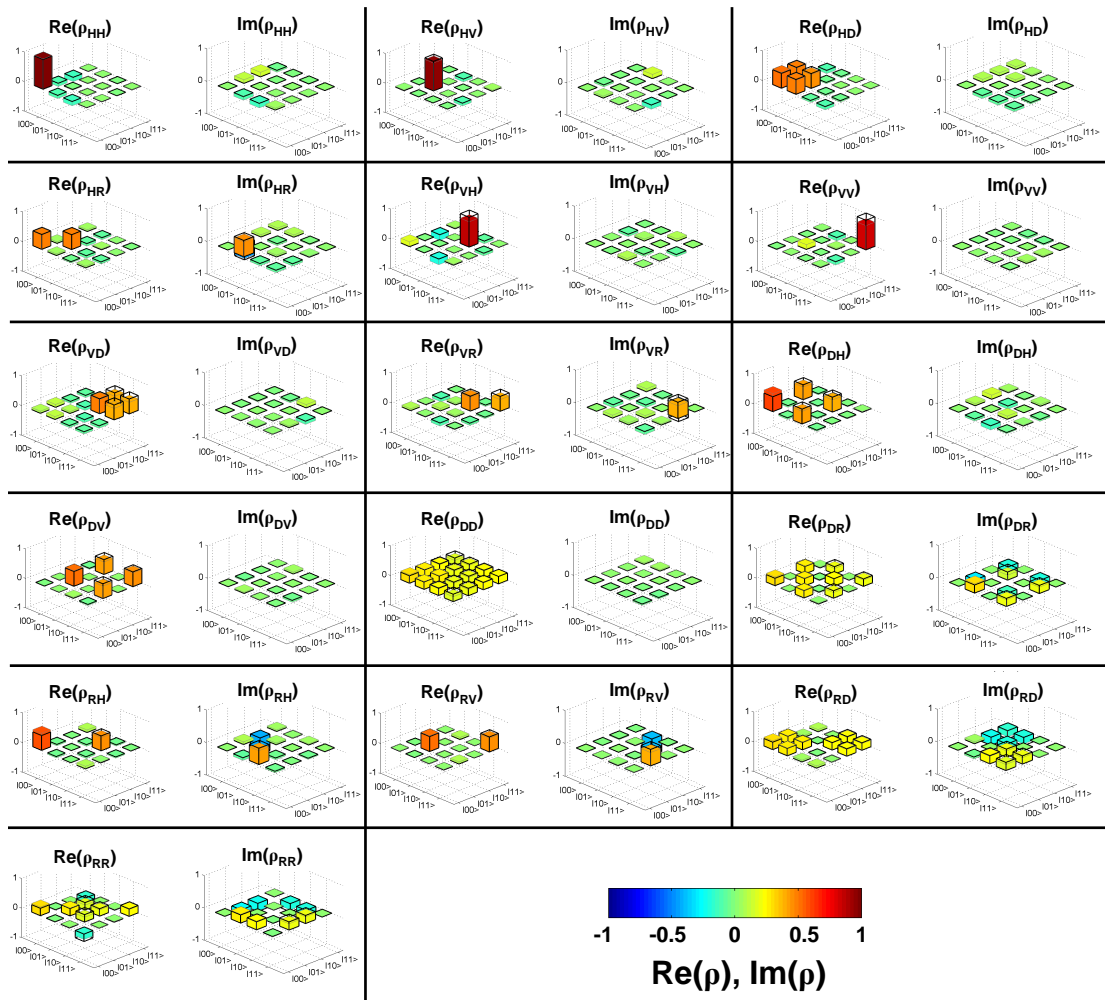


Figure 5.12: The full set of density matrices for the 16 two-qubit basis states as obtained via state tomography. Measurement crosstalk and visibility errors have been calibrated out from this data set, as described in the text. The real and imaginary parts of each density matrix are shown separately. The solid color bars are the experimental data and the transparent bars are the theory. The states are labeled according to the $\{H, V, D, R\}$ shorthand notation explained in the text and summarized in the table in Figure 5.10a.

benchmark a universal quantum gate.

Chapter 6

Demonstration and Characterization of A Universal Quantum Gate

6.1 What is a universal quantum gate?

A universal gate, in both classical and quantum computing, is the most basic computational element that can be used to construct any arbitrary logic operation. In classical computing there are a few different ways to construct a universal gate and one example, the NAND gate [80], is shown in Figure 6.1a. A table that gives the output of the NAND gate for all possible inputs is shown in Figure 6.1b. In Figure 6.1c, we show a flip-flop circuit, which acts as a simple memory element and is just one example of the arbitrary computational operations that can be performed using only NAND gates.

The output, Q , can be maintained at the same value or modified based on the inputs R and S , as given by the table in Figure 6.1c. In quantum computing, **universal quantum gates** [58, 38] consist of a multi-qubit device that can perform **entangling operations** along with **single qubit operations**. Using a universal quantum gate any arbitrary quantum computation can be performed [17]. In the previous section we showed that we could perform the full basis set of single-qubit operations with high fidelity by using single-qubit operations to prepare the 16 two-qubit basis states with 98% state fidelity. Now, we must show that alongside the single qubit operations, we can also create an entangling gate using the same system.

There are a few different ways to create an entangling gate. The entangling gate that has received the most attention thus far in the field of quantum computation has been the CNOT gate [58, 38, 63, 87]. Its quantum logic circuit is shown in Figure 6.2, where the two qubits are represented by the horizontal lines, with the gate input on the left and the output on the right. The actual symbol for the CNOT is the vertical line with the encircled cross.

It turns out that in our qubit architecture another entangling gate is simpler to construct than a CNOT because it arises directly from the time evolution of the Hamiltonian for two coupled flux-biased phase qubits [67]. This gate is called the “square root of i -swap gate” or **SQiSW** [78]. In our system, the CNOT is more complex because it needs to be constructed from two SQiSW gates and single qubit operations. Hence,

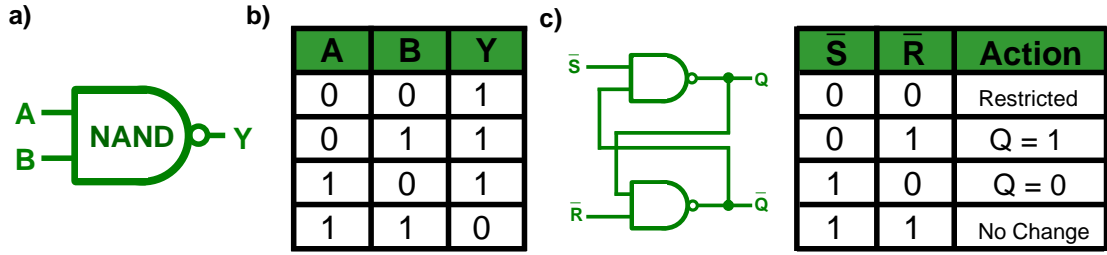


Figure 6.1: **Example of a universal gate in classical computing.** One example of a classical logic gate that can be used to perform any arbitrary classical computation is the NAND gate. **a)** Circuit symbol for a NAND universal classical gate **b)** Truth table for NAND gate showing inputs (A,B) and output (Y). **c)** The flip-flop memory element is an example of a simple logic element that can be built using NAND gates. The output of Q is controlled by the signals on R and S, as given in the table to the right of the flip-flop circuit.

the SQiSW gate also has a shorter pulse sequence and a short gate pulse sequence is important because we want to perform as many gate operations as possible before coherence is lost, as given by the T_1 and T_2 times that were measured in Chapter 4. The double-cross quantum circuit symbol that represents a SQiSW gate is shown in Figure 6.2, along with a quantum circuit that shows how to build a CNOT from SQiSW gates.

To make the SQiSW gate, we let two coupled qubits evolve under the interaction Hamiltonian in (5.1) for half the time required for a swap operation, *i.e.* $t_{swap} = \pi/(2g)$, so that the matrix for the coupling interaction, (5.5), reduces to

$$SQiSW \equiv U_{int}(t_{swap} = \pi/(2g)) = \begin{bmatrix} 1 & 0 & 0 & 0 \\ 0 & 1/\sqrt{2} & -i/\sqrt{2} & 0 \\ 0 & -i/\sqrt{2} & 1/\sqrt{2} & 0 \\ 0 & 0 & 0 & 1 \end{bmatrix} \quad (6.1)$$

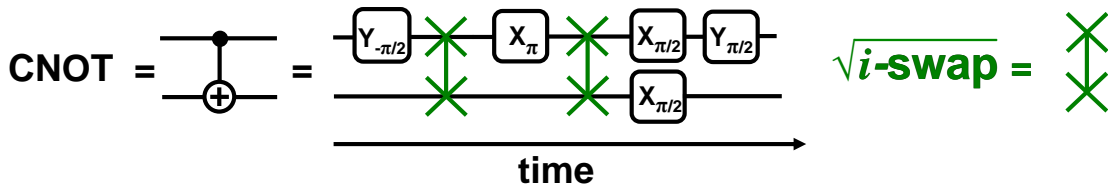


Figure 6.2: **Universal quantum gates.** In quantum computing literature, the universal quantum gate that is most often discussed is the CNOT gate. It is represented by the dot and encircled cross connecting the two horizontal lines that represent the two qubits. If the control qubit (marked by the dot) is in the excited state, then the the state of the qubit marked with the encircled cross is inverted. If the control qubit is in the ground state the state of the other qubit is left unchanged. In our system, the CNOT is not the most fundamental gate. It can be built from single qubit rotations and a universal gate called a square root of i -swap gate (SQiSW), as shown in the quantum circuit in the middle panel. The quantum circuit symbol for the SQiSW is the double cross, as shown on the far right.

This is the matrix for the SQiSW gate. To understand the SQiSW gate in a visual way, we can look back at the swap data in Figure 5.4b. The time at which the SQiSW gate occurs in the swap experiment is indicated by the vertical dotted line on the swap experiment data shown in Figure 5.4b. This time is half the time required for the qubits to fully swap, hence the “square-root” in square-root of i -swap.

In order to demonstrate that we have correctly constructed a SQiSW gate, we must map the output of the SQiSW gate for all possible input states. This is analogous to what was done to obtain a classical truth table like the one shown in Figure 6.1b. However, in classical computing, this is an easy task because the computational space is binary and hence small. For example, for the NAND gate there were four possible inputs $\{00, 01, 10, 11\}$. In quantum computing, the qubit Hilbert space is infinite because the phase and amplitude of a state can take on an infinite number of values. Therefore this

task is much more complex than just obtaining a truth table. Initially, it might seem impossible to map out the output states for a computational space of input states that is infinite, but it is possible to predict the output of a quantum gate for any arbitrary input by using a technique called **quantum process tomography (QPT)** as we discuss in the next section.

6.2 Experimental characterization of a universal quantum gate using quantum process tomography (QPT)

6.2.1 Motivation

Quantum process tomography [19] has its origins in system identification techniques from the field of control engineering [46]. In system identification, the task is to predict the behavior of a system that is modeled as an unknown black box by feeding it known inputs and observing and analyzing the outputs. Similarly, in QPT a specially selected set of quantum states is input into the quantum gate to be characterized, and the output quantum states of the gate are measured and analyzed. QPT is a characterization tool that is independent of the particular quantum computing architecture. This makes it a very useful tool for comparing quantum gate performance across different quantum computing architectures. It is a cross-platform benchmarking tool. In state tomography, the density matrix is the mathematical object which that fully describes the quantum

state. In QPT, the analogous mathematical object that fully describes the quantum gate's action on any arbitrary input state is called the χ matrix. *Once the χ matrix is obtained, the output of the quantum gate can be predicted for any input state.* The χ matrix is the quantum analog of the classical truth table.

There are many great resources that describe the theoretical foundations and the experimental implementations of QPT [19, 86, 65, 34, 18, 60]. However, the theory describing QPT can be mathematically convoluted and, as a result, it can be difficult to extract the fairly simple conceptual points that are key to understanding QPT:

1. Just as there is a basis set of *states* for qubits, there is also a basis set of *operations*. For a single qubit that set can be taken to be the Pauli basis $\{I, X, Y, Z\}$ [39, 58]. For two qubits, the set is

$$\begin{aligned}\hat{E} &\equiv \{I, X, Y, Z\} \otimes \{I, X, Y, Z\} \\ &= \{II, IX, IY, IZ, XI, XX, XY, XZ, YI, YX, YY, YZ, ZI, ZX, ZY, ZZ\}\end{aligned}\quad (6.2)$$

2. Quantum operations are linear transformations. As such, they can be written as linear combinations of the basis set of operations in (6.2).
3. The above two concepts can be used to mathematically model any quantum op-

eration, such as a quantum gate, using the equation

$$\varepsilon(\rho) = \sum_{mn} \chi_{mn} \hat{E}_m \rho \hat{E}_n^\dagger \quad (6.3)$$

where for two qubits $m, n = 1, 2, \dots, 16$ and \hat{E}_m is one of the two-qubit basis operations, and ρ and $\varepsilon(\rho)$ are the gate's input state and the resulting output state, respectively. The term χ_{mn} is the (m, n) th element of the χ matrix, a 16×16 matrix for two qubits. Now we can give a more mathematical definition of the χ matrix: *the elements of the χ matrix, χ_{mn} , are the coefficients in the linear expansion (6.3) of the gate operation in terms of the basis operations, \hat{E}_m .*

4. Once we obtain the χ matrix for a given basis set of two-qubit states, we can use that χ matrix to predict the output state for any arbitrary input state.

6.2.2 Quantum process tomography of the SQiSW gate

As illustrated in Figure 6.3, performing QPT on the SQiSW gate involves preparing the qubits in a spanning set of input basis states, $\{HH, HV, HD, HR, VH, VV, VD, VR, DH, DV, DD, DR, RH, RV, RD, RR\}$, operating with the gate on each of these states, and then carrying out complete state tomography on each corresponding output state. The definitions for the state labels $\{H, V, D, R\}$ are given in the table shown in Figure 5.10.

We have already characterized the 16 input states and have obtained their density

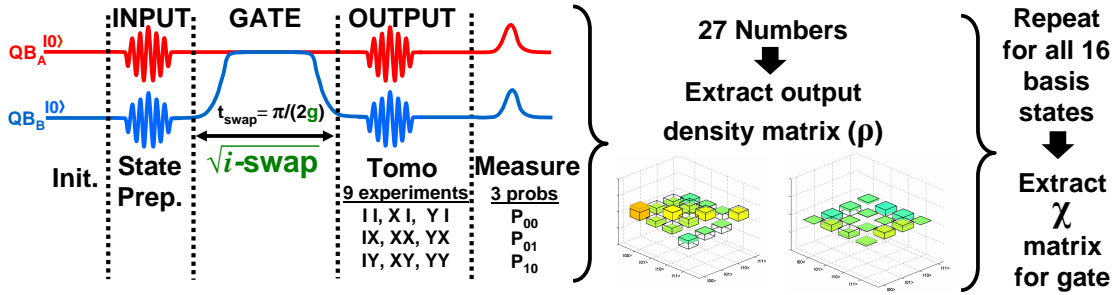


Figure 6.3: **Pulse sequence for quantum process tomography (QPT) of SQiSW**. QPT consists of inputting each of the 16 two-qubit basis states into the quantum process to be characterized and performing state tomography on each corresponding output state. Once the 16 input and output density matrices are obtained they can be used to mathematically extract the χ matrix for that particular quantum process.

matrices, as described in the last chapter. These input states are represented by the variable ρ in (6.3). We then operate on the input states with the SQiSW gate and carry out complete state tomography on the output states. The output states are represented by $\varepsilon(\rho)$ in (6.3). In Figure 6.4, we show the full set of 16 density matrices of the output states of the SQiSW gate corresponding to the 16 input state density matrices shown earlier in Figure 5.12. We are interested in the quality of the entangling gate itself, therefore we have calibrated out errors resulting from measurement; both from visibility errors and from measurement crosstalk, as described in Appendix D. The density matrices for the SQiSW gate input and output states, without the measurement crosstalk and visibility error calibrated out, are also given in Appendix D, in Figures D.1 and D.2. From the complete set of calibrated input (Figure 5.12) and output (Figure 6.4) density matrices, we can reconstruct the 16×16 χ matrix by using (6.3).

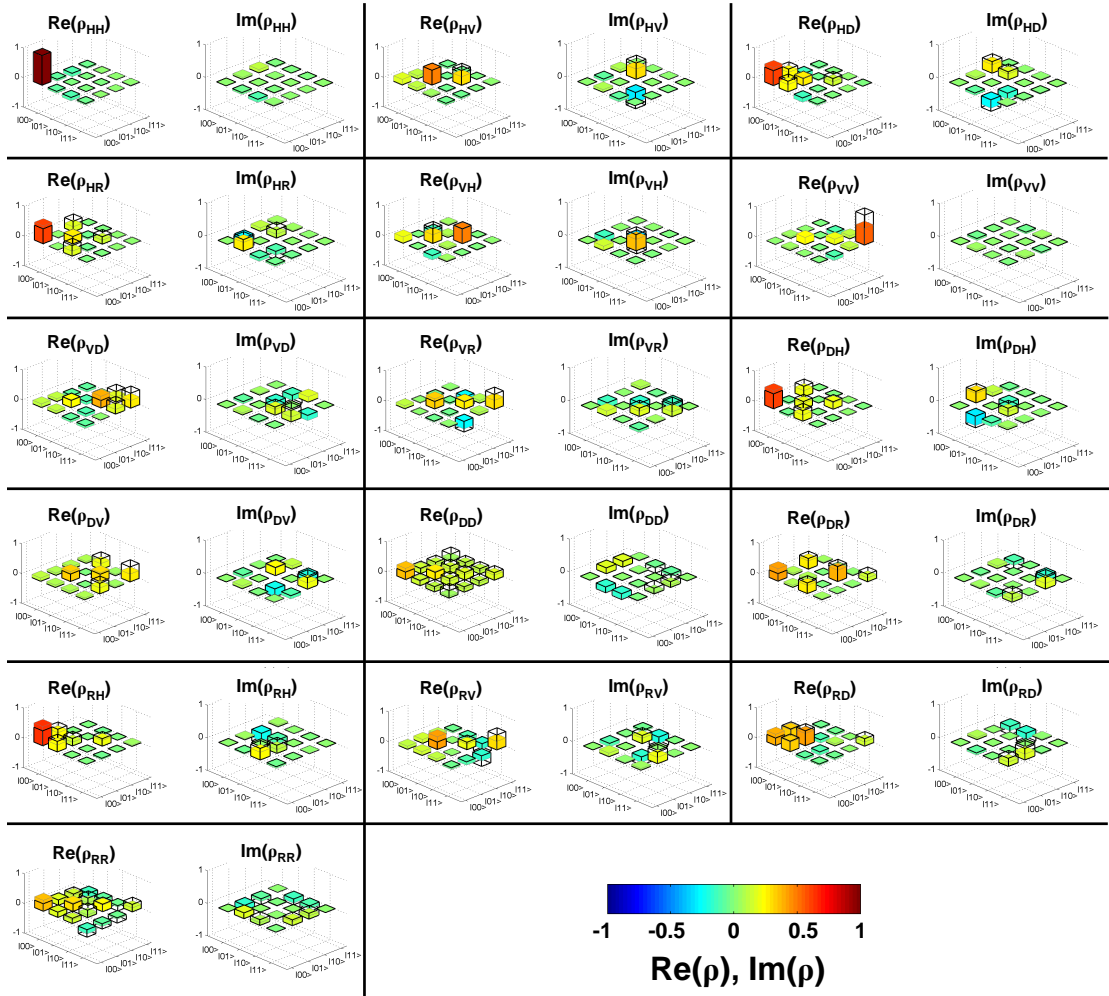


Figure 6.4: The full set of density matrices, obtained via state tomography, for the output states produced by the action of the SQiSW gate on the 16 two-qubit basis states shown previously in Figure 5.12. Measurement errors have been calibrated out from this dataset. The solid bars are the experimental data and the transparent bars are the theory. The states are labeled according to the input states used with the $\{H, V, D, R\}$ shorthand notation as defined in the table shown in Figure 5.10a.

Additionally, standard QPT typically produces an unphysical χ matrix because of inherent experimental noise [65, 60]. A physical χ matrix define a completely positive and trace preserving (CPTP) map [19, 41], which means that it must have positive

eigenvalues that sum to one. Our measured χ matrix has several negative eigenvalues, as discussed in Appendix D. As is commonly done in QPT experiments [65, 60], a χ matrix that satisfies the CPTP constraints must be obtained from the experimental data before the data can be compared to a theoretically predicted χ matrix, which is physical by construction. The problem of finding a physical approximation to unphysical QPT data can be shown to be a convex optimization problem [15, 16], a technique commonly used in control theory. We use a type of convex optimization called semidefinite programming [15] to find the physical χ matrix that best approximates our measured, unphysical χ matrix. Mathematically, for the experimentally obtained χ matrix and the physical approximation χ^p , we minimize the two-norm distance $\|\chi^p - \chi\|_2 \equiv \sqrt{\text{tr}\{(\chi^p - \chi)^2\}}$ with the constraints that χ^p be CPTP. This physical matrix χ_m^p , which also includes the calibrations for measurement errors, is shown in Figure 6.5. The experimentally obtained data is shown as the solid color bars and the theoretically expected χ matrix elements are shown using the transparent bars. This matrix closely matches the original data before corrections for CPTP (see Appendix D).

In both the real and imaginary parts of the χ_m^p matrix, we observe non-zero matrix elements in locations where such elements are expected, in qualitative agreement with the theory. Quantitative comparison is obtained by calculating the process fidelity, $F_p = \text{Tr}(\chi_t \chi_m^p)$, where $0 < F_p < 1$. The process fidelity gives a measure of how close χ_m^p is to theoretical expectations [60]. For the SQiSW gate demonstrated here, with

measurement calibration taken into account, we find $F_p = \text{Tr}(\chi_t \chi_m^p) = 0.63$, where χ_t is the theoretical χ matrix for the SQiSW gate. The χ_m and χ_e matrices are the unphysical χ matrices with and without measurement calibrations, respectively. The χ_e^p matrix is the physical approximation to the χ matrix that does not include the measurement calibrations. These are shown in Figures D.3-D.5 in Appendix D.

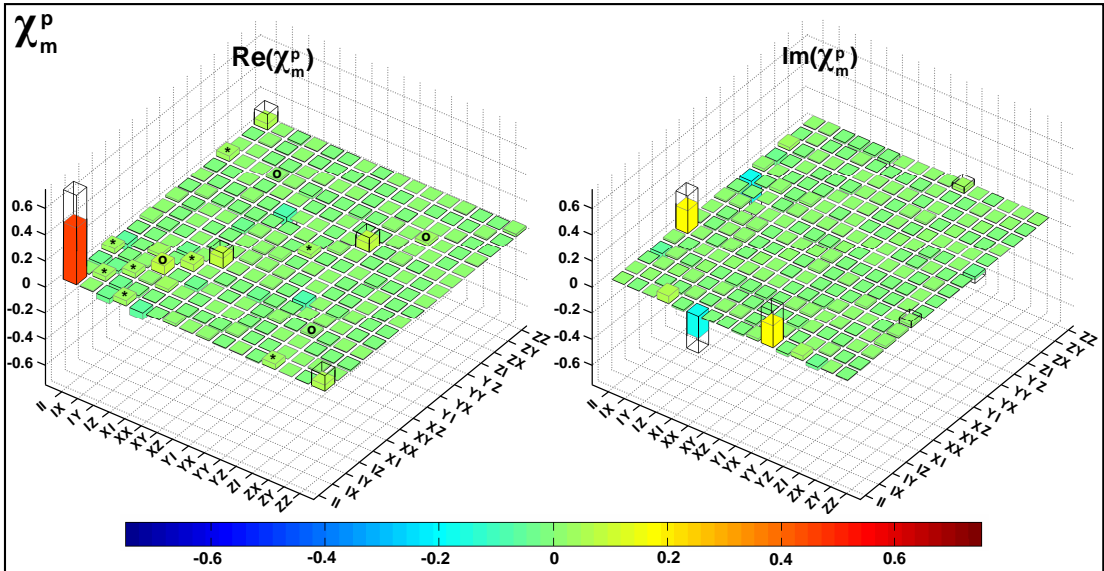


Figure 6.5: χ matrix for SQiSW gate. Real and imaginary parts of the reconstructed χ matrix for the SQiSW gate. Physical estimates to the experimental data are shown as solid bars. Transparent bars give the theoretically expected χ matrix, which does not include effects due to decoherence. Each bar represents the real and imaginary part of the coefficient of the particular two-qubit basis operation, \hat{E}_{mn} , in an expansion of the SQiSW operation in terms of the 16 two-qubit basis operations as given by (6.3). Errors from measurement crosstalk and visibility were calibrated out in this data. Technical details regarding calibrations and the physical estimation can be found in the text and in Appendix D. The matrix elements of χ_m^p that are non-zero because of energy relaxation and dephasing are marked with a “*” and “o” symbol, respectively. As discussed in the text, these elements can be used to extract numerical values for the dephasing time, T_2 , and to extract quantitative details about the noise acting on the coupled qubit system.

Errors in our SQiSW gate primarily arise because the time for the experiment (~ 50 ns) is not significantly shorter than the dephasing time of 120ns. This is confirmed using a recent theory [39] by Kofman *et al.*, which includes the effects of dephasing and decoherence on the SQiSW χ matrix. In particular, the elements marked with an asterisk and a circle in Figure 6.5 are non-zero because of energy relaxation and dephasing, respectively. The theoretical work done in [39] uses a modified basis of operators. Hence to compare the data here to the work in [39], the sign of the real part of $(\chi_m^p)_{XX,YY}$ and $(\chi_m^p)_{YY,XX}$, and the imaginary part of $(\chi_m^p)_{XX,II}$ and $(\chi_m^p)_{II,XX}$ must be changed. Using this theory and the real part of $(\chi_m^p)_{IZ,IZ}$ and $(\chi_m^p)_{IZ,ZI}$, we estimate our single-qubit dephasing time as $T_2 = (3\pi + 2)/16g(\chi_m^p)_{IZ,IZ}$. From Figure 6.5 we find $(\chi_m^p)_{IZ,IZ} = 0.105$ and $T_2 = 123$ ns, in close agreement with the value obtained in Chapter 4 from Ramsey experiments. We also estimate the degree of correlation of the dephasing noise between the coupled qubits using $\kappa \approx (\chi_m^p)_{IZ,ZI}/(\chi_m^p)_{IZ,IZ} - [(\pi - 2)/(3\pi + 2)]$. Our measurement of $(\chi_m^p)_{IZ,ZI} = 0.017$ yields $\kappa \simeq 0.11$, indicating that the dephasing is mostly uncorrelated. This is in agreement with previous work [12, 53, 68] that found a dephasing mechanism local to the individual qubits.

6.2.3 Improving gate performance

From the above experiments, it is clear that gate performance is limited by dephasing. This is not surprising because the time required for the SQiSW operation together with

the time required for the input state preparation and tomography pulses is already almost 50ns in length, a significant fraction of $\sim 120\text{ns}$ T_2 time. There are two ways get around the T_2 limitation.

The source of dephasing could be located and the qubit can be made from materials that do not contain this source of dephasing. Although conceptually this might seem like a simple solution, finding the source of dephasing in superconducting qubits has been a decades old problem that has remained unsolved despite a strong effort in both experimental and theoretical physics, and in materials science [53]. Evidence from recent work [12, 53, 68] does point to surface spin states as the source of dephasing, but this has not been verified thoroughly and is still under investigation.

Another way to get around the T_2 limit would be to make the swap operation faster as it is the longest operation in the sequence. This can be accomplished by increasing the coupling strength, g . At first glance there are serious problems with this. If the coupling strength is increased, the measurement crosstalk will also increase. At large coupling strengths the detuning, $\Delta_{off} \gg g$, required to turn off the interaction must also be larger thereby making it more difficult to get a high on/off ratio and further exacerbating the frequency crowding issue. The ideal solution to this would be a scheme for tunably coupling the qubits so that the coupling strength, g , could be turned on during entangling operations and turned off during measurement and single-qubit pulses. Therefore with tunable coupling the coupling strength can be made arbitrarily

large without increasing measurement crosstalk or generating errors due to the coupling being on during single-qubit operations. In the next chapter we demonstrate a tunable coupling architecture for flux-biased phase qubits.

Chapter 7

Connecting Phase Qubits Using

Tunable Coupling

7.1 Motivation and prior work

Tunable couplers have been previously demonstrated using superconducting qubits [33, 59, 2, 32], but only using designs that required the tuning element to be in close proximity to the qubits, making scalability difficult. Also, previous demonstrations have shown either limited time-domain control or low on/off ratios, thus providing a proof-of-concept, but limited use in realistic quantum operations. The design we present here for the first time, in a single device, addresses all of these shortcomings. It achieves control of the coupling strength on nanosecond time scales with a large on/off coupling

ratio and it is a novel design because it is completely modular, allowing for the coupling of qubits across large distances, not just nearest-neighbors. Additionally, this design allows for coupling to other superconducting circuit elements in addition to qubits. For example, it can be used to controllably couple a qubit to a resonator, an amplifier circuit, or even to a qubit from other quantum computing architectures. In this chapter, we introduce our tunable coupler design, characterize it, and demonstrate its use in tunable swap experiments.

7.2 This tunable coupler design

The electrical circuit for the tunably coupled flux-biased phase qubits is shown in Figure 7.1a and a corresponding optical micrograph is shown in Figures 7.1b-f. Each qubit still has the same parameter values as given in (4.2). The tunable coupling element (Figures 7.1d-f) is a four-terminal device constructed using a fixed negative mutual inductance $-M$ (Figure 7.1e) and a single, current-biased Josephson junction with critical current $I_0^c \simeq 1.6\mu\text{A}$ (Figure 7.1f) that acts as a tunable positive inductance L_c . This inductance changes with coupler bias I_{cb} according to (3.6), $L_c = (\Phi_0/2\pi I_0^c)/\sqrt{1 - (I_{cb}/I_0^c)^2}$.

where $I_0^c \simeq 1.6 \mu\text{A}$ is the coupler junction critical current. The coupler is biased using a current bias, labeled as I_{cb} and f in Figure 7.1. Although the coupler bias line will be represented by a single current bias line, I_{cb} , as shown in Figure 7.1, it is con-

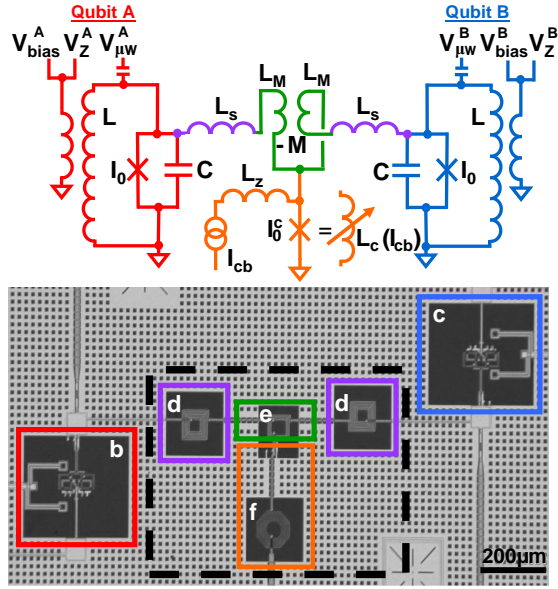


Figure 7.1: **Device circuit and micrograph of two Josephson phase qubits coupled using a tunable coupler.** The circuit shows the two qubits in red and blue and the coupler in purple, green and orange. A micrograph of a fabricated device is shown below the circuit where boxes *b* and *c* enclose the two qubits. Each qubit is designed in the same manner and with the same parameters as described in (4.2). The inductors $L_s \simeq 2700$ pH, $L_M \simeq 390$ pH, and the negative mutual inductance $-M \simeq -190$ pH, which form the non-tunable part of the coupler, are shown in purple and green, and boxes *d* and *e*. The current-biased coupler junction, with critical current $I_0^c \simeq 1.6\mu\text{A}$, forms the tunable element and is shown in orange and in box *f*. The inductor $L_z = 9$ nH isolates the coupler and qubits from the 50Ω characteristic impedance of the bias circuit. The entire coupler, a modular four-terminal device, is shown by the dashed box. The coupler connecting qubits *b* or *c* to inductor *d* can be made longer, if needed, to connect qubits over longer distances.

structured exactly like the flux bias and measurement/z-pulse lines shown in Appendix B. Fast (nanosecond scale) coupler bias signals are pulsed down a 50Ω attenuated line and slow (DC to microsecond scale) coupler bias signals are applied to a DC line with a 1 k Ω series resistance. These two lines are impedance matched using a bias tee in the same way that was done for the flux bias line, as described in Appendix B. As was

described for the single-qubit flux bias line in Chapter 4, the low characteristic impedance of the coupler bias line must be transformed up to a higher impedance in order to limit dissipation. This is accomplished using the 9 nH inductor shown in Figure 7.1f which increases the characteristic impedance of the coupler bias line.

The interaction Hamiltonian between qubits A and B for the tunable coupler is derived in detail in [62] and is given by

$$H_{int} \simeq \frac{g}{2} \left(\sigma_{X_A} \sigma_{X_B} + \frac{1}{6\sqrt{N_A N_B}} \sigma_{Z_A} \sigma_{Z_B} \right) \quad (7.1)$$

with

$$g = \frac{M - L_c}{(L_M + L_s)^2 \omega_{10} C} \quad (7.2)$$

where the $\{\sigma_X, \sigma_Z\}$ are Pauli operators, N_A (N_B) is the number of states in the qubit well of qubit A (B), g is the adjustable coupling strength, $C \simeq 1$ pF is the qubit capacitance, and $\omega_{01}/2\pi$ is the on-resonance frequency that the two qubits are biased to.

The direct connection of the qubits through this circuit creates a fixed coupling of much higher strength than what we would like for our experiments. To reduce the coupling magnitude to the desired 50 MHz range, series inductors $L_s \simeq 2700$ pH (Figure 7.1d) are inserted in the connecting wires that are significantly larger than the mutual inductance elements $L_M \simeq 390$ pH and the mutual inductance itself, $M \simeq 190$

pH. Because the number of levels in the potentials of qubits A and B are typically $N_A \simeq N_B \simeq 4 - 10$, the $\sigma_{Z_A}\sigma_{Z_B}$ term in equation (7.1) gives a small contribution of approximately 0.03 to the coupling strength. This interaction does not affect the results presented here and can be effectively removed using a refocusing pulse, if needed. With parameters $I_0^c \simeq 1.6\mu\text{ A}$ and $M = 190\text{ pH}$, and full adjustment of the bias current, we were able to vary the coupling strength, $g/2\pi$, from approximately 0 MHz to 100 MHz. However, the values of I_0^c and M can be chosen so that other ranges of coupling strength, both positive and negative in sign, are possible.

7.3 Coupler characterization and dynamic performance

The coupler can be operated in two modes. In the simplest “static” mode, the coupler is held at a fixed coupling strength throughout a two-qubit pulse sequence. However, the static mode cannot be used in more complex experiments because the coupling strength cannot be tuned on-the-fly during single-qubit operations and measurement. As mentioned earlier, having the coupler on during single-qubit operations or measurement would lead to errors. Hence, this coupler can also be operated in a “dynamic” mode where fast, nanosecond-scale pulses are used to turn the coupler on and off at any chosen time during a complex pulse sequence.

7.3.1 Static performance: tuning the avoided-level crossing

Using the static mode, we perform two-qubit spectroscopy at fixed coupler biases, which allows us to measure the energy splitting $g/2\pi$ at the avoided level crossing where the detuning $\Delta/2\pi = (\omega_{01}^A - \omega_{01}^B)/2\pi$ between the two qubits is zero. The pulse sequence for this experiment is shown in Figure 7.2a. The coupler bias (green) is set to the value I_{cb} , and is kept at this constant value throughout this static mode experiment. The dashed line indicates the coupler bias level that corresponds to zero coupling strength, $g/2\pi \simeq 0$ MHz. The qubits (red and blue) are initially detuned by 200 MHz and each starts in the $|0\rangle$ state. The bias of qubit B is then adjusted using a z-pulse to set its $0 \rightarrow 1$ transition frequency, $\omega_{01}^B/2\pi$, a distance $\Delta/2\pi$ from the qubit A frequency, $\omega_{01}^A/2\pi$. A microwave pulse of frequency $f_{\mu W}$ and duration $\sim 2 \mu s$ is then applied to each qubit. The two-qubit probabilities are then determined using a single-shot measurement, in the same way that was done in the capacitive coupling experiments. A representative subset of crossings for several coupler biases are shown in Figures 7.2b-e. The coupler clearly modulates the size of the spectroscopic splitting, and allows the setting and measuring of the coupling strength [62]. Although the data for 0 MHz shows no apparent splitting, the resolution at zero coupling is limited to ± 1.5 MHz by the 3 MHz linewidth of each qubit's $0 \rightarrow 1$ resonant response, which is slightly broadened due to the high power of the microwave pulse. Sub-megahertz resolution of the minimum coupling strength is obtained from the dynamic mode experiments, which

will be discussed shortly.

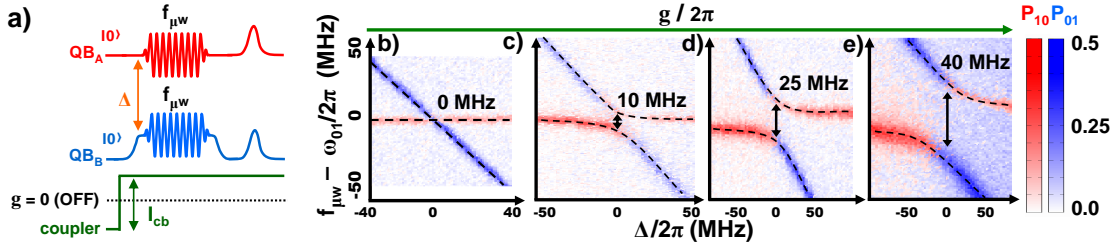


Figure 7.2: **Tuning the spectroscopic splitting.** a) Pulse sequence for two-qubit spectroscopy. Two-qubit spectroscopy was previously described in Chapter 5, but here we add a line to the pulse sequence diagram that represents the signal on the coupler line. The coupler is biased to a fixed value of the coupler bias I_{cb} and maintained at that value as the detuning Δ and the microwave source frequency $f_{\mu w}$ are scanned and the two-qubit probabilities P_{01} and P_{10} are measured. The panels b) to e) are plots of the measured probability P_{10} (A excited) and P_{01} (B excited) versus the detuning frequency $\Delta/2\pi$ and the difference in microwave and qubit A frequencies $f_{\mu w} - \omega_{01}^A$. Each panel shows a different coupler bias I_{cb} that increases from b) to e). The minimum splitting size is equal to the coupling strength $g/2\pi$ and is measured as the minimum distance between the two resonance curves on the spectroscopy data. The data in b) to e) shows the coupling strength being adjusted by the coupler and verifies static coupler performance. The dotted lines are a guide to the eye.

7.3.2 Static performance: Measurement crosstalk minimization

Since we have determined that the fidelity of gate operations is limited by qubit dephasing times, we want to reduce gate times by using stronger coupling. As mentioned at the end of last chapter, for devices with fixed coupling this strategy cannot be used effectively because of the rapid rise in measurement crosstalk with increased coupling [54, 40]. Therefore, it is important to demonstrate that measurement crosstalk can be reduced to a minimal value when the coupler is turned off. As shown is Figure 7.3a, we determine measurement crosstalk by driving only one qubit with Rabi oscillations,

and then simultaneously measuring the excitation probabilities of both qubits, a technique that was first used to measure crosstalk in [4]. The undriven qubit shows no response if there is no measurement crosstalk. The coupler (green) is set to a static bias I_{cb} . The coupler bias level corresponding to zero coupling strength, $g/2\pi \simeq 0$ MHz, is indicated by the dashed line. The qubits remain detuned by 200 MHz throughout the experiment, and only one qubit (shown here, A) is excited with the Rabi microwave pulse. The amplitude of the oscillation on the undriven divided by the amplitude of oscillation on the driven qubit gives a quantitative measure of the measurement crosstalk. The Rabi data is shown in Figures 7.3b and c for both the driven and undriven qubits, using representative coupling strengths of 0 MHz and ~ 17 MHz. The measurement crosstalk is plotted as a function of coupler bias in Figure 7.3d, where there is a broad region of coupler bias where the measurement crosstalk amplitude is minimized. This tunable coupler allows operation of phase qubits at large coupling strengths without the drawback of large measurement crosstalk.

7.3.3 Dynamic performance: the tunable swap operation

The dynamic mode of operation tests coupler performance with a sequence that mimics actual use in an algorithm, a swap experiment. This pulse sequence is illustrated in Figure 7.4a. The coupler (green) is first set to the coupler bias value corresponding to $g/2\pi \simeq 0$ MHz, as measured previously. The qubits (red and blue) are initially detuned

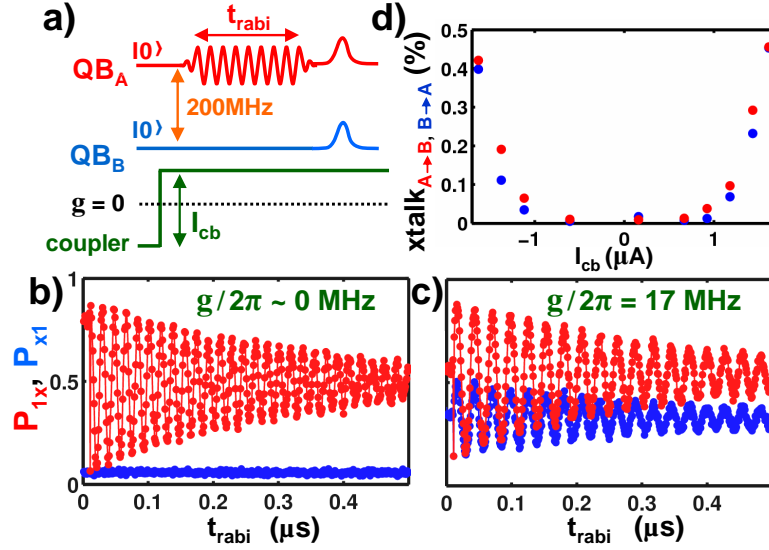


Figure 7.3: **Turning off measurement crosstalk.** **a)** Pulse sequence for determining the measurement crosstalk as a function of coupler bias. The coupler is set to a value of coupler bias I_{cb} and is kept at this value throughout the experiment. The qubits are biased off-resonance by $\Delta_{off} \simeq 200$ MHz and are kept off-resonance for the duration of the experiment. This is done to mimic how the operating biases are usually set during measurement, off-resonance by 200 MHz, as previously described in Chapter 5. Each qubit is initialized into the $|0\rangle$ state and a Rabi is excited on one qubit (shown here, qubit A). No microwave or z-pulses are applied to the other qubit (shown here, qubit B). The two-qubit probabilities are then measured using a single-shot measurement. The pulse sequence is repeated for various Rabi pulse lengths and a full Rabi scan is taken for a few representative values of the coupler bias, I_{cb} . **b)** For the tunable coupler turned off, we plot $P_{x1} = P_{01} + P_{11}$ and $P_{1x} = P_{10} + P_{11}$ versus the Rabi pulse time t_{rabi} . Rabi oscillations in P_{1x} (qubit A) are observed, with only a small amplitude oscillation of P_{x1} (qubit B) indicating that measurement crosstalk is present. **c)** Same as for b), but with coupling turned on to 17 MHz where a much larger measurement crosstalk signal is observed in P_{x1} . **d)** Measurement crosstalk amplitude as a function of coupler bias I_{cb} for the case of Rabi drive on qubit A (red) and qubit B (blue). For the case of drive on qubit A (qubit B), crosstalk amplitude is displayed as the ratio of the amplitudes of the oscillations of P_{x1} (P_{1x}) to that of P_{1x} (P_{x1}).

by $\Delta_{off} = 200$ MHz and start in the $|0\rangle$ state. A π microwave pulse is then applied to qubit A, exciting it to the $|1\rangle$ state. The coupling interaction remains off during this pulse to minimize errors resulting from two-qubit interactions. A fast bias pulse then detunes qubit B from qubit A by a frequency $\Delta/2\pi$, and at the same time compensates

for qubit bias shifts due to the coupler bias, which will be discussed in more detail below. Simultaneously, the coupler is turned on to a bias I_{cb} using a fast bias pulse with ~ 2 ns rise and fall times. The coupler and qubit biases are held at these values for a time t_{swap} , allowing the two-qubit system to evolve under the coupling interaction. The coupling produces a two-qubit swap operation which arises from the $\sigma_{X_A} \sigma_{X_B}$ operator in Eq. (7.1), and is the basis for universal gate operations as described in the last chapter. The qubits are then detuned again to $\Delta_{off} = 200$ MHz and I_{cb} is set back to the zero coupling strength value, allowing for a crosstalk-free, single-shot measurement of the two-qubit probabilities $P_{AB} = \{P_{01}, P_{10}, P_{11}\}$.

In Figure 7.4b, we show swap data at $\Delta/2\pi \simeq 0$ MHz for two representative settings of off and on coupling, $g/2\pi \simeq 0$ MHz and 40 MHz. The P_{11} signal is now minimized, indicating that measurement crosstalk has been turned off. In Figure 7.4c, swap data for P_{01} and P_{10} are shown where the detuning, $\Delta/2\pi$ was varied for several representative coupling strengths $g/2\pi \simeq 0, 11, 27, 45,$ and 100 MHz. The swaps exhibit the expected chevron pattern for the resonant interaction [54]. In Figure 7.4d the swap frequency is plotted versus coupler bias at $\Delta/2\pi \simeq 0$ MHz for representative coupler bias values. Coupling strengths up to 100 MHz are possible, although we find that the decay times of the swaps degrade above 60 MHz, presumably due to the coupler bias approaching the critical current of the coupler junction.

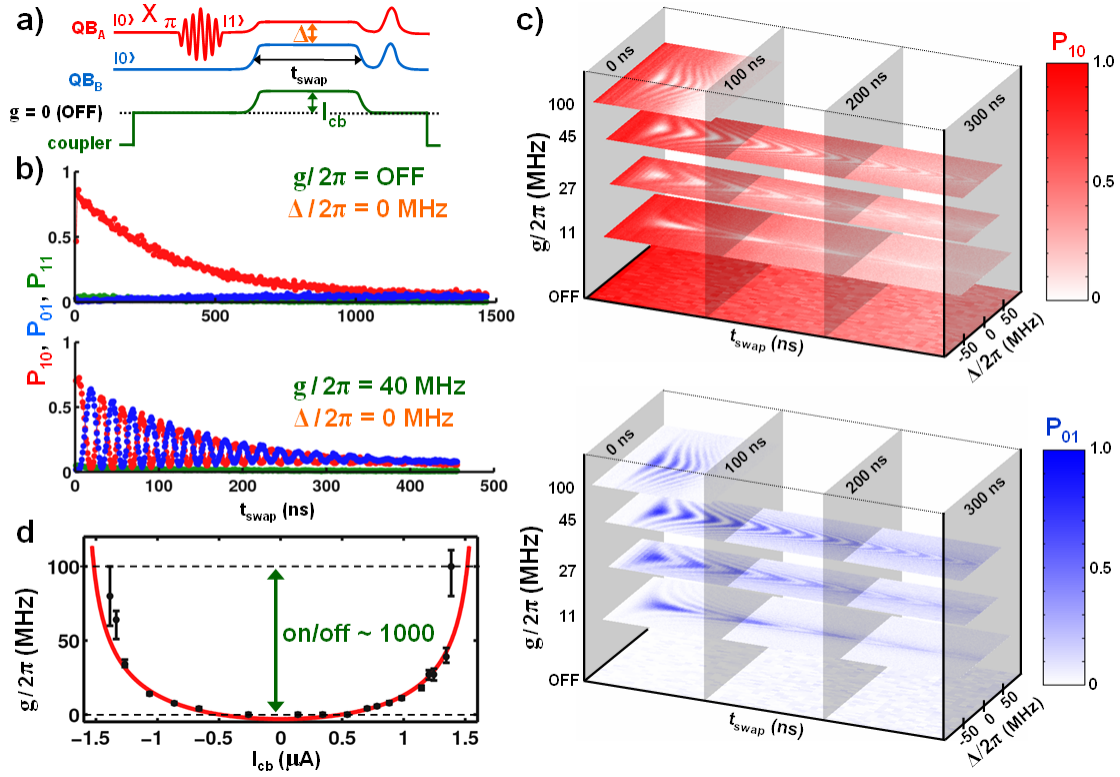


Figure 7.4: **Demonstration of dynamic coupler operation via swap experiment.** **a)** Pulse sequence demonstrating dynamic mode of coupler operation. The coupler is first biased to the I_{cb} value corresponding to zero coupling strength, $g/2\pi \simeq 0$, and each qubit is initialized into the $|0\rangle$ state. With the coupling off, qubit A can be excited into the $|1\rangle$ state using a π pulse and without generating single-qubit pulse errors due to the coupling interaction. The coupler is then turned on to a value I_{cb} and qubit B is simultaneously z-pulsed, biasing it to a frequency $\Delta/2\pi$ within resonance of qubit A. The system is then left to evolve for a time t_{swap} after which the coupler is returned to the off bias and the two-qubit probabilities are measured. With the coupler off during measurement, measurement crosstalk is not generated. **b)** The measured two-qubit probabilities P_{01} , P_{10} , and P_{11} are plotted versus t_{swap} for qubits on resonance $\Delta/2\pi = 0$ and two sets of coupling $g/2\pi$, corresponding to off (top) and on (bottom) conditions. **c)** Measured qubit probability, P_{10} , plotted versus t_{swap} and qubit detuning $\Delta/2\pi$ for representative coupling strengths $g/2\pi = 0$ MHz, 11 MHz, 27 MHz, 45 MHz, and 100 MHz. **d)** Swap frequency $g/2\pi$ versus coupler bias I_{cb} for all coupler biases measured in this experiment (solid dots). Solid red line is theory obtained from (7.2) and measured device parameters.

7.4 Scalability: the on/off ratio and stray capacitances, long-distance coupling and modularity

The determination of the minimum coupling strength, which quantifies how well the interaction can be turned off, is limited by the minimum detectable swap frequency of the qubits. Our ability to resolve this frequency is, in turn, limited by qubit decoherence because for low coupling strengths, energy relaxation (T_1) makes the swap oscillations decay before the occurrence of a full swap. Hence, it is difficult to quantify the time of a full oscillation period from the $g/2\pi = OFF$ data in Figure 7.4 and this limits our ability to measure the minimum coupling strength which is needed to calculate the on/off ratio. To determine the minimum coupling strength corresponding to the off data shown again in Figure 7.5a, we performed simulations of a two-qubit coupled system that included the $T_1 \sim 350$ ns decay as measured for each qubit. The computer code and a detailed description of the simulations can be found in reference [3]. We show in Figures 7.5b-d, the simulations for coupling strengths of 0.1 MHz, 0.3 MHz, and 0.5 MHz. The best fit to the data occurs at a simulated coupling strength of 0.1 MHz. Below coupling strengths of 0.1 MHz, the oscillations cannot be resolved due to T_1 decay. Therefore, we take the minimum coupling strength to be no greater than 0.1 MHz, giving a lower bound on the on/off ratio of $100\text{MHz}/0.1\text{MHz} = 1000$. However, we expect that the actual on/off ratio is much greater than this.

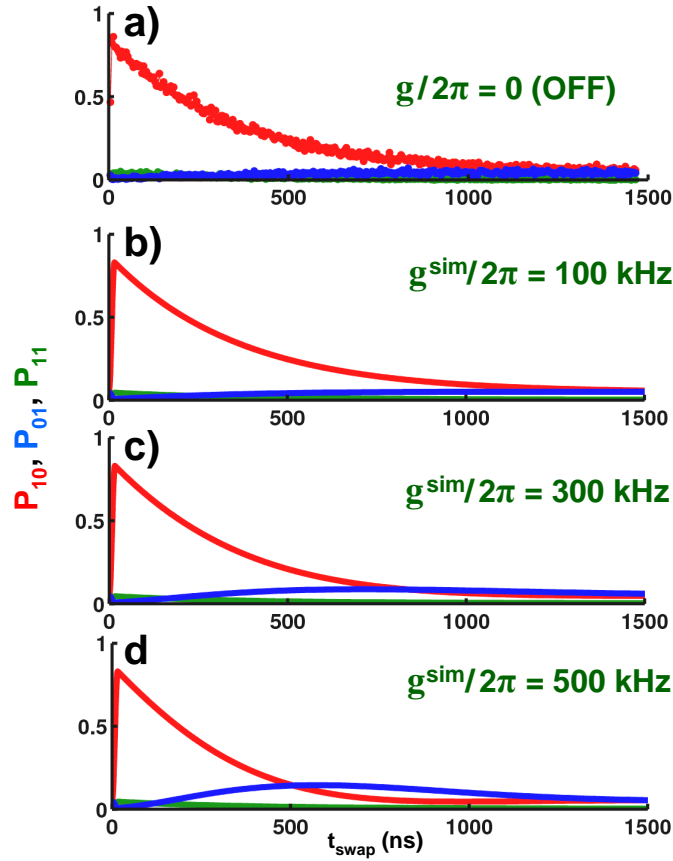


Figure 7.5: **Finding the minimum coupling strength.** Comparing the experimental swap data for $\Delta/2\pi \simeq 0$ **a)** with simulations for various coupling strengths **b)-d)** allows for the estimation of the minimum coupling strength. The simulation for 0.1 MHz best fits the data in **a)** hence the minimum coupling strength is no greater than 0.1 MHz. This gives an on/off ratio of at least $100 \text{ MHz}/0.1 \text{ MHz} \simeq 1000$.

Stray capacitances and inductances in the circuit introduce stray coupling that may limit the on/off ratio. In this design, the greatest contribution to stray coupling comes from the small ($\sim 50 \text{ fF}$), inherent capacitance of the coupler junction as represented by C_{cj} in Figure 7.6a. The coupler junction has a self-resonance frequency of $\omega_{c0}/2\pi \simeq 30 \text{ GHz}$, which implies that its effective inductance $L_c[1 - (\omega/\omega_{c0})^2]$ changes in value

from $\omega/2\pi = 0$ and 6 GHz by $\sim 4\%$ [62]. The $\sigma_{Z_A}\sigma_{Z_B}$ and $\sigma_{X_A}\sigma_{X_B}$ interactions in Eq. (7.1) will thus turn on and off at slightly different coupler biases and, along with virtual transitions as shown in Figure 7.6, will limit how far the coupler can be turned off [62, 5]. A useful feature of this coupler is that this imperfection can be compensated for by including a small shunt capacitor $C_S \simeq$ across the mutual inductance. The theoretical analysis behind this conclusion can be found in reference [62]. With this shunt, we should be able to attain on/off ratios up to 10^4 .

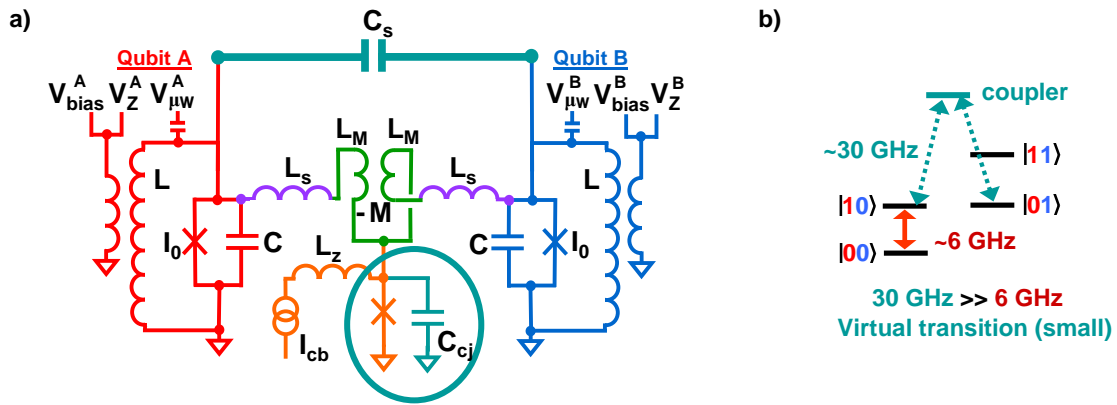


Figure 7.6: **Stray coupling.** a) The small capacitance due to the coupler junction, $C_{cj} \simeq 50$ fF, has a self-resonance frequency of $\omega_{c0}/2\pi \simeq 30$ GHz, which implies that its effective inductance $L_c[1 - (\omega/\omega_{c0})^2]$ changes in value from $\omega/2\pi = 0$ and 6 GHz by $\sim 4\%$. As discussed in [62], this will cause the $\sigma_{Z_A}\sigma_{Z_B}$ and $\sigma_{X_A}\sigma_{X_B}$ interactions in (7.1) to turn on and off at slightly different coupler biases leading to stray coupling. This stray coupling can be eliminated by shunting the coupler with a capacitance $C_S \simeq 0.6$ fF. b) An energy level diagram showing the qubit and coupler energy levels. A virtual transition through the coupler state at approximately 30 GHz, contributes to the stray coupling between the $|01\rangle$ and $|10\rangle$ states. The stray coupling is small, as described above, because the coupler transition at ~ 30 GHz is far off-resonance from the qubit transition at ~ 6 GHz.

This coupler design is unique compared to other tunable superconducting qubit couplers because it does not require the qubits and coupler to be in close proximity.

As shown in Figure 7.1, the wire connecting the qubits (labeled b and c) to the coupler inductors (labeled d), can be made longer to facilitate coupling of qubits over large distances. Also, the coupler is self-contained, as shown by the dashed box in Figure 7.1. These two features allow our coupler design to be used as a “drop-in” module for connecting qubits to other devices such as superconducting parametric amplifiers [9] or in coupling qubits to readout circuitry, superconducting resonators, or potentially even coupling superconducting qubits to qubits from other quantum computing architectures.

7.5 Technical points: multistability of the coupler circuit and influence of coupler bias on qubit bias

There are a few technical details which are important to the proper experimental implementation of the coupler. The coupler’s connection to ground via the qubits forms a loop which has multiple stable flux states. Therefore, similarly to the qubit flux bias reset discussed in Chapter 4, the coupler bias also needs to be reset as discussed below. Also, there are direct-current connections between the coupler bias and the qubits which produce small shifts in the qubit frequency due to changes in the coupler bias. These shifts can be readily compensated for using the qubit biases $V_Z^{A,B}$ and are also discussed below.

7.5.1 Coupler reset protocol

A direct-current connection between the coupler and qubits requires the coupler to be reset. Because the Josephson inductance of the qubit junctions is much larger than the shunt inductor L , current flowing from the coupler mostly flows through L . As a result, the coupler junction is effectively shunted by two loops with net inductance $(L_M + L_S + L)/2$, as shown in Figure 7.7a. A junction with a shunt inductance can have multiple stable operating points [6] if $\beta = 2\pi I_0^c (L_S + L_M + L)/2\Phi_0 > 1$; here $L_S + L_M + L \simeq 4.2$ nH and $I_0^c \simeq 1.6\mu\text{A}$, giving $\beta \simeq 20/2 = 10$. For these parameters, Figure 7.7b shows the expected behavior of the internal flux, Φ , in the loop versus external current bias I_{cb} , where the stable operating points are branches with positive slope A, B, C, D and E (solid lines), and unstable operating points are given by dashed lines. When the coupler is set to the bias labeled I_{cb}^{ON} , it can randomly assume any of the flux values given by the intersection of the gray dotted line with the stable branches A-E.

The branch must be precisely reset to place the coupler at a known bias. This may be accomplished using a similar reset technique to that used for single qubits and described in Chapter 4. For example, to place the coupler on branch C, the coupler bias is repeatedly varied between the two values I_{cb}^+ and I_{cb}^- . As occupation in any other branch will result in a switch out of that branch, with enough trials the coupler will eventually find itself in C, the only stable branch. Figure 7.7c shows how this reset protocol is simply integrated into the swap experiment. To determine I_{cb}^+ and I_{cb}^- , a

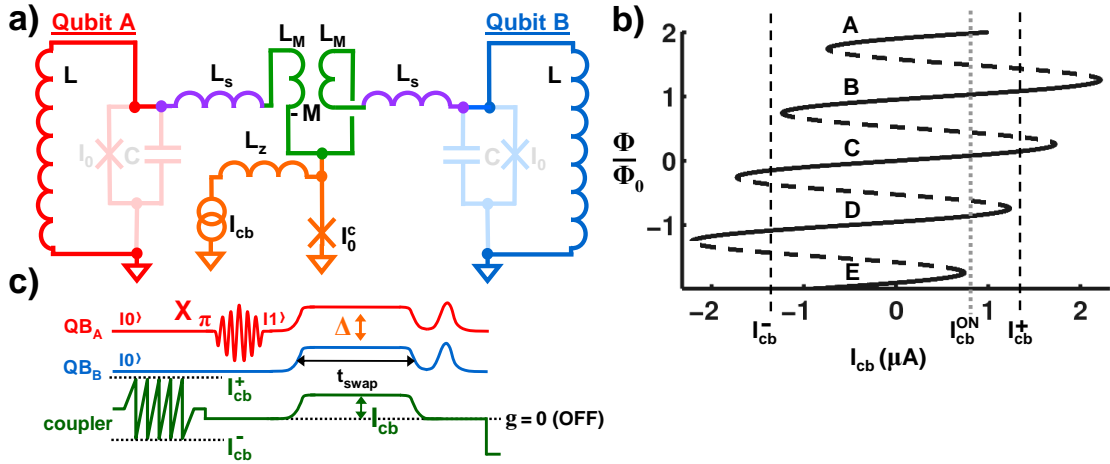


Figure 7.7: **The need for a coupler “reset”.** **a)** Unshaded parts of the circuit reveal the path from the coupler bias, through the qubit inductors, to ground, forming a Josephson junction in a loop which is known to display multi-stable behavior. **b)** Schematic depiction of multi-stability of coupler circuit. The internal flux, Φ , in the the unshaded circuit shown in a) is plotted as a function of coupler bias, I_{cb} . Solid lines are values of the coupler bias for which stable operating points exist and dashed lines are unstable operating points. This diagram is similar to the SQUID steps data, where there are multiple stable overlapping branches, here labeled A-E. **c)** Pulse sequence for the swap experiment which now also shows the coupler reset sequence. Similar to the single qubit reset procedure described in Chapter 4, we cycle the coupler bias, I_{cb} , between the two points I_{cb}^- and I_{cb}^+ that correspond to minimal overlap of the stable branch labeled C with the other branches. After repeating this for 30 cycles, the coupler will be initialized into the stable branch C, as discussed in detail in the text.

qubit can be used to detect when the coupler switches to a different branch. When switching happens, the direct-current coupling between the coupler and qubit causes a qubit bias shift, which in turn can be measured by monitoring the escape of the qubit $|0\rangle$ state using a step edge experiment where the operating bias is set to the steepest part of the step edge. For this measurement, we must first map out the position of the step edge as a function of coupler and qubit bias. The $|0\rangle$ state escape rate is given by (4.3).

In Figure 7.8a, we show the escape probability for the $|0\rangle$ state as a function of reset

offset $I_{cb}^R = I_{cb}^- = I_{cb}^+$ and the bias of qubit A. We take the dotted line as the condition where the $|0\rangle$ state had not escaped (below step-edge), and the dashed line as when the $|0\rangle$ state had fully escaped (above step-edge). We then plot in Figures 7.8b and c these conditions versus the two coupler biases I_{cb}^+ and I_{cb}^- . The data for the former case is shown in Figure 7.8b, where the region enclosed by the dashed box gives the values of I_{cb}^+ and I_{cb}^- where the coupler is properly reset, *i.e.* when the qubit does not escape from the $|0\rangle$ state due to changing of a branch. Figure 7.8c shows the scan for a bias above the step edge where this same region should now have the $|0\rangle$ state fully escaped. For optimal reset, I_{cb}^+ and I_{cb}^- were chosen at the center of the dashed box. Repeating these measurements for qubit B gave similar values.

Because a number of reset cycles must be used to reliably reset the coupler, the reset probability must be measured versus the number of resets. As shown in Figure 7.8d, we found an exponential decay with the number of reset cycles, as expected, and that 30 cycles produced an acceptable error of $\sim 1.5 \times 10^{-4}$.

We next confirmed that I_{cb}^+ and I_{cb}^- properly reset the coupler for all coupler and qubit bias values up to the critical current of the coupler junction. As shown in Figure 7.8e, we perform a step-edge experiment as a function of coupler bias. The slope in the curve is expected, and is due to the direct current connection between the coupler and qubit as discussed below. The increase in slope at the two ends of the curve arises from the non-linearity of the qubits Josephson inductance as the critical current is approached.

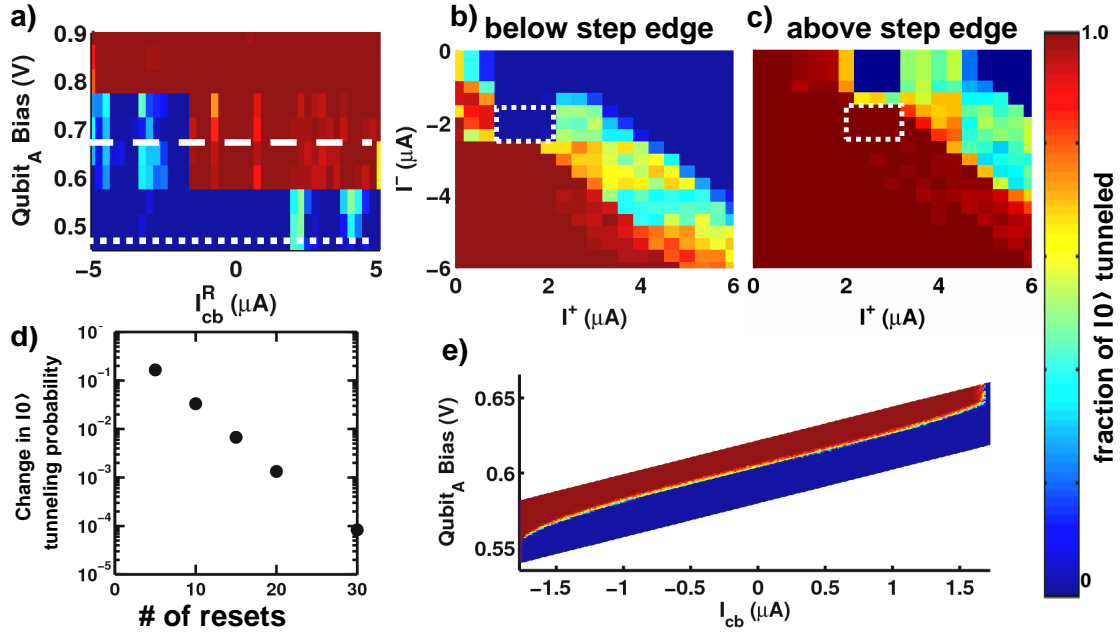


Figure 7.8: **Calibrating the reset.** **a) to c)** We must calibrate the values of I_{cb}^+ and I_{cb}^- needed to properly reset the coupler into one of the stable branches depicted in Figure 7.7b. This is done using a series of experiments that monitor the probability of $|0\rangle$ state tunneling as a function of coupler reset amplitudes, as described in the text. **d)** Measurement of qubit error versus the number of coupler resets indicates that in order to maintain the coupler in one particular stable branch with probability greater than $1 - 10^{-4}$, the coupler bias must be cycled between the values I_{cb}^+ and I_{cb}^- at least 30 times. **e)** Verification of proper coupler reset. We verify that the coupler is properly reset by performing the step edge experiment as a function of coupler bias. A sharp step edge with a smooth dependence on coupler bias indicates that the coupler has been reset properly and remains in a single stable branch for the full range of coupler bias values.

7.5.2 Compensation for qubit bias shift due to coupler bias

The coupler and qubit biases are connected via a direct-current path. As a result, a bias applied to the coupler also shifts the qubit biases. This can be seen in Figure 7.9a and b, which show the pulse sequence and data for two-qubit spectroscopy as a function of coupler bias. As the coupler bias I_{cb} increases, the qubit biases shift in a direction that increases the qubit resonance frequencies. The shifts are approximately the same for

both qubits, and can be negated by compensating z-pulses, as shown in Figures 7.9c and d. Here, the pulse sequence and spectroscopy data are the same except the qubit biases also contain a compensation pulse. With compensation, the qubit frequencies are approximately constant as a function of coupler bias, indicating the shifts have been minimized.

7.5.3 Future work on tunable coupling

The major issue with this tunable coupler design is the direct connection between the coupler bias and the qubits. In a future design, it is desirable for the coupler to be isolated from the qubit circuit by using capacitive coupling. The stray coupling discussed above is not an issue for a small number of qubits, but if this tunable coupling architecture is to be scaled up then this needs to be addressed. As a first step, a shunt capacitor like that in Figure 7.6a can be added. Furthermore, this design as presented in this thesis can already be used to connect qubits to other superconducting circuit elements. As this work was nearing completion, we began work on designing a device where the tunable coupler served as a tunable on/off switch between a qubit and a measurement circuit that allows for the quantum non-demolition measurement of the flux-biased phase qubits. This illustrates one of the many possible applications of this tunable coupler. We hope that this tunable coupling element will serve as a versatile circuit element in superconducting qubits and in other areas that use superconducting

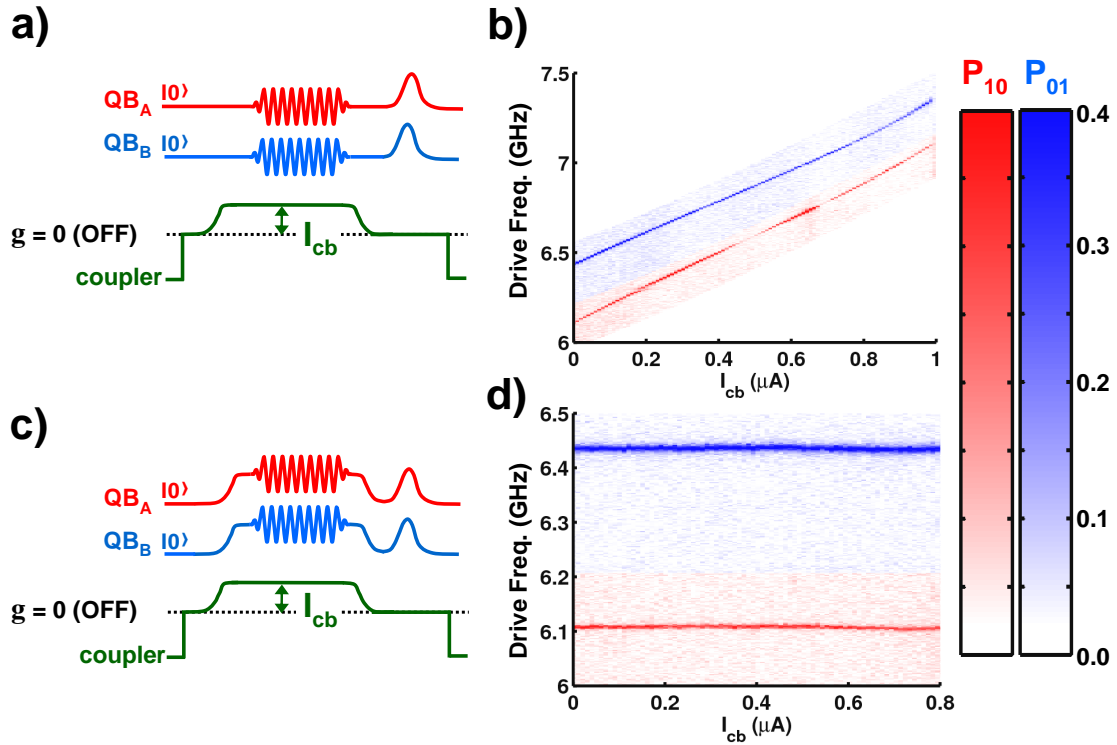


Figure 7.9: **Compensating for coupler induced qubit bias shifts.** The direct current connection between the coupler bias and the qubits leads to shifts in each qubit’s operating bias. These shifts can be measured by performing two-qubit fine spectroscopy as a function of coupler bias, I_{cb} . We can then compensate for the bias shifts using z-pulses. **a)** Pulse sequence and **b)** spectroscopy data without compensation for shift due to coupler bias. We excited each qubit with $\sim 2\mu\text{s}$ long microwave pulses and then measure P_{01} and P_{10} as a function of microwave drive frequency. We repeat this for increasing values of coupler bias to map out the qubit bias shift by measuring the shift in $\omega_{01}^{A,B}/2\pi$ with I_{cb} . **c) to d)** Same pulse sequence, but now with added z-pulses to compensate for the qubit bias shifts due to the increasing coupler bias. Now, the qubit frequencies do not change as a function of coupler bias indicating that we can successfully compensate for the shifts in qubit operating biases due to the coupler bias by using z-pulses.

circuits.

Appendix A

Device Fabrication

This appendix provides a brief overview of the steps involved in the microfabrication of the superconducting qubits discussed in this thesis. All the fabrication was done at the UC Santa Barbara Nanofabrication Facilities. Photolithography carried out using a SPR955 resist and MF701 developer. The resist was stripped using a sonicated acetone bath, although heated 1165 resist stripper followed by a deionized water rinse can also be used. The optical stepper used was a GCA 6300 Optical I-Line Wafer Stepper. Dry etching was done using a Panasonic E640 inductively coupled plasma etch system. Aluminum sputtering and oxidation carried out using a custom Kurt Lesker sputter and ion mill system. Dielectric materials were deposited using a UNAXIS high density plasma enhanced chemical vapor deposition (HD PECVD) system, pre-cleaned at 200°C with SF₆/O₂ for 40 minutes.

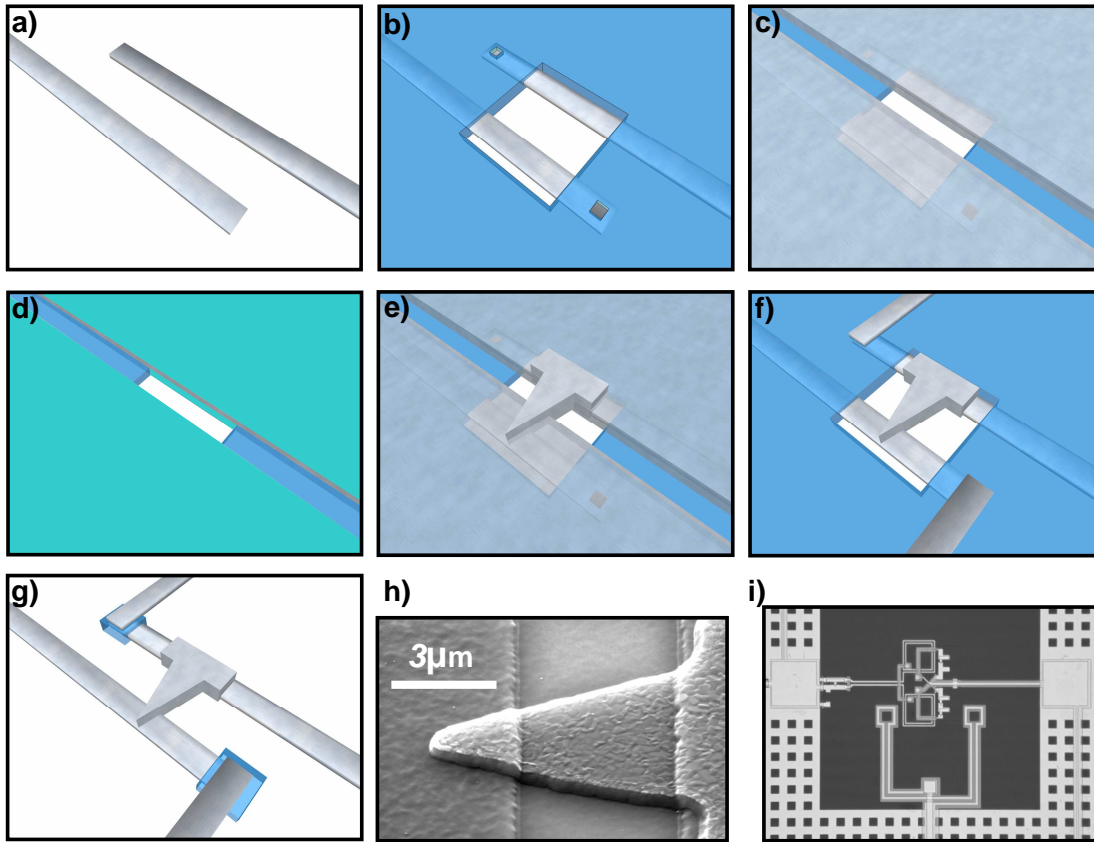


Figure A.1: **Microfabrication steps** CAD representations of qubit device microfabrication steps and micrographs of finished devices. Each step is discussed in detail in the text. **a)** Base wiring deposition and patterning. **(b)** Dielectric deposition and patterning. **(c)** Junction base electrode Al deposition and definition. **(d)-e)** Josephson junction oxidation and patterning. **(f)** Top wiring and shorting strap definition. **(g)** Dielectric etch **(h)** Scanning electron microscope image of an actual Josephson junction in a microfabricated qubit device. **(i)** Optical microscope image of microfabricated qubit.

A.0.4 Substrate

The qubit is fabricated on a crystalline sapphire substrate. The crystal orientation of the substrates used in this thesis was either c-plane or r-plane sapphire. Sapphire is used because it has a low loss tangent at GHz frequencies [53].

A.0.5 Base wiring deposition and patterning

Before sputtering the aluminum that will define the base layer of the qubit, the sapphire substrate is milled using an argon mill process at an Ar pressure of 2.0×10^{-4} Torr, 900 V beam voltage, 100 V accelerating voltage, and 35 V discharge voltage for ~ 2 mins. The mill is done at room temperature. After milling, 130 nm of Al is sputtered using an Ar gas plasma sputter source operating at 110 W at 5mT Ar. This gives a deposition rate of ~ 9 nm per min. This Al layer is patterned using optical lithography and etched using a BCl_3/Cl_2 inductively coupled Plasma (ICP) reactive ion etch (RIE). The etch is followed with a CF_4 gas passivation step and a post-passivation de-ionized (DI) H_2O dip to get rid of by-products generated by the interaction of Al and Cl. A computer generated representation of the device at the conclusion of this step is shown in Figure A.1a. Only the Al base wiring is shown, the sapphire substrate is not.

A.0.6 Dielectric deposition and patterning

After the base wiring is deposited, patterned, etched, and the resist is stripped, 250 nm of amorphous silicon hydride (a-Si:H) dielectric is deposited onto the base wiring. It will form the capacitor that shunts the qubit junction and will also provide insulation that will prevent overlapping wires from shorting together. This deposition is done at 100°C using a HD PECVD system. The dielectric is then patterned using optical lithography and etched using a CF_4/O_2 ICP RIE recipe. This creates vias that will be

used to make contact between the top and bottom wiring layers. Figure [A.1b](#) shows the device at the end of this step.

A.0.7 Junction base electrode Al deposition and definition

We have found that the HD PECVD dielectric deposition affects the base Al in a way that leads to non-functional Josephson junctions. Therefore, a fresh layer of Al untouched by the processing steps of the HD PECVD deposition is needed to make working Josephson junctions. This layer of Al will also be used for the top wiring, but the patterning and etching of the top wiring will be done in a later step. We sputter ~ 180 nm of fresh Al using the same parameters as for the base wiring deposition. We again include the pre-deposition mill to etch away any oxide or organic films that might have built up on the base layer Al. This layer of Al is then patterned using optical lithography and etched using the same BCl_3/Cl_2 ICP RIE process. The patterning and etching for this step punch a hole through the fresh Al metal only in a small rectangular region between the junction leads. This hole will prevent the junction electrodes from shorting together. A computer generated representation of the device at the end of this step is shown in Figure [A.1c](#).

A.0.8 Josephson junction oxidation and definition

In this step we form the actual Josephson junction. We first ion mill the surface of the fresh metal deposited in the previous step to remove any organics or oxide. The mill recipe is the same as the one used in the previous steps. We then oxidize at room temperature by bathing the sample in pure O_2 at 10 mTorr for ~ 10 minutes (Figure A.1d). We then sputter 130 nm of Al in the same way as described in the previous steps. This will be the top Al layer of the Josephson junction. The optical lithography is purposefully misaligned to the layers below it. This allows us to control the area of the junction by adjusting the amount of overlap between the triangular junction counter electrode and the oxidized Al layer below (see scanning electron microscope image of a finished Josephson junction in Figure A.1h). For this step, the plasma etch used is also different. We want to etch fully into the Al we just sputtered for the junction counter electrode, but not into the metal below it that we need for the base and top wiring. In order to do this we use an Ar/ Cl_2 etch rather than the BCl_3/Cl_2 etch. Compared to the chemical BCl_3/Cl_2 etch, the Ar/ Cl_2 etch is a physical etch which means that the Ar physically mills the Al. The Cl_2 is added to scavenge the milled byproducts so they can be pumped away. In addition to the more precise control, this physical etch also allows us to get nice, vertical sidewalls on the junction electrodes. We use the same ICP RIE system and break the etch up into small time intervals in order to monitor for etch completion, and thereby prevent overetching. However, the sample remains in the plasma etcher and is

unexposed to the cleanroom environment during visual inspections for completion. We follow up the etch with CF_4 gas passivation and a DI H_2O dip. The device at the end of this step is shown in Figure [A.1e](#).

A.0.9 Top wiring and shorting strap definition

Now we need to etch away the remaining metal so that only the top wiring and base wiring remain along with straps that are used as shorts between the Josephson junctions and ground. These straps will prevent pinholes in the junction oxide from being formed by the large electric fields present in the plasma etching steps. The straps will be etched away in the final processing step using a wet chemical etch. Again, optical lithography and the BCl_3/Cl_2 etch process are used to define the top wiring and strap layers. The device at the end of this step is depicted in Figure [A.1f](#) (shorting straps are not shown).

A.0.10 Dielectric etch

In this step we etch away any unnecessary dielectric material because it may contribute to dissipation and decrease qubit coherence times. We again use optical lithography and the same CF_4/O_2 ICP RIE etch. The end result is shown in Figure [A.1g](#).

A.0.11 Shorting strap etch

Finally, we remove the shorting straps using a wet chemical etch, consisting of submerging the device wafer into Transene etchant heated to 80°C for 10 – 20 seconds, and thoroughly rinsing with DI water. An optical micrograph of a finished device is shown in [Figure A.1i](#).

Appendix B

Electronics And Low Temperature

Experimental Set-up

B.1 Low temperature setup

Figure [B.1](#) shows the electronics and filtering present inside the dilution refrigerator, and Figure [B.2](#) is a photo of the actual dilution refrigerator internals that house the qubit sample and low temperature wiring and filtering.

Let us start at the qubit sample, at 25mK. The qubit chip is enclosed in an aluminum box. Each of the on-chip leads is wirebonded to a 50Ω SMA coaxial cable made from a copper conductor and a teflon insulator. These carry the signals out of the aluminum sample box and connect to the dilution fridge wiring. Making the sample box out of

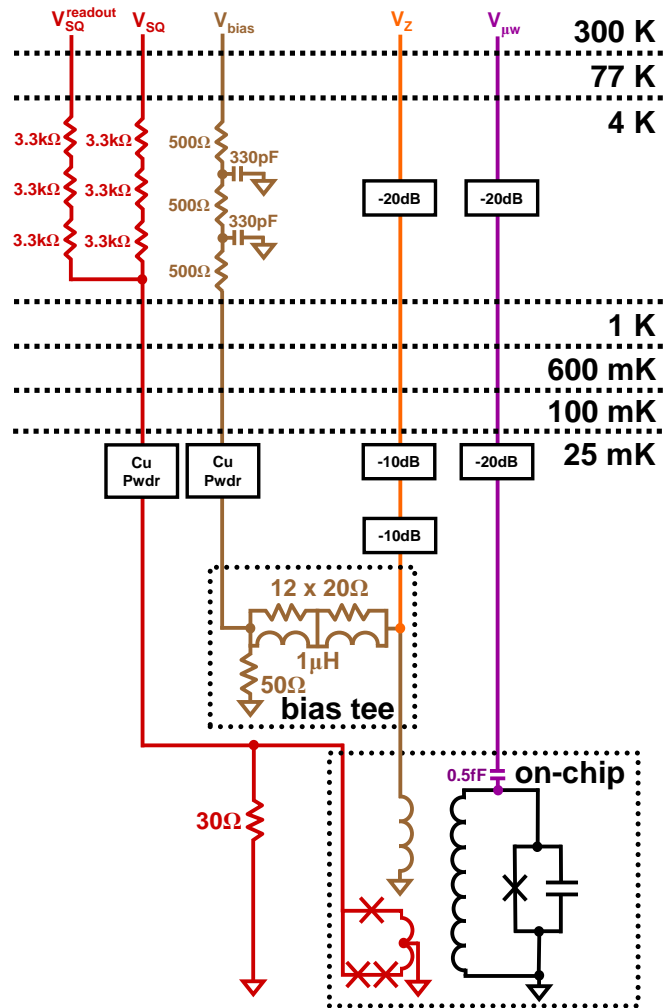


Figure B.1: The qubit is cooled to 25 mK in a dilution refrigerator. Above is a schematic of dilution refrigerator wiring for a single qubit, with the temperature of each stage as labeled on the right. Microwave (violet) and measurement/z-pulse (orange) lines have 50Ω characteristic impedances and are attenuated with 50Ω microwave attenuators. Flux (brown) and SQUID bias (red) lines are filtered using copper powder filters. Other circuit details are discussed in the text.

a superconducting metal provides electromagnetic shielding and may help prevent the trapping of magnetic flux in the chip groundplane when the sample is cooled below the superconducting transition temperature for aluminum, $T_c \simeq 1.2\text{K}$. It is important

to minimize trapped flux because it can generate dissipation [72]. Connected to the sample box, via SMA connectors, are the various control and bias lines as described in Figure 4.2. The aluminum sample box is clamped to the bottom most copper plate of the dilution refrigerator which sits at 25mK. Each of the signal lines coming out of the qubit chip will now be described, working up from the qubit sample box at 25 mK to room temperature, as shown in Figure B.1. and this box is clamped to the bottom most plate of the dilution refrigerator.

B.1.1 The SQUID lines

These were the lines labeled as V_{SQ} and $V_{SQ}^{readout}$ in Figure 4.2. At the sample box there is a $\sim 30\Omega$ resistor (R_{shunt}) that shunts the SQUID to ground, making the SQUID switch to a voltage that is about $1/3$ of the superconducting gap, $2\Delta_c$ for aluminum, greatly reducing the generation of quasiparticleas that can cause dissipation. Also at 25 mK, the SQUID line is fed through a copper-powder filter that attenuates signals above a few gigahertz. Further up at 4 K, the SQUID line splits into the V_{SQ} and $V_{SQ}^{readout}$ lines shown in Figure 4.2. Each of these two lines has a series $10\text{ k}\Omega$ resistance. At room temperature, the V_{SQ} line connects via a low-pass filter and a voltage divider into a low-noise DC bias source. The low-pass filter eliminates high frequency noise on this DC line. The $V_{SQ}^{readout}$ line is fed into an amplifier with a gain of 1000 that passes the amplified switching signal into another low-pass filter and comparator circuit.

B.1.2 The flux bias and measurement/z-pulse lines

Both the flux bias and measurement/z-pulse signals labeled as V_{bias} and V_Z in Figure 4.2, are applied to the same flux bias coil at the level of the qubit chip. As the flux bias signal leaves the qubit sample box, it enters a tee circuit which splits the line out into two separate lines: a microwave SMA coax line for the measurement/z-pulse line (V_Z) and a DC SMA coax line for the flux bias line (V_{bias}). The tee circuit is also at 25 mK and can be seen in Figure B.1. On the measurement/z-pulse line, there is one 10 dB, 50 Ω microwave attenuator on the bias tee, one 20 dB attenuator at the 25 mK plate and another 20 dB attenuator at 4 K. These attenuators reduce the thermally induced noise coming from the hotter stages of the refrigerator and from the room temperature electronics. At room temperature the measurement/z-pulse line connects to a digital-to-analog (DAC) board capable of sequencing arbitrary ns long pulses that will be briefly discussed below. When the flux bias part of the line (V_{bias}) exists the sample box, it gets passed through a copper-powder filter at 25mK that is identical to the one used for the SQUID line. Before connecting to a low-noise DC bias source, it also passes through a low-pass filter at 4K that has a series resistance of 1k Ω , as shown in Figure B.1.

B.1.3 The microwave line

On the actual chip, the microwave line labeled as $V_{\mu w}$ in Figure 4.2 is fed into the qubit using tapered microwave launchers that maintain a 50 Ω impedance as the size of the

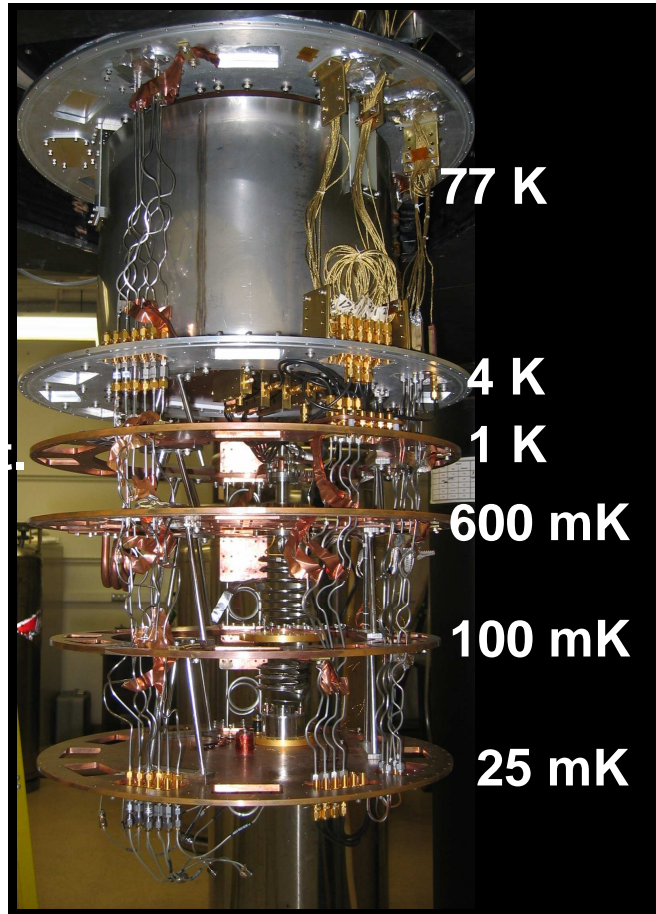


Figure B.2: A photograph of the actual dilution refrigerator that houses everything shown in Figure B.1. Radiation shields and vacuum cans have been removed for the photo and are not shown.

leads is reduced from that of the wirebond pad diameter to the $2\mu\text{m}$ microwave traces on-chip. From the chip, the microwave line is connected via SMA coax up through the various temperature stages of the dilution fridge and into a room temperature mixer that is used along with another room temperature DAC board to generate nanosecond microwave pulses with arbitrary phase and amplitude, as discussed in the next section.

Along the way however, the microwave line is attenuated once by 20 dB at 25 mK and again by 20 dB at 4 K to reduce noise injected at higher temperatures.

B.2 Room temperature electronics

The room temperature electronics for one qubit are schematically depicted in Figure B.3. Photos of the actual circuit boards and microwave components that make up the room temperature electronics are shown in Figure B.4. The flux bias and SQUID lines are controlled by 4 channel low-noise bias sources. As shown in Figure B.3, the measurement/z-pulse lines are pulsed using a 1 GHz DAC and filtered with a low-pass filter that rejects any frequencies above 200 MHz, to reduce the DAC clock feed-through and to produce a Nyquist filter.

The electronics used to generate microwave pulses with arbitrary frequency, phase, and amplitude are a little more complex and are found on a separate DAC board. An IQ mixer is used to generate the pulse where the I and Q values are set using 1 GHz DAC channels. A good discussion of IQ mixers and the basics of microwave electronics can be found in [64]. The 9 GHz low-pass prevents harmonics of the carrier frequency from reaching the qubit and exciting, the $0 \rightarrow 2$ transition. The microwave pulse frequency can be set in two ways. The easiest is to change the carrier frequency, however this method is not always practical, especially when controlling multiple qubits, because the same carrier signal is fed into multiple qubits to ensure phase stability across all

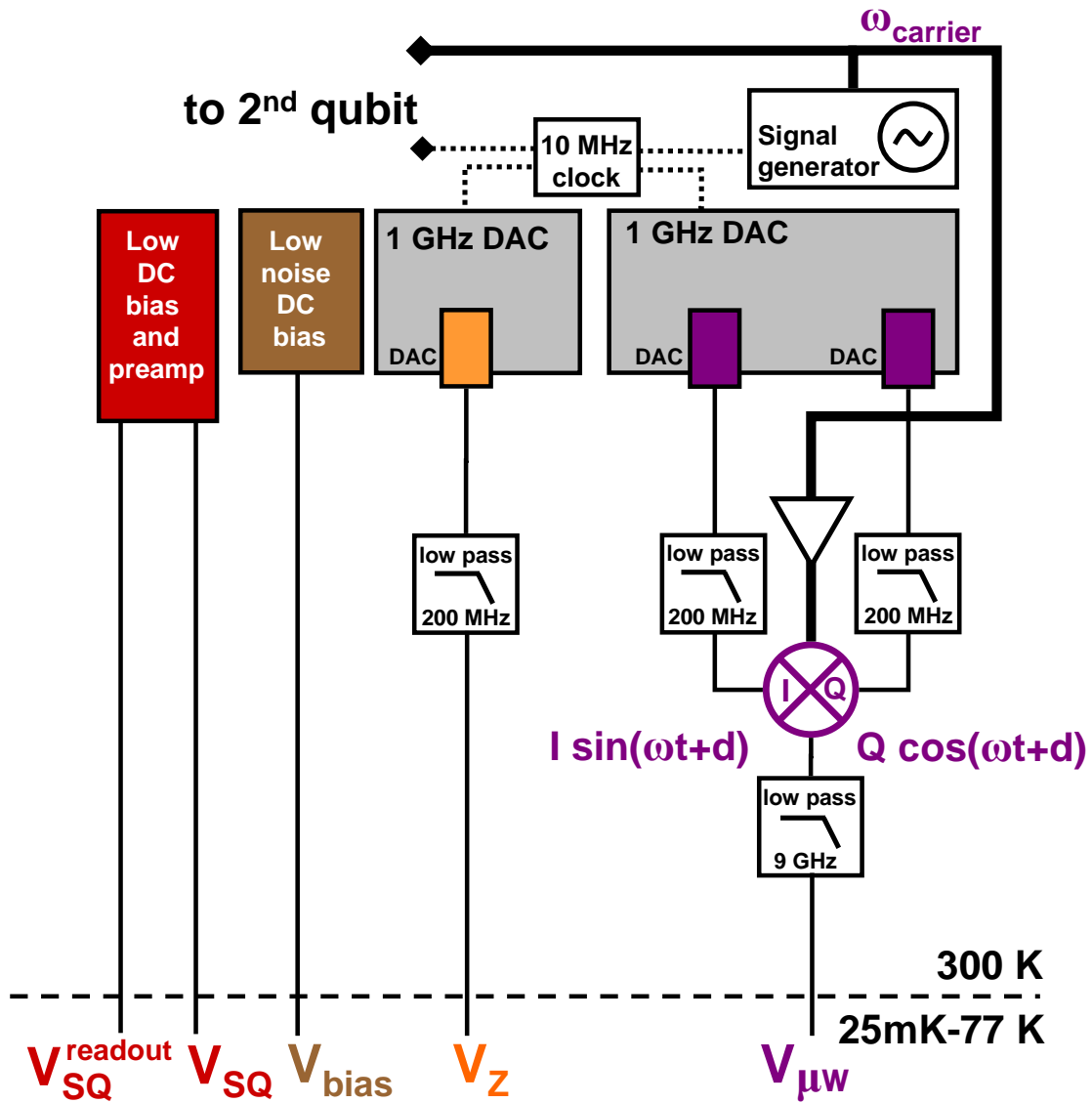
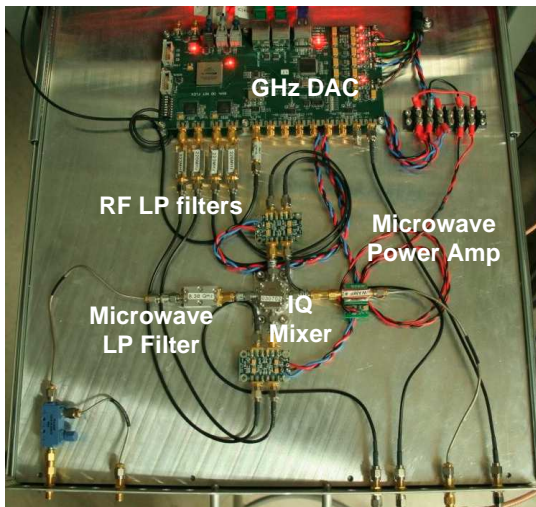


Figure B.3: Schematic depiction of the various components of the room temperature electronics needed to control a single qubit. The low-noise DC bias sources control the flux bias lines (V_{bias} and SQUID lines (V_{SQ} and $V_{\text{SQ}}^{\text{readout}}$). The 1 GHz Digital-to-Analog (DAC) board shape the pulses for the microwave lines ($V_{\mu w}$) and measurement/z-pulse lines (V_Z). The IQ Mixer gives us arbitrary phase and amplitude control for the microwave pulses as well as allowing us to perform sideband mixing to control the microwave pulse frequency [64].

qubits. Therefore we also control the microwave pulse frequency by sideband mixing using the IQ mixer [64]. Because there is one IQ mixer per qubit, this allows us to control the frequency of each qubit's pulses even when running multiple qubits at the same time from a single microwave generator.

The electronics hardware is controlled by a Python-based open-source software package called LabRAD, that was developed in-house and can be found at <http://sourceforge.net/projects/labrad/>.

a)



b)

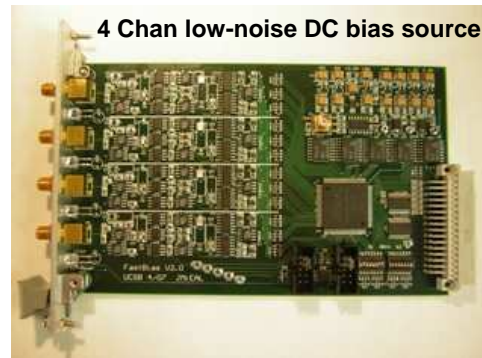


Figure B.4: Photographs of the actual circuit boards and components that make up **a)** the microwave electronics and **b)** the low-noise DC bias sources.

Appendix C

Calculation of capacitive coupling

Hamiltonian

Here we include a Mathematica notebook where we have calculated the interaction term for the Hamiltonian for two capacitively coupled qubits as depicted in Figure [5.1](#). The calculation also shows the transformation to the rotating frame of the microwave source. The comments in the Mathematica notebook include explanations behind most of the steps.

(* §1 Some definitions *)

$n \in \{a, b\}$, $a \equiv \text{qubit } a$, $b \equiv \text{qubit } b$

$$E_C = e_{e_-}^2 / (2 * C_J);$$

$$E_J = (I_C * \hbar) / (2 * e_{e_-});$$

$$\zeta = C_C / (C_C + C_J);$$

$$I_C = \left(\frac{2 e_{e_-}}{\hbar} \right) * E_J;$$

$$\phi_n = (\hbar * \gamma_n) / (2 * e_{e_-});$$

$$p_n = (\hbar * q_n) / (2 * e_{e_-});$$

$$\Rightarrow p_n = (\hbar_0 / 2 * \pi)^2 C_J * \gamma;$$

(* §2 Lagrangian for the capacitively coupled circuit.. see Devoret

"Quantum Fluctuations..." writeup for the general technique*)

(*Note: if want to use this as executable Mathematica code, then be aware that I is treated by Mathematica as Sqrt[-1]*)

$$L = \frac{C_C}{2} (\phi_a - \phi_b)^2 + \frac{C_J}{2} (\phi_a)^2 + \frac{C_J}{2} (\phi_b)^2 - \left(-I_a \phi_a - E_J \text{Cos} \left[\left(\frac{2 e_{e_-}}{\hbar} \right) * \phi_a \right] - I_b \phi_b - E_J \text{Cos} \left[\left(\frac{2 e_{e_-}}{\hbar} \right) * \phi_b \right] \right);$$

$$\text{Using definitions from §1} \Rightarrow L = \frac{C_C}{2} (\phi_a - \phi_b)^2 + \frac{C_J}{2} (\phi_a)^2 + \frac{C_J}{2} (\phi_b)^2 + E_J \left(\frac{I_a}{I_C} \gamma_a + \frac{I_b}{I_C} \gamma_b + \text{Cos}[\gamma_a] + \text{Cos}[\gamma_b] \right);$$

(*Now, following Devoret's method:*)

$$q_a = \frac{\partial L}{\partial \phi_a} = C_C (\phi_a - \phi_b) + C_J \phi_a = (C_C + C_J) \phi_a - (C_C \phi_b);$$

$$q_b = \frac{\partial L}{\partial \phi_b} = C_C (\phi_b - \phi_a) + C_J \phi_b = (C_C + C_J) \phi_b - (C_C \phi_a);$$

$$\Rightarrow \phi_a = \frac{(C_C + C_J) q_a}{(2 C_C C_J + C_J^2)} + \frac{C_C q_b}{(2 C_C C_J + C_J^2)};$$

$$\Rightarrow \phi_b = \frac{C_C q_a}{(2 C_C C_J + C_J^2)} + \frac{(C_C + C_J) q_b}{(2 C_C C_J + C_J^2)};$$

(* §3 Now can write down the Hamiltonian*)

$$H = \sum_n q_n \phi_n - L = T + U$$

$$\Rightarrow H = \frac{C_C}{2} \left(\frac{C_J q_a}{(2 C_C C_J + C_J^2)} - \frac{C_J q_b}{(2 C_C C_J + C_J^2)} \right)^2 + \frac{C_J}{2} \left(\frac{(C_C + C_J) q_a}{(2 C_C C_J + C_J^2)} + \frac{C_C q_b}{(2 C_C C_J + C_J^2)} \right)^2 + \frac{C_J}{2} \left(\frac{C_C q_a}{(2 C_C C_J + C_J^2)} + \frac{(C_C + C_J) q_b}{(2 C_C C_J + C_J^2)} \right)^2 - E_J \left(\frac{I_a}{I_C} \gamma_a + \frac{I_b}{I_C} \gamma_b + \text{Cos}[\gamma_a] + \text{Cos}[\gamma_b] \right);$$

$$\Rightarrow H = \frac{C_C (q_a + q_b)^2 + C_J (q_a^2 + q_b^2)}{2 (2 C_C C_J + C_J^2)} - E_J \left(\frac{I_a}{I_C} \gamma_a + \frac{I_b}{I_C} \gamma_b + \text{Cos}[\gamma_a] + \text{Cos}[\gamma_b] \right);$$

(* Note: let $U \equiv -E_J \left(\frac{I_a}{I_C} \gamma_a + \frac{I_b}{I_C} \gamma_b + \text{Cos}[\gamma_a] + \text{Cos}[\gamma_b] \right)$ and using the definitions from §1*)

$$H = \frac{C_C (q_a + q_b)^2 + C_J (q_a^2 + q_b^2)}{2 (2 C_C C_J + C_J^2)} + U;$$

$$\Rightarrow H = \frac{(C_C + C_J) q_a^2 + (C_C + C_J) q_b^2 + 2 C_C q_a q_b}{2 (2 C_C C_J + C_J^2)} + U;$$

$$\Rightarrow H = \frac{(C_C + C_J) q_a^2}{2 (2 C_C C_J + C_J^2)} + \frac{(C_C + C_J) q_b^2}{2 (2 C_C C_J + C_J^2)} + \frac{C_C q_a q_b}{(2 C_C C_J + C_J^2)} + U;$$

$$\Rightarrow H = \frac{q_a^2}{2 C_J (1 + \zeta)} + \frac{q_b^2}{2 C_J (1 + \zeta)} + \frac{C_C q_a q_b}{C_J (C_C + C_J) (1 + \zeta)} + U;$$

$$\Rightarrow H = \frac{E_C q_a^2}{(e_{e_-})^2 (1 + \zeta)} + \frac{E_C q_b^2}{(e_{e_-})^2 (1 + \zeta)} + \frac{2 E_C \zeta q_a q_b}{(1 + \zeta)} + U;$$

$$\Rightarrow H = \frac{E_C \left(\frac{2 e_{e_-}}{\hbar} \right)^2 p_a^2}{(e_{e_-})^2 (1 + \zeta)} + \frac{E_C \left(\frac{2 e_{e_-}}{\hbar} \right)^2 p_b^2}{(e_{e_-})^2 (1 + \zeta)} + \frac{2 E_C \zeta p_a p_b}{(e_{e_-})^2 (1 + \zeta)} \left(\frac{2 e_{e_-}}{\hbar} \right)^4 + U;$$

$$\Rightarrow H = \left(\frac{4 E_C}{(1 + \zeta) \hbar^2} \right) (p_a^2 + p_b^2 + 2 \zeta p_a p_b) - E_J \left(\frac{I_a}{I_C} \gamma_a + \frac{I_b}{I_C} \gamma_b + \text{Cos}[\gamma_a] + \text{Cos}[\gamma_b] \right);$$

(*This agrees with eqn. 3 in paper by Johnson et. al.: PRB 67 020509 (R) 2003*)

(* §4 SHO Approximation of interaction term *)

(* for a SHO: $x = \sqrt{\frac{\hbar}{2m\omega}} (a+a^\dagger) \equiv \frac{x_0}{\sqrt{2}} (a+a^\dagger)$ and $p = \hbar \sqrt{\frac{m\omega}{2}} (a^\dagger - a) \equiv \frac{\hbar p_0}{\sqrt{2}} (a^\dagger - a)$ where $[a, a^\dagger] = 1$ So: *)

$$x_n = \frac{x_0}{\sqrt{2}} (a_n + a_n^\dagger);$$

$$p_n = \frac{\hbar p_0}{\sqrt{2}} (a_n^\dagger - a_n);$$

(* from §3, the interaction term is: *)

$$H_{\text{int}} = \left(\frac{8 \zeta E_c}{(1+\zeta) \hbar^2} \right) p_a p_b;$$

$$\Rightarrow H_{\text{int}} = \left(\frac{4 \zeta E_c p_{0a} p_{0b}}{(1+\zeta) \hbar^2} \right) (a_n^\dagger - a_n) (a_b^\dagger - a_b);$$

(* Now let $a_n^\dagger \equiv \sigma^+ = \begin{pmatrix} 0 & 1 \\ 0 & 0 \end{pmatrix}$ $a_n \equiv \sigma^- = \begin{pmatrix} 0 & 0 \\ 1 & 0 \end{pmatrix}$ *)

$$\Rightarrow a_n^\dagger - a_n = \begin{pmatrix} 0 & 1 \\ -1 & 0 \end{pmatrix} = \hbar \sigma_{Yn};$$

$$\Rightarrow \hbar * (a_b^\dagger - a_b) = \sigma_{Yb};$$

$$\Rightarrow H_{\text{int}} = \left(\frac{4 \zeta E_c p_{0a} p_{0b}}{(1+\zeta) \hbar^2} \right) \sigma_{Ya} \sigma_{Yb} \stackrel{c_J \gg c_C}{\approx} -\frac{C_c}{2 C_J} \hbar \sqrt{\omega_a \omega_b} \sigma_{Ya} \sigma_{Yb};$$

(* §5 Moving to rotating frame *)

$$\text{Let } H_{\text{int}} = \left(\frac{4 \zeta E_c p_{0a} p_{0b}}{(1+\zeta) \hbar^2} \right) \sigma_{Ya} \sigma_{Yb} \equiv g \sigma_{Ya} \sigma_{Yb};$$

(* Note that: $\sigma_Y = \frac{\hbar}{2} (\sigma^+ - \sigma^-)$ and $\sigma_X = \frac{1}{2} (\sigma^+ + \sigma^-)$ *)

$$\sigma_{Ya} \sigma_{Yb} = \frac{\hbar}{2} (\sigma_a^+ - \sigma_a^-) \frac{\hbar}{2} (\sigma_b^+ - \sigma_b^-);$$

$$\Rightarrow \sigma_{Ya} \sigma_{Yb} = -\frac{1}{4} (\sigma_a^+ \sigma_b^+ - \sigma_a^+ \sigma_b^- - \sigma_a^- \sigma_b^+ + \sigma_a^- \sigma_b^-);$$

(* Now to go to the rotating frame must set: *)

$$\sigma_a^+ \rightarrow \sigma_a^+ \text{Exp} \left[\pm \frac{\hbar \omega_{a01} t}{\hbar} \right];$$

$$\sigma_b^+ \rightarrow \sigma_b^+ \text{Exp} \left[\pm \frac{\hbar \omega_{b01} t}{\hbar} \right];$$

(* Plugging this into H_{int} *)

$$H_{\text{int}} = g \sigma_{Ya} \sigma_{Yb} = -\frac{g}{4} (\sigma_a^+ \text{Exp}[\hbar \omega_{a01} t] \sigma_b^+ \text{Exp}[\hbar \omega_{b01} t] - \sigma_a^+ \text{Exp}[\hbar \omega_{a01} t] \sigma_b^- \text{Exp}[-\hbar \omega_{b01} t]$$

$$- \sigma_a^- \text{Exp}[-\hbar \omega_{a01} t] \sigma_b^+ \text{Exp}[\hbar \omega_{b01} t] + \sigma_a^- \text{Exp}[-\hbar \omega_{a01} t] \sigma_b^- \text{Exp}[-\hbar \omega_{b01} t]);$$

(* Now if qubits are approximately on resonance $\omega_{a01} \approx \omega_{b01} = \omega_{01}$ so the above becomes: *)

$$\Rightarrow H_{\text{int}} = -\frac{g}{4} (\sigma_a^+ \sigma_b^+ \text{Exp}[2 \hbar \omega_{01} t] - \sigma_a^+ \sigma_b^- - \sigma_a^- \sigma_b^+ + \sigma_a^- \sigma_b^- \text{Exp}[-2 \hbar \omega_{01} t]);$$

(* ... and if make the RWA and ignore the fast oscillating $\text{Exp}[-2 \hbar \omega_{01} t]$ terms *)

$$\Rightarrow H_{\text{int}} \approx \frac{g}{4} (\sigma_a^+ \sigma_b^- + \sigma_a^- \sigma_b^+);$$

(* Also, noting that: *)

$$\sigma_{Ya} \sigma_{Yb} = -\frac{1}{4} (\sigma_a^+ \sigma_b^+ - \sigma_a^+ \sigma_b^- - \sigma_a^- \sigma_b^+ + \sigma_a^- \sigma_b^-);$$

$$\sigma_{Xa} \sigma_{Xb} = \frac{(\sigma_a^+ + \sigma_a^-)}{2} \frac{(\sigma_b^+ + \sigma_b^-)}{2} = \frac{1}{4} (\sigma_a^+ \sigma_b^+ + \sigma_a^+ \sigma_b^- + \sigma_a^- \sigma_b^+ + \sigma_a^- \sigma_b^-);$$

$$\Rightarrow \sigma_{Xa} \sigma_{Xb} + \sigma_{Ya} \sigma_{Yb} = \frac{1}{2} (\sigma_a^+ \sigma_b^- + \sigma_a^- \sigma_b^+)$$

(* So that in the rotating frame and assuming RWA, H_{int} is given by an XX + YY coupling hamiltonian: *)

$$\Rightarrow H_{\text{int}} \approx \frac{g}{2} (\sigma_{Xa} \sigma_{Xb} + \sigma_{Ya} \sigma_{Yb});$$

Appendix D

Quantum Tomography calibrations and physicality

D.1 Calibrating out measurement errors

The origin of measurement errors in this experiment is understood as discussed in Chapters 4 and 5 and because the errors vary in a predictable way with parameters and biasing, they can be reliably removed using calibration procedures. The two dominant error mechanisms are measurement crosstalk and measurement fidelity. Defining the measurement probabilities P_{AB} of qubits A and B with the column vector $(P_{00}, P_{01}, P_{10}, P_{11})^T$, the intrinsic (actual) probabilities P_i will give measured probabilities P_m according to the matrix equation $P_m = XFP_i$, where X and F are the correction matrices for measure-

ment crosstalk and fidelity, respectively. The order of the matrices reflects the fact that errors in fidelity generate crosstalk (see below). By measuring the correction matrices, the intrinsic probabilities can be calculated from the measured values by the inverted relation $P_i = F^{-1}X^{-1}P_m$.

The procedure for calibrating measurement fidelity for single qubits has been discussed previously in reference [74]. Defining f_0 and f_1 as the probabilities to correctly identify the state as $|0\rangle$ and $|1\rangle$, respectively, the measurement fidelity matrix for two qubits is given by

$$\begin{aligned}
F &= \begin{bmatrix} f_0 & 1-f_1 \\ 1-f_0 & f_1 \end{bmatrix}_A \otimes \begin{bmatrix} f_0 & 1-f_1 \\ 1-f_0 & f_1 \end{bmatrix}_B \quad (\text{D.1}) \\
&= \begin{bmatrix} f_{0A}f_{0B} & f_{0A}(1-f_{1B}) & (1-f_{1A})f_{0B} & (1-f_{1A})(1-f_{1B}) \\ f_{0A}(1-f_{0B}) & f_{0A}f_{1B} & (1-f_{1A})(1-f_{0B}) & (1-f_{1A})f_{1B} \\ (1-f_{0A})f_{0B} & (1-f_{0A})(1-f_{1B}) & f_{1A}f_{0B} & f_{1A}(1-f_{1B}) \\ (1-f_{0A})(1-f_{0B}) & (1-f_{0A})f_{1B} & f_{1A}(1-f_{0B}) & f_{1A}f_{1B} \end{bmatrix}
\end{aligned}$$

We measure these fidelities by biasing only one qubit into operation, and then measuring the tunneling probabilities for the $|0\rangle$ and $|1\rangle$ states, with the latter produced by a microwave π -pulse optimized for the largest tunneling probability. This calibration depends on accurately producing a π pulse, which we have demonstrated can be done with 98% accuracy. The 2% error arises from T_1 energy decay, which can be measured and corrected for in the calibration [47].

Measurement crosstalk for two capacitively coupled Josephson phase qubits has been studied and understood in previous work [54]. As mentioned in Chapter 5, for

this mechanism, crosstalk contributes when one qubit state is measured as $|1\rangle$, causing the other qubit state, when in the $|0\rangle$ state, to have probability x to be excited and thus measured in the $|1\rangle$ state. The matrix describing measurement crosstalk for both qubits is thus

$$X = \begin{bmatrix} 1 & 0 & 0 & 0 \\ 0 & 1 - x_{BA} & 0 & 0 \\ 0 & 0 & 1 - x_{AB} & 0 \\ 0 & x_{BA} & x_{AB} & 1 \end{bmatrix} \quad (\text{D.2})$$

where x_{AB} (x_{BA}) is the probability of the $|1\rangle$ state of qubit A (qubit B) exciting a $0 \rightarrow 1$ transition on qubit B (qubit A).

The two unknowns in the X matrix can be directly determined from the 3 independent equations in $P_m = X(FP_i)$, where FP_i is obtained from the F matrix calibration procedure described above.

A more robust method is to compare the differences in tunneling of the first qubit caused by a change in tunneling of the second. From the four measurement probabilities P_{00} , P_{01} , P_{10} , and P_{11} , we extract for each qubit independent probabilities to be in the $|1\rangle$ state by performing a partial trace over the other qubit

$$\begin{aligned} P_{1A} &\equiv P_{10} + P_{11} \\ P_{1B} &\equiv P_{01} + P_{11} \end{aligned} \quad (\text{D.3})$$

We measure $P_{1A}(00)$ and $P_{1B}(01)$ for the two cases where we prepare the initial

states $|00\rangle$ and $|01\rangle$, respectively. Using the correction matrices for X and F , we calculate

$$\frac{P_{1A}(01) - P_{1A}(00)}{P_{1B}(01) - P_{1B}(00)} = \frac{f_{0A}}{1 - (1 - f_{0A})x_{AB}} x_{BA} \simeq f_{0A} x_{BA} \quad (\text{D.4})$$

where the approximate result arises from neglecting both correction terms in the denominator, since $1 - f_{0A}$ and x_{BA} , are both small. This result holds even if the states $|00\rangle$ and $|01\rangle$ are not prepared perfectly, as we calculate the ratio of the change in probabilities. A similar result for $f_{0B}x_{AB}$ is obtained for the initial states $|00\rangle$ and $|10\rangle$.

We also perform a consistency check on the measurements of x_{AB} and x_{BA} for the simple case of measuring only the $|00\rangle$ state when $f_{0A}, f_{0B} \neq 0$. Here, a general solution is not possible as there are four unknowns f_{0A} , f_{0B} , x_{AB} , and x_{BA} and only three equations for the probabilities. However, by assuming a fixed ratio between the two crosstalk parameters $k = x_{BA}/x_{AB}$, a solution can be found:

$$x_{AB} = \frac{P_{00} + kP_{00} - k + kP_{10} + P_{01} - 1}{2k(P_{00} - 1)} - \frac{\sqrt{((1 - P_{00} - P_{01}) - k(1 - P_{00} - P_{10}))^2 + 4kP_{10}P_{01}/P_{00}}}{2k(P_{00} - 1)} \quad (\text{D.5})$$

For a typical device measured in this thesis, the measurement fidelities were near unity: $f_{0A} = 0.95$ and $f_{1A} = 0.95$ for qubit A, and $f_{0B} = 0.93$ and $f_{1B} = 0.93$ for qubit B. Using the P_{11} probability in the capacitively coupled qubit swap experiments, crosstalk

was measured to be $x_{AB} = x_{BA} = 0.117$.

D.2 State tomography data and measurement calibration

This section contains the density matrix data obtained from state tomography of the 16 two-qubit basis states used as input to our SQiSW gate, and from the state tomography of the output density matrices after the action of the SQiSW gate. Again the $\{H, V, D, R\}$ shorthand is defined in the table shown in Figure 5.10. Figure D.1 shows the 16 input state density matrices experimentally obtained using quantum state tomography and without measurement errors calibrated out. Figure D.2 shows the 16 SQiSW gate output state density matrices experimentally obtained using quantum state tomography and without measurement errors calibrated out.

D.3 Physicality of the χ Matrix

We define the original χ matrix data as χ_e , and the data with measurement effects calibrated out as χ_m . Plots of χ_e and χ_m are shown Figures D.3 and D.4 respectively; some small negative eigenvalues are found for this data, which implies it is unphysical. To be physical, the experimentally obtained matrix must be a positive and trace preserving map. The closest physical estimates to these matrices given these constraints are χ_e^p

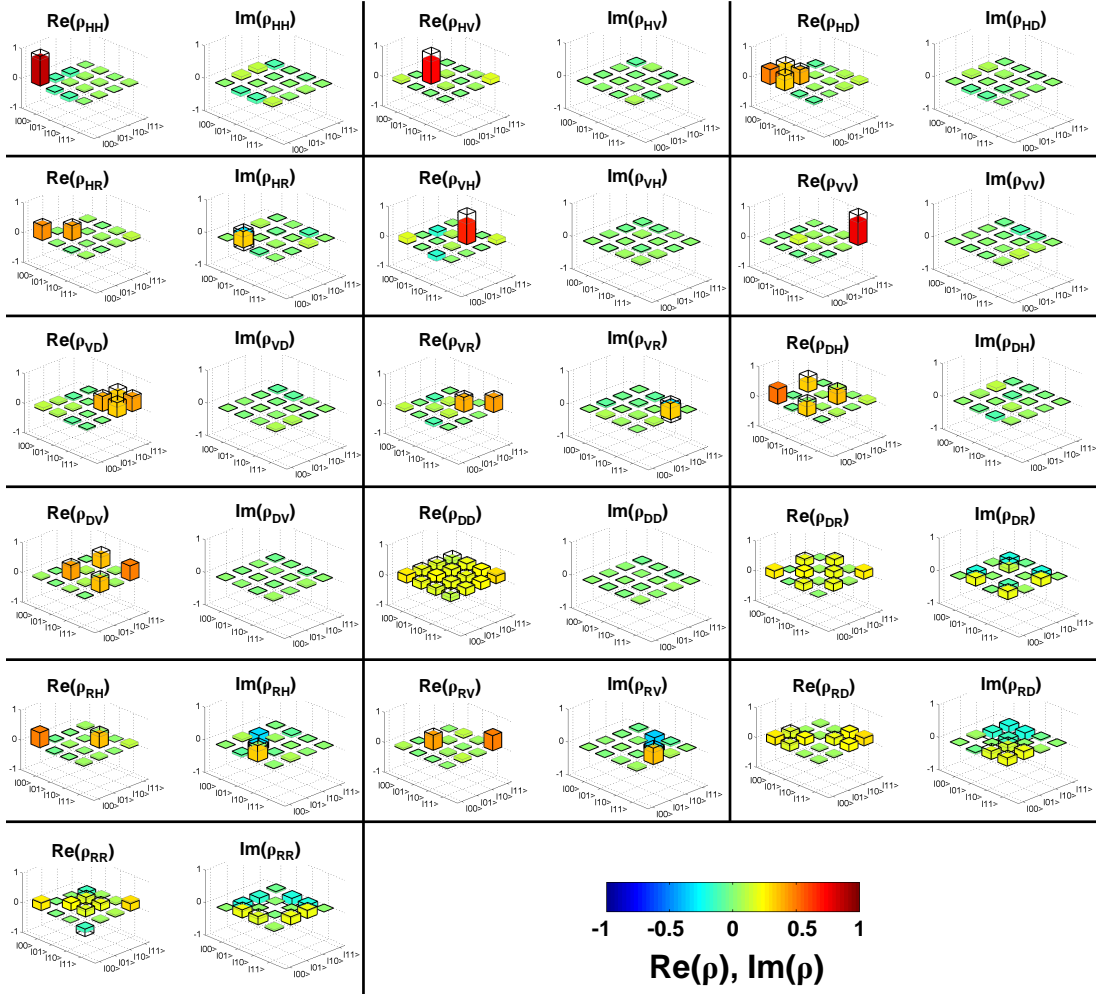


Figure D.1: The full set of density matrices for the 16 two-qubit basis states as obtained via state tomography. Measurement errors have not been calibrated out from this data set.

and χ_m^P , as shown in Figure D.5 and in Figure 6.5 of the main paper, respectively.

To perform the physical estimation, we used the MATLAB packages YALMIP (<http://users.isy.liu.se/johanl/yalmip/>) and SeDuMi (<http://sedumi.ie.lehigh.edu/>) to perform a semidefinite programming convex optimization. We find the physical χ matrix that best approximates our measured, unphysical χ matrix. Math-

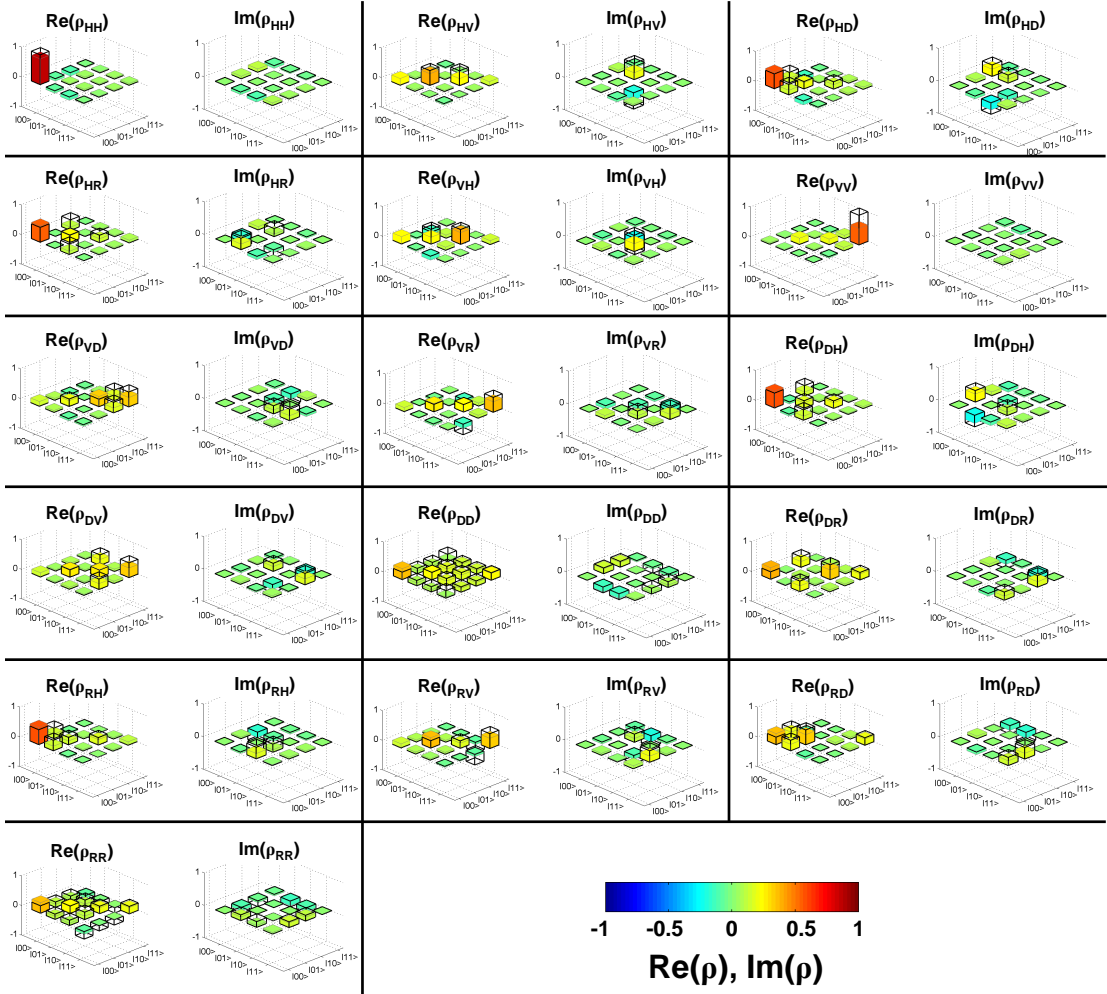


Figure D.2: The full set of density matrices, obtained via state tomography, for the output states produced by the action of the SQiSW gate on the 16 two-qubit basis states. Measurement errors have not been calibrated out from this dataset.

ematically, for the experimentally obtained χ matrix and the physical approximation χ^P , we minimize the two-norm distance $\|\chi^P - \chi\|_2 \equiv \sqrt{\text{tr}\{(\chi^P - \chi)^2\}}$ with the constraints that χ^P be CPTP. The source code for the convex optimization is included at the end of this appendix.

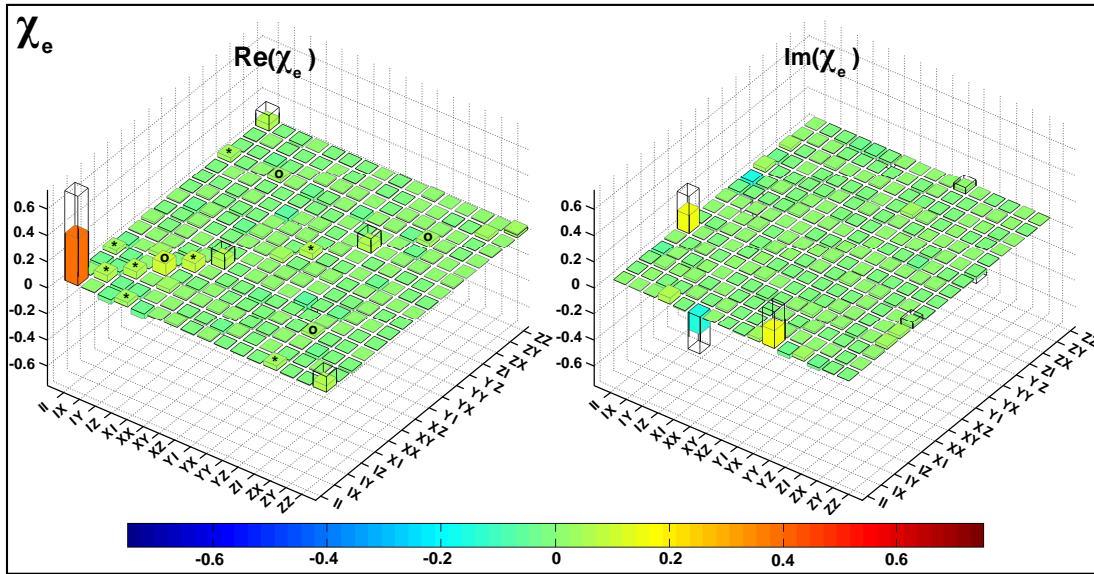


Figure D.3: The unphysical experimental χ matrix where measurement errors have not been calibrated out.

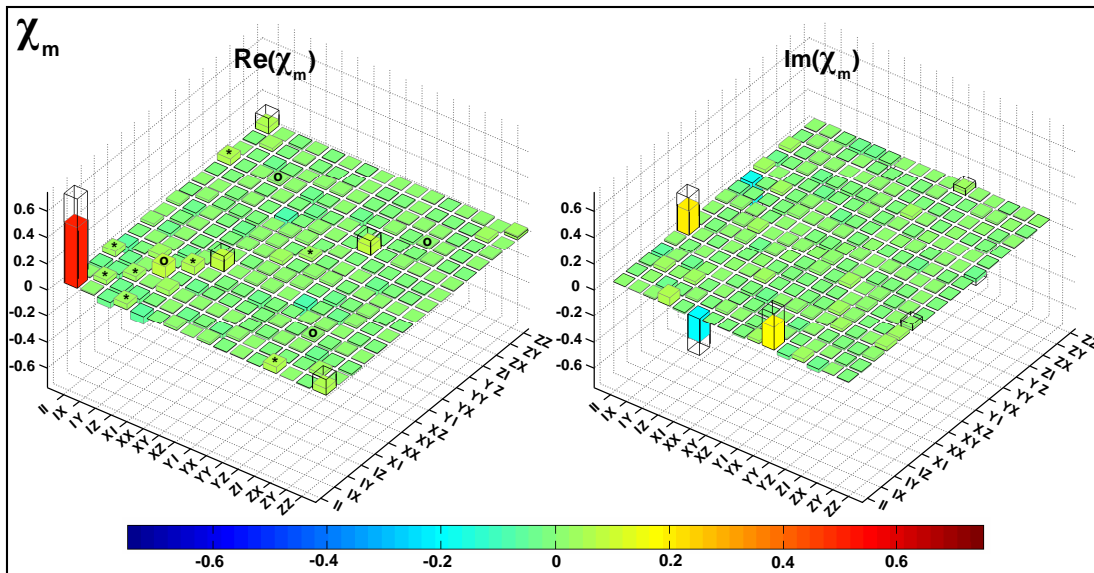


Figure D.4: The χ matrix where measurement errors have been calibrated out, but the matrix is still unphysical.

As in reference [60], we then histogrammed the differences Δ_p between the peak heights of χ_e and χ_e^p for the real parts of each of the 256 matrix elements. We fit a Gaussian, $\gamma e^{-\Delta_p^2/\sigma^2}$ to the histogram and obtained a sense of the relative error of the process tomography from its width σ . We repeated this procedure also for χ_m^p , and plotted these histograms and fits for χ_m^p and χ_m^p as shown in Figures D.6a and b. The fidelities of the above mentioned χ matrices are:

$$\text{Tr}(\chi_t \chi_e^p) = 0.49 \quad (\text{D.6})$$

$$\text{Tr}(\chi_t \chi_m^p) = 0.61 \quad (\text{D.7})$$

$$\text{Tr}(\chi_t \chi_e) = 0.51 \quad (\text{D.8})$$

$$\text{Tr}(\chi_t \chi_m) = 0.65 \quad (\text{D.9})$$

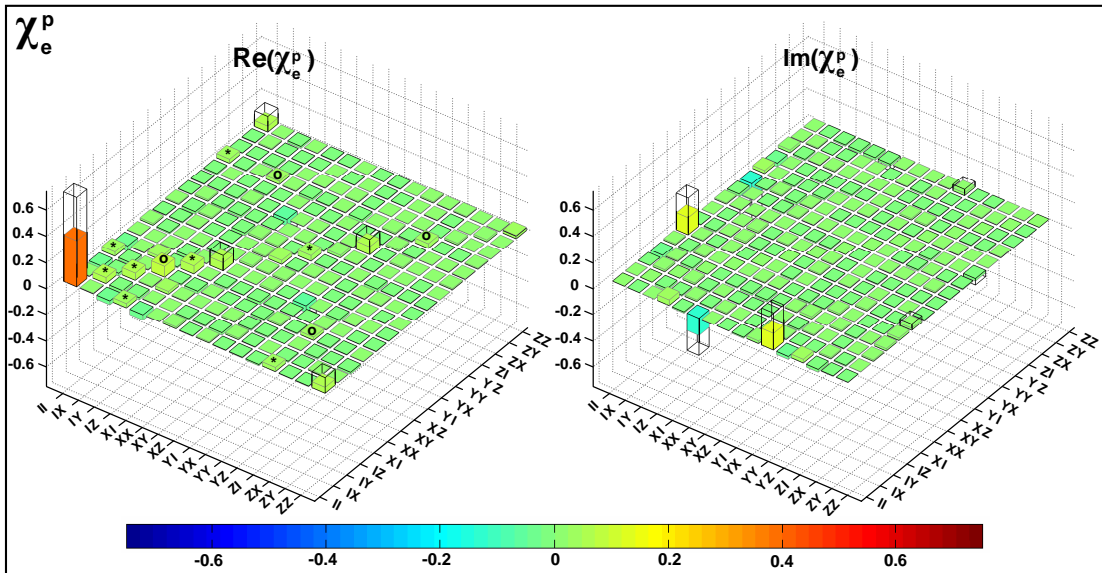


Figure D.5: The closest physical approximation to the experimentally obtained χ matrix where measurement errors have not been calibrated out.

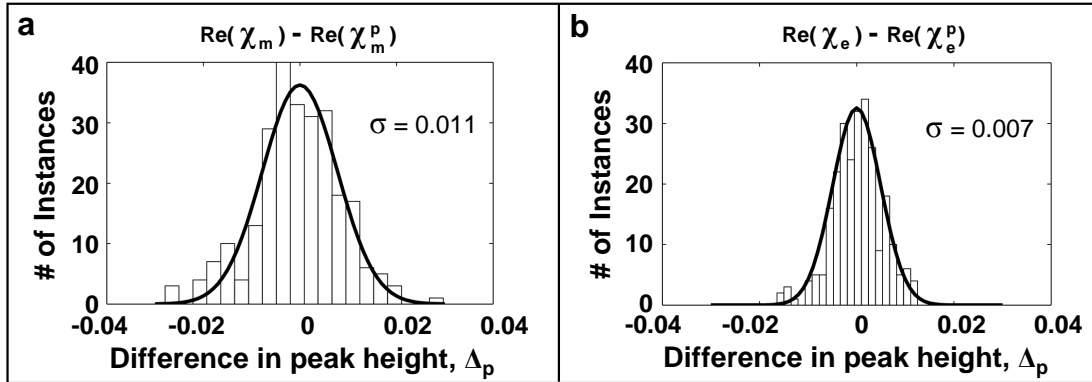


Figure D.6: In order to check that the physical approximations to the unphysical experimental χ matrices are accurate, we take the absolute value of the difference between an element of the unphysical χ matrix and the same element in the χ matrix that is the physical approximation. We do this for all elements and plot these differences, Δ_p , as a histogram. The small spread, σ , about $\Delta_p = 0$ indicates a good approximation.

D.4 MATLAB and Mathematica code used for state tomography analysis

D.4.1 State tomography pre-processing using Mathematica

The code for tomography is broken up into two parts. The first part requires symbolic manipulation, which is best done in Mathematica. The second part involves processing the actual experimental data and numerics therefore it is done in MATLAB. We begin with the Mathematica code. Mathematica comments are enclosed in “(*...*)” and the code comments contain the information necessary to understand the analysis. Much of the state tomography code is based on work by Matthias Steffen [73].

To obtain the density matrix from the state tomography data we first perform sym-

bolic manipulation on a parametrized density matrix using Mathematica. We parametrize a density matrix for any general state as

$$\rho = \begin{bmatrix} r_{11} & r_{12} & r_{13} & r_{14} \\ r_{21} & r_{22} & r_{23} & r_{24} \\ r_{31} & r_{32} & r_{33} & r_{34} \\ r_{41} & r_{42} & r_{43} & r_{44} \end{bmatrix} \quad (\text{D.10})$$

Using Mathematica, we symbolically operate on (D.10) using the tomography pulses $\{X, Y, I\}$ and obtain a set of 9 resulting density matrices $\{X\rho X^\dagger, X\rho Y^\dagger, X\rho I^\dagger, Y\rho X^\dagger, Y\rho Y^\dagger, Y\rho I^\dagger, I\rho X^\dagger, I\rho Y^\dagger, I\rho I^\dagger\}$ as shown in the source code in Figure D.8. As shown in Figure D.9, from each member of this set of 9 density matrices, we extract the 3 elements that correspond to the probabilities P_{01}, P_{10}, P_{11} . These elements give us the probabilities P_{01}, P_{10}, P_{11} as a function of the parameters r_{mn} in (D.10). So we have a total of 27 equations in terms of the 16 unknowns, r_{mn} , as shown in the source code in Figure D.10. We set each of these equal to the probabilities obtained in the actual state tomography experiment and perform a least squares fit to obtain the closest set of values r_{mn} to the experimental data (see Figures D.11 and D.12). The actual least squares fit is done using MATLAB as shown in Figures D.13 to D.17. Figures D.13 to D.16 define some of the variables obtained from the Mathematica calculation and read in and parse the experimental data from disk. The data is stored as time traces of the probabilities P_{01}, P_{10}, P_{11} as a function of the measurement time t_{meas} . The values of P_{01}, P_{10}, P_{11} used in the tomography analysis occur right after the tomography pulses,

at a time $t_{meas} = tomoTime$. Also the P_{01} , P_{10} , P_{11} probabilities in the data are stored as numbers 0 to 100 and not 0 to 1 therefore division by 100 is needed, as done in the code. Figure D.17 contains the code for the least squares fit and uses the MATLAB *mldivide* command to find the least squares solution.

```
<< LinearAlgebra`MatrixManipulation`

Off[General::spell];

(*define kronecker product operation*)
MatrixDirectProduct[a_List?MatrixQ, b_List?MatrixQ] := BlockMatrix[Outer[Times, a, b]]

(*define form of single qubit density matrices*)
Clear[X, Y, Z];

$$\rho_A = \begin{pmatrix} a_1 & c_1 + I * d_1 \\ c_1 - I * d_1 & b_1 \end{pmatrix};$$


$$\rho_B = \begin{pmatrix} a_2 & c_2 + I * d_2 \\ c_2 - I * d_2 & b_2 \end{pmatrix};$$


(*define single qubit rotation matrices*)

$$R_x[\theta_] := \begin{pmatrix} \text{Cos}[\theta/2] & -I \text{Sin}[\theta/2] \\ -I \text{Sin}[\theta/2] & \text{Cos}[\theta/2] \end{pmatrix}$$


$$R_y[\theta_] := \begin{pmatrix} \text{Cos}[\theta/2] & -\text{Sin}[\theta/2] \\ \text{Sin}[\theta/2] & \text{Cos}[\theta/2] \end{pmatrix}$$


$$R_z[\theta_] := \begin{pmatrix} \text{Exp}[-I \theta/2] & 0 \\ 0 & \text{Exp}[I \theta/2] \end{pmatrix}$$


(* define X,Y,Z rotations *)
Y = R_x[-π/2];
Y // MatrixForm
X = R_y[π/2];
X // MatrixForm
Z = R_z[0];
Z // MatrixForm
(*define two-qubit density matrix: ρ = ρ_A⊗ρ_B, but it's better to express ρ as ρ =

$$\begin{pmatrix} \rho_{11} & \rho_{12} & \rho_{13} & \rho_{14} \\ \rho_{21} & \rho_{22} & \rho_{23} & \rho_{24} \\ \rho_{31} & \rho_{32} & \rho_{33} & \rho_{34} \\ \rho_{41} & \rho_{42} & \rho_{43} & \rho_{44} \end{pmatrix}$$
 since will need to do a least squares fit to find the 16-1=15 parameters of ρ
so don't want them in terms of parameters of ρ_A and ρ_B to minimize the number of variables*)


$$\rho = \begin{pmatrix} r_{11} & r_{12} & r_{13} & r_{14} \\ r_{21} & r_{22} & r_{23} & r_{24} \\ r_{31} & r_{32} & r_{33} & r_{34} \\ r_{41} & r_{42} & r_{43} & r_{44} \end{pmatrix};$$

```

Figure D.7: First we initialize some variables and definitons that will be used later.

```
(*define density matrices for the results of
  applying the set of tomography pulses on the two-qubit state  $\rho$ . *)

 $\rho_{XX}$  = MatrixDirectProduct[X, X]. $\rho$ .MatrixDirectProduct[X, X]H;
 $\rho_{XY}$  = MatrixDirectProduct[X, Y]. $\rho$ .MatrixDirectProduct[X, Y]H;
 $\rho_{XZ}$  = MatrixDirectProduct[X, Z]. $\rho$ .MatrixDirectProduct[X, Z]H;
 $\rho_{YX}$  = MatrixDirectProduct[Y, X]. $\rho$ .MatrixDirectProduct[Y, X]H;
 $\rho_{YY}$  = MatrixDirectProduct[Y, Y]. $\rho$ .MatrixDirectProduct[Y, Y]H;
 $\rho_{YZ}$  = MatrixDirectProduct[Y, Z]. $\rho$ .MatrixDirectProduct[Y, Z]H;
 $\rho_{ZX}$  = MatrixDirectProduct[Z, X]. $\rho$ .MatrixDirectProduct[Z, X]H;
 $\rho_{ZY}$  = MatrixDirectProduct[Z, Y]. $\rho$ .MatrixDirectProduct[Z, Y]H;
 $\rho_{ZZ}$  = MatrixDirectProduct[Z, Z]. $\rho$ .MatrixDirectProduct[Z, Z]H;
```

Figure D.8: Now we mimic how a general two-qubit state would be transformed by the various tomography pulses.

```

(* Now calculate get the two-
qubit probabilities for each of the states defined by the above density matrices. So now have 36
measurements 27 of which are unique. Below  $P_{\alpha\beta}^{ij}$  is defined as:  $P_{\alpha\beta}^{ij} \equiv \langle ij | \rho_{\alpha\beta} | ij \rangle$ . Where  $\alpha$ ,
 $\beta = \{X,Y,Z\}$ . In terms of our set-up, we'll have to do 9 sweeps... because we collect  $P_{\alpha\beta}^{01}$ ,
 $P_{\alpha\beta}^{10}$ ,  $P_{\alpha\beta}^{11}$  during each sweep. *)

P00XX = Simplify[ $\rho_{XX}$  [[1, 1]]]
P01XX = Simplify[ $\rho_{XX}$  [[2, 2]]]
P10XX = Simplify[ $\rho_{XX}$  [[3, 3]]]
P11XX = Simplify[ $\rho_{XX}$  [[4, 4]]]

P00XY = Simplify[ $\rho_{XY}$  [[1, 1]]]
P01XY = Simplify[ $\rho_{XY}$  [[2, 2]]]
P10XY = Simplify[ $\rho_{XY}$  [[3, 3]]]
P11XY = Simplify[ $\rho_{XY}$  [[4, 4]]]

P00XZ = Simplify[ $\rho_{XZ}$  [[1, 1]]]
P01XZ = Simplify[ $\rho_{XZ}$  [[2, 2]]]
P10XZ = Simplify[ $\rho_{XZ}$  [[3, 3]]]
P11XZ = Simplify[ $\rho_{XZ}$  [[4, 4]]]

P00YX = Simplify[ $\rho_{YX}$  [[1, 1]]]
P01YX = Simplify[ $\rho_{YX}$  [[2, 2]]]
P10YX = Simplify[ $\rho_{YX}$  [[3, 3]]]
P11YX = Simplify[ $\rho_{YX}$  [[4, 4]]]

P00YY = Simplify[ $\rho_{YY}$  [[1, 1]]]
P01YY = Simplify[ $\rho_{YY}$  [[2, 2]]]
P10YY = Simplify[ $\rho_{YY}$  [[3, 3]]]
P11YY = Simplify[ $\rho_{YY}$  [[4, 4]]]

P00YZ = Simplify[ $\rho_{YZ}$  [[1, 1]]]
P01YZ = Simplify[ $\rho_{YZ}$  [[2, 2]]]
P10YZ = Simplify[ $\rho_{YZ}$  [[3, 3]]]
P11YZ = Simplify[ $\rho_{YZ}$  [[4, 4]]]

P00ZX = Simplify[ $\rho_{ZX}$  [[1, 1]]]
P01ZX = Simplify[ $\rho_{ZX}$  [[2, 2]]]
P10ZX = Simplify[ $\rho_{ZX}$  [[3, 3]]]
P11ZX = Simplify[ $\rho_{ZX}$  [[4, 4]]]

P00ZY = Simplify[ $\rho_{ZY}$  [[1, 1]]]
P01ZY = Simplify[ $\rho_{ZY}$  [[2, 2]]]
P10ZY = Simplify[ $\rho_{ZY}$  [[3, 3]]]
P11ZY = Simplify[ $\rho_{ZY}$  [[4, 4]]]

P00ZZ = Simplify[ $\rho_{ZZ}$  [[1, 1]]]
P01ZZ = Simplify[ $\rho_{ZZ}$  [[2, 2]]]
P10ZZ = Simplify[ $\rho_{ZZ}$  [[3, 3]]]
P11ZZ = Simplify[ $\rho_{ZZ}$  [[4, 4]]]

```

Figure D.9: From the density matrices in Figure D.8, we extract the entries for the two-qubit probabilities P_{10} , P_{01} , and P_{11} . Each of these is a function of the elements, r_{mn} , of the general two-qubit density matrix declared in Figure D.7.

$$\begin{aligned}
& \frac{1}{4} (r_{11} - r_{12} - r_{13} + r_{14} - r_{21} + r_{22} + r_{23} - r_{24} - r_{31} + r_{32} + r_{33} - r_{34} + r_{41} - r_{42} - r_{43} + r_{44}) \\
& \frac{1}{4} (r_{11} + r_{12} - r_{13} - r_{14} + r_{21} + r_{22} - r_{23} - r_{24} - r_{31} - r_{32} + r_{33} + r_{34} - r_{41} - r_{42} + r_{43} + r_{44}) \\
& \frac{1}{4} (r_{11} - r_{12} + r_{13} - r_{14} - r_{21} + r_{22} - r_{23} + r_{24} + r_{31} - r_{32} + r_{33} - r_{34} - r_{41} + r_{42} - r_{43} + r_{44}) \\
& \frac{1}{4} (r_{11} + r_{12} + r_{13} + r_{14} + r_{21} + r_{22} + r_{23} + r_{24} + r_{31} + r_{32} + r_{33} + r_{34} + r_{41} + r_{42} + r_{43} + r_{44}) \\
& \frac{1}{4} (r_{11} - \dot{r}_{12} - r_{13} + \dot{r}_{14} + \dot{r}_{21} + r_{22} - \dot{r}_{23} - r_{24} - r_{31} + \dot{r}_{32} + r_{33} - \dot{r}_{34} - \dot{r}_{41} - r_{42} + \dot{r}_{43} + r_{44}) \\
& \frac{1}{4} (r_{11} + \dot{r}_{12} + \dot{r}_{13} - r_{14} - r_{21} - \dot{r}_{22} + r_{23} + \dot{r}_{24} + \dot{r}_{31} - r_{32} - \dot{r}_{33} + r_{34} + r_{41} + \dot{r}_{42} - r_{43} - \dot{r}_{44}) \\
& \frac{1}{4} (r_{11} - \dot{r}_{12} + r_{13} - \dot{r}_{14} + \dot{r}_{21} + r_{22} + \dot{r}_{23} + r_{24} + r_{31} - \dot{r}_{32} + r_{33} - \dot{r}_{34} + \dot{r}_{41} + r_{42} + \dot{r}_{43} + r_{44}) \\
& \frac{1}{4} (r_{11} + \dot{r}_{12} + r_{13} + \dot{r}_{14} - \dot{r}_{21} + r_{22} - \dot{r}_{23} + r_{24} + r_{31} + \dot{r}_{32} + r_{33} + \dot{r}_{34} - \dot{r}_{41} + r_{42} - \dot{r}_{43} + r_{44}) \\
& \frac{1}{2} (r_{11} - r_{13} - r_{31} + r_{33}) \\
& \frac{1}{2} (r_{22} - r_{24} - r_{42} + r_{44}) \\
& \frac{1}{2} (r_{11} + r_{13} + r_{31} + r_{33}) \\
& \frac{1}{2} (r_{22} + r_{24} + r_{42} + r_{44}) \\
& \frac{1}{4} (r_{11} - r_{12} - \dot{r}_{13} - r_{14} - \dot{r}_{21} + \dot{r}_{22} - r_{23} + r_{24} - r_{31} + r_{32} + \dot{r}_{33} - \dot{r}_{34} + r_{41} - r_{42} - \dot{r}_{43} + \dot{r}_{44}) \\
& \frac{1}{4} (r_{11} + r_{12} - \dot{r}_{13} - \dot{r}_{14} + r_{21} + r_{22} - \dot{r}_{23} - \dot{r}_{24} + \dot{r}_{31} + \dot{r}_{32} + r_{33} + r_{34} + \dot{r}_{41} + \dot{r}_{42} + r_{43} + r_{44}) \\
& \frac{1}{4} (r_{11} - r_{12} + \dot{r}_{13} - r_{14} + \dot{r}_{21} - \dot{r}_{22} - r_{23} + r_{24} - r_{31} + r_{32} - \dot{r}_{33} + \dot{r}_{34} + r_{41} - r_{42} + \dot{r}_{43} - \dot{r}_{44}) \\
& \frac{1}{4} (r_{11} + r_{12} + \dot{r}_{13} + \dot{r}_{14} + r_{21} + r_{22} + \dot{r}_{23} + \dot{r}_{24} - \dot{r}_{31} - \dot{r}_{32} + r_{33} + r_{34} - \dot{r}_{41} - \dot{r}_{42} + r_{43} + r_{44}) \\
& \frac{1}{4} (r_{11} - \dot{r}_{12} - \dot{r}_{13} - r_{14} + \dot{r}_{21} + r_{22} + r_{23} - \dot{r}_{24} + \dot{r}_{31} + r_{32} + r_{33} - \dot{r}_{34} - r_{41} + \dot{r}_{42} + \dot{r}_{43} + r_{44}) \\
& \frac{1}{4} (r_{11} + \dot{r}_{12} - \dot{r}_{13} + r_{14} - \dot{r}_{21} + r_{22} - r_{23} - \dot{r}_{24} + \dot{r}_{31} - r_{32} + r_{33} + \dot{r}_{34} + r_{41} + \dot{r}_{42} - \dot{r}_{43} + r_{44}) \\
& \frac{1}{4} (r_{11} - \dot{r}_{12} + \dot{r}_{13} + r_{14} + \dot{r}_{21} + r_{22} - r_{23} + \dot{r}_{24} - \dot{r}_{31} - r_{32} + r_{33} - \dot{r}_{34} + r_{41} - \dot{r}_{42} + \dot{r}_{43} + r_{44}) \\
& \frac{1}{4} (r_{11} + \dot{r}_{12} + \dot{r}_{13} - r_{14} - \dot{r}_{21} + r_{22} + r_{23} + \dot{r}_{24} - \dot{r}_{31} + r_{32} + r_{33} + \dot{r}_{34} - r_{41} - \dot{r}_{42} - \dot{r}_{43} + r_{44}) \\
& \frac{1}{2} (r_{11} - \dot{r}_{13} + \dot{r}_{31} + r_{33}) \\
& \frac{1}{2} (r_{22} - \dot{r}_{24} + \dot{r}_{42} + r_{44}) \\
& \frac{1}{2} (r_{11} + \dot{r}_{13} - \dot{r}_{31} + r_{33}) \\
& \frac{1}{2} (r_{22} + \dot{r}_{24} - \dot{r}_{42} + r_{44}) \\
& \frac{1}{2} (r_{11} - r_{12} - r_{21} + r_{22}) \\
& \frac{1}{2} (r_{11} + r_{12} + r_{21} + r_{22}) \\
& \frac{1}{2} (r_{11} + \dot{r}_{13} - \dot{r}_{31} + r_{33}) \\
& \frac{1}{2} (r_{22} + \dot{r}_{24} - \dot{r}_{42} + r_{44}) \\
& \frac{1}{2} (r_{11} - r_{12} - r_{21} + r_{22}) \\
& \frac{1}{2} (r_{11} + r_{12} + r_{21} + r_{22}) \\
& \frac{1}{2} (r_{33} - r_{34} - r_{43} + r_{44}) \\
& \frac{1}{2} (r_{33} + r_{34} + r_{43} + r_{44}) \\
& \frac{1}{2} (r_{11} - \dot{r}_{12} + \dot{r}_{21} + r_{22}) \\
& \frac{1}{2} (r_{11} + \dot{r}_{12} - \dot{r}_{21} + r_{22}) \\
& \frac{1}{2} (r_{33} - \dot{r}_{34} + \dot{r}_{43} + r_{44}) \\
& \frac{1}{2} (r_{33} + \dot{r}_{34} - \dot{r}_{43} + r_{44}) \\
& r_{11} \\
& r_{22} \\
& r_{33} \\
& r_{44}
\end{aligned}$$

Figure D.10: The output of the segment of code in Figure D.9 shows the functional dependence of each probability on r_{mn} .

```

(* now the experimentally measured values... to be filled in after the experiment is done *)
Pex00xx;
Pex01xx;
Pex10xx;
Pex11xx;

Pex00xy;
Pex01xy;
Pex10xy;
Pex11xy;

Pex00xz;
Pex01xz;
Pex10xz;
Pex11xz;

Pex00yx;
Pex01yx;
Pex10yx;
Pex11yx;

Pex00yy;
Pex01yy;
Pex10yy;
Pex11yy;

Pex00yz;
Pex01yz;
Pex10yz;
Pex11yz;

Pex00zx;
Pex01zx;
Pex10zx;
Pex11zx;

Pex00zy;
Pex01zy;
Pex10zy;
Pex11zy;

Pex00zz;
Pex01zz;
Pex10zz;
Pex11zz;

```

Figure D.11: These symbolic variables represent the experimental two-qubit probability data that will be taken in the state tomography experiments.

```

(*)
  Now all that's left is to do a least squares minimization on  $\text{Pex}_{\alpha\beta}^{ij} - \tilde{\text{P}}_{\alpha\beta}^{ij}$ ,
  but in vector form:  $\min ||\text{Pex}_{\alpha\beta}^{ij} - \tilde{\text{P}}_{\alpha\beta}^{ij}||^2$ 
  That is, want a solution to the overconstrained problem :

   $\vec{\text{Pex}} = \vec{\tilde{\text{P}}}$ 

  where  $\vec{\text{Pex}}$  is a vector with the 36 scalars,  $\text{Pex}_{\alpha\beta}^{ij}$ , which were measured in the tomography experiment.
   $\vec{\tilde{\text{P}}}$  is a vector whose 36 elements are the 36 equations  $\tilde{\text{P}}_{\alpha\beta}^{ij}$  solved for
  symbolically above. Each equation,  $\tilde{\text{P}}_{\alpha\beta}^{ij}$ , is a function of the 16 parameters  $r_{11},$ 
   $r_{12}, r_{22}, \dots, r_{44}$  which are the elements of the density matrix  $\rho$ .
  *)

(*)
  If this is put into the form  $\vec{\text{Pex}} = \vec{\tilde{\text{B}}} \vec{r}$ 

  where  $\vec{r} = \begin{pmatrix} r_{11} \\ r_{12} \\ r_{13} \\ \vdots \\ r_{44} \end{pmatrix}$  is a 16x1 matrix.  $\vec{\tilde{\text{B}}}$  is a 36 x 16 matrix.  $\vec{\text{Pex}}$  is a
  36 x 1 matrix. Then we can use the matlab command mldivide to find the value of  $\vec{r}$ 
  which gives the least squares solution to  $\vec{\text{Pex}} = \vec{\tilde{\text{P}}}$ . Mldivide performs  $\vec{\text{Pex}}/\vec{\tilde{\text{B}}} = \vec{r}$ 
  *)

(*  $\vec{\tilde{\text{B}}}$  is just the matrix of coefficients so we don't need the experimental data
  to solve for it. We can use Mathematica to symbolically solve for the 36x16 matrix,
   $\vec{\tilde{\text{B}}}$ , of the coefficients of the  $r_{mn}$  in the 36 equations labeled as  $\tilde{\text{P}}_{\alpha\beta}^{ij}$  above *)

BB = LinearEquationsToMatrices[{P00XX == Pex00XX, P01XX == Pex01XX, P10XX == Pex10XX, P11XX == Pex11XX, P00XY == Pex00XY,
  P01XY == Pex01XY, P10XY == Pex10XY, P11XY == Pex11XY, P00XZ == Pex00XZ, P01XZ == Pex01XZ, P10XZ == Pex10XZ, P11XZ == Pex11XZ,
  P00YX == Pex00YX, P01YX == Pex01YX, P10YX == Pex10YX, P11YX == Pex11YX, P00YY == Pex00YY, P01YY == Pex01YY,
  P10YY == Pex10YY, P11YY == Pex11YY, P00YZ == Pex00YZ, P01YZ == Pex01YZ, P10YZ == Pex10YZ, P11YZ == Pex11YZ,
  P00ZX == Pex00ZX, P01ZX == Pex01ZX, P10ZX == Pex10ZX, P11ZX == Pex11ZX, P00ZY == Pex00ZY, P01ZY == Pex01ZY,
  P10ZY == Pex10ZY, P11ZY == Pex11ZY, P00ZZ == Pex00ZZ, P01ZZ == Pex01ZZ, P10ZZ == Pex10ZZ, P11ZZ == Pex11ZZ},
  {r11, r12, r13, r14, r21, r22, r23, r24, r31, r32, r33, r34, r41, r42, r43, r44}]

BB[[1]] // MatrixForm

```

Figure D.12: Now we perform the symbolic computations that extract the matrix that contains all the coefficients to the equations in Figure D.10. This matrix is the **BB** matrix in the code above.

D.4.2 State tomography data analysis using MATLAB

Now that we have calculated the B matrix, we can use MATLAB code to perform the least-squares minimization described in [Figure D.12](#).

```

1  function rho = get_rho(state,directory,tomoTime)
2
3
4  %state: label for state HH,HV,HD,HR,etc.
5  %directory: directory where data is stored
6  %tomoTime: pulse sequence time (in ns) at which tomography was done
7  %rho: the experimental density matrix of state specified by "state" as measured by data
    in directory specified by "directory"
8
9  %B matrix is the matrix with coefficients of r_mn terms that will be used to perform
    least squares minimization
10 %since we never got the symbolic toolbox for our copy of matlab: get B matrix from
    mathematica
11 B = [
12 1/4, -1/4, -1/4, 1/4, -1/4, 1/4, 1/4, -1/4, -1/4, 1/4, 1/4, -1/4, -1/4, 1/4, -1/4, 1/4;
13 1/4, 1/4, -1/4, -1/4, 1/4, 1/4, -1/4, -1/4, -1/4, -1/4, 1/4, 1/4, -1/4, -1/4, 1/4, 1/4;
14 1/4, -1/4, 1/4, -1/4, -1/4, 1/4, -1/4, 1/4, 1/4, -1/4, 1/4, -1/4, -1/4, 1/4, -1/4, 1/4;
15 1/4, 1/4, 1/4, 1/4, 1/4, 1/4, 1/4, 1/4, 1/4, 1/4, 1/4, 1/4, 1/4, 1/4, 1/4, 1/4;
16 1/4, -i/4, -1/4, i/4, i/4, 1/4, -i/4, -1/4, -1/4, i/4, 1/4, -i/4,-i/4, -1/4, i/4, 1/4;
17 1/4, i/4, -1/4, -i/4, -i/4, 1/4, i/4, -1/4, -1/4, -i/4, 1/4, i/4, i/4, -1/4, -i/4, 1/4;
18 1/4, -i/4, 1/4, -i/4, i/4, 1/4, i/4, 1/4, 1/4, -i/4, 1/4, -i/4, i/4, 1/4, i/4, 1/4;
19 1/4, i/4, 1/4, i/4, -i/4, 1/4, -i/4, 1/4, 1/4, i/4, 1/4, i/4, -i/4, 1/4, -i/4, 1/4;
20 1/2, 0, -1/2, 0, 0, 0, 0, 0, -1/2, 0, 1/2, 0, 0, 0, 0, 0;
21 0, 0, 0, 0, 0, 1/2, 0, -1/2, 0, 0, 0, 0, 0, 0, -1/2, 0, 1/2;
22 1/2, 0, 1/2, 0, 0, 0, 0, 0, 1/2, 0, 1/2, 0, 0, 0, 0, 0;
23 0, 0, 0, 0, 0, 1/2, 0, 1/2, 0, 0, 0, 0, 0, 0, 1/2, 0, 1/2;
24 1/4, -1/4, -i/4, i/4, -1/4, 1/4, i/4, -i/4, i/4, -i/4, 1/4, -1/4, -i/4, i/4, -1/4, 1/4;
25 1/4, 1/4, -i/4, -i/4, 1/4, 1/4, -i/4, -i/4, i/4, i/4, 1/4, 1/4, i/4, i/4, 1/4, 1/4;
26 1/4, -1/4, i/4, -i/4, -1/4, 1/4, -i/4, i/4, -i/4, i/4, 1/4, -1/4, i/4, -i/4, -1/4, 1/4;
27 1/4, 1/4, i/4, i/4, 1/4, 1/4, i/4, i/4, -i/4, -i/4, 1/4, 1/4, -i/4, -i/4, 1/4, 1/4;
28 1/4, -i/4, -i/4, -1/4, i/4, 1/4, 1/4, -i/4, i/4, 1/4, 1/4, -i/4, -1/4, i/4, i/4, 1/4;
29 1/4, i/4, -i/4, 1/4, -i/4, 1/4, -1/4, -i/4, i/4, -1/4, 1/4, i/4, 1/4, i/4, -i/4, 1/4;
30 1/4, -i/4, i/4, 1/4, i/4, 1/4, -1/4, i/4, -i/4, -1/4, 1/4, -i/4, 1/4, -i/4, i/4, 1/4;
31 1/4, i/4, i/4, -1/4, -i/4, 1/4, 1/4, i/4, -i/4, 1/4, 1/4, i/4, -1/4, -i/4, -i/4, 1/4;
32 1/2, 0, -i/2, 0, 0, 0, 0, 0, i/2, 0, 1/2, 0, 0, 0, 0, 0;
33 0, 0, 0, 0, 0, 1/2, 0, -i/2, 0, 0, 0, 0, 0, 0, i/2, 0, 1/2;
34 1/2, 0, i/2, 0, 0, 0, 0, 0, -i/2, 0, 1/2, 0, 0, 0, 0, 0;
35 0, 0, 0, 0, 0, 1/2, 0, i/2, 0, 0, 0, 0, 0, 0, -i/2, 0, 1/2;
36 1/2, -1/2, 0, 0, -1/2, 1/2, 0, 0, 0, 0, 0, 0, 0, 0, 0, 0, 0;
37 1/2, 1/2, 0, 0, 1/2, 1/2, 0, 0, 0, 0, 0, 0, 0, 0, 0, 0, 0;
38 0, 0, 0, 0, 0, 0, 0, 0, 0, 0, 1/2, -1/2, 0, 0, -1/2, 1/2;
39 0, 0, 0, 0, 0, 0, 0, 0, 0, 0, 1/2, 1/2, 0, 0, 1/2, 1/2;
40 1/2, -i/2, 0, 0, i/2, 1/2, 0, 0, 0, 0, 0, 0, 0, 0, 0, 0, 0;
41 1/2, i/2, 0, 0, -i/2, 1/2, 0, 0, 0, 0, 0, 0, 0, 0, 0, 0, 0;
42 0, 0, 0, 0, 0, 0, 0, 0, 0, 0, 1/2, -i/2, 0, 0, i/2, 1/2;
43 0, 0, 0, 0, 0, 0, 0, 0, 0, 0, 1/2, i/2, 0, 0, -i/2, 1/2;
44 1, 0, 0, 0, 0, 0, 0, 0, 0, 0, 0, 0, 0, 0, 0, 0, 0;
45 0, 0, 0, 0, 0, 1, 0, 0, 0, 0, 0, 0, 0, 0, 0, 0, 0;
46 0, 0, 0, 0, 0, 0, 0, 0, 0, 0, 1, 0, 0, 0, 0, 0, 0;
47 0, 0, 0, 0, 0, 0, 0, 0, 0, 0, 0, 0, 0, 0, 0, 0, 1];
48
49
50
51
52

```

Figure D.13: Part 1 of 5 of MATLAB code to obtain density matrix from experimental data.

```

53 % flags to indicate if full tdataset is present for each case
54 xxFlag=0;
55 xyFlag=0;
56 xzFlag=0;
57
58 yxFlag=0;
59 yyFlag=0;
60 yzFlag=0;
61
62 zxFlag=0;
63 zyFlag=0;
64 zzFlag=0;
65
66
67 % load data from disk but only at time specified by tomoTime
68 files = dir(sprintf('%s\\*.csv',directory));
69 for m = 1:length(files)
70
71     if length(strfind(files(m).name,'XX'))>0 && length(strfind(files(m).name,state))
72         filename = sprintf('%s\\%s',directory,files(m).name);
73         data = dlmread(filename,',' );
74         t_data_XX=data(:,1);
75         [blah tomoTime_index]=min(abs(tomoTime-t_data_XX));
76         data(tomoTime_index,1);
77         P_01_XX=data(tomoTime_index,2)/100;
78         P_10_XX=data(tomoTime_index,3)/100;
79         P_11_XX=data(tomoTime_index,4)/100;
80         P_00_XX=1-(P_11_XX+P_01_XX+P_10_XX);
81         xxFlag=1;
82     end
83
84     if length(strfind(files(m).name,'XY'))>0 && length(strfind(files(m).name,state))
85         filename = sprintf('%s\\%s',directory,files(m).name);
86         data = dlmread(filename,',' );
87         t_data_XY=data(:,1);
88         [blah tomoTime_index]=min(abs(tomoTime-t_data_XY));
89         data(tomoTime_index,1);
90         P_01_XY=data(tomoTime_index,2)/100;
91         P_10_XY=data(tomoTime_index,3)/100;
92         P_11_XY=data(tomoTime_index,4)/100;
93         P_00_XY=1-(P_11_XY+P_01_XY+P_10_XY);
94         xyFlag=1;
95     end
96
97     if (length(strfind(files(m).name,'XZ'))>0 || length(strfind(files(m).name,'XI'))>0)
&& length(strfind(files(m).name,state))
98         filename = sprintf('%s\\%s',directory,files(m).name);
99         data = dlmread(filename,',' );
100        t_data_XZ=data(:,1);
101        [blah tomoTime_index]=min(abs(tomoTime-t_data_XZ));
102        data(tomoTime_index,1);
103        P_01_XZ=data(tomoTime_index,2)/100;
104        P_10_XZ=data(tomoTime_index,3)/100;
105        P_11_XZ=data(tomoTime_index,4)/100;
106        P_00_XZ=1-(P_11_XZ+P_01_XZ+P_10_XZ);

```

Figure D.14: Part 2 of 5 of MATLAB code to obtain density matrix from experimental data.

```

107         xzFlag=1;
108     end
109
110     if length(strfind(files(m).name, 'YX'))>0 && length(strfind(files(m).name, state))
111         filename = sprintf('%s\\%s', directory, files(m).name);
112         data = dlmread(filename, ',');
113         t_data_YX=data(:,1);
114         [blah tomoTime_index]=min(abs(tomoTime-t_data_YX));
115         data(tomoTime_index,1);
116         P_01_YX=data(tomoTime_index,2)/100;
117         P_10_YX=data(tomoTime_index,3)/100;
118         P_11_YX=data(tomoTime_index,4)/100;
119         P_00_YX=1-(P_11_YX+P_01_YX+P_10_YX);
120         yxFlag=1;
121     end
122
123     if length(strfind(files(m).name, 'YY'))>0 && length(strfind(files(m).name, state))
124         filename = sprintf('%s\\%s', directory, files(m).name);
125         data = dlmread(filename, ',');
126         t_data_YY=data(:,1);
127         [blah tomoTime_index]=min(abs(tomoTime-t_data_YY));
128         data(tomoTime_index,1);
129         P_01_YY=data(tomoTime_index,2)/100;
130         P_10_YY=data(tomoTime_index,3)/100;
131         P_11_YY=data(tomoTime_index,4)/100;
132         P_00_YY=1-(P_11_YY+P_01_YY+P_10_YY);
133         yyFlag=1;
134     end
135
136     if (length(strfind(files(m).name, 'YZ'))>0 || length(strfind(files(m).name, 'YI'))>0)
137     && length(strfind(files(m).name, state))
138         filename = sprintf('%s\\%s', directory, files(m).name);
139         data = dlmread(filename, ',');
140         t_data_YZ=data(:,1);
141         [blah tomoTime_index]=min(abs(tomoTime-t_data_YZ));
142         data(tomoTime_index,1);
143         P_01_YZ=data(tomoTime_index,2)/100;
144         P_10_YZ=data(tomoTime_index,3)/100;
145         P_11_YZ=data(tomoTime_index,4)/100;
146         P_00_YZ=1-(P_11_YZ+P_01_YZ+P_10_YZ);
147         yzFlag=1;
148     end
149
150     if (length(strfind(files(m).name, 'ZX')) || length(strfind(files(m).name, 'IX'))) &&
151     length(strfind(files(m).name, state))
152         filename = sprintf('%s\\%s', directory, files(m).name);
153         data = dlmread(filename, ',');
154         t_data_ZX=data(:,1);
155         [blah tomoTime_index]=min(abs(tomoTime-t_data_ZX));
156         data(tomoTime_index,1);
157         P_01_ZX=data(tomoTime_index,2)/100;
158         P_10_ZX=data(tomoTime_index,3)/100;
159         P_11_ZX=data(tomoTime_index,4)/100;
160         P_00_ZX=1-(P_11_ZX+P_01_ZX+P_10_ZX);
161         zxFlag=1;

```

Figure D.15: Part 3 of 5 of MATLAB code to obtain density matrix from experimental data.

```

160     end
161
162     if (length(strfind(files(m).name,'ZY')) || length(strfind(files(m).name,'IY'))) &&
length(strfind(files(m).name,state))
163         filename = sprintf('%s\\%s',directory,files(m).name);
164         data = dlmread(filename,',' );
165         t_data_ZY=data(:,1);
166         [blah tomoTime_index]=min(abs(tomoTime-t_data_ZY));
167         data(tomoTime_index,1);
168         P_01_ZY=data(tomoTime_index,2)/100;
169         P_10_ZY=data(tomoTime_index,3)/100;
170         P_11_ZY=data(tomoTime_index,4)/100;
171         P_00_ZY=1-(P_11_ZY+P_01_ZY+P_10_ZY);
172         zyFlag=1;
173     end
174
175     if (length(strfind(files(m).name,'ZZ')) || length(strfind(files(m).name,'II'))) &&
length(strfind(files(m).name,state))
176         filename = sprintf('%s\\%s',directory,files(m).name)
177         data = dlmread(filename,',' );
178         t_data_ZZ=data(:,1);
179         [blah tomoTime_index]=min(abs(tomoTime-t_data_ZZ));
180         data(tomoTime_index,1);
181         P_01_ZZ=data(tomoTime_index,2)/100;
182         P_10_ZZ=data(tomoTime_index,3)/100;
183         P_11_ZZ=data(tomoTime_index,4)/100;
184         P_00_ZZ=1-(P_11_ZZ+P_01_ZZ+P_10_ZZ);
185         zzFlag=1;
186     end
187
188 end
189
190
191
192
193
194 %set up 36x1 P_ex matrix for P_ex=B r
195 P_ex=[
196     P_00_XX;
197     P_01_XX;
198     P_10_XX;
199     P_11_XX;
200     P_00_XY;
201     P_01_XY;
202     P_10_XY;
203     P_11_XY;
204     P_00_XZ;
205     P_01_XZ;
206     P_10_XZ;
207     P_11_XZ;
208     P_00_YX;
209     P_01_YX;
210     P_10_YX;
211     P_11_YX;
212     P_00_YY;

```

Figure D.16: Part 4 of 5 of MATLAB code to obtain density matrix from experimental data.

```

213     P_01_YY;
214     P_10_YY;
215     P_11_YY;
216     P_00_YZ;
217     P_01_YZ;
218     P_10_YZ;
219     P_11_YZ;
220     P_00_ZX;
221     P_01_ZX;
222     P_10_ZX;
223     P_11_ZX;
224     P_00_ZY;
225     P_01_ZY;
226     P_10_ZY;
227     P_11_ZY;
228     P_00_ZZ;
229     P_01_ZZ;
230     P_10_ZZ;
231     P_11_ZZ
232     ]];
233
234     %the least squares solution via the mldivide command
235     r=B\P_ex;
236
237     %the experimentally obtained density matrix
238     rho=[
239         r(1) r(2) r(3) r(4);
240         r(5) r(6) r(7) r(8);
241         r(9) r(10) r(11) r(12);
242         r(13) r(14) r(15) r(16)
243     ]];
244
245

```

Figure D.17: Part 5 of 5 of MATLAB code to obtain density matrix from experimental data.

D.5 MATLAB code used for process tomography analysis

D.5.1 MATLAB code used for process tomography

The MATLAB process tomography code requires some introduction. Let us call the column vector of the experimentally obtained density matrices of the 16 two-qubit basis states \mathbf{v}_{exp} . Each row of this vector is $\rho^{\alpha\beta}$, where α and β can be any one of $\{H, V, D, R\}$ state labels that we defined in the table shown in Figure 5.10a. These are the states that will be input to our gate. To obtain a χ matrix we follow the procedure described in [58] and [86]. First, to make things mathematically simple to work with, we transform the input state density matrices $\rho^{\alpha\beta}$ to an “easy basis”, $\rho^{(i,j)}$, where $\rho^{(i,j)}$ is a density matrix with a one at the (i, j) th element and zeros elsewhere. Let us call \mathbf{v}_{easy} the column vector whose rows are the easy basis density matrices, $\rho^{(i,j)}$. Then both these 16×1 column vectors can be written as

$$\mathbf{v}_{exp} = \begin{pmatrix} \rho^{HH} \\ \rho^{HV} \\ \rho^{HD} \\ \cdot \\ \cdot \\ \cdot \\ \rho^{RD} \\ \rho^{RR} \end{pmatrix} \quad (\text{D.11})$$

and

$$\mathbf{v}_{easy} = \begin{pmatrix} \rho^{11} \\ \rho^{12} \\ \rho^{13} \\ \cdot \\ \cdot \\ \cdot \\ \rho^{43} \\ \rho^{44} \end{pmatrix} \quad (\text{D.12})$$

and we are looking for the transformation 16×16 transformation matrix M such that

$$\mathbf{v}_{easy} = M^{-1} \mathbf{v}_{exp} \quad (\text{D.13})$$

Since equivalently $M \mathbf{v}_{easy} = \mathbf{v}_{exp}$, M can be written as the row representation of each experimentally obtained density matrix

$$M = \begin{bmatrix} \rho_{1,1}^{HH} & \rho_{1,2}^{HH} & \rho_{1,3}^{HH} & \cdot & \cdot & \cdot & \rho_{16,16}^{HH} \\ \rho_{1,1}^{HV} & \rho_{1,2}^{HV} & \rho_{1,3}^{HV} & \cdot & \cdot & \cdot & \rho_{16,16}^{HV} \\ \cdot & \cdot & \cdot & \cdot & \cdot & \cdot & \cdot \\ \cdot & \cdot & \cdot & \cdot & \cdot & \cdot & \cdot \\ \cdot & \cdot & \cdot & \cdot & \cdot & \cdot & \cdot \\ \rho_{1,1}^{RR} & \rho_{1,2}^{RR} & \rho_{1,3}^{RR} & \cdot & \cdot & \cdot & \rho_{16,16}^{RR} \end{bmatrix} \quad (\text{D.14})$$

Also if the input to the quantum gate is the density matrix ρ , then let us define the density matrix that defines the output of the gate as $\varepsilon(\rho)$.

So, in order to extract the χ matrix from the experimental state tomography data of the 16 input state density matrices and the 16 output state density matrices, we follow the steps below. These are explained in detail in Chapter 8 of reference [58]

1. Find M using the experimentally obtained input state density matrices $\rho^{\alpha\beta}$
2. Invert M
3. Using M , we can also transform the experimentally obtained gate output density matrices $\epsilon(\rho^{\alpha\beta})$ to the easy basis $\epsilon(\rho^{\alpha\beta})^{(i,j)}$. This is possible because quantum operations are linear.
4. Now, in order to find the χ matrix, we can plug $\epsilon(\rho^{\alpha\beta})^{(i,j)}$ into equations that can be found in [58, 19]

$$P = I \otimes ((\rho^{(1,1)} + \rho^{(2,3)} + \rho^{(3,2)} + \rho^{(4,4)}) \otimes I) \quad (\text{D.15})$$

$$d = \frac{1}{2} \begin{bmatrix} 1 & 0 & 0 & 1 \\ 0 & 1 & 1 & 0 \\ 0 & 1 & -1 & 0 \\ 1 & 0 & 0 & -1 \end{bmatrix} \quad (\text{D.16})$$

$$D^2 = d \otimes d \quad (\text{D.17})$$

$$\chi = D' P' \chi_{pre} P D; \quad (\text{D.18})$$

5. We then find the nearest physical χ matrix to the experimentally obtained χ matrix as described earlier in this appendix.

The following is the MATLAB code that performs these calculations:

```

1  function Chi = getChi(eps_HH,eps_HV,eps_HD,eps_HR,eps_VH,eps_VV,eps_VD,eps_VR,eps_DH,
eps_DV,eps_DD,eps_DR,eps_RH,eps_RV,eps_RD,eps_RR,i_HH,i_HV,i_HD,i_HR,i_VH,i_VV,i_VD,i_VR
,i_DH,i_DV,i_DD,i_DR,i_RH,i_RV,i_RD,i_RR)
2
3
4  %i_ab: the 16 two-qubit basis state density matrices used as input to gate
5  %eps_ab: the 16 two-qubit outputs after the i_ab were input into the gate
6  %Chi: the physical approximation to the experimentally obtained chi matrix
7
8  % matrix needed to transform input state density matrices to "easy basis"
9  M = [
10
11      i_HH(1,1) i_HH(1,2) i_HH(1,3) i_HH(1,4) i_HH(2,1) i_HH(2,2) i_HH(2,3) i_HH(2,4) i_HH
(3,1) i_HH(3,2) i_HH(3,3) i_HH(3,4) i_HH(4,1) i_HH(4,2) i_HH(4,3) i_HH(4,4);
12      i_HV(1,1) i_HV(1,2) i_HV(1,3) i_HV(1,4) i_HV(2,1) i_HV(2,2) i_HV(2,3) i_HV(2,4) i_HV
(3,1) i_HV(3,2) i_HV(3,3) i_HV(3,4) i_HV(4,1) i_HV(4,2) i_HV(4,3) i_HV(4,4);
13      i_HD(1,1) i_HD(1,2) i_HD(1,3) i_HD(1,4) i_HD(2,1) i_HD(2,2) i_HD(2,3) i_HD(2,4) i_HD
(3,1) i_HD(3,2) i_HD(3,3) i_HD(3,4) i_HD(4,1) i_HD(4,2) i_HD(4,3) i_HD(4,4);
14      i_HR(1,1) i_HR(1,2) i_HR(1,3) i_HR(1,4) i_HR(2,1) i_HR(2,2) i_HR(2,3) i_HR(2,4) i_HR
(3,1) i_HR(3,2) i_HR(3,3) i_HR(3,4) i_HR(4,1) i_HR(4,2) i_HR(4,3) i_HR(4,4);
15      i_VH(1,1) i_VH(1,2) i_VH(1,3) i_VH(1,4) i_VH(2,1) i_VH(2,2) i_VH(2,3) i_VH(2,4) i_VH
(3,1) i_VH(3,2) i_VH(3,3) i_VH(3,4) i_VH(4,1) i_VH(4,2) i_VH(4,3) i_VH(4,4);
16      i_VV(1,1) i_VV(1,2) i_VV(1,3) i_VV(1,4) i_VV(2,1) i_VV(2,2) i_VV(2,3) i_VV(2,4) i_VV
(3,1) i_VV(3,2) i_VV(3,3) i_VV(3,4) i_VV(4,1) i_VV(4,2) i_VV(4,3) i_VV(4,4);
17      i_VD(1,1) i_VD(1,2) i_VD(1,3) i_VD(1,4) i_VD(2,1) i_VD(2,2) i_VD(2,3) i_VD(2,4) i_VD
(3,1) i_VD(3,2) i_VD(3,3) i_VD(3,4) i_VD(4,1) i_VD(4,2) i_VD(4,3) i_VD(4,4);
18      i_VR(1,1) i_VR(1,2) i_VR(1,3) i_VR(1,4) i_VR(2,1) i_VR(2,2) i_VR(2,3) i_VR(2,4) i_VR
(3,1) i_VR(3,2) i_VR(3,3) i_VR(3,4) i_VR(4,1) i_VR(4,2) i_VR(4,3) i_VR(4,4);
19      i_DH(1,1) i_DH(1,2) i_DH(1,3) i_DH(1,4) i_DH(2,1) i_DH(2,2) i_DH(2,3) i_DH(2,4) i_DH
(3,1) i_DH(3,2) i_DH(3,3) i_DH(3,4) i_DH(4,1) i_DH(4,2) i_DH(4,3) i_DH(4,4);
20      i_DV(1,1) i_DV(1,2) i_DV(1,3) i_DV(1,4) i_DV(2,1) i_DV(2,2) i_DV(2,3) i_DV(2,4) i_DV
(3,1) i_DV(3,2) i_DV(3,3) i_DV(3,4) i_DV(4,1) i_DV(4,2) i_DV(4,3) i_DV(4,4);
21      i_DD(1,1) i_DD(1,2) i_DD(1,3) i_DD(1,4) i_DD(2,1) i_DD(2,2) i_DD(2,3) i_DD(2,4) i_DD
(3,1) i_DD(3,2) i_DD(3,3) i_DD(3,4) i_DD(4,1) i_DD(4,2) i_DD(4,3) i_DD(4,4);
22      i_DR(1,1) i_DR(1,2) i_DR(1,3) i_DR(1,4) i_DR(2,1) i_DR(2,2) i_DR(2,3) i_DR(2,4) i_DR
(3,1) i_DR(3,2) i_DR(3,3) i_DR(3,4) i_DR(4,1) i_DR(4,2) i_DR(4,3) i_DR(4,4);
23      i_RH(1,1) i_RH(1,2) i_RH(1,3) i_RH(1,4) i_RH(2,1) i_RH(2,2) i_RH(2,3) i_RH(2,4) i_RH
(3,1) i_RH(3,2) i_RH(3,3) i_RH(3,4) i_RH(4,1) i_RH(4,2) i_RH(4,3) i_RH(4,4);
24      i_RV(1,1) i_RV(1,2) i_RV(1,3) i_RV(1,4) i_RV(2,1) i_RV(2,2) i_RV(2,3) i_RV(2,4) i_RV
(3,1) i_RV(3,2) i_RV(3,3) i_RV(3,4) i_RV(4,1) i_RV(4,2) i_RV(4,3) i_RV(4,4);
25      i_RD(1,1) i_RD(1,2) i_RD(1,3) i_RD(1,4) i_RD(2,1) i_RD(2,2) i_RD(2,3) i_RD(2,4) i_RD
(3,1) i_RD(3,2) i_RD(3,3) i_RD(3,4) i_RD(4,1) i_RD(4,2) i_RD(4,3) i_RD(4,4);
26      i_RR(1,1) i_RR(1,2) i_RR(1,3) i_RR(1,4) i_RR(2,1) i_RR(2,2) i_RR(2,3) i_RR(2,4) i_RR
(3,1) i_RR(3,2) i_RR(3,3) i_RR(3,4) i_RR(4,1) i_RR(4,2) i_RR(4,3) i_RR(4,4)
27
28  ];
29
30  %take its inverse
31  M = inv(M);
32
33  %since quantum operations are linear can transform the output density matrices to easy
34  %basis using same method as that used for transforming input density matrices
35  eps_ll=M(1,1)*eps_HH + M(1,2)*eps_HV + M(1,3)*eps_HD + M(1,4)*eps_HR + M(1,5)*eps_VH + M
(1,6)*eps_VV + M(1,7)*eps_VD + M(1,8)*eps_VR + M(1,9)*eps_DH + M(1,10)*eps_DV + M(1,11)*
eps_DD + M(1,12)*eps_DR + M(1,13)*eps_RH + M(1,14)*eps_RV + M(1,15)*eps_RD + M(1,16)*

```

Figure D.18: Part 1 of 5 of MATLAB code to obtain the χ matrix.

```

eps_RR;
36 eps_12=M(2,1)*eps_HH + M(2,2)*eps_HV + M(2,3)*eps_HD + M(2,4)*eps_HR + M(2,5)*eps_VH + M
(2,6)*eps_VV + M(2,7)*eps_VD + M(2,8)*eps_VR + M(2,9)*eps_DH + M(2,10)*eps_DV + M(2,11)*
eps_DD + M(2,12)*eps_DR + M(2,13)*eps_RH + M(2,14)*eps_RV + M(2,15)*eps_RD + M(2,16)*
eps_RR;
37 eps_13=M(3,1)*eps_HH + M(3,2)*eps_HV + M(3,3)*eps_HD + M(3,4)*eps_HR + M(3,5)*eps_VH + M
(3,6)*eps_VV + M(3,7)*eps_VD + M(3,8)*eps_VR + M(3,9)*eps_DH + M(3,10)*eps_DV + M(3,11)*
eps_DD + M(3,12)*eps_DR + M(3,13)*eps_RH + M(3,14)*eps_RV + M(3,15)*eps_RD + M(3,16)*
eps_RR;
38 eps_14=M(4,1)*eps_HH + M(4,2)*eps_HV + M(4,3)*eps_HD + M(4,4)*eps_HR + M(4,5)*eps_VH + M
(4,6)*eps_VV + M(4,7)*eps_VD + M(4,8)*eps_VR + M(4,9)*eps_DH + M(4,10)*eps_DV + M(4,11)*
eps_DD + M(4,12)*eps_DR + M(4,13)*eps_RH + M(4,14)*eps_RV + M(4,15)*eps_RD + M(4,16)*
eps_RR;
39
40 eps_21=M(5,1)*eps_HH + M(5,2)*eps_HV + M(5,3)*eps_HD + M(5,4)*eps_HR + M(5,5)*eps_VH + M
(5,6)*eps_VV + M(5,7)*eps_VD + M(5,8)*eps_VR + M(5,9)*eps_DH + M(5,10)*eps_DV + M(5,11)*
eps_DD + M(5,12)*eps_DR + M(5,13)*eps_RH + M(5,14)*eps_RV + M(5,15)*eps_RD + M(5,16)*
eps_RR;
41 eps_22=M(6,1)*eps_HH + M(6,2)*eps_HV + M(6,3)*eps_HD + M(6,4)*eps_HR + M(6,5)*eps_VH + M
(6,6)*eps_VV + M(6,7)*eps_VD + M(6,8)*eps_VR + M(6,9)*eps_DH + M(6,10)*eps_DV + M(6,11)*
eps_DD + M(6,12)*eps_DR + M(6,13)*eps_RH + M(6,14)*eps_RV + M(6,15)*eps_RD + M(6,16)*
eps_RR;
42 eps_23=M(7,1)*eps_HH + M(7,2)*eps_HV + M(7,3)*eps_HD + M(7,4)*eps_HR + M(7,5)*eps_VH + M
(7,6)*eps_VV + M(7,7)*eps_VD + M(7,8)*eps_VR + M(7,9)*eps_DH + M(7,10)*eps_DV + M(7,11)*
eps_DD + M(7,12)*eps_DR + M(7,13)*eps_RH + M(7,14)*eps_RV + M(7,15)*eps_RD + M(7,16)*
eps_RR;
43 eps_24=M(8,1)*eps_HH + M(8,2)*eps_HV + M(8,3)*eps_HD + M(8,4)*eps_HR + M(8,5)*eps_VH + M
(8,6)*eps_VV + M(8,7)*eps_VD + M(8,8)*eps_VR + M(8,9)*eps_DH + M(8,10)*eps_DV + M(8,11)*
eps_DD + M(8,12)*eps_DR + M(8,13)*eps_RH + M(8,14)*eps_RV + M(8,15)*eps_RD + M(8,16)*
eps_RR;
44
45 eps_31=M(9,1)*eps_HH + M(9,2)*eps_HV + M(9,3)*eps_HD + M(9,4)*eps_HR + M(9,5)*eps_VH + M
(9,6)*eps_VV + M(9,7)*eps_VD + M(9,8)*eps_VR + M(9,9)*eps_DH + M(9,10)*eps_DV + M(9,11)*
eps_DD + M(9,12)*eps_DR + M(9,13)*eps_RH + M(9,14)*eps_RV + M(9,15)*eps_RD + M(9,16)*
eps_RR;
46 eps_32=M(10,1)*eps_HH + M(10,2)*eps_HV + M(10,3)*eps_HD + M(10,4)*eps_HR + M(10,5)*
eps_VH + M(10,6)*eps_VV + M(10,7)*eps_VD + M(10,8)*eps_VR + M(10,9)*eps_DH + M(10,10)*
eps_DV + M(10,11)*eps_DD + M(10,12)*eps_DR + M(10,13)*eps_RH + M(10,14)*eps_RV + M(10,15)
)*eps_RD + M(10,16)*eps_RR;
47 eps_33=M(11,1)*eps_HH + M(11,2)*eps_HV + M(11,3)*eps_HD + M(11,4)*eps_HR + M(11,5)*
eps_VH + M(11,6)*eps_VV + M(11,7)*eps_VD + M(11,8)*eps_VR + M(11,9)*eps_DH + M(11,10)*
eps_DV + M(11,11)*eps_DD + M(11,12)*eps_DR + M(11,13)*eps_RH + M(11,14)*eps_RV + M(11,15)
)*eps_RD + M(11,16)*eps_RR;
48 eps_34=M(12,1)*eps_HH + M(12,2)*eps_HV + M(12,3)*eps_HD + M(12,4)*eps_HR + M(12,5)*
eps_VH + M(12,6)*eps_VV + M(12,7)*eps_VD + M(12,8)*eps_VR + M(12,9)*eps_DH + M(12,10)*
eps_DV + M(12,11)*eps_DD + M(12,12)*eps_DR + M(12,13)*eps_RH + M(12,14)*eps_RV + M(12,15)
)*eps_RD + M(12,16)*eps_RR;
49
50 eps_41=M(13,1)*eps_HH + M(13,2)*eps_HV + M(13,3)*eps_HD + M(13,4)*eps_HR + M(13,5)*
eps_VH + M(13,6)*eps_VV + M(13,7)*eps_VD + M(13,8)*eps_VR + M(13,9)*eps_DH + M(13,10)*
eps_DV + M(13,11)*eps_DD + M(13,12)*eps_DR + M(13,13)*eps_RH + M(13,14)*eps_RV + M(13,15)
)*eps_RD + M(13,16)*eps_RR;
51 eps_42=M(14,1)*eps_HH + M(14,2)*eps_HV + M(14,3)*eps_HD + M(14,4)*eps_HR + M(14,5)*
eps_VH + M(14,6)*eps_VV + M(14,7)*eps_VD + M(14,8)*eps_VR + M(14,9)*eps_DH + M(14,10)*
eps_DV + M(14,11)*eps_DD + M(14,12)*eps_DR + M(14,13)*eps_RH + M(14,14)*eps_RV + M(14,15)

```

Figure D.19: Part 2 of 5 of MATLAB code to obtain the χ matrix.

```

) *eps_RD + M(14,16) *eps_RR;
52 eps_43=M(15,1)*eps_HH + M(15,2)*eps_HV + M(15,3)*eps_HD + M(15,4)*eps_HR + M(15,5)*
eps_VH + M(15,6)*eps_VV + M(15,7)*eps_VD + M(15,8)*eps_VR + M(15,9)*eps_DH + M(15,10)*
eps_DV + M(15,11)*eps_DD + M(15,12)*eps_DR + M(15,13)*eps_RH + M(15,14)*eps_RV + M(15,15
) *eps_RD + M(15,16)*eps_RR;
53 eps_44=M(16,1)*eps_HH + M(16,2)*eps_HV + M(16,3)*eps_HD + M(16,4)*eps_HR + M(16,5)*
eps_VH + M(16,6)*eps_VV + M(16,7)*eps_VD + M(16,8)*eps_VR + M(16,9)*eps_DH + M(16,10)*
eps_DV + M(16,11)*eps_DD + M(16,12)*eps_DR + M(16,13)*eps_RH + M(16,14)*eps_RV + M(16,15
) *eps_RD + M(16,16)*eps_RR;
54
55 %%%%%%%%%%%%%%%%%%%%%%%%%%%%%%%%%%%%%%%%%%%%%%%%%%%%%%%%%%%%%%%%%%%%%%%%%
56 % calculate chi matrix according to procedure in Nielsen and Chuang
57 % Quantum Information text
58 %%%%%%%%%%%%%%%%%%%%%%%%%%%%%%%%%%%%%%%%%%%%%%%%%%%%%%%%%%%%%%%%%%%%%%%%%
59
60 preChi=[
61     eps_11(1,1) eps_11(1,2) eps_11(1,3) eps_11(1,4) eps_12(1,1) eps_12(1,2) eps_12(1,3)
eps_12(1,4) eps_13(1,1) eps_13(1,2) eps_13(1,3) eps_13(1,4) eps_14(1,1) eps_14(1,2)
eps_14(1,3) eps_14(1,4);
62     eps_11(2,1) eps_11(2,2) eps_11(2,3) eps_11(2,4) eps_12(2,1) eps_12(2,2) eps_12(2,3)
eps_12(2,4) eps_13(2,1) eps_13(2,2) eps_13(2,3) eps_13(2,4) eps_14(2,1) eps_14(2,2)
eps_14(2,3) eps_14(2,4);
63     eps_11(3,1) eps_11(3,2) eps_11(3,3) eps_11(3,4) eps_12(3,1) eps_12(3,2) eps_12(3,3)
eps_12(3,4) eps_13(3,1) eps_13(3,2) eps_13(3,3) eps_13(3,4) eps_14(3,1) eps_14(3,2)
eps_14(3,3) eps_14(3,4);
64     eps_11(4,1) eps_11(4,2) eps_11(4,3) eps_11(4,4) eps_12(4,1) eps_12(4,2) eps_12(4,3)
eps_12(4,4) eps_13(4,1) eps_13(4,2) eps_13(4,3) eps_13(4,4) eps_14(4,1) eps_14(4,2)
eps_14(4,3) eps_14(4,4);
65
66     eps_21(1,1) eps_21(1,2) eps_21(1,3) eps_21(1,4) eps_22(1,1) eps_22(1,2) eps_22(1,3)
eps_22(1,4) eps_23(1,1) eps_23(1,2) eps_23(1,3) eps_23(1,4) eps_24(1,1) eps_24(1,2)
eps_24(1,3) eps_24(1,4);
67     eps_21(2,1) eps_21(2,2) eps_21(2,3) eps_21(2,4) eps_22(2,1) eps_22(2,2) eps_22(2,3)
eps_22(2,4) eps_23(2,1) eps_23(2,2) eps_23(2,3) eps_23(2,4) eps_24(2,1) eps_24(2,2)
eps_24(2,3) eps_24(2,4);
68     eps_21(3,1) eps_21(3,2) eps_21(3,3) eps_21(3,4) eps_22(3,1) eps_22(3,2) eps_22(3,3)
eps_22(3,4) eps_23(3,1) eps_23(3,2) eps_23(3,3) eps_23(3,4) eps_24(3,1) eps_24(3,2)
eps_24(3,3) eps_24(3,4);
69     eps_21(4,1) eps_21(4,2) eps_21(4,3) eps_21(4,4) eps_22(4,1) eps_22(4,2) eps_22(4,3)
eps_22(4,4) eps_23(4,1) eps_23(4,2) eps_23(4,3) eps_23(4,4) eps_24(4,1) eps_24(4,2)
eps_24(4,3) eps_24(4,4);
70
71     eps_31(1,1) eps_31(1,2) eps_31(1,3) eps_31(1,4) eps_32(1,1) eps_32(1,2) eps_32(1,3)
eps_32(1,4) eps_33(1,1) eps_33(1,2) eps_33(1,3) eps_33(1,4) eps_34(1,1) eps_34(1,2)
eps_34(1,3) eps_34(1,4);
72     eps_31(2,1) eps_31(2,2) eps_31(2,3) eps_31(2,4) eps_32(2,1) eps_32(2,2) eps_32(2,3)
eps_32(2,4) eps_33(2,1) eps_33(2,2) eps_33(2,3) eps_33(2,4) eps_34(2,1) eps_34(2,2)
eps_34(2,3) eps_34(2,4);
73     eps_31(3,1) eps_31(3,2) eps_31(3,3) eps_31(3,4) eps_32(3,1) eps_32(3,2) eps_32(3,3)
eps_32(3,4) eps_33(3,1) eps_33(3,2) eps_33(3,3) eps_33(3,4) eps_34(3,1) eps_34(3,2)
eps_34(3,3) eps_34(3,4);
74     eps_31(4,1) eps_31(4,2) eps_31(4,3) eps_31(4,4) eps_32(4,1) eps_32(4,2) eps_32(4,3)
eps_32(4,4) eps_33(4,1) eps_33(4,2) eps_33(4,3) eps_33(4,4) eps_34(4,1) eps_34(4,2)
eps_34(4,3) eps_34(4,4);
75

```

Figure D.20: Part 3 of 5 of MATLAB code to obtain the χ matrix.

```

76     eps_41(1,1) eps_41(1,2) eps_41(1,3) eps_41(1,4) eps_42(1,1) eps_42(1,2) eps_42(1,3)
eps_42(1,4) eps_43(1,1) eps_43(1,2) eps_43(1,3) eps_43(1,4) eps_44(1,1) eps_44(1,2)
eps_44(1,3) eps_44(1,4);
77     eps_41(2,1) eps_41(2,2) eps_41(2,3) eps_41(2,4) eps_42(2,1) eps_42(2,2) eps_42(2,3)
eps_42(2,4) eps_43(2,1) eps_43(2,2) eps_43(2,3) eps_43(2,4) eps_44(2,1) eps_44(2,2)
eps_44(2,3) eps_44(2,4);
78     eps_41(3,1) eps_41(3,2) eps_41(3,3) eps_41(3,4) eps_42(3,1) eps_42(3,2) eps_42(3,3)
eps_42(3,4) eps_43(3,1) eps_43(3,2) eps_43(3,3) eps_43(3,4) eps_44(3,1) eps_44(3,2)
eps_44(3,3) eps_44(3,4);
79     eps_41(4,1) eps_41(4,2) eps_41(4,3) eps_41(4,4) eps_42(4,1) eps_42(4,2) eps_42(4,3)
eps_42(4,4) eps_43(4,1) eps_43(4,2) eps_43(4,3) eps_43(4,4) eps_44(4,1) eps_44(4,2)
eps_44(4,3) eps_44(4,4)
80     ];
81
82
83     rho_11 = [ 1 0 0 0;
84               0 0 0 0;
85               0 0 0 0;
86               0 0 0 0];
87
88     rho_23 = [ 0 0 0 0;
89               0 0 1 0;
90               0 0 0 0;
91               0 0 0 0];
92
93     rho_32 = [ 0 0 0 0;
94               0 0 0 0;
95               0 1 0 0;
96               0 0 0 0];
97
98     rho_44 = [ 0 0 0 0;
99               0 0 0 0;
100              0 0 0 0;
101              0 0 0 1];
102
103     P_matrix = kron(eye(2),kron(rho_11+rho_23+rho_32+rho_44,eye(2)));
104
105     Delta_matrix = .5*[1 0 0 1;
106                      0 1 1 0;
107                      0 1 -1 0;
108                      1 0 0 -1];
109
110     Delta2_matrix = kron(Delta_matrix,Delta_matrix);
111
112     Chi=Delta2_matrix'*P_matrix'*preChi*P_matrix*Delta2_matrix;
113
114     %%%%%%%%%%%%%%%%%%%%%%%%%%%%%%%%%%%%%%%%%%%%%%%%%%%%%%%%%%%%%%%%%%%%%%%%%
115     % Perform convex optimization, i.e. find the best two-norm approximation with a physical
116     % chi matrix of a process
117     %%%%%%%%%%%%%%%%%%%%%%%%%%%%%%%%%%%%%%%%%%%%%%%%%%%%%%%%%%%%%%%%%%%%%%%%%
118
119     % The dimension of the chi matrix
120     n=16;
121
122     % the unphysical chi matrix

```

Figure D.21: Part 4 of 5 of MATLAB code to obtain the χ matrix.

```

123 chiunphys = Chi; %corrected_chi_real + i*corrected_chi_imag;
124
125 % let sdpvar know that chi matrix will be complex and hermitian
126 Chi=sdpvar(n,n,'hermitian','complex');
127
128 % enforce constraint of unit trace
129 F=set(trace(Chi)==1);
130
131 % enforce complete positivity
132 F=F+set(chi>=0);
133
134 % find the best two-norm approximation
135 solvesdp(F,trace((Chi-chiunphys)*(Chi-chiunphys)));
136 TwoNorm=sqrt(double(real(trace((Chi-chiunphys)*(Chi-chiunphys))))));
137 TwoNormChi=double(Chi);
138

```

Figure D.22: Part 5 of 5 of MATLAB code to obtain the χ matrix.

Bibliography

- [1] L. Allen and J. H. Eberly. *Optical Resonance and Two-Level Atoms*. Dover Publications, 1987.
- [2] M. Allman, F. Altomare, J. Whittaker, K. Cicak, D. Li, A. Sirois, J. Strong, J. D. Teufel, and R. W. Simmonds. *Phys. Rev. Lett.*, 104:177004, 2010.
- [3] M. Ansmann. *Benchmarking the Superconducting Josephson Phase Qubit: The Violation of Bell's Inequality*. PhD thesis, University of California, Santa Barbara, 2009.
- [4] M. Ansmann, H. Wang, R. C. Bialczak, M. Hofheinz, E. Lucero, M. Neeley, A. D. O'Connell, D. Sank, M. Weides, J. Wenner, A. N. Cleland, and J. M. Martinis. *Nature*, 461:504, 2009.
- [5] S. Ashhab, A. O. Niskanen, K. Harrabi, Y. Nakamura, T. Picot, P. C. de Groot, C. J. Harmans, J. Mooij, and F. Nori. *Phys. Rev. B*, 77:014510, 2008.
- [6] A. Barone and G. Paterno. *Physics and Applications of the Josephson Effect*. John Wiley and Sons, 1982.
- [7] J. S. Bell. On the problem of hidden variables in quantum mechanics. *Rev. Mod. Phys.*, 38(3):447–452, 1966.
- [8] C. H. Bennett, G. Brassard, C. Crépeau, R. Jozsa, A. Peres, and W. K. Wootters. Teleporting an unknown quantum state via dual classical and einstein-podolsky-rosen channels. *Phys. Rev. Lett.*, 70(13):1895–1899, Mar 1993.
- [9] N. Bergeal, F. Schackert, M. Metcalfe, R. Vijay, V. E. Manucharyan, L. Frunzio, D. E. Prober, R. J. Schoelkopf, S. M. Girvin, and M. H. Devoret. *Nature*, 465:64, 2010.

- [10] R. C. Bialczak, M. Ansmann, M. Hofheinz, M. Lenander, E. Lucero, M. Neeley, A. D. O’Connell, D. Sank, H. Wang, M. Weides, J. Wenner, T. Yamamoto, A. N. Cleland, and J. M. Martinis. Fast tunable coupler for superconducting qubits. *Phys. Rev. Lett.*, 106(6):060501, 2011.
- [11] R. C. Bialczak, M. Ansmann, M. Hofheinz, E. Lucero, M. Neeley, A. D. O’Connell, D. Sank, H. Wang, J. Wenner, M. Steffen, A. N. Cleland, and J. M. Martinis. Quantum process tomography of a universal entangling gate implemented with josephson phase qubits. *Nature Physics*, 6:409–413, 2010.
- [12] R. C. Bialczak, R. McDermott, M. Ansmann, M. Hofheinz, N. Katz, E. Lucero, M. Neeley, A. D. O’Connell, H. Wang, A. N. Cleland, and J. M. Martinis. $1/f$ flux noise in josephson phase qubits. *Phys. Rev. Lett.*, 99(18):187006, 2007.
- [13] V. Bouchiat, D. Vion, P. Joyez, D. Esteve, and M. H. Devoret. Quantum coherence with a single cooper pair. *Physica Scripta*, 1998(T76):165, 1998.
- [14] D. Bouwmeester, A. K. Ekert, and A. Zeilinger. *The Physics of Quantum Information: Quantum Cryptography, Quantum Teleportation, Quantum Computation*. Springer, Germany, 2010.
- [15] S. Boyd and L. Vandenberghe. *Convex Optimization*. Cambridge University Press, 2004.
- [16] M. P. A. Branderhorst, N. J., W. I. A., and K. R. L. Simplified quantum process tomography. *New Journal of Physics*, 11(11):115010, 2009.
- [17] M. J. Bremner, C. M. Dawson, J. L. Dodd, A. Gilchrist, A. W. Harrow, D. Mortimer, M. A. Nielsen, and T. J. Osborne. Practical scheme for quantum computation with any two-qubit entangling gate. *Phys. Rev. Lett.*, 89(24):247902, 2002.
- [18] A. M. Childs, I. L. Chuang, and D. W. Leung. Realization of quantum process tomography in nmr. *Phys. Rev. A*, 64(1):012314, 2001.
- [19] I. L. Chuang and M. A. Nielsen. Prescription for experimental determination of the dynamics of a quantum black box. *Journal of Modern Optics*, 44(11):2455–2467, 1997.
- [20] A. Church. An unsolvable problem of elementary number theory. *American Journal of Mathematics*, 58:345–363, 1936.
- [21] C. CohenTannoudji, B. Diu, and F. Laloe. *Quantum Mechanics (2 vol. set)*. Wiley-Interscience, 2006.

- [22] G. A. D’Ariano and L. Maccone. Quantum tomography for imaging. *Electronic Notes in Discrete Mathematics*, 20:133 – 150, 2005.
- [23] D. Deutsch. Quantum theory, the church-turing principle and the universal quantum computer. *Proceedings of the Royal Society of London. A. Mathematical and Physical Sciences*, 400(1818):97–117, 1985.
- [24] M. Devoret. *Fluctuations Quantiques / Quantum Fluctuations: Les Houches Session LXIII, June 27 - July 28, 1995. A UJFG / a NATO Advanced Study Institute conference. Edited by S. Reynaud, E. Giacobino and J. Zinn-Justin.* Elsevier, Amsterdam, The Netherlands, 1997.
- [25] M. Devoret, A. Wallraff, and J. Martinis. Superconducting qubits: A short review. *arXiv:cond-mat/0411174v1 [cond-mat.mes-hall]*, 2004.
- [26] M. H. Devoret and J. M. Martinis. Implementing qubits with superconducting integrated circuits. *Quantum Information Processing*, 3:163–203, 2004.
- [27] D. P. DiVincenzo. The physical implementation of quantum computation. *Fortschritte der Physik*, 48(9-11):771–783, 2000.
- [28] R. Feynman. Simulating physics with computers. *International Journal of Theoretical Physics*, 21:467–488, 1982.
- [29] K. Gottfried and T. M. Yan. *Quantum Mechanics: Fundamentals.* Springer, 2004.
- [30] L. Grover. A fast quantum mechanical algorithm for database search. *Proceedings, 28th Annual ACM Symposium on the Theory of Computing*, page 212, May 1996.
- [31] S. Haroche and J. Raimond. *Exploring the Quantum: Atoms, Cavities, and Photons (Oxford Graduate Texts).* Oxford University Press, USA, 2006.
- [32] R. Harris, A. J. Berkley, M. W. Johnson, P. Bunyk, S. Govorkov, M. C. Thom, S. Uchaikin, A. B. Wilson, J. Chung, E. Holtham, J. D. Biamonte, A. Y. Smirnov, M. H. S. Amin, and A. M. van den Brink. *Phys. Rev. Lett.*, 98, 2007.
- [33] T. Hime, P. A. Reichardt, B. L. T. Plourde, T. L. Robertson, C. E. Wu, A. V. Ustinov, , and J. Clarke. *Science*, 314:1427, 2006.
- [34] M. Howard, J. Twamley, C. Wittmann, T. Gaebel, F. Jelezko, and J. Wrachtrup. Quantum process tomography and linblad estimation of a solid-state qubit. *New Journal of Physics*, 8(3):33, 2006.

- [35] D. F. V. James, P. G. Kwiat, W. J. Munro, and A. G. White. Measurement of qubits. *Phys. Rev. A*, 64(5):052312, 2001.
- [36] P. R. Johnson, F. W. Strauch, A. J. Dragt, R. C. Ramos, C. J. Lobb, J. R. Anderson, and F. C. Wellstood. Spectroscopy of capacitively coupled josephson-junction qubits. *Phys. Rev. B*, 67(2):020509, 2003.
- [37] N. Katz, M. Ansmann, R. C. Bialczak, E. Lucero, R. McDermott, M. Neeley, M. Steffen, E. M. Weig, A. N. Cleland, J. M. Martinis, and A. N. Korotkov. Coherent State Evolution in a Superconducting Qubit from Partial-Collapse Measurement. *Science*, 312(5779):1498–1500, 2006.
- [38] P. Kaye, R. Laflamme, and M. Mosca. *An Introduction to Quantum Computing*. Oxford University Press, USA, 2007.
- [39] A. G. Kofman and A. N. Korotkov. Two-qubit decoherence mechanisms revealed via quantum process tomography. *Phys. Rev. A*, 80(4):042103, 2009.
- [40] A. G. Kofman, Q. Zhang, J. M. Martinis, and A. N. Korotkov. Theoretical analysis of measurement crosstalk for coupled josephson phase qubits. *Phys. Rev. B*, 75(1):014524, 2007.
- [41] R. L. Kosut. Quantum Process Tomography via L1-norm Minimization. *arXiv:0812.4323v2 [quant-ph]*, 2008.
- [42] T. D. Ladd, F. Jelezko, R. Laflamme, Y. Nakamura, C. Monroe, and J. L. O’Brien. *Nature*, 94:45–53, 2010.
- [43] M. Lenander, H. Wang, R. C. Bialczak, E. Lucero, M. Mariani, M. Neeley, A. D. O’Connell, D. Sank, M. Weides, J. Wenner, T. Yamamoto, Y. Yin, J. Zhao, A. N. Cleland, and J. M. Martinis. Energy decay and frequency shift of a superconducting qubit from non-equilibrium quasiparticles. *arXiv:1101.0862v1 [cond-mat.supr-con]*, 2011.
- [44] B. G. Levi. *Physics Today*, 62:14, 2009.
- [45] Y.-x. Liu, L. F. Wei, and F. Nori. Tomographic measurements on superconducting qubit states. *Phys. Rev. B*, 72(1):014547, 2005.
- [46] L. Ljung. *System Identification: Theory for the User*. Prentice Hall, 1999.
- [47] E. Lucero, M. Hofheinz, M. Ansmann, R. C. Bialczak, N. Katz, M. Neeley, A. D. O’Connell, H. Wang, A. N. Cleland, and J. M. Martinis. High-fidelity gates in a single josephson qubit. *Phys. Rev. Lett.*, 100(24):247001, 2008.

- [48] J. Martinis. *Macroscopic Quantum Tunneling and Energy-Level Quantization in the Zero Voltage State of the Current-Biased Josephson Junction*. PhD thesis, University of California, Berkeley, 1985.
- [49] J. Martinis. Superconducting phase qubits. *Quantum Information Processing*, 8:81–103, 2009.
- [50] J. M. Martinis, K. B. Cooper, R. McDermott, M. Steffen, M. Ansmann, K. D. Osborn, K. Cicak, S. Oh, D. P. Pappas, R. W. Simmonds, and C. C. Yu. Decoherence in josephson qubits from dielectric loss. *Phys. Rev. Lett.*, 95(21):210503, 2005.
- [51] J. M. Martinis, S. Nam, J. Aumentado, K. M. Lang, and C. Urbina. Decoherence of a superconducting qubit due to bias noise. *Phys. Rev. B*, 67(9):094510, 2003.
- [52] J. M. Martinis, S. Nam, J. Aumentado, and C. Urbina. Rabi oscillations in a large josephson-junction qubit. *Phys. Rev. Lett.*, 89(11):117901, 2002.
- [53] R. McDermott. Materials origins of decoherence in superconducting qubits. *Applied Superconductivity, IEEE Transactions on*, 19(1):2–13, 2009.
- [54] R. McDermott, R. W. Simmonds, M. Steffen, K. B. Cooper, K. Cicak, K. D. Osborn, S. Oh, D. P. Pappas, and J. M. Martinis. Simultaneous State Measurement of Coupled Josephson Phase Qubits. *Science*, 307(5713):1299–1302, 2005.
- [55] J. E. Mooij, T. P. Orlando, L. Levitov, L. Tian, C. H. van der Wal, and S. Lloyd. Josephson persistent-current qubit. *Science*, 285(5430):1036–1039, 1999.
- [56] Y. Nakamura, Y. A. Pashkin, and J. S. Tsai. Coherent control of macroscopic quantum states in a single-cooper-pair box. *Nature*, 398(6730):786–788, 1999.
- [57] M. Neeley, M. Ansmann, R. C. Bialczak, M. Hofheinz, N. Katz, E. Lucero, A. O’Connell, H. Wang, A. N. Cleland, and J. M. Martinis. Transformed dissipation in superconducting quantum circuits. *Phys. Rev. B*, 77(18):180508, 2008.
- [58] M. A. Nielsen and I. L. Chuang. *Quantum Computation and Quantum Information*. Cambridge University Press, 2000.
- [59] A. O. Niskanen, K. Harrabi, F. Yoshihara, Y. Nakamura, S. Lloyd, and J. S. Tsai. *Science*, 316:723–6, 2007.
- [60] J. L. O’Brien, G. J. Pryde, A. Gilchrist, D. F. V. James, N. K. Langford, T. C. Ralph, and A. G. White. Quantum process tomography of a controlled-not gate. *Phys. Rev. Lett.*, 93(8):080502, 2004.

- [61] M. Paris and J. Rehacek. *Quantum State Estimation: Series: Lecture Notes in Physics*, volume 649. Springer, 2004.
- [62] R. A. Pinto, A. N. Korotkov, M. R. Geller, V. S. Shumeiko, and J. M. Martinis. Analysis of a tuneable coupler for superconducting phase qubits, 2010.
- [63] J. H. Plantenberg, P. C. de Groot, C. J. P. M. Harmans, and J. E. Mooij. Demonstration of controlled-NOT quantum gates on a pair of superconducting quantum bits. *Nature*, 447(7146):836–839, 2007.
- [64] D. M. Pozar. *Microwave Engineering*. Wiley, 2004.
- [65] M. Riebe, K. Kim, P. Schindler, T. Monz, P. O. Schmidt, T. K. Korber, W. Hansel, H. Haffner, C. F. Roos, and R. Blatt. Process tomography of ion trap quantum gates. *Phys. Rev. Lett.*, 97(22):220407, 2006.
- [66] J. Sakurai. *Modern Quantum Mechanics (Revised Edition)*. Addison Wesley, 1993.
- [67] N. Schuch and J. Siewert. Natural two-qubit gate for quantum computation using the xy interaction. *Phys. Rev. A*, 67(3):032301, 2003.
- [68] S. Sendelbach, D. Hover, A. Kittel, M. Mück, J. M. Martinis, and R. McDermott. Magnetism in squids at millikelvin temperatures. *Phys. Rev. Lett.*, 100(22):227006, 2008.
- [69] P. W. Shor. Polynomial-time algorithms for prime factorization and discrete logarithms on a quantum computer. *SIAM Review*, 41(2):303–332, 1999.
- [70] R. W. Simmonds, K. M. Lang, D. A. Hite, S. Nam, D. P. Pappas, and J. M. Martinis. Decoherence in josephson phase qubits from junction resonators. *Phys. Rev. Lett.*, 93(7):077003, 2004.
- [71] R. Solovay and V. Strassen. A fast monte-carlo test for primality. *SIAM Journal on Computing*, 6(1):84–85, 1977.
- [72] C. Song, M. P. DeFeo, K. Yu, and B. L. T. Plourde. *Appl. Phys. Lett.*, 95:232501, 2009.
- [73] M. Steffen. *A Prototype Quantum Computer Using Nuclear Spins in Liquid Solution*. PhD thesis, Stanford University, 2003.

- [74] M. Steffen, M. Ansmann, R. C. Bialczak, N. Katz, E. Lucero, R. McDermott, M. Neeley, E. M. Weig, A. N. Cleland, and J. M. Martinis. Measurement of the Entanglement of Two Superconducting Qubits via State Tomography. *Science*, 313(5792):1423–1425, 2006.
- [75] M. Steffen, M. Ansmann, R. McDermott, N. Katz, R. C. Bialczak, E. Lucero, M. Neeley, E. M. Weig, A. N. Cleland, and J. M. Martinis. State tomography of capacitively shunted phase qubits with high fidelity. *Phys. Rev. Lett.*, 97(5):050502, 2006.
- [76] M. Steffen, J. M. Martinis, and I. L. Chuang. Accurate control of josephson phase qubits. *Phys. Rev. B*, 68(22):224518, 2003.
- [77] O. Steuernagel and J. A. Vaccaro. Reconstructing the density operator via simple projectors. *Phys. Rev. Lett.*, 75(18):3201–3205, 1995.
- [78] F. W. Strauch, P. R. Johnson, A. J. Dragt, C. J. Lobb, J. R. Anderson, and F. C. Wellstood. Quantum logic gates for coupled superconducting phase qubits. *Phys. Rev. Lett.*, 91(16):167005, 2003.
- [79] S. Thornton and J. B. Marion. *Classical Dynamics of Particles and Systems*. Brooks Cole, 2003.
- [80] R. J. Tocci, N. Widmer, and G. Moss. *Digital Systems: Principles and Applications*. Prentice Hall, 2006.
- [81] A. M. Turing. On computable numbers, with an application to the entscheidungsproblem. *Proceedings of the London Mathematical Society*, s2-42(1):230–265, 1937.
- [82] D. Vion, A. Aassime, A. Cottet, P. Joyez, H. Pothier, C. Urbina, D. Esteve, and M. Devoret. Rabi oscillations, ramsey fringes and spin echoes in an electrical circuit. *Fortschritte der Physik*, 51(4-5):462–468, 2003.
- [83] A. Wallraff, D. I. Schuster, A. Blais, L. Frunzio, J. Majer, M. H. Devoret, S. M. Girvin, and R. J. Schoelkopf. Approaching unit visibility for control of a superconducting qubit with dispersive readout. *Phys. Rev. Lett.*, 95(6):060501, Aug 2005.
- [84] M. Weissbluth. *Photon-Atom Interactions*. Academic Press, 1989.
- [85] G. Wendin and V. Shumeiko. *Superconducting Quantum Circuits, Qubits and Computing (prepared for Handbook of Theoretical and Computational Nanotechnology)*. Cambridge University Press, 2006.

- [86] A. G. White, A. Gilchrist, G. J. Pryde, J. L. O'Brien, M. J. Bremner, and N. K. Langford. Measuring two-qubit gates. *J. Opt. Soc. Am. B*, 24(2):172–183, 2007.
- [87] T. Yamamoto, Y. Pashkin, O. Astafiev, Y. Nakamura, and J. S. Tsai. Demonstration of conditional gate operation using superconducting charge qubits. *Nature*, 425(6961):941–944, 2003.
- [88] Q. Zhang, A. G. Kofman, J. M. Martinis, and A. N. Korotkov. Analysis of measurement errors for a superconducting phase qubit. *Phys. Rev. B*, 74(21):214518, 2006.